Simulation of the Atmospheric Pressure Interface of a Mass Spectrometry Device

vorgelegt von
M. Sc.
Laurent Bernier

an der Fakultät V – Verkehrs- und Maschinensysteme
der Technischen Universität Berlin
zur Erlangung des akademischen Grades

Doktor der Ingenieurwissenschaften
- Dr. Ing. -

genehmigte Dissertation

Promotionsausschuss:

Vorsitzender: Prof. Dr.-Ing. Ennes Sarradj
Gutachter: Prof. Dr. Tobias Lau
Gutachter: Prof. Dr.-Ing. Dieter Peitsch
Gutachter: Prof. Dr. Stefan Rauschenbach
Gutachter: Prof. Dr. Julius Reiss

Tag der wissenschaftlichen Aussprache: 19. November 2021

Berlin 2022

TECHNISCHE UNIVERSITÄT BERLIN

DOCTORAL THESIS

Simulation of the Atmospheric Pressure Interface of a Mass Spectrometry Device

Author:
Laurent BERNIER

Supervisor:
Prof. Dr. Julius REISS

Examining committee:
Prof. Dr. Tobias LAU
Prof. Dr. Dieter PEITSCH
Prof. Dr. Stephan RAUSCHENBACH
Prof. Dr. Julius REISS

Chairman:
Prof. Dr. Ennes SARRADJ

A thesis submitted in fulfillment of the requirements for the degree of Doctor of Engineering

in the

Department of Numerical Fluid Dynamics
Institute of Fluid Dynamics and Technical Acoustics

March 22, 2022

TECHNISCHE UNIVERSITÄT BERLIN

Abstract

Fakultät V - Mechanical Engineering and Transport Systems
Institute of Fluid Dynamics and Technical Acoustics

Doctor of Engineering

Simulation of the Atmospheric Pressure Interface of a Mass Spectrometry Device

by Laurent BERNIER

This thesis presents the results of the simulation of two different parts from the typical atmospheric interface found in a mass spectrometer: the transfer capillary and the ion funnel. These are usually found in combination with electrospray ionization and allow the transition between atmospheric pressure and vacuum. The main goal of the study is to simulate the trajectory of the ions transported through such devices. We thus consider all significant effects involved: the underlying gas flow, the diffusion, and the electric forces, both intrinsic because of the charge of the ions (space charge effects) and caused by external settings, typically electrodes.

In the case of the capillary, we could qualitatively reproduce typical effects observed in real devices, such as the transmission limit caused by space charge effects and the influence of the heating. We could also simulate the influence of the geometry of the capillary and reproduce the experimental behavior induced by the transport of a mix of ions from different species. These results are based on the assumption of a laminar gas flow. Further simulations are presented regarding the affinity of such flow towards turbulence. It results that, despite its strong pressure gradient, this system can sustain a fully turbulent flow without significantly affecting the properties of turbulence.

Further results are presented involving an existing design of the ion funnel. Detailed simulations of the gas flow and the electric fields created by the electrodes are performed and used to describe the transport of the ions. We compare the influence of the amplitude of the external electric field and of the background pressure level on the transmission of the ions with experimental results to show that this first attempt delivers promising results. An evolution of the design of the ion funnel is also considered. While it does not deliver the expected improvement regarding the transmission, it offers an insight into the mechanisms involved and provides some information about how a desirable system could look like.

TECHNISCHE UNIVERSITÄT BERLIN

Zusammenfassung

Fakultät V - Mechanical Engineering and Transport Systems
Institute of Fluid Dynamics and Technical Acoustics

Doctor of Engineering

Simulation of the Atmospheric Pressure Interface of a Mass Spectrometry Device

von Laurent BERNIER

Diese Arbeit stellt die Ergebnisse der Simulationen von zwei verschiedenen Anteilen eines typischen atmosphärischen Druck-Interface vor, die in einem Massenspektrometer zu finden sind: die Transferkapillare und den Ionentrichter. Diese werden oft in Kombination mit einer Elektrosprayionenquelle verwendet und stellen die Schnittstelle zwischen atmosphärischem Druck und Vakuum dar. Das Hauptziel der Studie besteht darin, die Flugbahn der durch diese Anteile transportierten Ionen zu simulieren. Dafür werden alle relevante Einflüsse berücksichtigt: die Gasströmung, die Diffusionseffekte und die elektrischen Kräfte, die sowohl wegen der Ladung der Ionen (Raumlagundseffekte) als auch aus externen Quellen wie Elektroden entstehen.

Im Fall der Kapillare konnten wir bestimmte Effekte qualitativ reproduzieren. Dazu zählen die Transmissionsgrenze, die aus der Raumladung entsteht, und die Auswirkung der Heizung. Wir konnten auch den Einfluss der Geometrieparameter simulieren und das experimentelle Verhalten des Transports einer Mischung von Ionen reproduzieren. Diese Ergebnisse basieren auf der Annahme einer laminaren Strömung. Weitere Simulationen werden auch gezeigt, die die Turbulenzaffinität einer solchen Strömung untersuchen. Es ergibt sich, dass Systeme mit starken Druckgradienten in der Lage sind, eine volle turbulente Strömung zu erhalten, ohne signifikant die Eigenschaften der Turbulenz zu beeinflussen.

Weitere Ergebnisse über einen existierenden Ionentrichter werden vorgezeigt. Detaillierte Simulationen der Gasströmung und der von den Elektroden erzeugten elektrischen Felder wurden durchgeführt und weiterverwendet, um den Transport der Ionen zu beschreiben. Wir vergleichen den Einfluss der Amplitude der externen elektrischen Felder und des Drucks auf der Transmission der Ionen mit experimentellen Ergebnissen und zeigen, dass dieser erste Versuch vielversprechende Ergebnisse liefert. Eine mögliche Evolution des Designs des Ionentrichters wird auch untersucht. Obwohl dies keine positiven Ergebnisse bezüglich der Ionentransmission erbringt, ermöglichen diese Simulationen einen Einblick in die involvierten Mechanismen und liefern somit Informationen über die gewünschten Eigenschaften eines verbesserten Systems.

Acknowledgements

This thesis has been funded by the Deutsche Forschungsgemeinschaft, mainly in project number 268758079, with additional funding by the research cluster SFB 1029.

I would not have been able to complete this project successfully without the help of many colleagues, family, and friends, throughout these three and a half years. I dedicate this work to all of them.
I would like to thank specifically Julius Reiss, who has been my supervisor for many years. He offered me the opportunity to work on this project and has always been of good help to overcome the difficulties that occurred during the project.
I also would like to thank Stephan Rauschenbach who has always been ready to share his practical knowledge about mass spectrometry and his deeper understanding of the systems we wanted to simulate. I also associate here Paul Fremdling, who performed the experiments exposed in this work and helped me to decipher the results he produced. Without their help and dedication, our simulations wouldn't have the same relevance.
I also could always count on my colleagues on the Schleusininsel. I sincerely thank all of them for the fruitful discussions and constant support. Furthermore, Philipp Krah has done a tremendous job by implementing many new features in the WABBIT-code to simulate the ion funnel. That allowed Loukas Kyriakidis to test many configurations, and his results have been of great help. Gabriele Camerlengo was also of great help to explore the features of NSF and to deliver meaningful turbulent results.
And finally, many thanks to my family members back in France who always supported me when I most needed it.

Contents

Chapter 1

Introduction

1.1 Mass spectrometry

1.1.1 Discovery of mass spectrometry

Mass spectrometry goes back to the first decades of the twentieth century when Joseph John Thomson was able to separate two isotopes of neon in 1913 (Thomson 1913). After discovering the electron, he followed the work of Goldstein who discovered the positive ray (Kanalstrahlen) and analyzed the deflection of positively charged gas beams, as recalled by I. W. Griffiths (1997). This experience is considered as the first meaningful occurrence of the underlying principle of mass spectrometry and launched the development of this technique still used until now.

It relies on the fact that particles with different electric charge and mass have different behaviors when moving within an electromagnetic field. The main parameter to consider is the ratio mass over charge, often referred to as m/z. This was a significant step forward at a time when the atomic structure of the different elements was not as well understood as it is now. At that time, ions of neon were produced inside a gas-discharge tube. Electric and magnetic fields led to deviations of the path of the different ions, materialized via photographic plates. Different isotopes having different masses, they produce different patterns on the photographic plate and Thomson was thus able to demonstrate the existence of two isotopes of neon in his experiment: ^{20}Ne and ^{22}Ne.

1.1.2 Primary usages and their evolution

This experiment was not only significant for the understanding of the atomistic structure but also paved the way for the development of a range of methods used to identify species in numerous contexts. As an analytical tool, mass spectrometers are used for various applications. Its historical one, the differentiation of different isotopes of an element, is still valuable and can be used to analyze isotope of the ions, as described by Gross (2011, chapter 2). But it was also extended to the detection and analysis of species and mix of species. When the ions present in a sample are unknown, the mass spectrometry analysis allows to identify them according to the m/z ratio measured. This finds application for example in forensics when investigators try to confirm whether a probe contains a specific species.

It is also used in different domains such as biology, including proteomics, lipidomics, metabolomics, DNA or RNA studies, etc. which all propose to analyze molecules or processes involved in living bodies. In such contexts, mass spectrometry is either used to identify complete molecules or to study the structure of a given molecule. The idea is then to analyze the structure of a molecule considering its fragments. The weakest bounds of the molecules are broken in a controlled process. The

resulting fragments are usually known basic structures, which can then be identified using mass spectrometry.

1.2 Ion sources

1.2.1 Historic sources

All these applications require to first produce ions out of the considered samples, whatever the subsequent usage is. The historical means consisted of applying a strong electric potential between two electrodes placed in a glass container. The gas object of the study was inside and started to glow under appropriate conditions. That meant that positively and negatively charged ions were forming. However, this technique only applied to a limited number of elements and the ionization became the focus of different studies. Smyth and Bleakney, e.g., focused on the ionization of mercurial in the 1920s, using streams of electrons produced by a heated filament, a technique called electron ionization (EI) developed by Dempster in 1918, as reported in Traeger (2016). This marked the start of the development of techniques based on electron beams, which remain relevant nowadays. However, the expansion of usages of mass spectrometry meant that always more complex molecules were considered, up to very large organic ones as present in biologic samples.

1.2.2 Development of soft methods

This initiated the development, in the last four decades, of softer techniques which can ionize large molecules such a way that they keep their entire structure or even their initial conformation. Different options are now available. MALDI (matrix-assisted laser desorption ionization) uses a matrix that contains the sample to analyze. A laser beam is focused on the matrix, out of which gas-phase ions are produced. During this process, molecules of the sample are also transferred to the gas phase and can exchange electric charges with the matrix ions, thus creating the ions further used in the mass spectrometer. This process can occur either in vacuum or at atmospheric pressure.

Another widespread technique, the electrospray ionization (ESI), creates ions at atmospheric pressure. It was first reported in 1984 by Masamichi Yashamita and John Fenn and published in Fenn et al. (1989). John Fenn was awarded the Nobel Prize for this work in 2002. The technique applies to samples present in a liquid solvent and relies on the limited electric charge that a droplet can contain before instabilities occur. The idea is to create droplets of the solvent containing ions of the sample of interest. These droplets are produced by applying a strong potential difference between a capillary containing the solvent and the sample molecules on the one hand and an external element, or counter-electrode, on the other hand. In such conditions, a so-called Taylor cone forms at the tip of the capillary. Droplets then detach from this structure. By evaporation of the solvent, called desolvation, the charge becomes too large with respect to the volume of the droplet. The resulting instabilities trigger the production of droplet cascades eventually delivering gas-phase ions. While the exact process is not yet fully understood, a description proposed by Kebarle and Tang (1993) is widely accepted as reasonable. However, further mechanisms, depending on the kind of analyte in the sprayed solution, have been exposed in Konermann et al. (2013). This kind of ionization generally works at atmospheric pressure and is the one used in the device further studied in this

work. Devices involving ESI at lower pressure have also been developed as described in Tang et al. (2012), even if such ones are much less widespread.

An evolution of this technique, the DESI (desorption electrospray ionization), differs from ESI by the fact that the sample molecules are not contained in the solvent. The potential difference is rather applied between the capillary containing the solvent and the sample. The charged solvent droplets created are thus directed towards the sample. Their interaction produces the gas-phase ions out of the sample.

It is not uncommon to further extend the techniques involved in the production of the ions sample introduced in the mass spectrometer. In particular, a first separation of the species contained in the primary system to study can be performed. The first kind of such techniques involved chromatography, realized either in gaseous or liquid phases and leading to systems called gas chromatography - mass spectrometry (GC-MS) or liquid chromatography - mass spectrometry (LC-MS). Further combinations have been developed, forming a large range of options, sometimes referred to as *hyphenated techniques* (due to their denomination), as reported in Gross (2011, chapter 14).

1.2.3 Consequences for the applications

These soft ionization techniques, especially ESI, have made it possible to consider a new range of molecule and to analyze them with mass spectrometry. Classic methods are usually limited to relatively small molecules or the fragments of larger ones. Also, the conformation of those molecules may be altered by the traditional ionization process. In contrast, soft methods are often used in combination with very large and complex molecules, in particular when they should be analyzed as complete structures. This allowed the development of new domains, for example in biology. A specific application is native mass spectrometry, for which an overview can be found in Heck (2008), and Leney and Heck (2017). The goal is to understand the fine processes at stake in such molecules, especially the topology and dynamics of proteins, while keeping their structure intact during the investigation. Soft ionization methods also enable the analysis of very large structures such as RNA, DNA, or viruses. A difference can be reported between ESI and MALDI. The latter tends to produce singly charged ions only. This means that one species is likely to produce only one signal in the spectrum. On the contrary, ESI can lead to multiply charged ions and such several signals for a single species, reflecting the different charge status. However, a larger charge implies a smaller m/z ratio. Those large structures are thus more likely to fall within the range of m/z the mass spectrometer can deal with.

Other applications are also expanding, making use of the appliance built around the mass spectrometer but for different purposes. It has been used to separate isotopes of an element, with applications ranging from nuclear reactions to the quantification of these isotopes for dating purposes. A review of such usages can be found e.g. in Litherland, Zhao, and Kieser (2011). The interaction of the ions with surfaces also opens up important applications. Especially coupled with mild ionization techniques, in order to keep intact large molecules and their functional structure, and using relatively small landing energies (so-called soft landing), it makes it possible to create tailored surfaces. Reviews of these applications can be found in Verbeck, Hoffmann, and Walton (2012) and Rauschenbach et al. (2016).

1.3 Towards atmospheric pressure interface

1.3.1 Development of complex systems

Between the production of the ions and the mass spectrum produced by the devices, the ions are transported and traditionally undergo different steps to produce a signal dependent on the m/z ratio. While the first experiments used a qualitative detection involving a photographic plate to detect the position of the ion beams in a given plane, modern techniques use different technologies and combinations of elementary steps to produce the expected signal.

This signal results from the behavior of the ions being specific to the m/z ratio. This is achieved via different ions' trajectories in a vacuum when evolving in an electromagnetic field. Several options can be used there. Historically, a different deflection angle of the ions when going through a specific magnetic field lead, as on the photographic plate, to spatial localization of the different species. Modern devices deliver quantitative results in the form of mass spectra. This is generally done by measuring the current passing through an electrode as the result of ions hitting it. It can be based on different physical principles yielding different results depending on the m/z ratio. The historical method of different deviations can be realized using magnetic sectors. Using different ions' velocities is also an option. This occurs either in line, in so-called time-of-flight (TOF) devices, or around an axis and then using a Fourier transform to gain the mass spectrum (cyclotrons devices). A principle similar to the latter is found in orbitrap devices, where an additional oscillation of the ions is considered. Another category relies on the trapping induced by multipoles (often, but not only, quadrupoles) submitted to a specific electric field.

In modern applications, several blocks deriving from the listed techniques can be stacked together to improve the sensitivity of the analyses or develop specific features. Historically, the electron ionization did not only produce the expected analyte but also fragments thereof, due to the internal energy transferred during the ionization process. It was thus possible to directly get information regarding the structure of the molecule. However, the development of softer methods led to cleaner samples and cleaner spectra, where only the presence of the analyte is detected. Tandem mass spectrometers were developed, as described in Gross (2011, chapter 9), in order to adapt the usage to this new environment. Classically, two stages of mass spectrometry are present in the device, often referred to as MS/MS. After the first detection of the analyte, some kind of fragmentation is performed, allowing one to get indications on the structure of the molecule.

The two stages of mass spectrometry can be performed by different elements in the devices. A common combination is, for example, a quadrupole followed by a time-of-flight analyzer. Several other associations are also found, though. In such case, one refers to them as *tandem-in-space*, because the mass spectrometry is performed by two physically different stages of the spectrometer. However, one also finds so-called *tandem-in-time* devices, where the mass spectrometry analysis is delivered by the same stage. First the analyte is selected, e.g. in a quadrupole, the other species being discarded. After a fragmentation performed in place, a second analysis can be realized to get an insight into the structure of the molecule. This process can even be repeated more than twice, to deliver an even more refined analysis of the species considered. A review of these different techniques and their combination can also be found in El-Aneed, Cohen, and Banoub (2009).

Overall, the development of the usages associated to mass spectrometry, and the sophistication of the techniques involved, lead to always more complex devices.

This includes stages involving fragmentation, chemical reactions, ion deposition and increase the number of stages and environments the ions are going through. Especially, all the techniques just presented work in a vacuum or at least at very low pressure, where the trajectory of the ions is directly defined by electromagnetic fields and does not depend on any surrounding gas. This means that when the ion source operates at atmospheric pressure, as this is usually the case for electrospray ionization, a strong pressure gradient exists between the different stages. In such case, the ion source is called atmospheric pressure ionization (API) and needs to be combined with an interface to the rest of the mass spectrometer. The study and simulation of one type of such interface is the purpose of this work.

1.3.2 Interface between high and low pressure elements

This interface can take several forms. Typically, the ions generated at atmospheric pressure enter the mass spectrometer via a capillary, which is a long and thin tube. However, its dimensions vary a lot depending on the device considered. Some designs limit it to a pinhole as reported in Lin and Sunner (1994), or further studied in Zhou et al. (2006) and Zhou and Ouyang (2016). After the capillary, the pressure is significantly lower than the atmospheric pressure. Depending on the design, it can reach values around 1 - 10 mbar. These values remain still too high for proper usage of the mass spectrometer, which requires pressure levels in the order of magnitude of 10^{-4} - 10^{-6} mbar. Pumping stages are thus present between the ion source and the mass spectrometer itself, which tend to extract the remaining gas from the system. Each step presents a pressure some orders of magnitude lower than the previous one. Two options are usually possible for the first stage. The historical one is a so-called skimmer, which is a cone located shortly after the gas jet coming out of the capillary or pinhole. It has a thin hole at its tip to allow the ions to enter the next stage, while the major part of the gas is deflected along its sides. A static electric field is used to guide the ions. This structure is sometimes also shifted from the symmetry axis of the capillary, to limit the quantity of gas entering the next chamber, as described in Gimelshein et al. (2014). Another design was later developed: the ion funnel. It was first presented by Shaffer et al. (1997) and consists of a succession of electrodes to which an alternating electric field is applied. The electrodes present a hole in their center and are placed orthogonally to the symmetry axis of the capillary. This forms a cavity with a funnel shape towards the next chamber. The gas and the ions come from the capillary inside this cavity. The gas is pumped out and flows between the electrodes, while the electric field applied to them make sure that the ions remain in the cavity. A static electric field and the remaining gas flow ensure that these ions are transported towards the next chamber.

Due to the very different properties of the environment at both ends of the atmospheric pressure interface, the processes involved present significant differences. Especially, the trajectory of the ions is not influenced the same way. Electromagnetic fields are essential at very low pressure. All methods presented here to produce mass spectra indeed rely at some level on the response of the charged particles to a given external field. This factor is then mostly sufficient to describe the ions' behavior. However, at higher pressure levels, the presence of the surrounding gas leads to different effects. While the external fields are still relevant, other influences need to be taken into account in order to properly describe the trajectory of the ions. The molecular interaction between the gas particles and the ions results in a complex behavior, for example when a macroscopic movement of the gas occurs. It thus

becomes difficult to understand and predict the influence of the different elements present in the device.

1.4 Framework of the present work

1.4.1 Understanding of the transport and loss processes

One of the main objectives following the production of the ions at atmospheric pressure is to transport them towards the core of the mass spectrometer, where the analysis occurs or even further when other applications are considered. However, losses may occur throughout the transfer. Many causes are involved, but Kelly et al. (2008) report that the majority of the losses are concentrated at the ion production stage and within the atmospheric pressure interface. In some designs, the quantity of analyte even decrease by three orders of magnitudes through the interface, as reported by Gao, Cooks, and Ouyang (2008). The first hurdle is to let the newly created ions enter the mass spectrometer via the capillary. This is a first and potentially significant source of losses. Many parameters are to consider though, from the desolvation process to the number of ions expected to enter the device. In some cases, the flow of ions is orthogonal to the capillary and a counter-flow of curtain gas can enhance the evaporation of the solvent. The ions are then sucked into the device due to the gas flow and the electric potential difference used for the electrospray ionization. In other cases, the emitter is located in line with the capillary and relatively close to it. In any case, the ions are then guided into the first pump chamber via the capillary. This element is also a source of losses, due to the interaction between the ions and the walls. In the next stage, the first pumping chamber, where an initial separation between ions and gas is performed. Losses are again expected in this area, e.g. depending on the operating conditions of the electrodes with an ion funnel. The amplitude of the alternating field applied or its frequency affect the electric forces used to counter the gas flow and influence the transmission of the ions towards the second pumping stage.

In many applications, from the classic analysis of the species present to the deposition on surfaces, the quantity of ions transferred up to the core of the device is an important criterion to deliver proper results. In the traditional usage of a mass spectrometer, the quantity of ions is indeed responsible for the sensitivity of the mass spectrum. Too small quantities can deliver noisy spectra or even alter the detection of species. For other usages, where the goal is to transfer the ions on a target surface via soft-landing, the quantity of ions is also of significant importance. As described in Gunaratne et al. (2015), higher quantities of ions transported through the device mean that higher quantities of ions can be deposited on a given surface in a reasonable amount of time. The authors report that several hours of continuous deposition are necessary to coat a surface smaller than 1 cm^2 for them to be analyzed with infrared techniques. As a matter of illustration, a current of 1 nA would deliver the required amount of singly charged ions in slightly less than half an hour. Accounting for multiply charged ions and/or losses during the deposition process, this order of magnitude is coherent. However, this also means that treating larger surfaces or requiring larger quantities (e.g. to use with nuclear magnetic resonance spectroscopy) remains out of reach for current devices. Increasing the quantity of ions transported further makes it possible to use detection techniques or the production of numerous products for which the quantity of molecules is important. It is thus essential to reduce the losses and enhance the absolute quantity of ions transported to make the method more competitive.

The goal of the present work is to shed light on the processes occurring during the transfer of the ions through this atmospheric pressure interface by simulating the precise behavior of the ions. The chosen set up mimics an ESI emitter, followed by a capillary using a funnel-shaped inlet and finally leading to an ion funnel. Two designs of the ion funnel are considered: a classic one and a tentative evolution. In the latter, the shape of the cavity formed by the electrodes and the distance between them has been modified.

1.4.2 Usage of the numerical simulations

As already stated, mass spectrometry devices and especially atmospheric pressure interfaces are very complex systems. Furthermore, direct experimental measurements within the device are difficult because of the lack of accessibility or the risk of modifying the operating condition when installing massive measurement devices. We thus strive to develop a comprehensive numerical simulation of such systems, in order to describe the behavior of the ions during their transport. The environment affecting this behavior is also part of the analysis. This encompasses the gas flow created by the differential pumping in the first chamber as well as the electric field created by the potential imposed on the different components of the system. The numerical model is not able to reproduce all effects present. First because including everything in the model would lead to an impractical model, unable to deliver results in a reasonable amount of time. Second because some parameters of the system are not well known, especially regarding the boundary conditions to impose. The purpose of the numerical model is thus not to exactly reproduce the experimental system, but to deliver a better description of the phenomena involved in the transport of the ions. Using simple but sensible hypotheses, it allows to produce global results which are compared to experimental measurements. This enables some degree of validation of the model. Furthermore, it offers a more detailed description of the ions' behavior, offering in turn micro-scale explanations for the macroscopic results generally observed.

1.4.3 State of the art

Numerous studies have been done to improve the number of ions transmitted. The capillary has been studied in Page et al. (2007), where the influence of different parameters regarding the ions transmission has been studied. Its geometry was also considered, from its length in Page et al. (2009) to the shape in S. Wu et al. (2006) and Pauly et al. (2014). The results of the latter were the starting point of the present work. The first pumping chamber was also thoroughly studied. A major improvement was brought by the first use of the ion funnel, compared to the previous designs. The first concept described in Shaffer et al. (1997) announces transmissions up to an order of magnitude higher than a similar experience with a then traditional skimmer design. We present here the characteristics relative to the capillary and ion funnel, which we are interested in for this work, as well as the existing attempts to simulate their operating condition.

Capillary

The capillary is a thin pipe connecting the atmospheric pressure region to the subsequent apparatus. It was introduced by Whitehouse et al. (1985). This principle remains in most of the designs and intends to transfer thermal energy to the droplets

created by the electrospray ionization to enhance the desolvation process. Despite its apparent simplicity, different arrangements of capillary can be found. First, length and diameter of the pipe can vary in different devices or depending on the application. The diameter is traditionally smaller than 1 mm, for example 0.11 mm as reported in Wißdorf et al. (2016). The ones described in Page et al. (2009) go up to 0.49 mm or in M. Skoblin et al. (2017) up to 0.6 mm. For specific usages, especially when large amounts of ions are required, this can even go up to 1 mm, as proposed in Pauly et al. (2014). In all cases, the diameter directly influences the quantity of gas which enters the devices. The pumping power in the following chambers should then be adapted accordingly. The length of the capillary varies largely, typically between a few centimeters up to 20 cm. The geometry of the capillary itself can also be slightly modified in order to enhance the transmission. A flared or funnel-shaped inlet is added in front of the straight pipe to enhance the transmission, as presented in S. Wu et al. (2006) and Pauly et al. (2014).

Several options exist for the material out of which the capillary is made of. The first design used a glass capillary. It was argued that a non-conductive material enables a potential difference between both ends of the capillary, thus enhancing the transport of the ions. Furthermore, it should prevent the loss of their charge, if they hit the walls. This option remains available nowadays. However, metal capillaries became widespread as well. It is also common to heat the capillary, such that the energy transfer to the droplets created by the ion source is increased. According to Lin and Sunner (1994), this can even be used to fragment the gas-phase ions when the temperature is high enough.

Further modifications of the setup have been studied. For example, some groups have created clusters of capillaries, as reported in Kelly et al. (2008). The solution used in the ESI coming from a liquid chromatography being given, it is divided into several emitters to keep the flow small enough in each of them, when good sensitivity can be expected. Following, a similar number of capillaries are used, creating several entrances into the mass spectrometer device. Other groups have tried to modify the relative position of the capillary from the rest of the device. In Chen, Fillmore, et al. (2015) or in Su et al. (2019), for example, the capillaries are built at right angle with the main axis of the following ion funnel. Further options have also been tested, for example encompassing both the ESI-emitter and the capillary inlet in a venturi device to improve the transfer, as exposed in Hawkridge et al. (2004). However, the classic setup remains common in current devices.

Ion funnel

The ion funnel was developed in Shaffer et al. (1997) to improve the transmission of ions in the first pumping chamber of the device. While several modifications have been proposed since it was first introduced, the basic concept remains unchanged. A series of ring electrodes creates a funnel-shaped cavity. The ions are guided through it until the next chamber by means of radio-frequency and direct electric fields. The surrounding gas, however, is pumped out of the chamber between the electrodes. A first evolution concerned the basic geometry of the system. Especially the inner diameter of the last electrode was identified as playing a significant role in the transmission of ions with a low m/z ratio (Shaffer et al. 1999). Novel designs also include more electrodes than the 28 of the initial design, with models including 100 plates being common, as presented in Kelly et al. (2010). While the inner diameter of the electrodes continuously decreased in the original design, some of the additional electrodes present a constant inner diameter at the beginning of the cavity.

This intends to increase the residence time of the ions in the funnel to enhance the desolvation of remaining droplets and to allow a full expansion of the gas coming form the capillary within the cavity.

A further modification aiming to improve the transfer of ions have been the introduction of a so-called *jet-disrupter* (Kelly et al. 2010). This is a small electrode placed in the center of the cavity. Like the extension of the cavity it helps to limit the quantity of gas reaching the end of the cavity. The losses of ions on this electrode are limited by applying an appropriate potential. The exact mechanisms induced by the disrupter remain, however, not well explained.

Other systems integrates successive ion funnels, each at different pressure levels. This enables higher gas loads through the capillary and can be found in Gunaratne et al. (2015). Variations on the same principle but without capillary can be found in Varentsov and Wada (2004). Different forms of the cavity have also been considered, especially rectangular shaped ones, as reported in Chen, Webb, et al. (2015). This was developed to couple the new system with structures for lossless ions manipulations (SLIM) located further downstream, yielding better results than the classic ring electrodes.

Simulations

Several attempts have been made to simulate the trajectory of ions within such systems. The first major contribution can be attributed to Lin and Sunner (1994). They focus their work on the transport of ions within the capillary. It considers the effects of diffusion and of the surrounding gas as well as the influence of the charge of the ions. This is treated by elementary models dealing with the decay over time of the charge density in an ion cloud. There are basically two different options to consider the movement of the ions: either a continuous model using the charge density to describe the distribution of the ions, as considered by Lin and Sunner (1994). Or a discrete model, where the ions are described individually. These two approaches have been studied in Wissdorf et al. (2012) and compared to experimental results. In the case considered in that publication, the discrete approach delivers better results. However, both methods present different particularities and may both be useful in different contexts.

Further simulations have been conducted to better understand the flow within the capillary, especially discussing its laminar or turbulent nature, as in Wißdorf et al. (2016) and M. Skoblin et al. (2017). One of the few studies considering the effects of space charge effects, M. G. Skoblin et al. (2017), is based on results from the latter and uses a continuous approach.

Some simulations of the ion funnel can also be found. The tool SIMION is widespread to simulate the trajectory of ions. This has been the case from the early stage of the development of these systems, in Shaffer et al. (1997) and Shaffer et al. (1998). However, these studies do not take into account the space charge effects that can occur. Furthermore, the gas flow is not fully taken into account in these studies. Further simulations, including the evolution of the design, have overcome this last weakness, including numerical simulations of the gas flow expected within the funnel, as reported in Tridas et al. (2015). However, the space charge effects remain largely neglected.

1.4.4 Outline

To achieve the goal of better understanding the transport of ions and their losses within the atmospheric pressure interface, we developed a methodology that tries to consider all relevant effects a priori affecting the trajectory of the ions. This includes the gas flow, the Brownian motion caused by the collisions between the gas molecules and the ions, the space charge effects between the ions, and the external electric field, mainly created by the electrodes in the ion funnel. We try to better understand the occurring mechanisms by simulating basic experiments or cases. These are based on a relatively standard device, consisting of a capillary with a funnel shaped inlet, followed by an ion funnel. We thus create a tool that enables us to explore new designs of the atmospheric pressure interface and offers the potential to help to improve the current design.

The present work, however, does not cover the entire spectrum of processes likely to influence the transmission of the ions. Especially, we do not cover the emission of the ions by the ESI source. Furthermore, all trajectories considered here are for gas-phase ions, that is, analytes from the ESI that have already been through the desolvation process.

The work is organized as follows. In chapter 2 we describe the systems considered: the capillary and its different geometries as well as the two different ion funnel designs. Furthermore, the main principles of the physical models used to describe the trajectory of the particles are exposed. This presents how the effects of the underlying gas flow, the external electric fields and the space charge effects are combined in order to compute the forces applied to the ions.

In chapter 3, the computation of the gas flow is presented. It starts with the description of the equations used and their adaptation to the specific cases considered here. The results related to the capillary are then exposed. It especially focuses on the influence of the geometry and heating in the case of a laminar flow, as well as some elements regarding the occurrence of turbulence in such a system. Results for both ion funnels considered are later presented. This chapter thus encompasses all results related to the gas flow expected in the simulated parts of the atmospheric pressure interface.

Chapter 4 is dedicated to the computation of the electric fields relevant for the trajectory of the ions. Especially, it presents the tools developed in order to efficiently take into account the space charge effects in the systems considered. It also exposes the different options available to describe the influence of harmonic electric fields imposed in the ion funnel. The resulting external electric fields computed for both ion funnel designs are also exposed.

In chapter 5, we combine the results of the previous chapters in order to compute the trajectory of ions in the atmospheric pressure interface. The results for the capillary and the ion funnels are presented separately and different cases are considered each time, in order to understand the influence of different parameters on the behavior of the particles. Furthermore, experimental results are considered in order to compare the simulations in the case of the classic ion funnel design. Eventually, conclusions are drawn in chapter 6. We especially focus on the assessment of the simulation tools developed and deliver some insights on the efficiency of the current designs.

Chapter 2

Model description

This chapter is dedicated to the presentation of the main framework of the present work. It starts with a description of the systems considered, which encompass two parts of the atmospheric pressure interface. First, the transfer capillary, typically located shortly after the ESI source. And second, the first pumping chamber that directly follows. Two different designs of the pumping chamber are presented, both based on the concept of the ion funnel. Then we focus on the models used to describe the trajectory of the ions within such systems, as well as some insights into the implementation of these models.

2.1 System's setups

2.1.1 Capillary

In the type of devices considered throughout this work, the capillary represents the interface between the production of the ions *via* electrospray ionization, at atmospheric pressure, and the first pumping chamber. It is thus submitted to a strong pressure gradient between its both ends. The most simple and widespread version of this interface is a long thin tube. It can usually be heated, so that metal versions with good thermal conductivity are common. However, capillaries made of glass are also found in commercial appliances. For example, both types are used in Wißdorf et al. (2016). While its role is to provide some entry point for the generated ions, it must also ensure that the quantity of gas that enters the device along with the ions is small enough to be later pumped out without excessive efforts. This

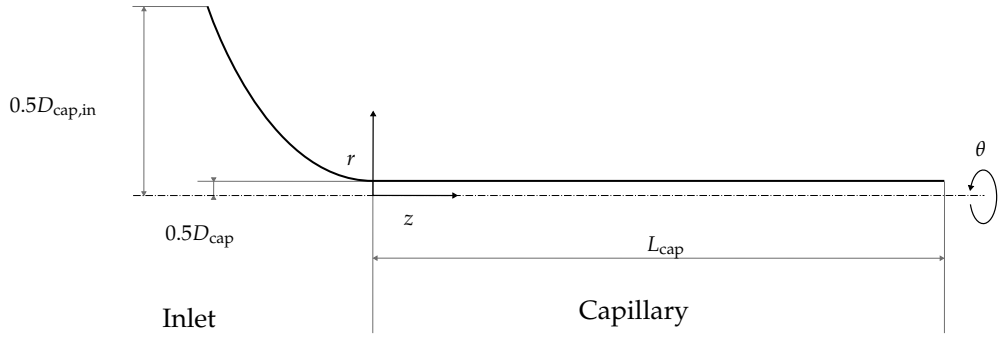

FIGURE 2.1: Sketch of the geometry of the transfer capillary considered in this work. The geometry is symmetric around the axis depicted with a dot-dashed line.

limitation leads to rather poor efficiency of the transmission of ions through the capillaries and attempts have been made to improve it. We base our work on one of the proposed improvements delivered in Pauly et al. (2014). It shows that adding a funnel-shaped inlet to the capillary can significantly improve the transmission ratio of the ions reached by the capillary. Experiments could show that the funnel-shaped inlet makes it possible to increase the efficiency of the transfer through the capillary up to almost total transmission, while it only reaches up to about 20 % with a flat inlet. High transmission is only possible under specific conditions when the transfer is not limited by other phenomena such as space charge effects. These results nevertheless show a significant improvement due to the funnel inlet.

The complete capillary further considered is divided into two parts: a straight part represented by its length L_{cap} and diameter D_{cap}, and the preceding funnel-shaped inlet. The general shape is represented in figure 2.1. Both ends of the straight part are open. The surface of the pipe is considered a hard wall. During the gas flow simulations, non-slip conditions are considered for the velocity. Two options are available for the energetic conditions: either adiabatic, where no thermal transfer through the wall is allowed, or isothermal, where the temperature of the gas at the wall is directly enforced. The former represents a theoretic and reference case, not directly related to experiments when metal capillaries are considered. On the other hand, the latter tends to represent a heated capillary. For the ions, this wall, as all other surfaces present in the simulations, is considered as a sink. This means that all particles hitting the wall are considered lost and do not participate in the simulations anymore.

The coordinate system is chosen cylindrical, with its symmetry axis coinciding with the symmetry axis of the capillary. The coordinates are chosen, as depicted in figure 2.1, as (r, θ, z). The symbol r classically represents the radial direction, starting from the symmetry axis; θ is the azimuthal coordinate and z the axial one. The origin of the system is placed at the junction between the inlet and the straight part. This means that all points with negative values of z are located within the funnel-shaped inlet, while points with positive values of z are located in the straight part of the capillary.

The dimensions of the funnel-shaped inlet are directly correlated to its following straight part. Its length is fixed to $L_{\text{cap,in}} = 2\,\text{mm}$ and its largest diameter at the beginning of the capillary called $D_{\text{cap,in}}$ is chosen as being eight times the diameter of the straight part: $D_{\text{cap,in}} = 8\,D_{\text{cap}}$. Its smallest diameter is exactly the diameter of the straight part D_{cap} and the shape is fitted to avoid any discontinuity at the transition (the derivative of the shape in the axial direction and at the junction is zero). With $D_{\text{cap,fun}}(z)$ the diameter of the capillary within the funnel-shaped inlet (that is for $-2\,\text{mm} \leq z \leq 0\,\text{mm}$), the dimensions are defined by:

$$D_{\text{cap,fun}}(z) = D_{\text{cap,in}} \left(\frac{z}{L_{\text{cap,in}}} \right)^2 + D_{\text{cap}} \,. \tag{2.1}$$

The dimensions of the capillary considered in this work are listed in table 2.1.

2.1.2 Ion funnel - classic design

In the first chamber after the capillary, some mechanisms are put in place to perform a first separation between the ions transported and the surrounding gas. We consider here an ion funnel system similar to the one built in the facilities of the Nano-Bio Interfaces group in the Nanoscale Science department of the Max Plack

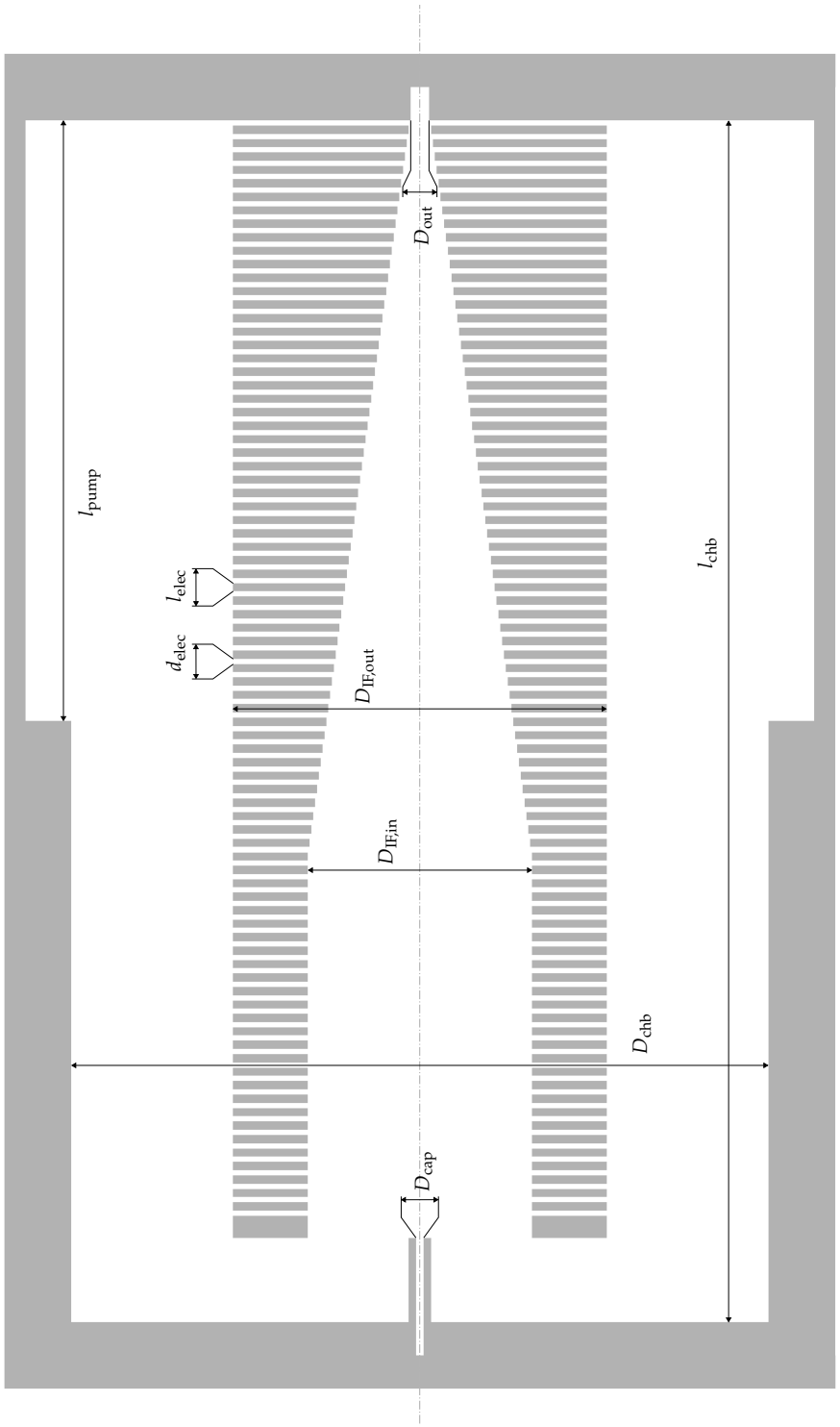

FIGURE 2.2: Sketch of the geometry of the ion funnel - classic design.
The geometry is symmetric around the axis depicted with a dot-dashed line.

	$D_{\text{cap,in}}$	D_{cap}	L_{cap}
#1	8.00 mm	1.00 mm	6.0 cm
#2	8.00 mm	1.00 mm	16.5 cm
#3	6.00 mm	0.75 mm	6.0 cm
#4	6.00 mm	0.75 mm	3.8 cm
#5	4.00 mm	0.50 mm	6.0 cm
#6	2.00 mm	0.25 mm	6.0 cm

TABLE 2.1: Dimensions of the capillaries considered.

	dimension	description
D_{chb}	9.324 cm	chamber diameter
L_{chb}	16.074 cm	chamber length
D_{cap}	1.0 mm	capillary diameter
$D_{\text{IF,in}}$	3.0 cm to 2.5 mm	inner electrode diameter
$D_{\text{IF,out}}$	5.0 cm	outer electrode diameter
D_{out}	2.5 mm	outlet diameter
d_{elec}	0.7 mm	spacing between electrodes
l_{elec}	1.1 mm	electrode thickness
l_{pump}	8.037 cm	length of the pumping area

TABLE 2.2: Dimensions of the ion funnel geometry - classic design.

Institute for Solid State Research in Stuttgart[1] and used for the research presented, e.g., in Rinke et al. (2015). 81 electrodes of the same thickness ($l_{\text{elec}} = 1.1\,\text{mm}$) are placed in the chamber plus a thicker one located at the beginning of the structure. All electrodes are equally spaced (distance between two electrodes $d_{\text{elec}} = 0.7\,\text{mm}$). Together, they form a cavity centered around the same symmetry axis as the capillary. All electrodes are simplified in the present work and are represented as rings, for which the outer diameter is constant: $D_{\text{IF,out}} = 5.0\,\text{cm}$, and the inner diameter $D_{\text{IF,in}}$ varies along the axis. The elements necessary to hold the electrodes in place and to set the potentials for the electric field are neglected. The first 28 electrodes have a constant inner diameter of $D_{\text{IF,in}} = 3.0\,\text{cm}$. The inner diameter of the 54 following ones decreases linearly along the axial direction. The smallest inner diameter, being the transition into the next chamber, reaches $D_{\text{out}} = 2.5\,\text{mm}$.

The first electrode, thicker than the others, begins where the capillary ends so that the ions transported through the capillary directly enter the cavity formed by the electrodes. The geometry of the chamber fitting around the electrodes is simplified and assumed to be axially symmetric. Besides the simplification of the electrodes previously discussed, this mostly affects the openings where the pump is connected. While the experimental designs generally provide two or four openings for the pump distributed around the chamber, we consider only one opening encompassing the entire circumference of the chamber, which length is $l_{\text{pump}} = 5.0\,\text{cm}$. The general design, presented for a slice in the radial direction, is presented in figure 2.2 and the dimensions are listed in table 2.2.

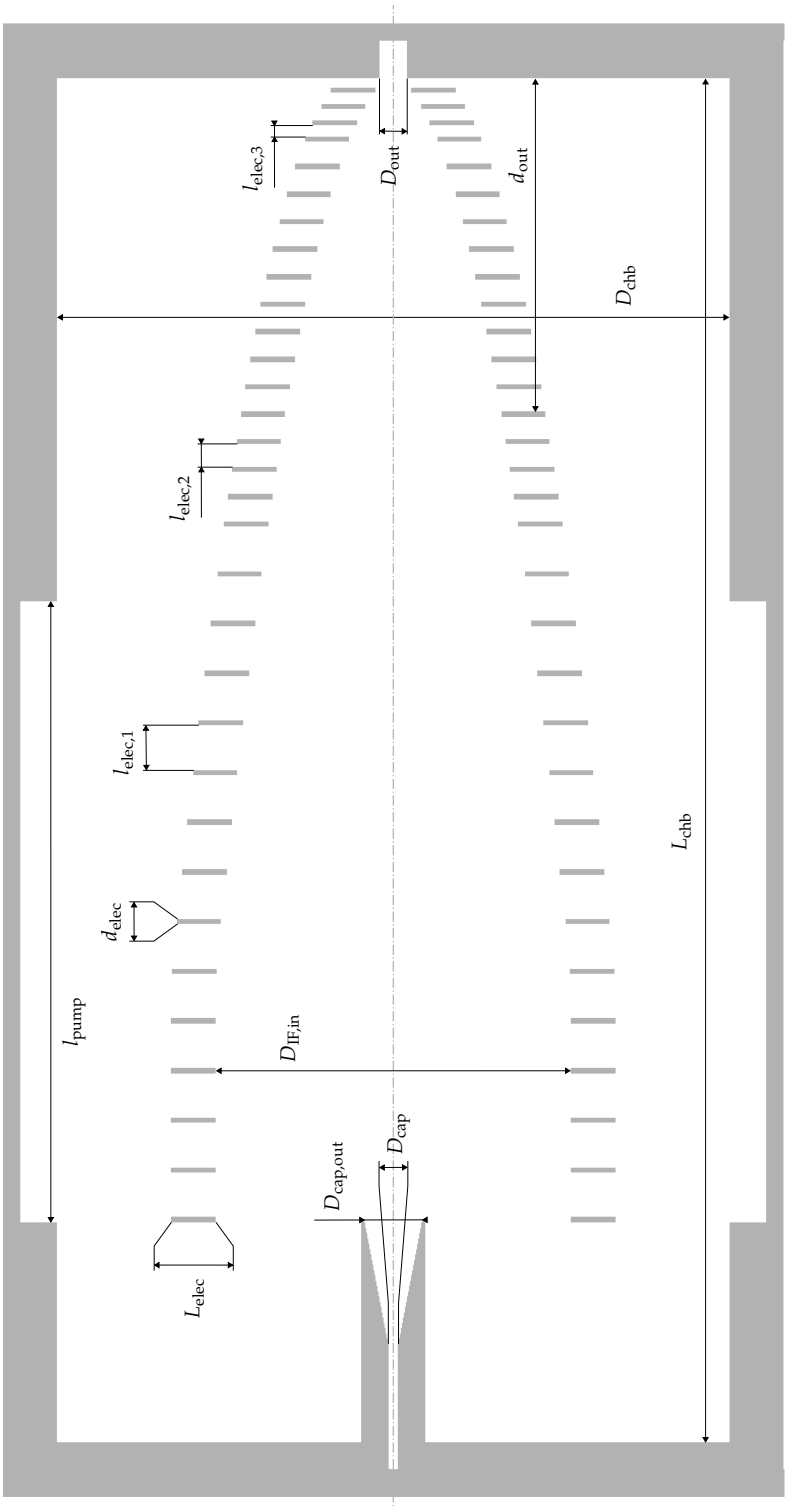

FIGURE 2.3: Sketch of the geometry of the ion funnel - evolution of the design. The geometry is symmetric around the axis depicted with a dot-dashed line.

2.1.3 Ion funnel - evolution of the design

An evolution of the classic ion funnel design is also considered, as presented in figure 2.3. Several modifications were implemented in order to better understand the implications on the transport of the ions and to provide some input for the design of new kinds of ion funnels. The new design was proposed by Stephan Rauschenbach and Paul Fremdling from the University of Oxford[2]. It consists of 32 electrodes for which their length, that is the difference between the outer and inner diameter, is always constant: $L_{\text{elec}} = 5.0\,\text{mm}$. They all have the same thickness $l_{\text{elec}} = 0.6\,\text{mm}$. The shape of the cavity is parabolic (convex), compared to a linear one in the previous model. The inner diameter of the electrodes is defined by the following equation:

$$D_{\text{IF.in}}\left(d_{\text{out}}\right) = \sqrt{\frac{1591}{400}\left(d_{\text{out}} + \frac{900}{1591}\right)}, \tag{2.2}$$

where d_{out} represents the distance between the right edge of the electrode and the outlet towards the next chamber. All dimensions are in millimeters. Furthermore, the inner diameter cannot be smaller than 4.0 mm or greater than 4.0 cm. The spacing between the electrodes varies along the cavity: the first 14 spaces between two electrodes (starting from the capillary) are defined with $d_{\text{elec}} = 5.0\,\text{mm}$, the 14 following with $d_{\text{elec}} = 2.5\,\text{mm}$, and the last 3 spaces as well as between the last electrode and the following wall are $d_{\text{elec}} = 1.25\,\text{mm}$. The pump opening is $l_{\text{pump}} = 7.0\,\text{cm}$ long and slightly shifted towards the capillary, compared to the previous design. Furthermore, a funnel-shaped opening has been added after the capillary. These dimensions are represented in figure 2.3 and listed in table 2.3.

Further details regarding the changes made compared to the classic design are later discussed alongside the results of the simulation. However, some basic ideas can be outlined here. First, a noticeably smaller number of electrodes alongside greater spacing between the electrodes have been chosen, mainly with the hope that it would help the gas flow between the electrodes and thus facilitate the separation from the ions. The funnel-shaped outlet put at the end of the capillary is intended to facilitate the expansion of the pipe chocked flow into the pumping chamber. Finally, the parabolic form of the funnel cavity intends to delay the collimation of the ions, to reduce the repulsion effects due to their electric charge. These modifications should be seen as tries rather than fully justified developments. The resulting simulations then intend to give some insight into what could occur in a new device if it were to be built this way.

2.2 The trajectory of a particle

In such systems as described before, the main goal is to transport as many ions from their production to the effective usage made of them, being for classic analytic purposes or e.g. advanced deposition. Furthermore, this transport shall be realized in a controlled manner to make sure that the outcome of the transport remains in line with the ions produced from the sample of interest. The simulation of reliable trajectories of the particles is thus an important objective to better understand the processes at stake. The idea of the present section is to deliver an overview of the phenomena affecting the movement of ions in a gas flow, which are later considered

1. Webpage of the group: www.fkf.mpg.de/85625/06_Nano-Bio_Interfaces
2. Webpage of the research group: rauschenbach.chem.ox.ac.uk

	dimension	description
D_{chb}	7.60 cm	chamber diameter
L_{chb}	15.42 cm	chamber length
D_{cap}	1.0 mm	capillary diameter
$D_{\text{cap,out}}$	3.0 mm	capillary outlet diameter
$D_{\text{IF,in}}$	4.0 cm to 4.0 mm	inner electrode diameter
L_{elec}	5.0 mm	electrode length
D_{out}	2.5 mm	outlet diameter
$d_{\text{elec,1}}$	5.0 mm	spacing between electrodes (1)
$d_{\text{elec,2}}$	2.5 mm	spacing between electrodes (2)
$d_{\text{elec,3}}$	1.25 mm	spacing between electrodes (3)
l_{elec}	0.6 mm	electrode thickness
L_{elec}	5.0 mm	electrode length
l_{pump}	7.0 cm	length of the pumping area

TABLE 2.3: Dimensions of the ion funnel geometry - evolution of the design.

with further details. Two main effects are considered within the present work: the electric forces and the influence of the surrounding gas. As will be done throughout this work, we assume that the ions can be represented as point particles. All considered forces are thus applied to the fictive center of the particle and the net resulting force $\vec{F}_{\text{net}}$ can be written as follows:

$$\vec{F}_{\text{net}} = \vec{F}_{\text{elec}} + \vec{F}_{\text{fluid}} \,. \tag{2.3}$$

2.2.1 Electric field

There are two different sources of electric forces influencing the movement of the ions: the self-induced space charge effects, due to the own charge of the ions and the resulting Coulombic forces between them on the one hand; and the external electric fields, used for example by the electrospray ionization or by the ion funnel on the other hand.

In theory, not only electric forces but more generally electromagnetic ones should be considered. However, no intrinsic magnetic sources are expected within the considered parts of the system. Furthermore, the velocity of the ions remains several orders of magnitudes lower than the light velocity, so that the magnetic term in the Lorentz forces is neglected. This estimation is further developed in section 4.3.1.

Moreover, two different components of the electric field are typically used to guide the ions: a field constant over time, often referred to as the DC (direct current) field; and a field that changes over time, usually with a specific periodicity. This second component is often referred to as the RF (radio frequency) field. In summary, three different electric fields should be considered in the system:

- the space charge effects (SCE);
- the time-independent (DC) external fields;
- the time-dependent (RF) external fields.

As a result, the electric part of the net resulting force is divided as follows:

$$\vec{F}_{\text{elec}} = \vec{F}_{\text{SCE}} + \vec{F}_{\text{DC}} + \vec{F}_{\text{RF}} = q\left(\vec{E}_{\text{SCE}} + \vec{E}_{\text{DC}} + \vec{E}_{\text{RF}}\right) , \tag{2.4}$$

with q the electric charge of the ion and $\vec{E}$ representing the different electric fields.

This subdivision has consequences from a practical point of view. The DC field being constant over time, it is sufficient to know the position of the considered particles to know the corresponding electric field and thus the applied force by multiplying with the charge. Without using any further model, the RF term requires additionally to know the precise time or the phase for typical periodic (harmonic) fields. Finally, the SCE term representing the interaction between all particles present, and given that the long-range interaction cannot be neglected a priori, it is necessary to know the position of every other particle to compute the corresponding electric field. Computing these terms independently is an approximation though. Further details regarding this issue are presented in section 4.3.2.

2.2.2 Flow effects

The presence of the gas flow also influences the trajectory of the particles. Because of the molecular collisions, the ions tend to follow the gas flow in the absence of any other effects considered, especially electric effects (that is, e.g. considering a single ion in a Faraday cage, i.e. without SCE or external electric fields). Macroscopically, this can be expressed with a force depending both on the local velocity of the gas $\vec{u}_{\text{f}}$ and the own velocity of the particle $\vec{u}_{\text{p}}$, which tends to reduce the difference between both. This force is thus assumed to have the following form for an ion of mass m:

$$\vec{F}_{\text{fluid}} = \frac{m}{\tau_{\text{p}}}\left(\vec{u}_{\text{f}} - \vec{u}_{\text{p}}\right) . \tag{2.5}$$

It represents a traction force, whose magnitude is directly proportional to the difference between the gas and particle velocities. The proportionality factor depends on the mass of the ion, to take into account its inertia and for dimensional reasons, a specific time τ_{p} is introduced. This relaxation time is species-specific and depends on the local parameters of the gas flow. It is further referred to as particle response time and can be defined as:

$$\tau_{\text{p}} = \frac{mK}{q} , \tag{2.6}$$

where K is the ion mobility. The ion mobility further depends on the flow conditions (pressure p and temperature T) as follows:

$$K = K_0 \frac{p_0}{p}\frac{T}{T_0} , \tag{2.7}$$

with K_0 the so-called reduced mobility taking the value at a gas pressure of p_0 and temperature of T_0 and for a given species. The references p_0 and T_0 are usually chosen as the standard condition, K_0 being then the standard mobility. It thus builds a local parameter depending on the flow state.

This form of the fluid force applied on the ion can be compared to the traditional Langevin equation, used to describe the Brownian motion of a particle in gas at rest. This approach is detailed in Tolmachev et al. (1997). Two fundamental points differ between both models:

- The Langevin equation is designed to describe the Brownian motion of the ion, using a stochastic term on the right-hand side, which is not present in the model considered here. The diffusion effects resulting from the Brownian motion are taken into account in this work but using a different approach presented in section 2.2.4;
- We not only consider a gas at rest but having a velocity $\vec{u}_\mathrm{f}$. As a consequence, the force term does not only depends on the ion velocity as in the Langevin equation but is proportional to the difference between the local gas velocity and the ion velocity $\vec{u}_\mathrm{f} - \vec{u}_\mathrm{p}$.

Nevertheless, both models attempt to describe the same phenomenon (excluding the Brownian motion): because of the collisions between the gas molecules and the ion, the latter tend to reach the macroscopic gas velocity after a given time. This justifies the choice of the particle response time made here, which is the same as the time constant chosen in the Langevin equation in Tolmachev et al. (1997).

2.2.3 Combination of both effects

When both effects are combined, the ion mobility gets a rather intuitive meaning which justifies the choice made for the particle response time. Let us assume a very simple system, where a single ion with charge q is introduced in a chamber, filled with gas at rest in which a homogeneous electric field is imposed. The latter can be, for example, created by a potential difference between two parallel plates, where boundary effects are neglected. We further assume that the system reaches equilibrium so that no acceleration of the ion occurs and the forces applied to it sum up to zero. Only two forces are present here: the time constant electric field $\vec{F}_\mathrm{DC}$ and the fluid force, where the gas velocity is set to zero. One thus ends up with the following equation:

$$\frac{m}{\tau_\mathrm{p}}\vec{u}_\mathrm{p} = \vec{F}_\mathrm{DC} = q\vec{E}_\mathrm{DC}\,, \tag{2.8}$$

where $\vec{E}_\mathrm{DC}$ is the electric field created by the potential difference between the plates.

This situation gets back to the definition of the ion mobility given in Creaser et al. (2004) when the corresponding conditions are fulfilled. In such a situation, the ion is accelerated by the electric field, but this effect is balanced when it suffers a collision with a gas molecule, before being accelerated again in the direction of the field lines. Macroscopically, both effects are balanced and the ion reaches on average a well-defined velocity, proportional to the electric field via the ion mobility:

$$\vec{u}_\mathrm{p} = K\vec{E}_\mathrm{DC}\,. \tag{2.9}$$

Replacing this expression of the ion velocity into equation 2.8, one ends up with the definition of the particle response time given in equation 2.6.

This easy case shows the importance of both aspects regarding the behavior of the ion. In the absence of gas, the ion would have a constant acceleration $\vec{a}_\mathrm{p}$ directly defined by the magnitude of the electric field:

$$\vec{a}_\mathrm{p} = \frac{q}{m}\vec{E}_\mathrm{DC}\,. \tag{2.10}$$

Similarly, in the absence of electric fields, the ion would not show any movement caused by a macroscopic force. However, some Brownian motion would still be observable, being the results of collisions between the gas molecules and the ion.

This Brownian motion is an effect that always occurs and the ion velocity presented in equation 2.9 should be seen as an average velocity to which this stochastic motion should be added.

2.2.4 Diffusion effects

At a larger scale, *i.e.* when considering a larger amount of ions, the microscopic effects due to the molecular collisions add up to build the diffusion effects. As a general rule, the ions located in regions already containing many other ones tend to drift towards regions where fewer ions are present. Those effects are modeled via the diffusion equation, also referred to as Fick's law. It describes the evolution of the density of a quantity. This quantity would be, in our system, the ion concentration in the global system consisting of the gas molecules and the ions together. This quantity is further referred to as ρ_p and follows the differential equation:

$$\frac{\partial \rho_\mathrm{p}}{\partial t} = \nabla \cdot \left(D \nabla \rho_\mathrm{p} \right) \,, \tag{2.11}$$

where D is the so-called diffusion coefficient. It is *a priori* unknown but can be expressed using different properties of the ions, in a first approach. Using The Nernst-Towsend-Einstein relation, one can write, following Mason and McDaniel (1988, p. 139):

$$D = \frac{K k_\mathrm{B} T}{q} \,, \tag{2.12}$$

with k_B the Boltzmann constant. The diffusion constant is thus locally defined, depending on the flow conditions, but also species-specific via the ion mobility and the charge. This relation assumes once again that the ions are in near equilibrium, implying weak fields and small gradients.

2.2.5 Outlook on the simplification

The present work, which is intended as a first try to combine all relevant effects, only relies on the aforementioned models to simulate the motion of the ions. However, this is a simplification of the effects really at stake and we provide here some information regarding possible extensions. The equation 2.9 is only valid for near equilibrium, that is weak fields and small gradients, as described in Mason and McDaniel (1988, chapter 1-1). As explained in the same reference, the behavior is a bit different when the electric field is stronger and the energy delivered to the ion through it is not negligible compared to the (thermal) energy provided by the molecular collisions with the surrounding gas. In such a case, part of the electric energy is also used to divert the ion from the trajectory it would have without any collision with gas molecules. This means that the effective Brownian motion is not only due to the thermal energy but the electric field also participates in it. As a consequence, the ion mobility is not easily expressed as defined in equation 2.7 but a further dependency on the magnitude of the electric field should be considered. Further, the diffusion coefficient is not a scalar value anymore but should be considered as a tensor. It takes different values in the direction parallel to the electric field and the directions orthogonal to it. This picture can get even more complicated if magnetic effects are to be considered, where both ion mobility and diffusion coefficient get a tensor form. Further references to this subject can be found in Mason and McDaniel (1988, chapter 1-1).

2.3 Implementation of the model

The model presented in the previous section is implemented to simulate the trajectory of the ions in several systems. The computation of the trajectory of the particle in this work is performed in two steps. We first consider the net force applied to the ions as described in 2.3. From the given distribution of ions, it computes a new set of positions after the time step considered due to this force. It is there important to consider the different time scales involved, especially the ratio between time step Δt and particle response time τ_p. In a second step, the Brownian motion is considered. The implementation follows the idea of a random walk method. The ions are also introduced in a certain area in the domain, as the production process of electrospray ionization is not modeled and only gas-phase ions are considered. Finally, boundary conditions are also taken into account to deal with particles reaching the limits of the computational or physical domain. The different aspects of this implementation are presented in the following.

2.3.1 Random walk method

The random walk is a stochastic method that delivers a macroscopic description of diffusion effects. In the form considered, the time step consists in shifting the position of the ions in the three Cartesian dimensions by a given length l. The direction, positive or negative, of the shift is randomly chosen. It can be seen as three simultaneous one-dimensional diffusion processes, all using the same diffusion constant. Only considering diffusion with the exclusion of other sources of motion, the displacement of the position after a time t is called Δx. The mean squared displacement can be expressed following a normal distribution and is given e.g., in Berry, Rice, and Ross (2000):

$$\langle \Delta x^2 \rangle = \frac{l^2 t}{\Delta t} \,. \tag{2.13}$$

Additionally, a relation between the mean square displacement and the diffusion constant D exists, also stated in Berry, Rice, and Ross (2000):

$$\langle \Delta x^2 \rangle = 2Dt \,. \tag{2.14}$$

A combination of equations 2.13 and 2.14 directly delivers the length of the shift l to be performed during the time step Δt to mimic a diffusion process of constant D:

$$l = \sqrt{2D\Delta t} \,. \tag{2.15}$$

Taking into account expression 2.12 relating the diffusion constant to ion-specific parameters, it follows:

$$l = \sqrt{\frac{2Kk_b T \Delta t}{q}} \,. \tag{2.16}$$

This final expression is the one used in the implementation. It is worth noting here that the superposition of three one-dimensional diffusion processes considered here is not the only option available. It is also possible to consider the displacement of a given length in the three-dimensional domain. This means that the next position is located on a sphere with the direction between the old and the new position chosen randomly. The relation 2.14 should however be adapted. Both options deliver, statistically, the same results. We chose the superposition of three one-dimensional

steps for its simplicity and the fact that the diffusion effects are expected small in comparison to the fluid and electric effects.

The method calls for the use of random numbers at each time step and for each ion involved in the simulation. To this end, we make use of a pseudo-random number generator based on the *xoroshiro128+* algorithm[3]. It allows us to deliver long sequences of uncorrelated numbers, as needed in our application. When used in a parallel environment, each process uses a dedicated series of pseudo-random numbers. Furthermore, the seeding process delivers reproducible results, as long as the parameters and initial conditions as well as the number of parallel threads remain identical.

2.3.2 System of equations and particle response time

From the net force applied to the ions, one can derive the equation defining the acceleration of the ion, taking into account the influence of the fluid and the electric fields:

$$\vec{a}_\mathrm{p} = \frac{1}{\tau_\mathrm{p}} \left(\vec{u}_\mathrm{f} - \vec{u}_\mathrm{p} \right) + \frac{q}{m} \left(\vec{E}_\mathrm{DC} + \vec{E}_\mathrm{RF} + \vec{E}_\mathrm{SCE} \right) . \tag{2.17}$$

It is thus possible to build the system of equations used to compute the trajectory of the ions:

$$\begin{aligned} \frac{\mathrm{d}\vec{u}_\mathrm{p}}{\mathrm{d}t} =& \frac{1}{\tau_\mathrm{p}} \left(\vec{u}_\mathrm{f} - \vec{u}_\mathrm{p} \right) + \frac{q}{m} \left(\vec{E}_\mathrm{DC} + \vec{E}_\mathrm{RF} + \vec{E}_\mathrm{SCE} \right) \\ \frac{\mathrm{d}\vec{x}_\mathrm{p}}{\mathrm{d}t} =& \vec{u}_\mathrm{p} \, , \end{aligned} \tag{2.18}$$

with $\vec{x}_\mathrm{p}$ representing the position of the ions in the system. The particle response time represents a characteristic time for the system of equation and it is important to consider it with respect to the time step of the integration scheme considered. The response time τ_p can indeed become very small for large pressures or equivalently for high-density values in the gas flow. This situation is encountered for instance in the capillary, where the thermodynamic conditions remain relatively close to the atmospheric ones. For the test species that we use in this work, rhodamine B, it delivers particle response times in the order of magnitude of 10^{-10} s, which is extremely small compared to a typical convection time through the capillary of 10^{-4} s.

This is problematic for explicit time integration methods such as the one used in this work. The time step shall indeed remain similar or smaller than the particle response time, leading to an unrealistic number of steps required. An adapted model is considered to avoid this constraint. It uses the limit value of the velocity that would occur when the fields surrounding the ion's position are only weakly changing. This is reached when the ion's acceleration becomes zero. A well-defined velocity can thus be expressed:

$$\vec{u}_\mathrm{p} = \vec{u}_\mathrm{f} + \frac{\tau_\mathrm{p}\, q}{m} \left(\vec{E}_\mathrm{DC} + \vec{E}_\mathrm{RF} + \vec{E}_\mathrm{SCE} \right) . \tag{2.19}$$

3. A fortran implementation found at github.com/jannisteunissen/rng_fortran combined to a tailored interface is used.

Replacing the expression of the particle response time with its definition 2.6, the cinematic equation follows:

$$\frac{\mathrm{d}\vec{x}_\mathrm{p}}{\mathrm{d}t} = \vec{u}_\mathrm{f} + K\left(\vec{E}_\mathrm{DC} + \vec{E}_\mathrm{RF} + \vec{E}_\mathrm{SCE}\right) . \tag{2.20}$$

Equations 2.18 and 2.20 represent two different models to describe the trajectory of the ions, which should be considered depending on the time step used in the simulation and the local value of the particle response time. In areas such as the capillary, it is easy to decide which model suits better. As already stated, the particle response time for the test species is about six orders of magnitudes smaller than the convection time necessary to simulate the transfer of the ions and thus remains significantly smaller than the typical time step chosen. As a consequence, the capillary simulations only make use of the cinematic model described in equation 2.20.

In the case of the ion funnel, the situation is a bit more complex. The gas density varies strongly, from large values at the capillary outlet to significantly smaller values close to the pumping system and towards the next chamber. The particle response time itself thus presents a large amplitude. This calls for an adapted model that dynamically chooses between the purely cinematic description of equation 2.20 and the inertial description of equations 2.18. To that end, a specific criterion is considered. It relies on the analytic solution of the inertial model in the absence of electric fields and considering a homogeneous gas velocity field $\vec{u}_\mathrm{f}$. For an initial ion velocity $\vec{u}_{\mathrm{p},0}$ at time $t = 0$, it follows:

$$\vec{u}_\mathrm{p}(t) = \vec{u}_\mathrm{f} + \left(\vec{u}_{\mathrm{p},0} - \vec{u}_\mathrm{f}\right) e^{-\frac{t}{\tau_\mathrm{p}}} . \tag{2.21}$$

If one considers the difference between the analytic solution 2.21 and the cinematic description $\vec{u}_\mathrm{f}$ after a time step Δt, normalized with the difference at the initial time, one gets:

$$\frac{\left\|\vec{u}_\mathrm{f} - \vec{u}_\mathrm{p}(\Delta t)\right\|}{\left\|\vec{u}_{\mathrm{p},0} - \vec{u}_\mathrm{f}\right\|} = e^{-\frac{\Delta t}{\tau_\mathrm{p}}} . \tag{2.22}$$

This basically represents the normalized error made by the cinematic model. The idea of the criterion is to define a threshold α to this normalized error: if it is lower than the threshold, the cinematic model is considered as accurate enough. If it is greater, the inertial model, supposedly more accurate, should be used. The error is smaller than α when

$$\frac{\Delta t}{\tau_\mathrm{p}} \geq -\ln \alpha . \tag{2.23}$$

The particle response time can be computed at each ion's position and the criterion considered. If the ratio $\Delta t / \tau_\mathrm{p}$ is larger than $-\ln \alpha$, the cinematic model is considered, otherwise the inertial description is used.

The choice of α is however not necessarily straightforward or arbitrary. The picture described here only considers the difference between the analytic solution of the inertial model and the cinematic model and not the effective result produced by the time integration scheme considered. Thus a meaningful bound for the ratio $\Delta t / \tau_\mathrm{p}$ shall be chosen for each time integration method considered. For example, with an explicit Euler time step, as used in this work, the inertial model results in a linear evolution of the particle velocity with respect to the time step considered:

$$\vec{u}_\mathrm{p}(\Delta t) = \vec{u}_{\mathrm{p},0} + \frac{\Delta t}{\tau_\mathrm{p}}\left(\vec{u}_\mathrm{f} - \vec{u}_{\mathrm{p},0}\right) . \tag{2.24}$$

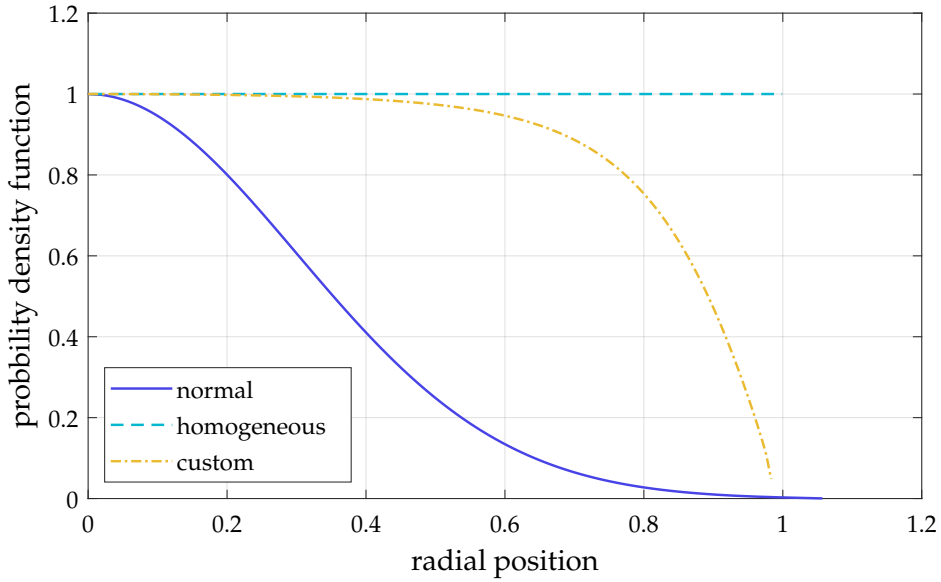

FIGURE 2.4: Radial distributions of the ions introduced during the simulation. The probability density functions have been normalized to one at the center of the distribution ($r = 0$).

A reasonable choice is to limit the application of the inertial model for time steps Δt such that the resulting evolution of the particle velocity $\|\vec{u}_\mathrm{p}(\Delta t) - \vec{u}_{\mathrm{p},0}\|$ remains smaller than $\|\vec{u}_\mathrm{f} - \vec{u}_{\mathrm{p},0}\|$. This corresponds to $\Delta t/\tau_\mathrm{p} \leq 1$. One thus chooses α such that $-\ln\alpha = 1$ or $\alpha \approx 0.36$.

2.3.3 Introduction of the ions in the domain

The principle of the trajectory's simulations is to describe, statistically, the behavior of the ions within a given system. We don't simulate the creation of ions in the electrospray system. Therefore, we need to artificially introduce ions in the computational domain. The preferred trajectory of the ions within the systems considered is the starting point to define a proper distribution. The main path for the ions is to go through the system following the capillary and further within the cavity formed by the ions funnel. They are expected to preferably go along the symmetry axis of each system. We thus choose to introduce the new ions in a plane orthogonal to this direction, that is in a polar plane at a given axial position. At each time step, a specific number of new ions are introduced, depending on the electric current that we intend to simulate. Those ions are randomly set in the plane according to different distribution functions, depending on the case considered. Three options are available in the current implementation:

- a normal distribution, whose center and standard deviation are given as parameters;
- a homogeneous distribution, whose center and radius are given as parameters;
- a custom distribution, which intends to mimic the distribution at the end of the capillary. Its center and radius are given as parameters.

A graphic representation of these distributions along the radius is proposed in figure 2.4. In addition to this distribution within a given plane, a further, homogeneous

distribution in the axial direction is performed. It intends to avoid the formation of clusters of ions that would occur if all new ones were introduced in the same plane at each time step. The length of the distribution in the axial direction is estimated with the velocity of ions already present in the domain and recently introduced.

The random numbers needed to deliver these distributions are produced by the same generator as described for the random walk method in section 2.3.1.

2.3.4 Boundary conditions

Once the ions are introduced in the domain, their motion is computed according to the models presented in section 2.3.2. During the trajectory, they may encounter obstacles, either the limits of the computational domain or physical obstacles such as walls or electrodes in the ion funnel. At this point, boundary conditions for the ions need to be defined.

In the model presented here and used throughout this work, two outcomes are possible in such cases. Either the ion is considered as lost, i.e. it is not viable anymore for the intended usage of the device (typically, analysis via mass spectrometry or deposition). Or it enters a new chamber, not included in the computational domain but still relevant for the intended usage. Here, this second case refers to ions transferred through the capillary and entering the first pumping chamber or ions transported within the ion funnel and entering the second pumping chamber. Either lost or entering a new chamber, the ions are eliminated from the simulation and counting is performed to determine how many ions are lost and transmitted over time. The transmission area is generally well defined and is relatively small in comparison to the computational domain. However, the losses can occur at various locations, especially in the ion funnel. We thus additionally store the position of the ions when they leave the system. This allows a more detailed investigation of the causes of the losses and opens up the possibility to propose some solutions against the processes involved.

The losses mechanisms can be more complicated than the model presented here. As soon as an ion hits a surface, it cannot participate to the simulation anymore. However, it has been reported in Wißdorf et al. (2016) that the mechanisms involved at this point may be more complex. Especially some charge accumulation at the wall as well as exchange chemistry might occur at this interface. In the cases considered here though, all surfaces are made out of metal. This means that the charge transfers between the ions and the surface are very easy. As a consequence, it is expected that the probability for the ions to lose their electric charge is very high when they hit a metallic surface. This means that they cannot be efficiently guided by electric fields further in the device and are a priori excluded from any effective usage. The condition for the losses taken on in this work is thus considered as well suited for the cases simulated here. Other systems, for example with glass capillaries, should be treated more carefully though.

Chapter 3

Flow description

One of the particularities of the systems considered in this work is that the ions are not evolving in vacuum but in a gaseous environment. Their behavior is thus influenced by the surrounding gas and having a good understanding of the underlying flow is necessary to properly simulate the trajectory of the ions. From a molecular point of view, collisions between the gas molecules and the ions lead to an alteration of the behavior of the ions. Is the gas at rest, it leads to a canceling of the acceleration of the ion, which reaches a limit velocity defined by the electric field otherwise applied to it. Has the gas a macroscopic motion, the ions tend, in addition, to follow this motion. It is thus important to consider the flow field to correctly describe the trajectory of the ions.

As the first stages of the devices considered in this work operate at relatively high-pressure levels, we consider the classic Navier-Stokes equations, and more precisely their axially symmetric form. We also consider the limits of this approach encountered in the ion funnel, when the pressure becomes significantly lower. We further present the method used to consider objects located within the computation domain, without specific adaptation of the grid. This is used for the ion funnel, where, e.g., several electrodes are altering the gas flow. We finally present the results of the two stages of the device considered, that is the transfer capillary and the ion funnel.

3.1 Gas flow modeling and NAVIER-STOKES equation

3.1.1 Skew-symmetric form of the NAVIER-STOKES equations

The basis of all flow computations presented in this work is the skew-symmetric formulation of the Navier-Stokes equations presented in Reiss and Sesterhenn (2014). This formulation offers a built-in property of energy conservation with an adequate numerical treatment of the spatial and time discretization. This is of special importance when considering the energetic evolution of a system, for example during a combustion reaction or when considering thermal exchanges. Even if this is not directly the focus of the simulations performed here, this feature remains valuable, as thermal conditions play a non-negligible role in the behavior of the devices considered, especially for the capillary.

We first present the general, coordinate-independent, form of these equations. The nabla operator is used throughout the chapter. Its signification depends on the kind of field (scalar, vector, second-order tensor) it is applied to and the relation between the operator and the field (direct, "dot" product, "cross" product, etc.). A summary of the underlying mathematical operations is given in appendix A.

In the following, ρ represents the (mass) density of the flow, $\vec{u}$ the velocity vector, p the pressure field, $\underline{\underline{\tau}}$ the stress tensor, and $\vec{\phi}$ the heat flux. We further assume

that the simulated gas is air, following the ideal gas law with γ the corresponding adiabatic index. The symbol used for the velocity of the gas, $\vec{u}$, corresponds to $\vec{u}_\mathrm{f}$ from chapter 2. We dropped the index f to enhance the readability of the equation, as there is no risk of confusion in this chapter. The equations considered are now presented:

Continuity equation

$$2\sqrt{\rho}\,\frac{\partial\sqrt{\rho}}{\partial t} = -\nabla\cdot(\rho\vec{u}) \tag{3.1}$$

Momentum equation

$$\sqrt{\rho}\,\frac{\partial\sqrt{\rho}\vec{u}}{\partial t} = -\frac{1}{2}\left(\nabla\cdot(\rho\vec{u}\otimes\vec{u}) + (\nabla\otimes\vec{u})\,(\rho\vec{u})\right) - \nabla p + \nabla\cdot\underline{\underline{\tau}} \tag{3.2}$$

Energy equation

$$\frac{\partial p}{\partial t} = -\gamma\nabla\cdot(p\vec{u}) + (\gamma-1)\left(\vec{u}\cdot\nabla p - \vec{u}\cdot\left(\nabla\cdot\underline{\underline{\tau}}\right) + \nabla\cdot\left(\underline{\underline{\tau}}\,\vec{u}\right) - \nabla\cdot\vec{\phi}\right) \tag{3.3}$$

Stress tensor

$$\underline{\underline{\tau}} = \mu\left((\nabla\otimes\vec{u}) + (\nabla\otimes\vec{u})^{\mathbf{Tr}}\right) + \left(\mu_\mathrm{d} - \frac{2}{3}\mu\right)(\nabla\cdot\vec{u})\,\mathbb{I}\,, \tag{3.4}$$

where μ is the (dynamic) viscosity of the fluid, μ_d the bulk viscosity, and $\mathbb{I}$ the identity matrix. μ_d depends on the nature of the fluid considered and is rigorously zero for dilute monoatomic gases. We assume that this still holds for air in the simulated conditions, see e.g. Bird, Stewart, and Lightfoot (2001, p. 18).

Sutherland's law

An additional relation used is Sutherland's law. It represents the temperature dependency of the viscosity and is considered in the following form, as found in Chapman and Cowling (1991, p. 233), e.g.:

$$\mu\,(T) = \mu(T_\mathrm{R})\left(\frac{T}{T_\mathrm{R}}\right)^{\frac{3}{2}}\frac{T_\mathrm{R}+S}{T+S}\,, \tag{3.5}$$

with T_R and $\mu(T_\mathrm{R})$ a reference temperature and the corresponding viscosity, respectively. S is a so-called effective temperature and is specific for the gas considered. In this work, the parameters are set to:

- $T_\mathrm{R} = 273.15\,\mathrm{K}$
- $\mu(T_\mathrm{R}) = 1.71\times10^{-5}\,\mathrm{Pa}\cdot\mathrm{s}$
- $S = 110.4\,\mathrm{K}$

This relation is semi-empiric, based on the diatomic properties of the molecules present in the air as well as fitting parameters to recover values close to experimental ones. In our cases, a large range of temperatures are involved, which may push the model to its limits. However, even for fairly rarefied gases, it still delivers good results, according to Hänel (2004, p. 33). We thus consider that this model is good enough for the present work.

Heat flux

$$\vec{\phi} = -\lambda \nabla T \,, \tag{3.6}$$

where λ is the thermal conductivity of the fluid. This parameter is not independent but can be computed using the Prandtl number Pr, the viscosity μ, and the specific heat capacity at constant pressure c_P such that:

$$\lambda = \mu \frac{c_\mathrm{P}}{\mathrm{Pr}} \,, \tag{3.7}$$

following the definition of Pr as found for example in Bird, Stewart, and Lightfoot (2001, p. 268). Both c_P and Pr are considered as constant for air and take the following values (see e.g. Schlichting and Gersten (2017, p. 280) or Bird, Stewart, and Lightfoot (2001, p. 277)):

$$c_\mathrm{P} = 1.005\,\mathrm{J}\cdot\mathrm{K}^{-1}\cdot\mathrm{kg}^{-1} \tag{3.8}$$

$$\mathrm{Pr} = 0.71 \tag{3.9}$$

Ideal gas law

As previously stated, we assume that the simulated air follows the ideal gas law. It reads:

$$\frac{p}{\rho} = R_\mathrm{s} T \,, \tag{3.10}$$

where R_s is the specific gas constant. It is defined as $R_\mathrm{s} = R/M$, with R the universal gas constant and M the molar mass of the considered species or mix. For air, we use $R_\mathrm{s} = 287\,\mathrm{m}^2\cdot\mathrm{s}^{-2}\cdot\mathrm{K}^{-1}$. This relation is used to compute the temperature of the flow, which is not a primary variable of the system but still participates in the equations via the heat flux and Sutherland's law.

3.1.2 Axially symmetric form of the equations

The systems considered in this work are all approximated as axially symmetric. While this is a very accurate hypothesis for the capillary, this is more debatable for the ion funnel. The pumping system, for example, is not axially symmetric but concentrated in one or several outlets. The electric circuits necessary to produce the field at the electrodes also contain a certain asymmetry. However and in a first approximation, this complexity is not expected to strongly modify the gas flow in the core of the device, which is the driving part for the trajectory of the ions. We therefore further consider the axially symmetric form of the Navier-Stokes equations.

It consists in developing the operators of equations 3.1 to 3.6 for cylindrical coordinates and simplify the equations, assuming that the fields do not have any dependency along the azimuthal coordinate. For the sake of generality, we keep open the possibility to have an azimuthal component of the velocity field. This does not break

the axial symmetry assumption as long as this component does not depend on the azimuthal coordinate. We denote the radial, azimuthal, and axial cylindrical coordinates as (r, θ, z). The corresponding velocity components are denoted (u_r, u_θ, u_z) respectively.

Continuity equation

$$2\sqrt{\rho}\,\frac{\partial\sqrt{\rho}}{\partial t} = -\left(\frac{\partial \rho u_r}{\partial r} + \frac{\rho u_r}{r} + \frac{\partial \rho u_z}{\partial z}\right) \tag{3.11}$$

Momentum equations

$$\begin{aligned}\sqrt{\rho}\,\frac{\partial\sqrt{\rho}u_r}{\partial t} = &-\frac{1}{2}\left(\frac{\partial \rho u_r u_r}{\partial r} + \frac{\rho}{r}\left(u_r u_r - u_\theta u_\theta\right) + \frac{\partial \rho u_z u_r}{\partial z}\right)\\ &-\frac{1}{2}\left(\rho u_r\frac{\partial u_r}{\partial r} - \rho u_\theta\frac{u_\theta}{r} + \rho u_z\frac{\partial u_r}{\partial z}\right) - \frac{\partial p}{\partial r}\\ &+\frac{\partial}{\partial r}\left(\frac{2\mu}{3}\left(2\frac{\partial u_r}{\partial r} - \frac{u_r}{r} - \frac{\partial u_z}{\partial z}\right)\right) + \frac{2\mu}{r}\left(\frac{\partial u_r}{\partial r} - \frac{u_r}{r}\right)\\ &+\frac{\partial}{\partial z}\left(\mu\left(\frac{\partial u_z}{\partial r} + \frac{\partial u_r}{\partial z}\right)\right)\end{aligned} \tag{3.12}$$

$$\begin{aligned}\sqrt{\rho}\,\frac{\partial\sqrt{\rho}u_\theta}{\partial t} = &-\frac{1}{2}\left(\frac{\partial \rho u_r u_\theta}{\partial r} + \frac{2\rho u_r u_\theta}{r} + \frac{\partial \rho u_z u_\theta}{\partial z}\right)\\ &-\frac{1}{2}\left(\rho u_r\frac{\partial u_\theta}{\partial r} + \rho u_\theta\frac{u_r}{r} + \rho u_z\frac{\partial u_\theta}{\partial z}\right)\\ &+\frac{\partial}{\partial r}\left(\mu\left(\frac{\partial u_\theta}{\partial r} - \frac{u_\theta}{r}\right)\right) + \frac{2\mu}{r}\left(\frac{\partial u_\theta}{\partial r} - \frac{u_\theta}{r}\right)\\ &+\frac{\partial}{\partial z}\left(\mu\frac{\partial u_\theta}{\partial z}\right)\end{aligned} \tag{3.13}$$

$$\begin{aligned}\sqrt{\rho}\,\frac{\partial\sqrt{\rho}u_z}{\partial t} = &-\frac{1}{2}\left(\frac{\partial \rho u_r u_z}{\partial r} + \frac{\rho u_r u_z}{r} + \frac{\partial \rho u_z u_z}{\partial z}\right)\\ &-\frac{1}{2}\left(\rho u_r\frac{\partial u_z}{\partial r} + \rho u_z\frac{\partial u_z}{\partial z}\right) - \frac{\partial p}{\partial z}\\ &+\frac{\partial}{\partial r}\left(\mu\left(\frac{\partial u_z}{\partial r} + \frac{\partial u_r}{\partial z}\right)\right) + \frac{\mu}{r}\left(\frac{\partial u_z}{\partial r} - \frac{\partial u_r}{\partial z}\right)\\ &+\frac{\partial}{\partial z}\left(\frac{2\mu}{3}\left(-\frac{\partial u_r}{\partial r} - \frac{u_r}{r} + 2\frac{\partial u_z}{\partial z}\right)\right)\end{aligned} \tag{3.14}$$

Energy equation

For readability reasons, the energy equation is split into terms expressed separately.

$$\begin{aligned}\frac{\partial p}{\partial t} =& -\gamma\left(\frac{\partial p u_r}{\partial r}+\frac{p u_r}{r}+\frac{\partial p u_z}{\partial z}\right)\\ &+(\gamma-1)\left(u_r\frac{\partial p}{\partial r}+u_z\frac{\partial p}{\partial z}-\vec{u}\cdot\left(\nabla\cdot\underline{\underline{\tau}}\right)+\nabla\cdot\left(\underline{\underline{\tau}}\,\vec{u}\right)-\nabla\cdot\vec{\phi}\right)\end{aligned} \tag{3.15}$$

The different terms, still written with a general operator formulation, take the following special forms when considering an axially symmetric case:

$$\begin{aligned}\vec{u}\cdot\left(\nabla\cdot\underline{\underline{\tau}}\right) =& u_r\frac{\partial}{\partial r}\left(\frac{2\mu}{3}\left(2\frac{\partial u_r}{\partial r}-\frac{u_r}{r}-\frac{\partial u_z}{\partial z}\right)\right)+u_r\frac{2\mu}{r}\left(\frac{\partial u_r}{\partial r}-\frac{u_r}{r}\right)\\ &+u_r\frac{\partial}{\partial z}\left(\mu\left(\frac{\partial u_z}{\partial r}+\frac{\partial u_r}{\partial z}\right)\right)+u_\theta\frac{\partial}{\partial r}\left(\mu\left(\frac{\partial u_\theta}{\partial r}-\frac{u_\theta}{r}\right)\right)\\ &+u_\theta\frac{2\mu}{r}\left(\frac{\partial u_\theta}{\partial r}-\frac{u_\theta}{r}\right)+u_\theta\frac{\partial}{\partial z}\left(\mu\frac{\partial u_\theta}{\partial z}\right)\\ &+u_z\frac{\partial}{\partial r}\left(\mu\left(\frac{\partial u_z}{\partial r}+\frac{\partial u_r}{\partial z}\right)\right)+u_z\frac{\mu}{r}\left(\frac{\partial u_z}{\partial r}-\frac{\partial u_r}{\partial z}\right)\\ &+u_z\frac{\partial}{\partial z}\left(\frac{2\mu}{3}\left(-\frac{\partial u_r}{\partial r}-\frac{u_r}{r}+2\frac{\partial u_z}{\partial z}\right)\right)\end{aligned} \tag{3.16}$$

$$\begin{aligned}\nabla\cdot\left(\underline{\underline{\tau}}\,\vec{u}\right) =& \frac{1}{r}\frac{\partial}{\partial r}\left(r u_r\frac{2\mu}{3}\left(2\frac{\partial u_r}{\partial r}-\frac{u_r}{r}-\frac{\partial u_z}{\partial z}\right)\right)+\frac{1}{r}\frac{\partial}{\partial r}\left(\mu u_\theta\left(r\frac{\partial u_\theta}{\partial r}-u_\theta\right)\right)\\ &+\frac{1}{r}\frac{\partial}{\partial r}\left(r u_z\mu\left(\frac{\partial u_z}{\partial r}+\frac{\partial u_r}{\partial z}\right)\right)+\frac{\partial}{\partial z}\left(\mu u_r\left(\frac{\partial u_z}{\partial r}+\frac{\partial u_r}{\partial z}\right)\right)\\ &+\frac{\partial}{\partial z}\left(\mu u_\theta\frac{\partial u_\theta}{\partial z}\right)+\frac{\partial}{\partial z}\left(u_z\frac{2\mu}{3}\left(-\frac{\partial u_r}{\partial r}-\frac{u_r}{r}+2\frac{\partial u_z}{\partial z}\right)\right)\end{aligned} \tag{3.17}$$

$$\nabla\cdot\vec{\phi} = -\frac{1}{r}\frac{\partial}{\partial r}\left(r\lambda\frac{\partial T}{\partial r}\right)-\frac{\partial}{\partial z}\left(\lambda\frac{\partial T}{\partial z}\right) \tag{3.18}$$

The implementation of the axially symmetric Navier-Stokes equations used for the ion funnel further assumes that the velocity vector does not have any azimuthal component. It consists in setting $(u_\theta = 0)$ in the previous equations and thus simplifies the expressions.

3.1.3 Alternative axially symmetric formulation

While the axially symmetric equations just derived can be readily used on an equidistant, Cartesian grid, it becomes more complicated when grid transformations are considered. In the case of the laminar capillary, this is especially complex as two different transformations of the grid are present: grid stretching in the radial direction to better resolve the boundary layer in the vicinity of the walls and geometric transformation to reproduce the funnel shape of the inlet.

For the standard, Cartesian right-hand side, these deformations and their consequences on the mathematical operators are dealt with via metric factors, which

consider the transformation between an orthogonal, equidistant grid, called computational grid, and the transformed physical grid. The formalism of such a method can be found in Thompson, Warsi, and Mastin (1985), and its application to the skew-symmetric formulation of the Navier-Stokes equation is reported in Reiss and Sesterhenn (2014). The idea behind this alternative formulation of axially symmetric equations is to make use of the formalization of the metric factors used in Cartesian coordinates. It allows to only slightly transform the existing right-hand side, rather than applying the formalism of metric factors to the lengthy formulation of axially symmetric Navier-Stokes equations presented in section 3.1.2.

The idea behind metric factors is to describe the transformation existing between the computational grid and the physical one. Because of its simplicity, the derivation operators on the computational grid are easy to define. The metric factors then provide a mathematical means to transform these derivatives into their equivalent applied to the physical grid. The expression of these factors is based on the derivation of the physical coordinates with respect to the computational ones. A detailed formulation is provided in appendix B.

In the following, the Cartesian coordinates are represented by (x, y, z), the cylindrical ones by (r, θ, z), and the computational ones by (ξ, η, ζ). The method exposed here relies on a specific formulation of the coordinates:

$$x = \cos(\theta(\eta))\, r(\xi, \zeta) \ , \tag{3.19}$$

$$y = \sin(\theta(\eta))\, r(\xi, \zeta) \ , \tag{3.20}$$

$$z = z(\xi, \zeta) \ . \tag{3.21}$$

It is worth noting that both the radial and the longitudinal transformations (r, z) depend exclusively on the first and third computational variables (ξ, ζ) and that the azimuthal transformation (θ) depends exclusively on the second computational variable (η). More complex transformations would make little sense for a system supposedly axially symmetric.

The metric factors are represented by a matrix $\underline{\underline{m}}$. Its determinant J, called the Jacobian determinant, is a measure of the modification of the volume of a computational grid cell into the corresponding physical volume. Each operator of the Navier-Stokes equation can be written using the metric factors and the Jacobian determinant. Different formulations are possible for each operator. These are mathematically equivalent but can lead to numerical differences. To ensure energy conservation with finite differences schemes, a specific choice is described in Reiss and Sesterhenn (2014).

The hypothesis of an axially symmetric solution is taken into account as follows. In a first, intermediary step, each operator of the coordinates independent Navier-Stokes equations presented in section 3.1.1 can be replaced by its expression using metric factors and the Cartesian components of the vector variables $(\vec{v} = (v_x, v_y, v_z))$. Each term is then expressed using the cylindrical components, both in the metric factors and in the vector components $(\vec{v} = (v_r, v_\theta, v_z))$. These expressions can then be simplified, using elementary analytical properties resulting from the specific choice of coordinates of equations 3.19 to 3.21 and from the fact that the scalar fields and the different cylindrical components of the vector fields are independent of θ (hypothesis of axial symmetry). A specific azimuthal position is finally chosen, where the expressions are considered. We here use $\theta = 0$ to simplify the equations. The resulting expressions for the operators present in the equations relevant in this case, as well as the different steps summarized here, are detailed in appendix B. The order of the transformation is important. Choosing a specific value for θ as the last step

brings additional terms for some operators, which would have been omitted if the choice of a specific azimuthal position was performed earlier.

This finally leads to the adapted equations used in this work, as presented in the following. The additional terms responsible for the axial symmetry of the solution, in comparison to a two-dimensional Cartesian domain, are highlighted in blue and red. The Einstein summation rule applies to all computational coordinates. Furthermore, $\vec{m}^{\xi}$, $\vec{m}^{\eta}$, and $\vec{m}^{\zeta}$ represent vectors extracted from the metric factors, as described in appendix B.

Continuity equation

$$2\sqrt{\rho}\,\frac{\partial\sqrt{\rho}}{\partial t} = -\frac{\partial}{\partial\xi}\left(\rho\left(m_1^{\xi}u_r + m_3^{\xi}u_z\right)\right) - \frac{\partial}{\partial\zeta}\left(\rho\left(m_1^{\zeta}u_r + m_3^{\zeta}u_z\right)\right) \tag{3.22}$$

Momentum equations

$$\begin{aligned} J\sqrt{\rho}\,\frac{\partial\sqrt{\rho}u_r}{\partial t} =& -\frac{1}{2}\left(\frac{\partial}{\partial\xi}\left(\rho u_r\left(m_1^{\xi}u_r + m_3^{\xi}u_z\right)\right) - m_2^{\eta}\rho u_{\theta}^2\right) \\ &-\frac{1}{2}\left(\frac{\partial}{\partial\zeta}\left(\rho u_r\left(m_1^{\zeta}u_r + m_3^{\zeta}u_z\right)\right)\right) \\ &-\frac{\rho}{2}\left(u_r\left(m_1^{\xi}\frac{\partial u_r}{\partial\xi} + m_1^{\zeta}\frac{\partial u_r}{\partial\zeta}\right) - m_2^{\eta}u_{\theta}^2\right) \\ &-\frac{\rho}{2}\left(u_z\left(m_3^{\xi}\frac{\partial u_r}{\partial\xi} + m_3^{\zeta}\frac{\partial u_r}{\partial\zeta}\right)\right) \\ &-m_1^{\xi}\frac{\partial p}{\partial\xi} - m_1^{\zeta}\frac{\partial p}{\partial\zeta} \\ &+\frac{\partial}{\partial\xi}\left(m_1^{\xi}\tau_{rr} + m_3^{\xi}\tau_{rz}\right) - \theta_{\eta}m_2^{\eta}\tau_{\theta\theta} + \frac{\partial}{\partial\zeta}\left(m_1^{\zeta}\tau_{rr} + m_3^{\zeta}\tau_{rz}\right) \end{aligned} \tag{3.23}$$

$$\begin{aligned} J\sqrt{\rho}\,\frac{\partial\sqrt{\rho}u_{\theta}}{\partial t} =& -\frac{1}{2}\left(\frac{\partial}{\partial\xi}\left(\rho u_{\theta}\left(m_1^{\xi}u_r + m_3^{\xi}u_z\right)\right) + m_2^{\eta}\rho u_r u_{\theta}\right) \\ &-\frac{1}{2}\left(\frac{\partial}{\partial\zeta}\left(\rho u_{\theta}\left(m_1^{\zeta}u_r + m_3^{\zeta}u_z\right)\right)\right) \\ &-\frac{\rho}{2}\left(u_r\left(m_1^{\xi}\frac{\partial u_{\theta}}{\partial\xi} + m_1^{\zeta}\frac{\partial u_{\theta}}{\partial\zeta}\right) + m_2^{\eta}u_r u_{\theta}\right) \\ &-\frac{\rho}{2}\left(u_z\left(m_3^{\xi}\frac{\partial u_{\theta}}{\partial\xi} + m_3^{\zeta}\frac{\partial u_{\theta}}{\partial\zeta}\right)\right) \\ &+\frac{\partial}{\partial\xi}\left(m_1^{\xi}\tau_{r\theta} + m_3^{\xi}\tau_{\theta z}\right) + \theta_{\eta}m_2^{\eta}\tau_{r\theta} + \frac{\partial}{\partial\zeta}\left(m_1^{\zeta}\tau_{r\theta} + m_3^{\zeta}\tau_{\theta z}\right) \end{aligned} \tag{3.24}$$

$$
\begin{aligned}
J\sqrt{\rho}\,\frac{\partial\sqrt{\rho}u_z}{\partial t} = &-\frac{1}{2}\left(\frac{\partial}{\partial\xi}\left(\rho u_z\left(m_1^\xi u_r + m_3^\xi u_z\right)\right) + \frac{\partial}{\partial\zeta}\left(\rho u_z\left(m_1^\zeta u_r + m_3^\zeta u_z\right)\right)\right)\\
&-\frac{\rho}{2}\left(u_r\left(m_1^\xi\frac{\partial u_z}{\partial\xi} + m_1^\zeta\frac{\partial u_z}{\partial\zeta}\right) + u_z\left(m_3^\xi\frac{\partial u_z}{\partial\xi} + m_3^\zeta\frac{\partial u_z}{\partial\zeta}\right)\right)\\
&-m_3^\xi\frac{\partial p}{\partial\xi} - m_3^\zeta\frac{\partial p}{\partial\zeta}\\
&+\frac{\partial}{\partial\xi}\left(m_1^\xi\tau_{rz} + m_3^\xi\tau_{zz}\right) + \frac{\partial}{\partial\zeta}\left(m_1^\zeta\tau_{rz} + m_3^\zeta\tau_{zz}\right)
\end{aligned}
\tag{3.25}
$$

Energy equation

$$
\begin{aligned}
J\frac{\partial p}{\partial t} = &-\gamma\left(\frac{\partial}{\partial\xi}\left(p\left(m_1^\xi u_r + m_3^\xi u_z\right)\right) + \frac{\partial}{\partial\zeta}\left(p\left(m_1^\zeta u_r + m_3^\zeta u_z\right)\right)\right)\\
&+(\gamma-1)\left(u_r\left(m_1^\xi\frac{\partial p}{\partial\xi} + m_1^\zeta\frac{\partial p}{\partial\zeta}\right) + u_z\left(m_3^\xi\frac{\partial p}{\partial\xi} + m_3^\zeta\frac{\partial p}{\partial\zeta}\right)\right)\\
&-(\gamma-1)\,u_r\left(\frac{\partial}{\partial\xi}\left(m_1^\xi\tau_{rr} + m_3^\xi\tau_{rz}\right) - \theta_\eta m_2^\eta\tau_{\theta\theta} + \frac{\partial}{\partial\zeta}\left(m_1^\zeta\tau_{rr} + m_3^\zeta\tau_{rz}\right)\right)\\
&-(\gamma-1)\,u_\theta\left(\frac{\partial}{\partial\xi}\left(m_1^\xi\tau_{r\theta} + m_3^\xi\tau_{\theta z}\right) + \theta_\eta m_2^\eta\tau_{r\theta} + \frac{\partial}{\partial\zeta}\left(m_1^\zeta\tau_{r\theta} + m_3^\zeta\tau_{\theta z}\right)\right)\\
&-(\gamma-1)\,u_z\left(\frac{\partial}{\partial\xi}\left(m_1^\xi\tau_{rz} + m_3^\xi\tau_{zz}\right) + \frac{\partial}{\partial\zeta}\left(m_1^\zeta\tau_{rz} + m_3^\zeta\tau_{zz}\right)\right)\\
&+(\gamma-1)\frac{\partial}{\partial\xi}\left(u_r\left(m_1^\xi\tau_{rr} + m_3^\xi\tau_{rz}\right) + u_\theta\left(m_1^\xi\tau_{r\theta} + m_3^\xi\tau_{\theta z}\right) + u_z\left(m_1^\xi\tau_{rr} + m_3^\xi\tau_{rz}\right)\right)\\
&+(\gamma-1)\frac{\partial}{\partial\zeta}\left(u_r\left(m_1^\zeta\tau_{rr} + m_3^\zeta\tau_{rz}\right) + u_\theta\left(m_1^\zeta\tau_{r\theta} + m_3^\zeta\tau_{\theta z}\right) + u_z\left(m_1^\zeta\tau_{rr} + m_3^\zeta\tau_{rz}\right)\right)\\
&-(\gamma-1)\left(\frac{\partial}{\partial\xi}\left(m_1^\xi\phi_r + m_3^\xi\phi_z\right) + \frac{\partial}{\partial\zeta}\left(m_1^\zeta\phi_r + m_3^\zeta\phi_z\right)\right)
\end{aligned}
\tag{3.26}
$$

Stress tensor

$$J\tau_{rr} = 2\mu\left(m_1^\xi\frac{\partial u_r}{\partial\xi} + m_1^\zeta\frac{\partial u_r}{\partial\zeta}\right) + \left(\mu_d - \frac{2}{3}\mu\right)(\nabla\cdot\vec{u}) \tag{3.27}$$

$$J\tau_{\theta\theta} = 2\mu\theta_\eta m_2^\eta u_r + \left(\mu_d - \frac{2}{3}\mu\right)(\nabla\cdot\vec{u}) \tag{3.28}$$

$$J\tau_{zz} = 2\mu\left(m_3^\xi\frac{\partial u_z}{\partial\xi} + m_3^\zeta\frac{\partial u_z}{\partial\zeta}\right) + \left(\mu_d - \frac{2}{3}\mu\right)(\nabla\cdot\vec{u}) \tag{3.29}$$

$$J\tau_{r\theta} = \mu\left(m_1^\xi\frac{\partial u_\theta}{\partial\xi} + m_1^\zeta\frac{\partial u_\theta}{\partial\zeta} - \theta_\eta m_2^\eta u_\theta\right) \tag{3.30}$$

$$J\tau_{rz} = \mu\left(m_3^\xi\frac{\partial u_r}{\partial\xi} + m_3^\zeta\frac{\partial u_r}{\partial\zeta} + m_1^\xi\frac{\partial u_z}{\partial\xi} + m_1^\zeta\frac{\partial u_z}{\partial\zeta}\right) \tag{3.31}$$

$$J\tau_{\theta z} = \mu\left(m_3^\xi\frac{\partial u_\theta}{\partial\xi} + m_3^\zeta\frac{\partial u_\theta}{\partial\zeta}\right) \tag{3.32}$$

$$\tag{3.33}$$

The velocity divergence in the stress tensor is computed as following:

$$\nabla \cdot \vec{u} = \left(\frac{\partial}{\partial \xi} \left(m_1^\xi u_r + m_3^\xi u_z \right) \frac{\partial}{\partial \zeta} \left(m_1^\zeta u_r + m_3^\zeta u_z \right) \right) . \tag{3.34}$$

Heat flux

$$J\phi_r = -\lambda \left(m_1^\xi \frac{\partial T}{\partial \xi} + m_1^\zeta \frac{\partial T}{\partial \zeta} \right) \tag{3.35}$$

$$J\phi_z = -\lambda \left(m_3^\xi \frac{\partial T}{\partial \xi} + m_3^\zeta \frac{\partial T}{\partial \zeta} \right) \tag{3.36}$$

In the simplified case of this work, where no azimuthal component of the velocity is considered, only the additional terms highlighted in red, involving $\tau_{\theta\theta}$ in the radial momentum equation 3.23 and in the energy equation 3.26, make a difference compared to a two-dimensional Cartesian case. The other additional terms, highlighted in blue, effectively modify the equations only when an azimuthal component of the velocity is present.

3.1.4 Volume penalization and artificial source terms

The computation of the gas flow in this work relies on finite differences methods. This makes the consideration of complex geometries challenging because obstacles are present within the system and hinder the flow. It becomes indeed difficult to adapt the computational grid to these obstacles so that the solution is only considered where the gas is present and proper boundary conditions are applied. To overcome this difficulty, the entire domain is discretized, including the obstacles. The principle then relies on the modification of the Navier-Stokes equations in the regions where the obstacles are located. In our cases, this represents mainly parts of the walls and the electrodes of the ion funnel, as presented in sections 2.1.2 and 2.1.3. The additional terms considered in the equations ensure that non-slip boundary conditions of the velocity field are enforced at the boundaries of the fluid domain. It also assumes a given temperature inside the non-fluid parts of the computational domain.

The additional terms are generally referred to as Brinkman terms because it can be shown that they are equivalent to solving a so-called Brinkman equation, as presented in Brinkman (1949). In this calculation, one considers a fluid passing through a "dense swarm of particles" usually modeled as a porous media, the ratio between particles and fluid being associated to a factor called permeability. A typical example of this kind of system is water flowing through a bed of sand. This principle can be pushed to its limits. When the permeability factor tends to zero, the porous media represents a solid located in the domain. The same method can then be used to represent a complex geometry embedded in an elementary domain, where the non-fluidic parts are represented via a porous media in the limit of zero permeability.

The general theory for incompressible flows is presented in Angot, Bruneau, and Fabrie (1999). The theory was further extended to compressible flows. A first approach is presented in Liu and Vasilyev (2007). It keeps the principle of a porous media, that is the continuity equation is adapted to correctly reproduce the behavior of the fluid where the porous media is located. The modifications of the other Navier-Stokes equations remain similar to the incompressible case. Especially, it

directly uses the velocity for the correction term in the momentum equations. Another extension, dedicated to solid obstacles, was presented in Boiron, Chiavassa, and Donat (2009). As only real obstacles (that is no porous media) are considered, the continuity equation is not modified. Furthermore, the correction term in the momentum equations uses momentum values instead of velocities, which supposedly allows efficient computation of flow with high Mach numbers and shocked flows. This corresponds to the characteristics of the flow expected in the ion funnels. We thus proceed with the penalization method described in Boiron, Chiavassa, and Donat (2009).

Application to the skew symmetric formulation of the NAVIER-STOKES equations

This methodology has been applied to the skew-symmetric form of the Navier-Stokes equation from Reiss and Sesterhenn (2014). Different parameters are considered to apply the method:

- the form of the object: it is represented by a mask function χ_{VPM} that takes 0 in the fluid regions and 1 in the obstacle regions;
- the velocity of the obstacle $\vec{v}_{\mathrm{VPM}}$: in this work, we only consider fixed objects, the velocity is thus zero;
- the temperature of the object T_{VPM};
- the permeability η_{VPM}.

Using these parameters, terms are added at the right-hand side of equations 3.2 and 3.3, or their corresponding transformation in axially symmetric systems. The momentum equation becomes:

$$\begin{aligned}\sqrt{\rho}\,\frac{\partial\sqrt{\rho}\vec{u}}{\partial t} =& -\frac{1}{2}\left(\nabla\cdot\left(\rho\vec{u}\otimes\vec{u}\right)+\left(\nabla\otimes\vec{u}\right)\left(\rho\vec{u}\right)\right)-\nabla p\\ &+\nabla\cdot\underline{\underline{\tau}}-\frac{\chi_{\mathrm{VPM}}}{\eta_{\mathrm{VPM}}}\rho\left(\vec{u}-\vec{v}_{\mathrm{VPM}}\right),\end{aligned} \tag{3.37}$$

and the energy equation becomes:

$$\begin{aligned}\frac{\partial p}{\partial t} =& -\gamma\nabla\cdot\left(p\vec{u}\right)+\left(\gamma-1\right)\left(\vec{u}\cdot\nabla p-\vec{u}\cdot\left(\nabla\cdot\underline{\underline{\tau}}\right)+\nabla\cdot\left(\underline{\underline{\tau}}\,\vec{u}\right)-\nabla\cdot\vec{\phi}\right)\\ &-\frac{\chi_{\mathrm{VPM}}}{\eta_{\mathrm{VPM}}}\left(p-\rho R_{\mathrm{s}}T_{\mathrm{VPM}}\right),\end{aligned} \tag{3.38}$$

with R_{s} the specific molar mass of air, following the ideal gas law as described in equation 3.10.

Extension to sponge terms to set boundary conditions

A similar method can be used to set boundary conditions in the domain using so-called absorbing layers or sponge terms. An interesting presentation of this method, in the broader context of artificial boundary conditions for incompressible flows, can be found in Colonius (2004), where different kinds of such modifications of the equations are presented.

The additional terms introduced in this context allow to enforce the solution at specific locations in the domain, e.g. to define the values in the inlet or outlet areas. Any component of the state field can be set via these terms. In our case, the parameters considered are:

- the form of the affected region: it is represented by a mask function χ_{sp} that takes 0 in the fluid regions and 1 in the affected region, using a transition area from one zone to the other;
- the density of the fluid in this region ρ_{sp};
- the velocity of the fluid in this region $\vec{u}_{\text{sp}}$;
- the pressure of the fluid in this region p_{sp};
- a sponge factor η_{sp}.

In the considered regions, all components of the state fluid are not necessarily known and, unless a solution of the Navier-Stokes equation is known, only some of the components should be enforced, the others being set to the current state. The mass equation thus becomes:

$$2\sqrt{\rho}\,\frac{\partial\sqrt{\rho}}{\partial t} = -\nabla\cdot(\rho\vec{u}) - \frac{\chi_{\text{sp}}}{\eta_{\text{sp}}}\left(\rho-\rho_{\text{sp}}\right)\,, \tag{3.39}$$

the momentum equation:

$$\begin{aligned}\sqrt{\rho}\,\frac{\partial\sqrt{\rho}\vec{u}}{\partial t} =& -\frac{1}{2}\left(\nabla\cdot(\rho\vec{u}\otimes\vec{u}) + (\nabla\otimes\vec{u})\,(\rho\vec{u})\right) - \nabla p \\ &+ \nabla\cdot\underline{\underline{\tau}} - \frac{\chi_{\text{sp}}}{\eta_{\text{sp}}}\rho\left(\vec{u}-\vec{u}_{\text{sp}}\right)\,,\end{aligned} \tag{3.40}$$

and the energy equation:

$$\begin{aligned}\frac{\partial p}{\partial t} =& -\gamma\nabla\cdot(p\vec{u}) + (\gamma-1)\left(\vec{u}\cdot\nabla p - \vec{u}\cdot\left(\nabla\cdot\underline{\underline{\tau}}\right) + \nabla\cdot\left(\underline{\underline{\tau}}\,\vec{u}\right) - \nabla\cdot\vec{\phi}\right) \\ &- \frac{\chi_{\text{sp}}}{\eta_{\text{sp}}}\left(p-p_{\text{sp}}\right)\,.\end{aligned} \tag{3.41}$$

This concludes the presentation of the methodology used to describe the gas flow present in the different systems considered. In the following, the results of such computations are exposed.

3.2 Results of the gas flow in the capillary - Laminar case

The first part of the device considered is the capillary, which plays the role of the interface between the atmospheric pressure ionization and the next chambers at lower pressure, being it an ion funnel, as further considered, or a skimmer, for instance. The geometry of this part is usually quite simple and is often, as its name indicates, a long thin pipe. Some improvements of the geometry, to increase the transmission ratio of the ions flowing through it, have been studied. A promising one is presented in Pauly et al. (2014), where a funnel-shaped inlet is added to the pipe. The results presented in this work are based on this geometry, as described in section 2.1.1.

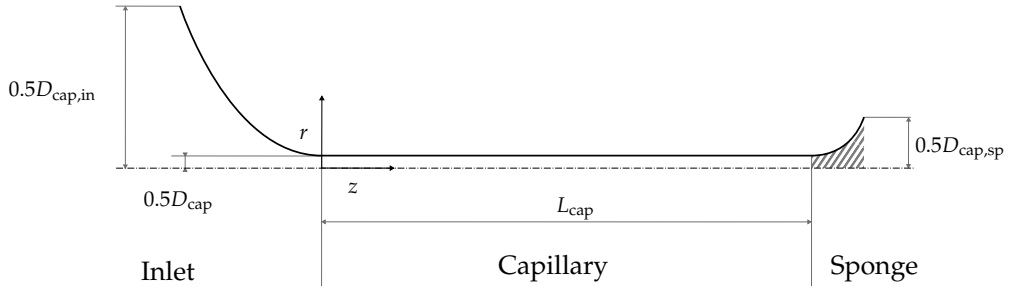

FIGURE 3.1: Sketch of the geometry of the transfer capillary considered for the laminar computation, including a sponge area at its outlet.

In this section, we focus on laminar flows, that is excluding the onset of turbulent effects in the flow. The reason for this is twofold: first, the exact nature of the flow taking place in the capillary remains a question. Recent works have brought different answers to this question. While the study presented in M. Skoblin et al. (2017) presents measurements compatible with the assumption that the flow is laminar within the capillary, another work published by Wißdorf et al. (2016) shows that experimental results tend to prove the presence of transitional or turbulent flow. This aspect is further exposed in section 3.3. Furthermore, a preliminary study published in Bernier et al. (2018) made the hypothesis that the appearance of a turbulent flow could be related to lower transmission ratios through the capillary. Thus, we first focus on the laminar flow that can be expected in the capillary.

3.2.1 Settings and considered cases

The geometry of the different considered cases here is always similar and is sketched in figure 3.1. Two geometric parameters vary: the length of the straight part of the capillary and its diameter. The length of the funnel-shaped inlet is kept constant, while its diameter is proportional to the one of the pipe.

To ensure the proper stability of the computation, a second funnel-shaped part is added after the outlet. This is a sponge area, as presented in section 3.1.4, where only the pressure is enforced. The maximal diameter of this part $D_{cap,sp}$ is directly proportional to the diameter of the capillary: $D_{cap,sp} = 6\,D_{cap}$. This intends to reproduce the expected chocking of the flow due to friction and heat exchange effects when the pressure difference between both ends of a pipe is high enough such that sonic conditions are reached and the fluid quantity transmitted limited. This phenomenon, called choking, is well described in Shapiro (1953, pp. 234-236). The other boundary conditions are the following:

- non-reflecting boundary conditions at the inlet set to normal conditions (atmospheric pressure, temperature of 298.15 K, no velocity);
- non-reflecting boundary conditions at the outlet of the sponge area, with the reference set to the closest inner grid points, to let waves leave the computational domain;
- isothermal non-slip boundary conditions at the wall. The temperature in the straight part is set to a defined temperature T_{wall}. A linear transition between

Capillary length L_{cap} (cm)	Capillary diameter D_{cap} (mm)	Inlet diameter $D_{cap,in}$ (mm)	Sponge diameter $D_{cap,sp}$ (mm)	Number of points - axial	Number of points - radial	Wall temperature (K)	Sponge reference pressure (Pa)	Mass flow ($kg \cdot s^{-1}$)
6.0	0.25	2.0	0.4	64	512	-	5066.25	3.61×10^{-6}
6.0	0.25	2.0	0.4	64	512	350	10132.50	2.92×10^{-6}
6.0	0.25	2.0	0.4	64	512	500	10132.50	1.79×10^{-6}
6.0	0.50	4.0	0.8	96	512	-	5066.25	2.59×10^{-5}
6.0	0.50	4.0	0.8	96	512	350	10132.50	2.30×10^{-5}
6.0	0.50	4.0	0.8	96	512	500	10132.50	1.71×10^{-5}
3.8	0.75	6.0	1.2	128	384	-	5066.25	7.54×10^{-5}
3.8	0.75	6.0	1.2	128	384	375	5066.25	6.88×10^{-5}
6.0	0.75	6.0	1.2	128	512	-	10132.50	7.00×10^{-5}
6.0	0.75	6.0	1.2	128	512	350	10132.50	6.47×10^{-5}
6.0	0.75	6.0	1.2	128	512	375	10132.50	6.25×10^{-5}
6.0	0.75	6.0	1.2	128	512	400	10132.50	6.05×10^{-5}
6.0	0.75	6.0	1.2	128	512	425	10132.50	5.86×10^{-5}
6.0	0.75	6.0	1.2	128	512	450	10132.50	5.67×10^{-5}
6.0	0.75	6.0	1.2	128	512	475	10132.50	5.49×10^{-5}
6.0	0.75	6.0	1.2	128	512	500	10132.50	5.32×10^{-5}
6.0	0.75	6.0	1.2	128	512	525	10132.50	5.16×10^{-5}
6.0	0.75	8.0	1.6	128	512	550	10132.50	5.00×10^{-5}
6.0	1.00	8.0	1.6	128	512	-	10132.50	1.37×10^{-4}
6.0	1.00	8.0	1.6	128	512	350	10132.50	1.29×10^{-4}
6.0	1.00	8.0	1.6	128	512	500	10132.50	1.11×10^{-4}
16.5	1.00	8.0	1.6	128	1024	-	5066.25	1.14×10^{-4}
16.5	1.00	8.0	1.6	128	1024	350	5066.25	1.04×10^{-4}
16.5	1.00	8.0	1.6	128	1024	500	5066.25	8.15×10^{-5}

TABLE 3.1: List of the capillary gas flow simulations and their corresponding parameters. When no wall temperature is given, adiabatic boundary conditions have been used for the entire set of wall boundaries. The mass flow is computed from the results of the simulation and thus not an input parameter.

the normal conditions and the straight part temperature is imposed within the funnel-shaped inlet.[1].

The non-reflecting boundary conditions considered here are based on the characteristics method and make use of the Reynolds invariants that can be derived from the Euler equations. The latter are the equivalent of the Navier-Stokes equations presented in previous sections when the friction and diffusion features are neglected. They are thus an approximation for the present case but effectively let the structure present in the flow leave the computational domain without being reflected on the artificial boundaries. A detailed description of the implementation is provided in Stein (2019).

Three parameters have been varied during this study: the length of the straight part of the capillary, its diameter, and the temperature of the wall. The first two parameters allow us to describe the influence of the geometry on the expected flow. The latter reproduces common settings of commercial devices, where the temperature of the capillary can be easily varied. The list of cases is presented in table 3.1. In all cases, fourth-order spatial derivatives and a fourth-order Runge-Kutta time integration scheme are used. A Padé filter (as described in Gaitonde and Visbal (2000)) is applied in axial and radial direction every 550^{th} time step. The presented results are considered as converged simulation, that is when total pressure, mass, and energy in the domain remain constant over time.

3.2.2 General results

Most of the results presented here and in the next sections referring to the laminar capillary flow have been published in Bernier et al. (2020).

Choking and sonic conditions

When submitted to a strong pressure difference between its both ends, it has been observed that the choking of the flow occurs. It means that once this ratio becomes larger than a specific value, the quantity of gas that goes through the pipe is limited. This phenomenon can be observed in our simulations, where the pressure reached at the outlet of the pipe is much larger than the one set in the sponge area further downstream. This can be observed in figure 3.2 and is consistently repeated in all cases presented here. The pressure profile inside the straight part of the capillary, corresponding to classic pipe flows, is very similar to the ones measured in similar conditions and reported in Frössel (1936). The experiments were performed with thermal isolation of the pipe, and thus correspond to the adiabatic case and not directly to the isothermal cases depicted in figure 3.2. Once the sponge term comes into action, that is on the right of the vertical solid line in the picture, the pressure drops abruptly and reaches values closer to the reference or even lower. The pressure level in the physical domain is independent of this reference, as long as this is low enough compared to the expected level at the end of the physical capillary. More detailed results focused on the aspects just mentioned are available in appendix C. This behavior is attributed to viscous effects that limit the velocity of the gas within the pipe. The classic theory to explain this phenomenon is called the Fanno flow theory. It is based on a one-dimensional description of the flow and assumes a constant wall friction coefficient. The corresponding theory can be found in Shapiro (1953).

1. Several cases have been simulated using adiabatic non-slip boundary conditions as comparison point and are presented in appendix C

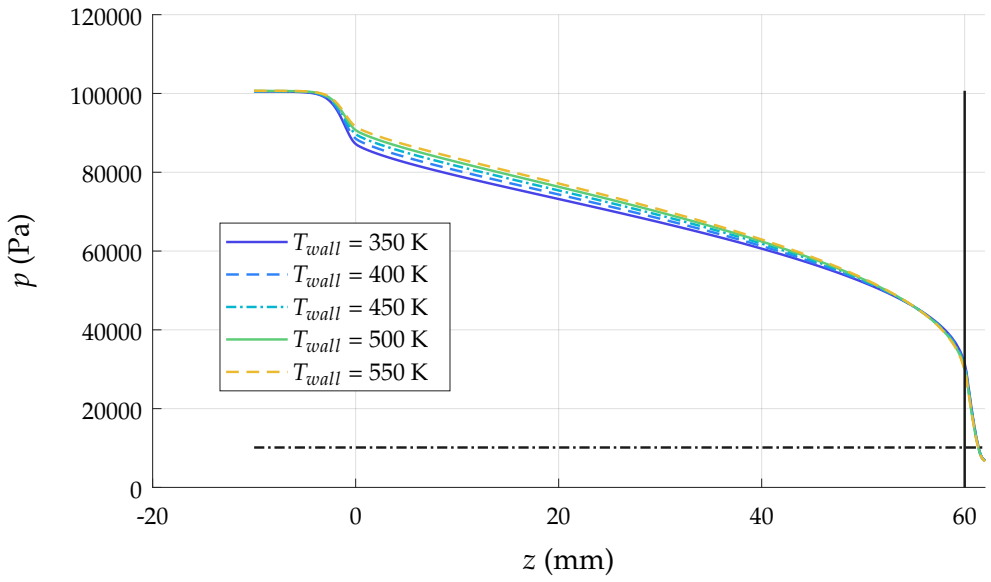

FIGURE 3.2: Pressure in the center of the capillary along the axial direction. Diameter of 0.75 mm and length of the straight part of 6.0 cm. The end of the physical domain is materialized with the vertical solid line. The pressure reference in the sponge domain is represented by the horizontal dash-dotted line.

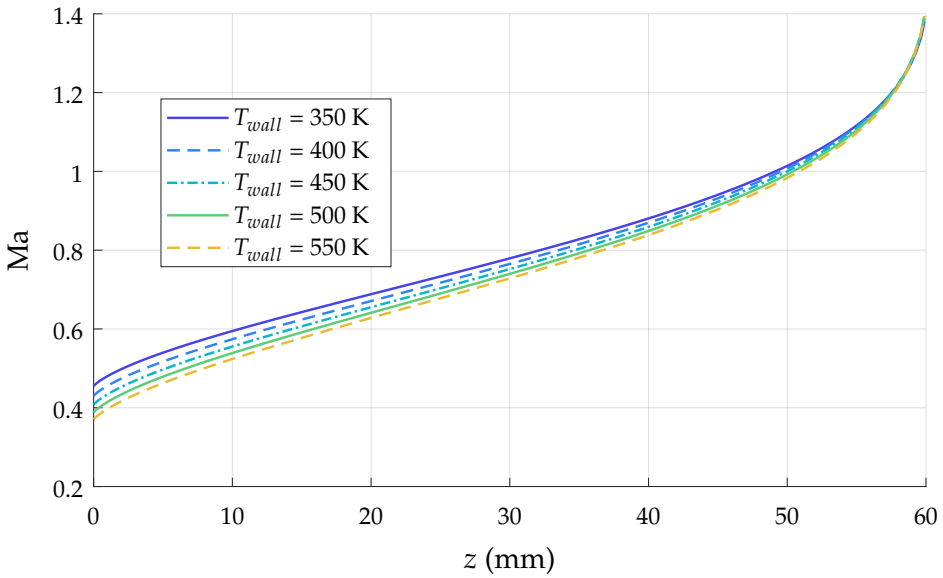

FIGURE 3.3: Mach number of at the center of the capillary along the axial direction. Diameter of 0.75 mm and length of 6.0 cm. Only the straight part of the capillary is considered here.

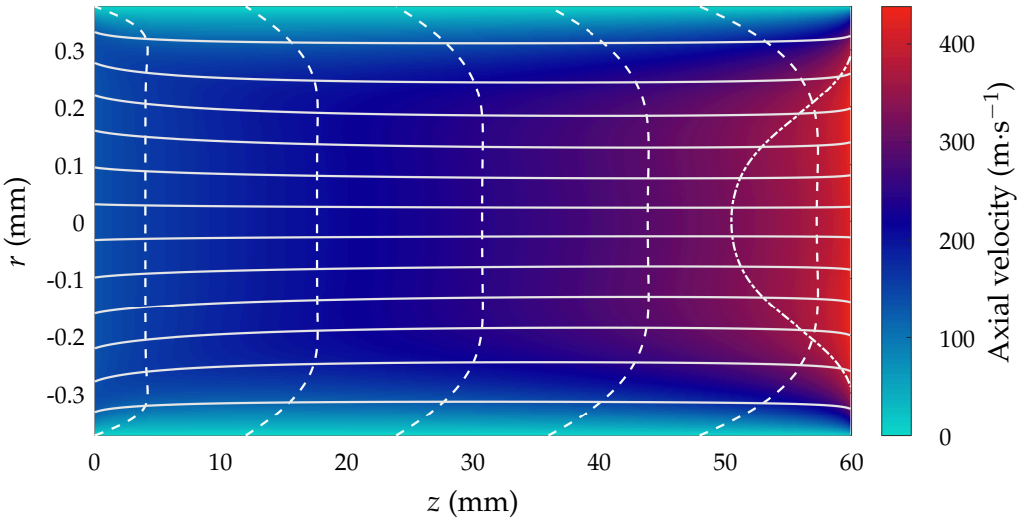

FIGURE 3.4: Two-dimensional profile of the axial velocity in the straight part of the capillary. Diameter of 0.75 mm length of 6.0 cm and wall temperature of 500 K. The dashed lines represent the profile of the velocity at different axial positions. The solid lines represent streamlines within the capillary. The dimensions of the domain are not to scale.

This leads to the condition that sonic conditions (Mach number Ma $= 1$) are reached at the end of the pipe, causing acceleration when the flow is initially subsonic, as is the case here, or deceleration when the flow is supersonic. In the case of isothermal conditions at the wall, further losses should be considered due to the transfer of thermal energy. The equations taking into account such effects, and assuming that the friction terms are neglected, can be found in Bartlmä (1975) and also predict sonic conditions at the end of the pipe flow. This was the assumption made to mimic the flow profile in a previous publication (Bernier et al. 2018).

The present simulations do not consider the assumptions previously mentioned and directly apply the Navier-Stokes equations to a two-dimensional, axially symmetric case. They show a more complex picture close to the outlet. When looking at the Mach number computed along the centerline of the flow in figure 3.3, a supersonic area appears with values of the local Mach number reaching not less than 1.4. That value contradicts the prevision of the Fanno theory. This unexpected feature could however be found in some publications. A study of the behavior of the flow has been performed in Murphy and Miller (1984), where different outlet geometries are compared. Measurements show that the Mach number at the outlet of a straight pipe, similar to the capillaries considered here, is indeed well larger than 1.

This behavior can be explained by the fact that the effective pipe is not one-dimensional. The Fanno theory does not take into account the radial variations of the flow, which can explain the difference. In figure 3.4 the streamlines along the capillary for an exemplary case are represented and show that they are not parallel to the walls but present a small bending. This is a sign that the boundary layer gets thinner when approaching the outlet. This phenomenon can also be seen in the same figure, considering the values of the axial velocity depicted in the background. This can be interpreted as an effective variation of the cross-section that should be considered in a one-dimensional approach. This would still be an approximation though, as the

bending of the streamlines is due to a non-zero, even if very small, radial component of the velocity vector. The field is thus two-dimensional. This situation can further be considered as a convergent-divergent nozzle, building up an effective Laval nozzle. The sonic condition is reached in the minimal cross-section of this effective nozzle and not at the end of the capillary. However, other considerations for the Mach number are possible, for example the bulk Mach number. This is defined as the ratio between the mean velocity in each cross-section, called bulk velocity, and the speed of sound at the wall. The resulting value is significantly lower than the local value in the middle of the pipe because the effects of the boundary layer are integrated into the final value. For the cases presented in figure 3.3, it only reaches between 0.89 for a wall temperature of 350 K and 0.79 for 550 K at the end of the capillary.

A detailed numerical study of this phenomenon has been delivered by Lijo, Kim, and Setoguchi (2010), where the local supersonic flow is specifically addressed. The main differences between the computation performed in that publication and the present work are that the former does not limit the computational domain to the capillary but computes the following chamber alongside. In the present work, this chamber is mimicked using the sponge area. Furthermore, a turbulent flow is considered, using the Reynolds-averaged formulation of the Navier-Stokes equations and the $k-\omega$ model for closure. This second difference is justified by the fact that the diameter of 15 mm is 15 times larger than the largest diameter considered here, delivering significantly larger Reynolds numbers for the system, while the rest of the conditions are similar. Furthermore, the boundary conditions at the wall are adiabatic. However, this choice in the present work does not lead to significant modifications of the choking properties of the flow. It is thus remarkable that the shape of the supersonic area at the end of the pipe found in Lijo, Kim, and Setoguchi (2010) is very similar to the one represented with the solid line in figure 3.8.

Velocity field

It is further interesting to consider the local velocity of the gas, as it has a direct influence on the trajectory of the particles, in which we are interested (see equations 2.18 and 2.20). Different parameters influence the velocity profiles, the geometrical ones as well as the wall temperature. Nevertheless, a general picture can be drawn. At the beginning of the straight part of the pipe (that is at the junction between the funnel-shaped inlet and the capillary itself), the profile is close to a typical top-hat form. Further downstream, the boundary layer gets thicker and evolves toward a profile closer to the parabolic form expected for a fully developed laminar pipe flow. This is represented in an exemplary case in figure 3.5. Two main parameters affect this picture though. First, the specific behavior observed close to the outlet and discussed in the previous section is related to a thinner boundary layer. This means that the approaching parabolic form of the profile in this area is altered. The second parameter is the length of the straight section or rather the ratio between the length of the straight section and the diameter of the pipe L/D. The building of the parabolic profile is progressive along the axis and thus can only be truly observed for geometries where the ratio L/D exceeds values of 200 to 300, according to an empirical formula given in Prandtl, Oswatitsch, and Wieghardt (1993, p. 244). The example considered only reaches a ratio of 120.

Further, an unexpected effect can be observed when the heating of the capillary walls is significant. In such cases, the maximum of the axial velocity is reached at a position off the centerline. This phenomenon has been represented in figure 3.6.

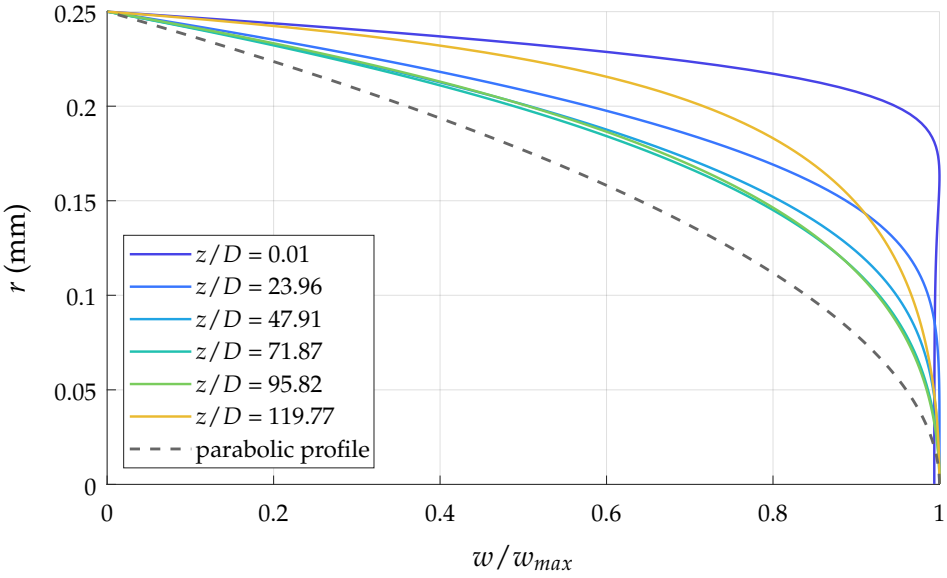

FIGURE 3.5: Normalized axial velocity in cross-sections of the capillary at different axial positions. Diameter of 0.50 mm, length of the straight part of the capillary of 6.0 cm, and wall temperature of 350 K.

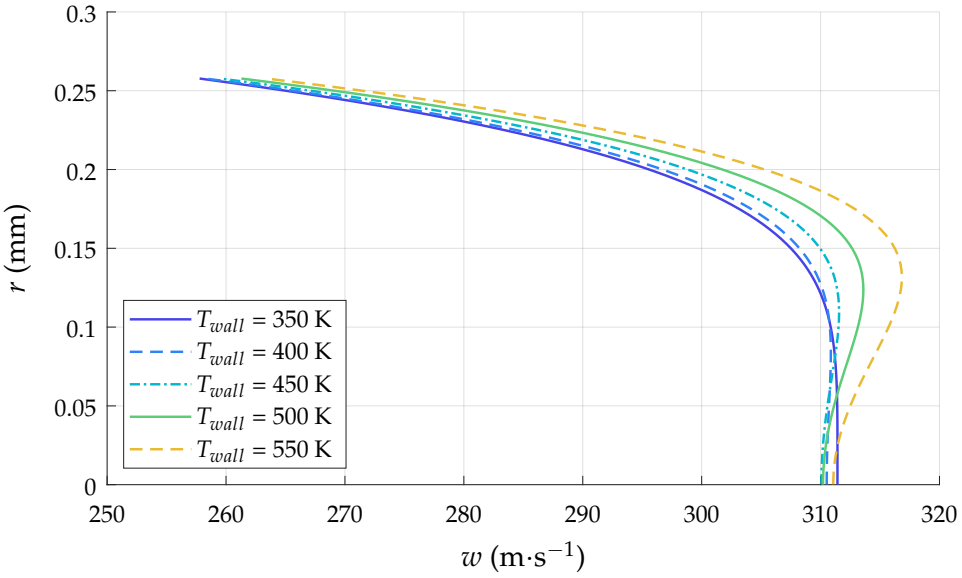

FIGURE 3.6: Axial velocity in a cross-section of the capillary with different wall temperatures at an axial position of $z \approx 4.8$ cm. Diameter of 0.75 mm and length of the straight part of the capillary of 6.0 cm. Only the central part of the domain is represented.

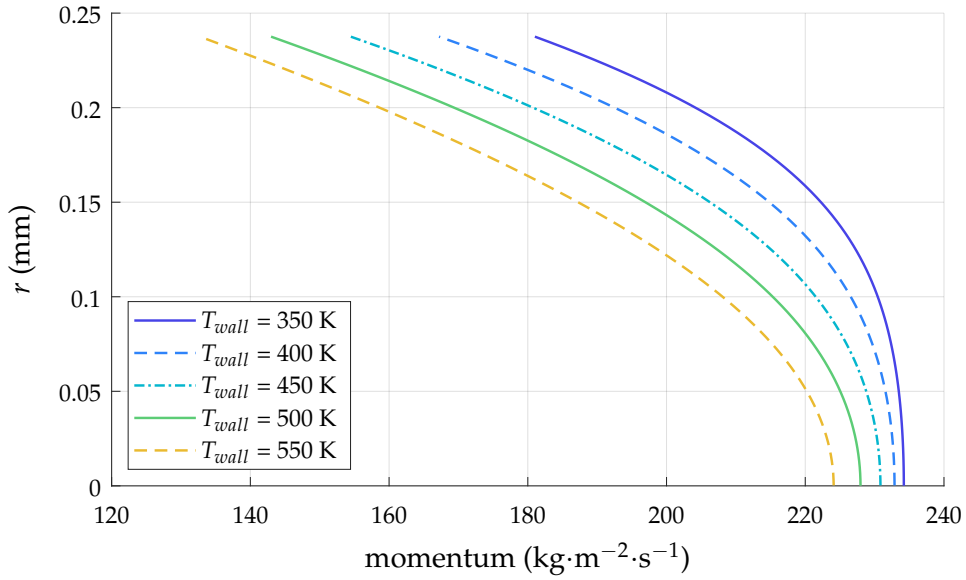

FIGURE 3.7: Axial specific momentum in a cross-section of the capillary with different wall temperatures at an axial position of $z \approx 4.8\,\text{cm}$. Diameter of 0.75 mm and length of the straight part of the capillary of 6.0 cm. Only the central part of the domain is represented.

It thus builds a ring of high velocities centered around the central axis. This behavior has not been, to the knowledge of the author, reported in other cases and can appear as counter-intuitive at a first glance. One could indeed expect the fluid elements located in the central area surrounded by the faster elements to be accelerated and catch up with the ring. However, this deduction is only based on the velocity component. The conservative value described by the Navier-Stokes equations is the momentum (velocity multiplied by mass density, when considering a specific value). This quantity shows the classic shape with a maximum at the centerline and a monotonous decrease up to the wall, as shown in figure 3.7. This is a sign of the stability of the solution presented.

This behavior can further be qualitatively explained considering elementary concepts. The main engine of the gas flow within the capillary is the pressure gradient in the axial direction. The pressure can be considered as constant in each cross-section with a good approximation. As a consequence, the force applied to the fluid elements is approximately similar within the cross-section. The heat transfer that occurs at the walls implies that the gas within the temperature boundary layer is lighter and the acceleration caused by the pressure gradient is larger. This effect is compensated by the friction within the velocity boundary layer. However, velocity and temperature boundary layers do not present the same thickness. Thus, an area remains where the temperature boundary layer is observed but not the velocity boundary layer. The stronger acceleration is not compensated by friction effects in this area, which leads to the ring of higher velocities surrounding an area of comparatively lower velocities, as previously described. The difference in thickness between the velocity and temperature boundary layers is expected. It depends on the value of the Prandtl number previously presented in section 3.1.1. This number represents the ratio of the viscous transports compared to the diffusive ones. Thus a Prandtl number of 1 indicates that both effects occur with the same intensity so

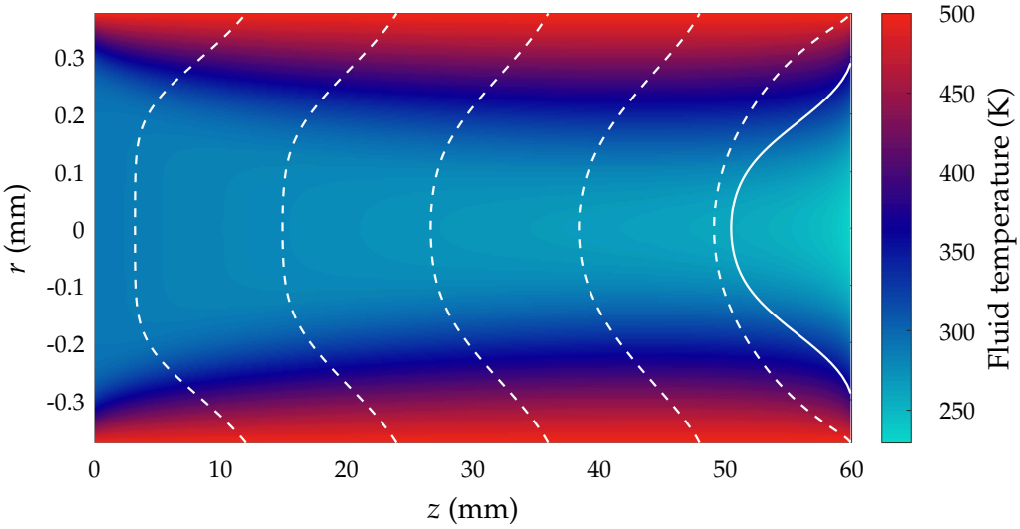

FIGURE 3.8: Two-dimensional profile of the fluid temperature in the straight part of the capillary. Diameter of 0.75 mm, length of 6.0 cm, and wall temperature of 500 K. The dashed lines represent the profile of the temperature at different axial positions. The solid line represents the limit between the subsonic (left of the line) and supersonic (right of the line) parts of the flow. The dimensions of the domain are not to scale.

that the (viscous) velocity boundary layer and the (diffusive) temperature boundary layer have the same thickness. In the case of air, where the Prandtl number is smaller than one (0.71), the viscous transports are weaker than the diffusive ones. As a consequence, the boundary effects caused by viscous effects are thinner than the ones caused by diffusion, consistent with the results presented here. A detailed explanation of such effects can be found in Schlichting and Gersten (2017, p. 215).

Temperature field

To conclude the study of the gas flow within the capillary, we focus on the temperature field. Temperature is indeed involved in different aspects and is thus significant not only for the transport of ions presented here. Especially, the heating of the capillary is classically justified by the necessity to enhance the desolvation of the droplets created during the ionization process. Furthermore, high temperatures and the related molecular collisions can trigger transformations of the species involved, for example unfolding, declustering, or fragmentation of the transported ions. The present work does not specifically consider these aspects. The results regarding the temperature field could be used to study some of them in more detail though.[2] Finally, one aspect that has direct consequences on the transport of the ions considered here is the influence of the temperature on the ion mobility.

In a similar fashion to the velocity field, a strong stratification of the temperature field towards the axis can be observed in figure 3.8. This builds the temperature boundary layer already mentioned. An interesting feature of this boundary layer is

2. The present results might not be sufficient to study all the effects listed here. Especially no heat radiation has been considered, which could play a non negligible role when the capillary is strongly heated.

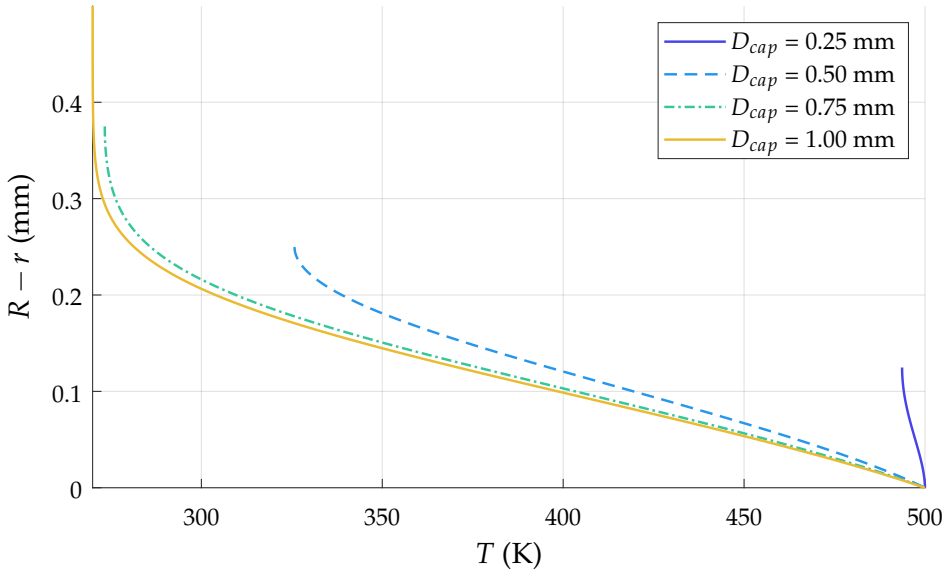

FIGURE 3.9: Temperature of the fluid represented for different values of the diameter at an axial position of $z \approx 2.4$ cm according to the distance to the wall. Length of the straight part of 6.0 cm and wall temperature of 500 K.

that its thickness seems to be roughly independent of the diameter of the capillary. Figure 3.9 shows for a similar wall temperature the radial profile of the gas temperature when the diameter varies. Especially, the two cases with the largest diameters (0.75 mm and 1.0 mm) present very similar shapes. This is important for the design of such elements because it means that the effects of heating are limited to a specific layer close to the walls and cannot reach the middle of the pipe when the diameter exceeds a certain value, not far from the usual diameters encountered in common devices.

This phenomenon can also be observed when considering the temperature of the gas along the axis, again for different diameters and represented in figure 3.10. For thin pipes, the temperature of the gas in the center of the flow is very close to the temperature enforced at the walls, as long as the cross-section considered is far enough from the inlet or outlet areas. However, wider pipes present a constant decrease in the temperature caused by the acceleration and expansion of the gas.

For large enough diameters, one can also observe that the heating does not have a significant influence on the temperature observed in the center of the pipe. Figure 3.11 presents the radial profile of the temperature for a capillary of 0.75 mm in diameter and varying wall temperatures. Here again, the boundary layer roughly presents the same thickness in all cases, and the temperature in the center is only weakly affected (between 260 K and 275 K), while the wall temperature varies over a large range (350 K to 550 K).

These results have consequences regarding the purpose of heating the capillaries. If it is intended to enhance the desolvation process of remaining droplets from the ionization, it is likely that this is significantly less efficient for capillaries with a large diameter than for thinner ones, as droplets transported through the center of the pipe are barely affected by the heating. On the other hand, such large capillaries might be able to transport, within their cold core region, sensitive ions that could be otherwise

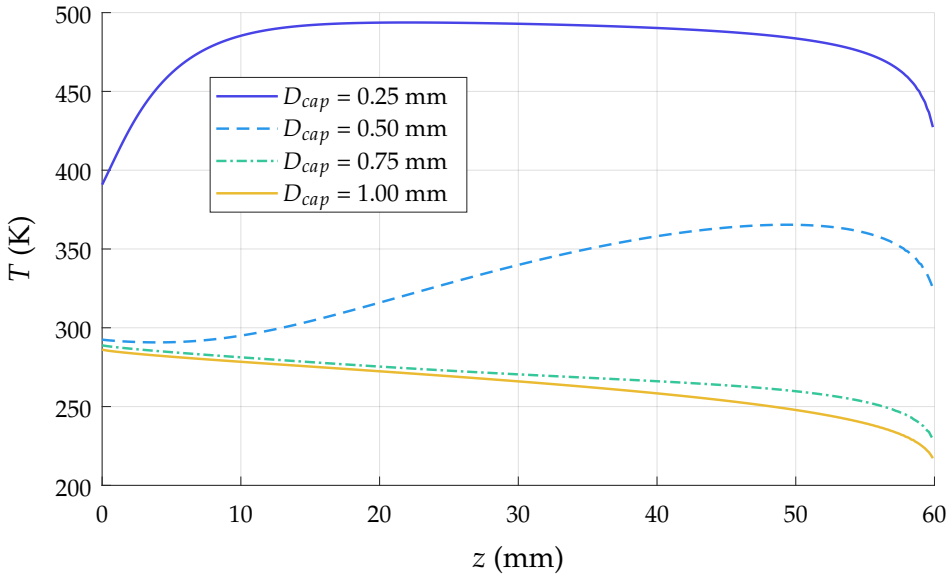

FIGURE 3.10: Temperature of the fluid at the center of the capillary along the axial dimension for different diameters of the capillary. Length of the straight part of 6.0 cm and wall temperature of 500 K.

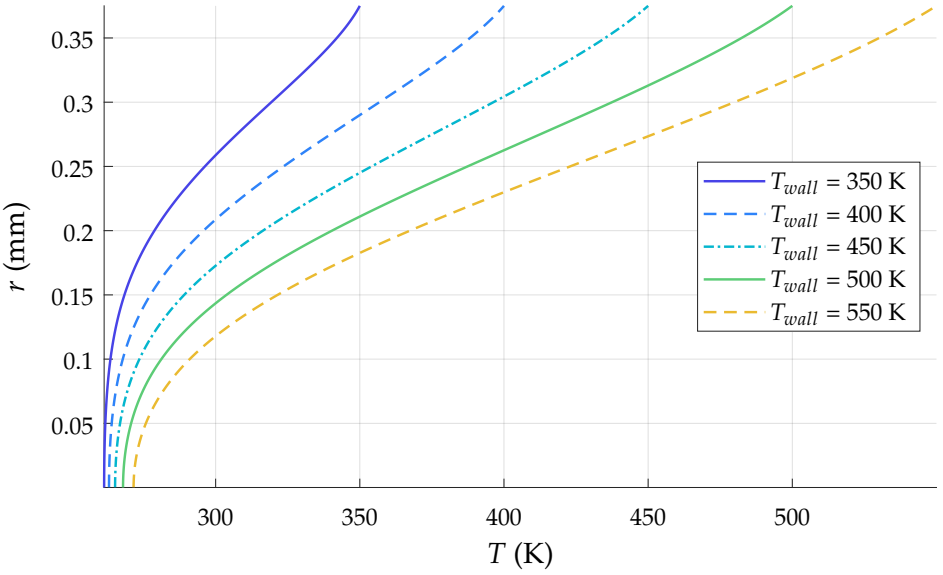

FIGURE 3.11: Radial profile of the fluid temperature for different temperatures set at the wall at an axial position of $z \approx 3.6$ cm. Diameter of 0.75 mm and length of 6.0 cm.

affected by the heating in thinner capillaries. This means that the geometry of the capillary can significantly affect the conditions of transmission of the ions. Its choice is therefore as important as the design of further parts of the device and should be carefully considered, depending on the operating conditions.

3.3 Results of the gas flow in the capillary - turbulent case

In a preliminary work published in Bernier et al. (2018), some estimations hinted that the onset of turbulence within the capillary could have a strong impact on the efficiency of ion transmission. Considering the Reynolds number in the laminar simulations, both kind of flow, laminar or turbulent, can occur a priori. The Reynolds number computed for the different wall temperatures with a 6.0 cm long capillary and a diameter of 0.75 mm range between 1,800 and 3,700. These values are computed using the bulk velocity at the outlet of the capillary and the viscosity at the wall in the corresponding cross-section. The resulting number is called bulk Reynolds number. For a diameter of 1.0 mm, it reaches 7,900 with adiabatic walls. These values thus range from close to well above the transition threshold for a standard pipe Poiseuille flow, estimated to 2,300, as reported in Hinze (1975, p. 707) even if laminar flows with Reynolds numbers up to 100,000 have been observed experimentally.

We tried to conduct some investigations to determine whether the kind of flow typically found within a capillary has an affinity to turbulence. The system presents particularities, including a strong pressure gradient and a relatively short length compared to the one typically needed to establish a fully developed state. Such systems are not very well studied in the existing literature.

3.3.1 Attempt to perturb the laminar flow

As an introduction to the following results, we first present some work about the transition of the laminar flow into turbulence. In a first tentative, we indeed tried to set a perturbation in the laminar capillary flow with a diameter of 0.75 mm. The idea is to set this perturbation at the inlet of the straight part of the pipe and to let it evolve along the capillary. We especially wanted to detect possible breakdowns of the perturbation which could point to a transition towards a turbulent flow.

The form of the perturbation was inspired from the one reported in Zikanov (1996) to present a large transient growth for infinitesimal perturbation, even if the amplitudes considered here are not infinitesimal. It takes the form of two vortexes located in the polar plane, centered on each side of the symmetry line, as depicted in figure 3.12. This perturbation can be expressed as the following:

$$u_x(r,\theta) = u_{x,0} + A_0\left(\left(1-3r^2+2r^3\right)\cos^2\theta + \left(1-9r^2+8r^3\right)\sin^2\theta\right), \tag{3.42}$$

$$u_y(r,\theta) = u_{y,0} + 6A_0\left(r^3-r^3\right)\cos\theta\sin\theta, \tag{3.43}$$

where r and θ are the polar coordinates, u_x and u_y the Cartesian components of the flow in the polar plane, and $u_{x,0}$ and $u_{y,0}$ the corresponding components of the unperturbed, laminar flow. The amplitude A_0 was chosen equal to $20\,\mathrm{m}\cdot\mathrm{s}^{-1}$.

Some results of this simulation are presented in figure 3.13 for the velocity components in the cross-section and figure 3.14 for the axial component of the velocity. The results are considered in the cross-section located about 5 cm after the beginning of the straight part of the capillary. One can observe that the perturbation evolves

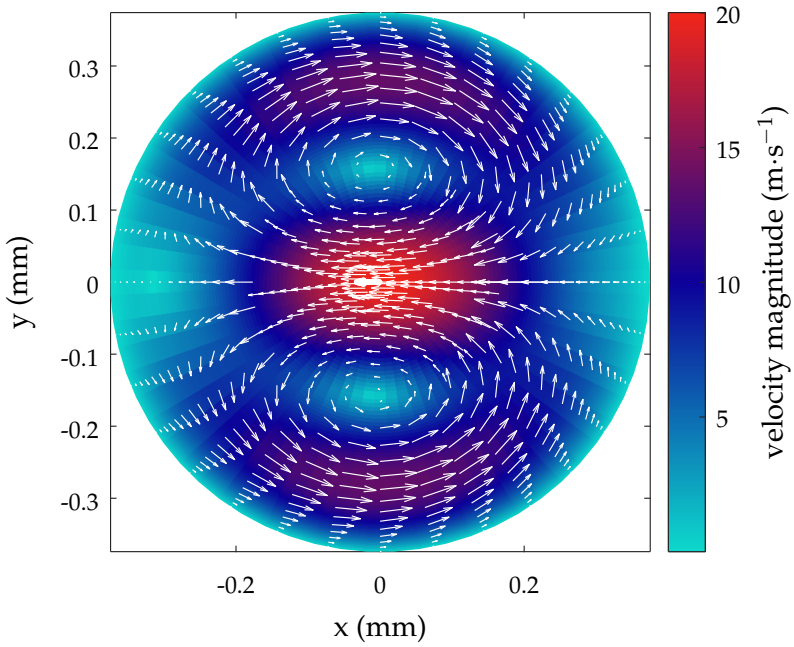

FIGURE 3.12: Form of the perturbation set at the beginning of the straight part of the capillary. The axial component of the velocity is the same as the profile computed in the axially symmetric laminar computation. The magnitude of the velocity components in the cross-section of the capillary alongside the direction of the resulting velocity vector are represented. The length of the vectors is proportional to the velocity magnitude.

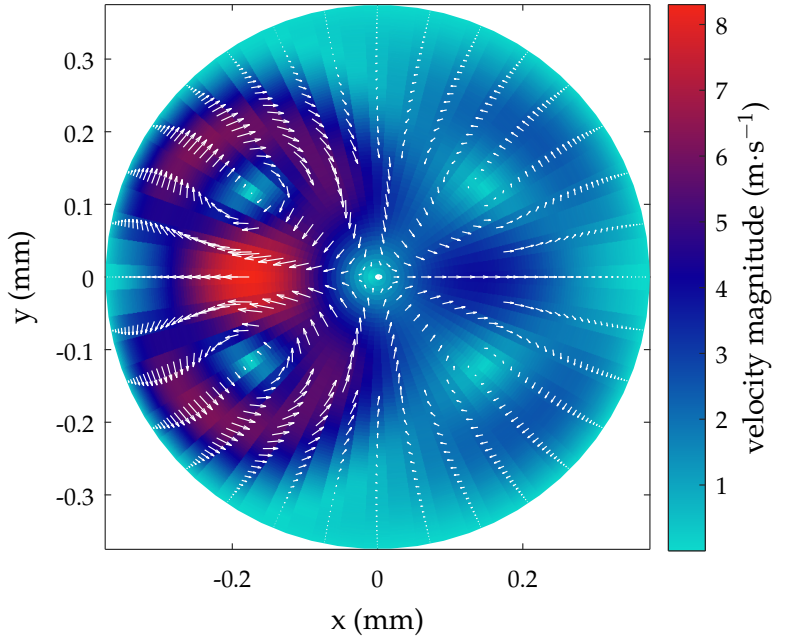

FIGURE 3.13: Magnitude and direction of the velocity components in the cross-section of the capillary at $z/D \approx 50$ (the length of the vector indicating the direction is proportional to their magnitude).

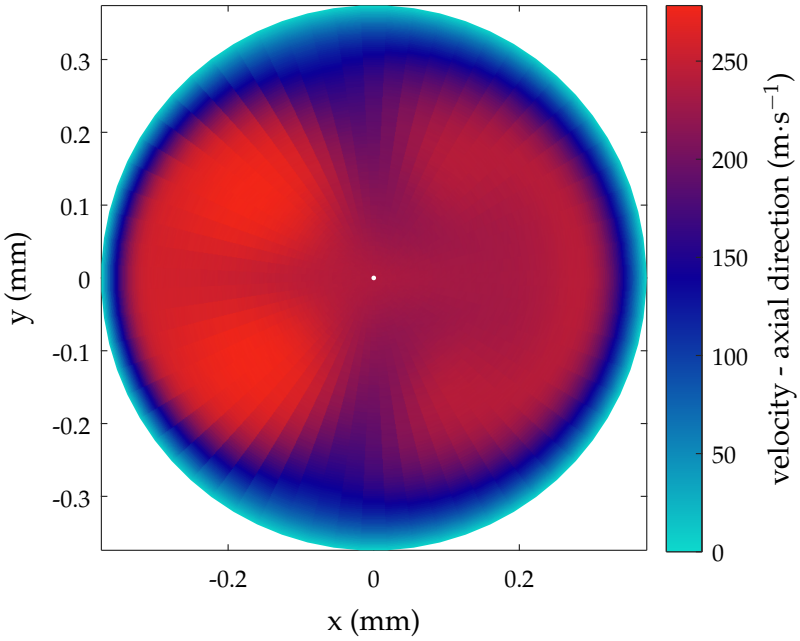

FIGURE 3.14: Axial component of the velocity at $z/D \approx 50$.

along the pipe. The profile of the axial velocity is shifted towards the walls and is thus strongly different from the initial laminar flow, as well as from the parabolic shape of a classic Poiseuille flow. Furthermore, the two distinct vortexes created at the inlet degenerate into four: two stronger ones on the left-hand side of the figure, and two weaker ones on the right-hand side. No further significant evolution of these vortexes is observed along the pipe, but the mean amplitude of the corresponding velocity components tends to decrease, from about $8.7\,\mathrm{m}\cdot\mathrm{s}^{-1}$ at the inlet to $1.3\,\mathrm{m}\cdot\mathrm{s}^{-1}$ close to the outlet, before an increase due to the adaptation to the reference values. It also presents the characteristic of two distinct local maxima of the axial velocity (see figure 3.14). This feature is presented in Zikanov (1996) as important to initiate instabilities. However, the simulation never displayed the occurrence of any transition towards turbulence and the profile presented here could be sustained for a significant time, corresponding to about 1.6 times the time needed for flow particles located close to the symmetry axis to travel through the pipe.

These tests are no definitive proof of the ability of the system to transition from laminar flow to turbulent one. Especially the settings would not offer the resolution needed to fully capture the occurrence of turbulent onsets. However, we expect that in such a case, effects could have been observed in the fields. Furthermore, a detailed study of turbulent transition in pipe flows is a complex subject. Long-lasting results of a similar system, though without strong acceleration along the pipe and for incompressible equations, are reported in X. Wu et al. (2015). This investigation tends to show that the Reynolds numbers expected in the system studied in this work are above the new limits reported (between 5,700 and 6,000) for which turbulence is expected. However, the length of the system computed to obtain such results was significantly longer than the present case (125 times the diameter vs. 80 times, respectively). This difference might also play a role in the absence of a conclusion for the results presented. We thus decided to consider the study of an already developed turbulent inlet flow and its evolution along the pipe in the presence of a strong

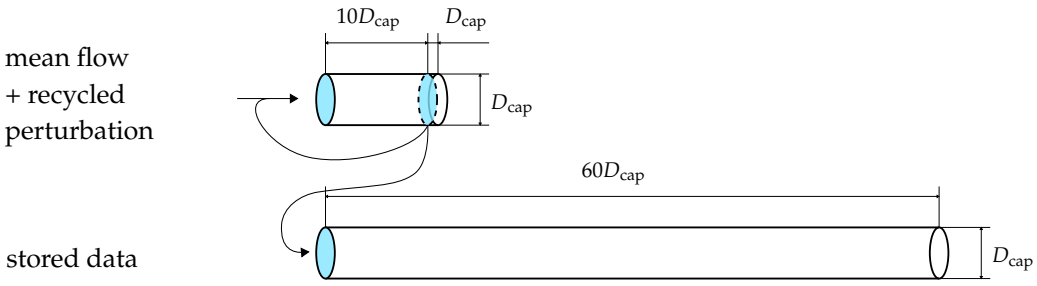

FIGURE 3.15: Sketch presenting the structure of the simulation in two stages: auxiliary simulation at the top and primary one at the bottom. Axial and radial directions are not to scale.

	Auxiliary sim.	Primary sim.
Capillary length L_{cap} (cm)	1.1	6.0
Capillary diameter D_{cap} (mm)	1.0	1.0
Number of points - axial	960	5760
Number of points - radial	120	120
Number of points - azimuthal	240	240
Time step (s)	4.8×10^{-9}	4.8×10^{-9}

TABLE 3.2: Parameters of the primary and auxiliary simulations performed for the turbulent flow in the capillary.

pressure gradient.

3.3.2 Settings of the fully turbulent simulation

The principle of the simulation presented here is to introduce a fully turbulent flow at the inlet and to observe its evolution through the capillary. It is performed using the program called NSF developed in the department for numerical fluid dynamics at the Technische Universität Berlin. It has been extensively used for several DNS, in particular in Peña Fernández and Sesterhenn (2017), with a wave-formulation of the Navier-Stokes equations or in Stein (2019) with the same skew-symmetric formulation as considered in the present work. We use two stages for the simulation, as described below, to create data for a turbulent inlet, which is then applied at the beginning of the straight part of the capillary. In both stages, we make use of cylindrical grids. The equations considered are the skew-symmetric Cartesian ones and the grid transformation is performed using the metric factors. This formulation is detailed in Reiss and Sesterhenn (2014).

We avoid the intrinsic singularity of such grids on their symmetry axis by using the solution described in Mohseni and Colonius (2000). With this approach, the radial direction is not considered along a radius of the domain but a full diameter. Using an even number of points in this direction, one thus avoids any grid point on the axis and following the issues arising with the singularity of such points. A sketch of the two simulation stages is presented in figure 3.15 and the corresponding parameters are listed in table 3.2.

The spatial derivatives are computed using fourth-order central schemes and the time integration is performed with a fourth-order Runge-Kutta method. In both

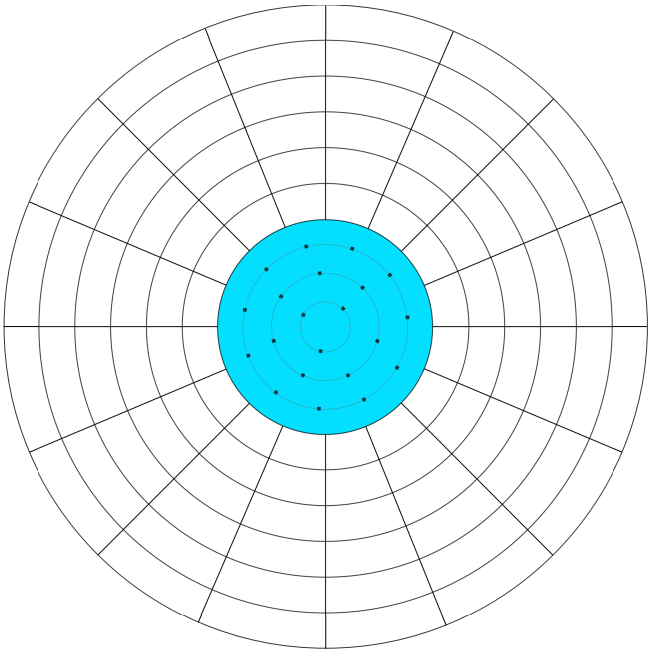

FIGURE 3.16: Sketch presenting the principle of the sharp filter used. The outer part is the regular grid, where no modification is applied. The inner, colored section, outlines the region where the effective resolution of the grid is reduced by the filter.

stages, a specific treatment is performed in the azimuthal direction for the points close to the pipe axis. The principle is to cancel the high-frequency components present in the central area where the density of grid points is much higher than in the areas located further away from the axis. Translated into the formalism of discrete Fourier transforms, the reduced number of components allowed in the spectral domain effectively corresponds to fewer discretization points than actually present in the grid, or equivalently to an effective grid spacing larger than the real one.

The target grid spacing is chosen as the best option, that is the smaller equivalent grid spacing, between the grid precision at the wall and the effective grid precision delivered by a minimal number of components for the points located close to the symmetry axis. For each radial position, we can then define the number of components in the spectral domain required to reach the target grid spacing.

In our case, the innermost points with a minimal number of spectral components fixed to three define the target. This means that the precision close to the symmetry axis remains better than close to the wall despite the very limited number of components retained in the spectral domain. Further away from the center of the domain, the number of components increases, until the grid spacing offered by the grid gets larger than the target. It means that even when keeping all components in the spectral domain, which is the best precision reachable with the grid, the target grid spacing cannot be enforced anymore. From this location and until the wall, there is no need to filter and one keeps the results without transformation. This is outlined in figure 3.16. The outer region keeps the feature of a traditional cylindrical grid, while the (colored) inner one presents an effective resolution (lower than offered by the grid) once the filter is applied. In the considered cases, the filter is applied for the 9 innermost layers of grid points out of 120. The 111 remaining ones are not modified by the described treatment.

Furthermore, a sixth-order Padé filter as presented in Gaitonde and Visbal (2000) is applied every 220^{th} time steps in the radial and axial directions and every 660^{th} time steps in the azimuthal one to remove numerical instabilities.

Settings of the auxiliary simulation

The auxiliary simulation consists of a capillary of 1.0 mm diameter and 11 mm length. The initial field reuses turbulent data from a periodic pipe flow of the same diameter. It is fitted with the inlet conditions of the laminar flow to obtain the same mass flow through both pipes. The pressure and temperature of the gas close to the axis are also fitted according to the results of the laminar fields, considered after the funnel-shaped inlet, at the transition with the straight part of the capillary. We thus consider the following values:

- pressure $p_0 = 8.24 \times 10^5$ Pa;
- temperature $T_0 = 281$ K;
- mass flow $\dot{m}_0 = 1.35 \times 10^{-4}\,\text{kg} \cdot \text{s}^{-1}$.

The simulation further consists of recycling the perturbation of the flow within a cross-section located around 10 mm after the inlet. These perturbations are reintroduced, after a proper scaling, at the inlet as superposition to the mean flow. This method has been developed by Pirozzoli, Bernardini, and Grasso (2010).

Both inlet and outlet sections use non-reflecting boundary conditions with the characteristics method. The same implementation as for the simulations of the laminar capillary flow is used and a detailed description can be found in Stein (2019). Non-slip adiabatic boundary conditions are considered for the walls. The described settings allow to compute a turbulent flow that is not decaying over time, as would do an artificially periodic pipe. The flow state is stored in the recycling cross-section. This data is then used as the reference state for the inlet conditions in the primary simulation.

Settings of the primary simulation

The primary simulation consists of a pipe simulation of a capillary of 1.0 mm in diameter and a length of 6.0 cm. This geometry is equivalent to the one considered in Bernier et al. (2018). The boundary conditions at the inlet and outlet are non-reflecting, as for the auxiliary simulation. The reference value at the outlet is fixed and chosen as the corresponding laminar solution. It ensures that the expected pressure gradient is sustained. At the inlet, the reference is set for each time step to the values stored from the auxiliary simulation. It thus mimics a physical turbulent inlet. Non-slip adiabatic boundary conditions are considered for the walls. Both the auxiliary and the primary simulations use the same fixed time step. This results in a CFL number of about 0.79, considering the equivalent grid spacing close to the symmetry axis in the azimuthal direction and not the real grid spacing.

3.3.3 Results of the simulation

In the following, the results of the simulation are presented. It focuses on the propagation of the turbulence through the domain as well as the consequences we can learn from it, regarding the nature of the flow expected within the transfer capillary. The definition of the different variables used throughout this section to describe and analyze the turbulent flow are presented in the appendix section D.

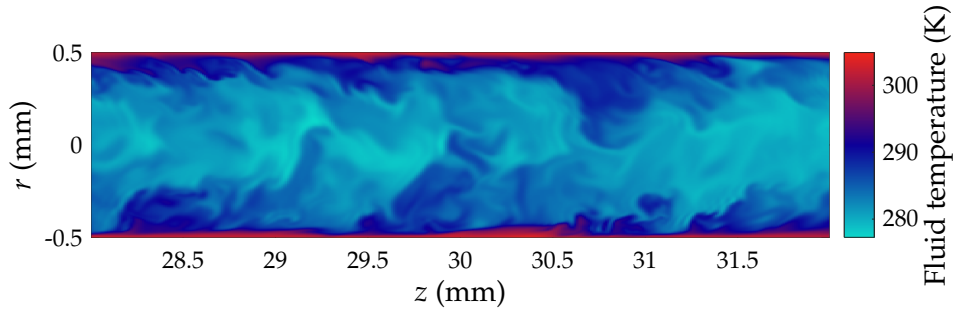

FIGURE 3.17: Snapshot of the gas temperature in the central part of the capillary. Radial and axial dimensions are represented to scale.

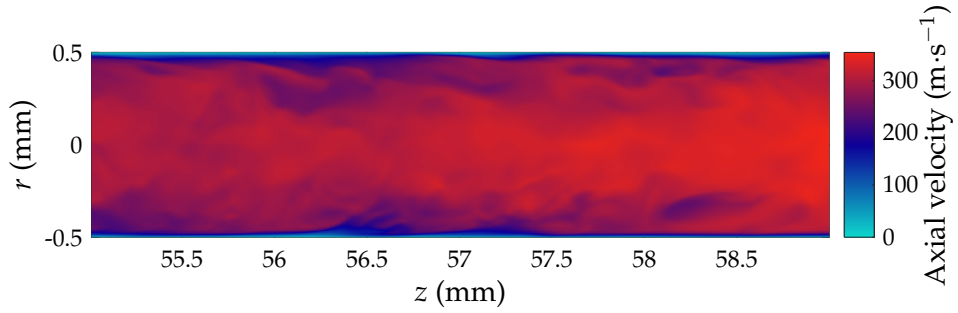

FIGURE 3.18: Snapshot of the axial velocity close to the outlet of the capillary. Radial and axial dimensions are represented to scale.

General results

For the sake of illustration, we present in figures 3.17 and 3.18 a snapshot of the results. They depict the temperature field in the central area of the capillary and the axial velocity close to its outlet. The turbulence is present throughout the domain. It tends to show that the flow can sustain a turbulent onset. This is not unexpected, as the bulk Reynolds number in the flow reaches values close to 8,300 at the inlet, that is well above the generally admitted threshold of 2,300 for pipe flows. Even if this value drop along the capillary, it remains relatively large at the outlet ($\approx$ 7,200) However and as already mentioned, this threshold does not necessarily predict the onset of turbulence and specific conditions, especially the strong pressure gradient and their possible consequence on the turbulence behavior of the flow, have not been precisely described to our knowledge. In the following, we thus focus on a closer description of this flow.

An interesting parameter to evaluate the reliability of the results is the energy spectrum. In standard configurations, it has been thoroughly studied and specific relations could be computed to link the scale of the structures found in the flow and the associated kinetic energy. This is described in the most cited work of Kolmogoroff (1941). Several hypotheses made for the precise description of the spectrum are not compatible with the computation presented here. Especially it assumes isotropic turbulence, which is a priori not ensured in a pipe flow, where the axial dimension of the domain strongly differs from the others. Moreover, we consider compressible equations, while the theory is derived for incompressible flows. It means that even if

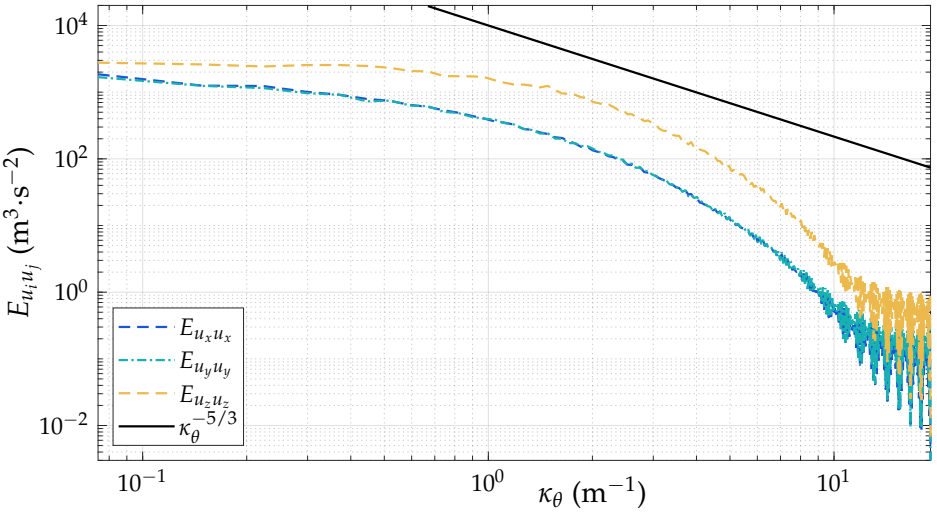

FIGURE 3.19: Average energy spectrum of the turbulent pipe computed along the azimuthal direction.

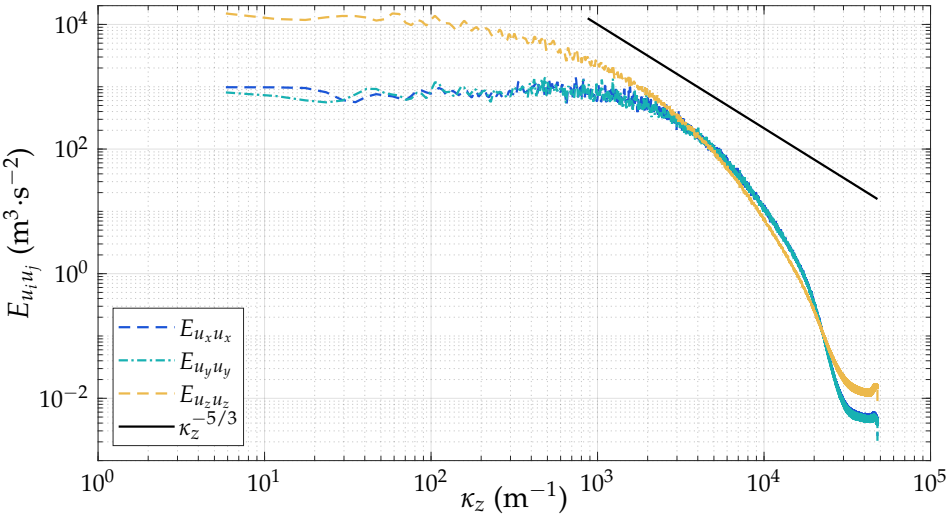

FIGURE 3.20: Average energy spectrum of the turbulent pipe computed along the axial direction.

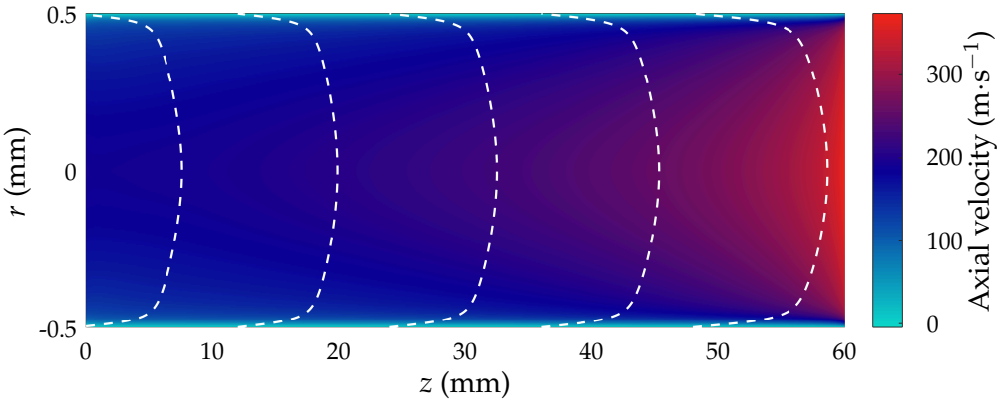

FIGURE 3.21: Mean axial velocity component in the capillary domain. The dashed line represents the form of the profile along the radial direction, at the axial position where it touches the wall. Radial and axial dimensions are not to scale.

this theory represents a good working basis, a total agreement of the present results is not expected.

In the simulation, the kinetic energy is computed using the auto-correlation of the cylindrical components of the velocity fluctuations, in the spectral domain. The results are presented in figures 3.19 and 3.20, computed for the azimuthal and axial directions, respectively. The spectra are averaged in the other directions of the domain, i.e. in axial and radial directions for the azimuthal spectra and the radial and azimuthal directions for the axial spectra. While the axial direction of the system is not periodic, the spectra are nevertheless considered to show a comparison. Therefore, the data are padded with zeros to build a pseudo periodic signal. Furthermore, the spectra are computed with the Cartesian components of the velocity vector, as these components are considered in the formulation of the Navier-Stokes equations.

In both cases, the standard decrease anticipated by Kolmogorov has been represented as a comparison. In both directions considered, the energy spectra show a transition corresponding to this prediction, followed by a steeper decrease for greater wave numbers, i.e. for smaller structures.

Figures 3.21 and 3.22 represent the mean fields for the axial velocity component and the temperature, respectively. These are analogous to figures 3.4 and 3.8 for the laminar capillary, however with adiabatic wall boundary conditions for the turbulent case and isothermal ones for the laminar case. One can especially see that the evolution of the boundary layer within the turbulent pipe flow is less pronounced than in the laminar case. This is likely linked to the different kind of inlet conditions. The laminar case takes into account the development of the flow form a reservoir located before the funnel-shaped inlet. In contrast, pseudo fully developed turbulent data are directly set as a reference at the beginning of the straight part in the turbulent case. It is thus not surprising that no significant evolution of the boundary layer is observed. As expected, it also confirms that the boundary layer in the turbulent case is significantly thinner than in the laminar one.

Another aspect of turbulent flows that has been precisely described is the behavior of the main velocity component in a boundary layer. The theory describes different parts, or sublayers. A model describes the mean velocity in each of these parts. This relies on a specific normalization, both for the distance from the wall and the velocity, sometimes called wall units. The normalization of the velocity relies on

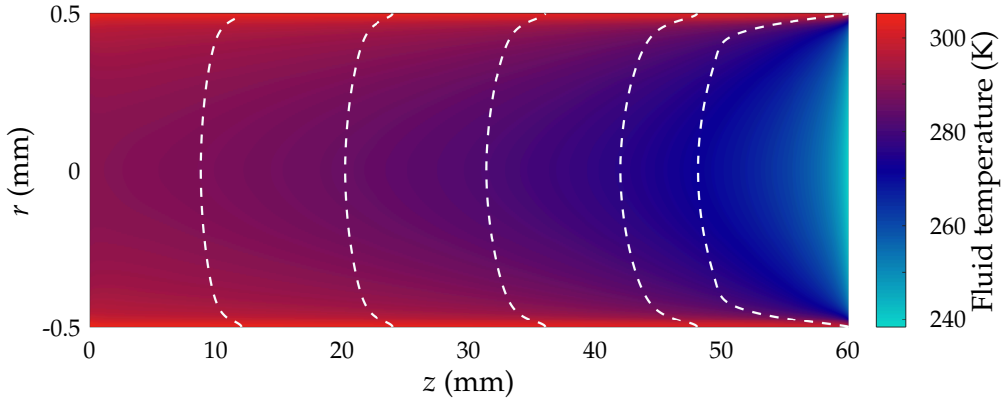

FIGURE 3.22: Mean temperature in the capillary domain. The dashed line represent the form of the profile along the radial direction, at the axial position where it touches the wall. Radial and axial dimensions are not to scale.

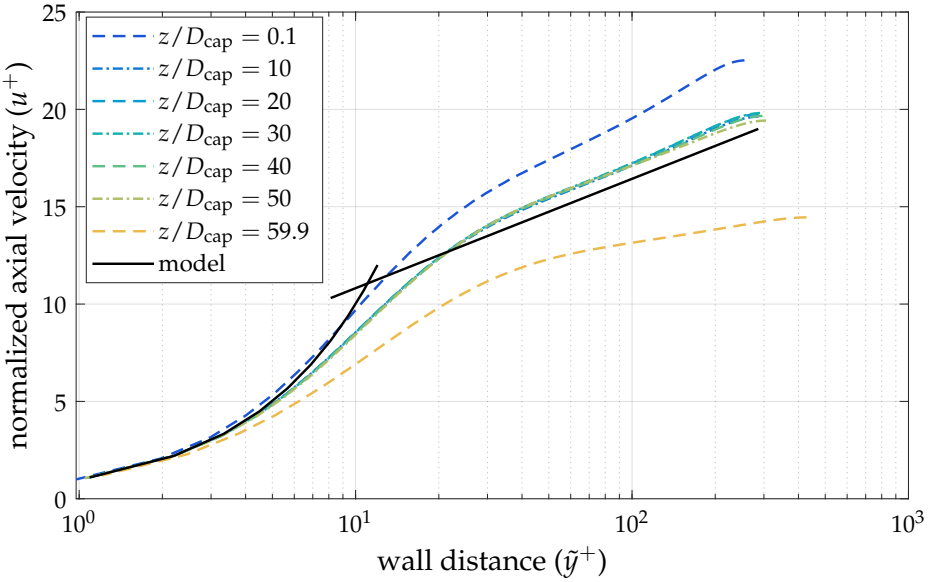

FIGURE 3.23: Normalized axial velocity in the cross-section of the pipe represented over the normalized wall distance and for different axial positions along the pipe. The dashed lines represent the standard law, that is $u^+ = \tilde{y}^+$ for lower values of $\tilde{y}^+$ and $u^+ = 1/0.41 \ln \tilde{y}^+ + 5.2$ for larger values of $\tilde{y}^+$.

a so-called friction velocity u_τ, defined at each axial position by:

$$u_\tau = \sqrt{\frac{\bar{\tau}_{zr,\mathrm{w}}}{\bar{\rho}_\mathrm{w}}}\,, \tag{3.44}$$

with $\bar{\tau}_{zr,\mathrm{w}}$ the mean shear stress at the wall in the axial and radial direction and $\bar{\rho}_\mathrm{w}$ the mean density at the wall. The component of the mean shear stress representing the axial and azimuthal direction is not considered, as it is negligible compared to the axial-radial component due to the axial symmetry of the system and the lack of mean velocity in the azimuthal direction. The normalization of the distance to the wall $\tilde{y}$ is based on this friction velocity by defining a viscous length scale $\tilde{y}^*$ as follows:

$$\tilde{y}^* = \frac{\bar{\nu}_\mathrm{w}}{u_\tau}\,, \tag{3.45}$$

with $\bar{\nu}_\mathrm{w}$ the mean kinematic viscosity at the wall. We can thus normalize both the axial velocity and the distance to the wall, denoted with a $+$ superscript, at different positions along the axis. These profiles are represented in figure 3.23. This figure also represents the standard models typically found for conventional turbulent boundary layers. Close to a wall, up to about $\tilde{y}^+ \approx 10$ holds $u^+ = \tilde{y}^+$. This part is called the viscous sublayer. For greater values of $\tilde{y}^+$, the so-called law of the wall applies, which defines a logarithmic dependency of the normalized axial velocity with respect to the wall distance:

$$u^+ = \frac{1}{0.41}\ln \tilde{y}^+ + 5.2\,, \tag{3.46}$$

where the numerical parameters have been experimentally determined.

One can see that both profiles considered close to the inlet and outlet of the capillary significantly differ from the other ones and the models. Close to the inlet, the normalized velocity delivers values larger than expected by the model, while close to the outlet, it is smaller than expected. In both cases, this is not surprising, as boundary effects are expected. The hypothesis of a fully developed flow is debatable at the inlet. Further, the strong acceleration of the flow very close to the outlet is a cause of divergence with the models. We showed in the laminar case that it influences the thickness of the boundary layer and this phenomenon is also expected in the turbulent case.

Nevertheless, the other profiles along the capillary are remarkably close to each other. This means that even if the typical conditions of a fully developed flow are not met, due to the strong pressure gradient, this does not hinder the building of similar profiles. However, a slight divergence between these profiles and the theory can still be reported. This is however no specificity of the present simulation. For example, results for sub and supersonic compressible flow without pressure gradient, published by Modesti and Pirozzoli (2019), show a similar trend. In that publication, no case presents the same parameters as the present ones, but one can still compare it with the case P13 of that publication, where the Reynolds number of 6,362 is close to the present one (from 7,200 to 8,300 along the pipe) and the bulk Mach number of 1.3 greater (in the present simulation it varies between about 0.45 and 1.0). These results show that the presence of a strong pressure gradient in the pipe flow does not alter, a priori, the global behavior. However, we still have not considered the intensity of the turbulence, which is now studied.

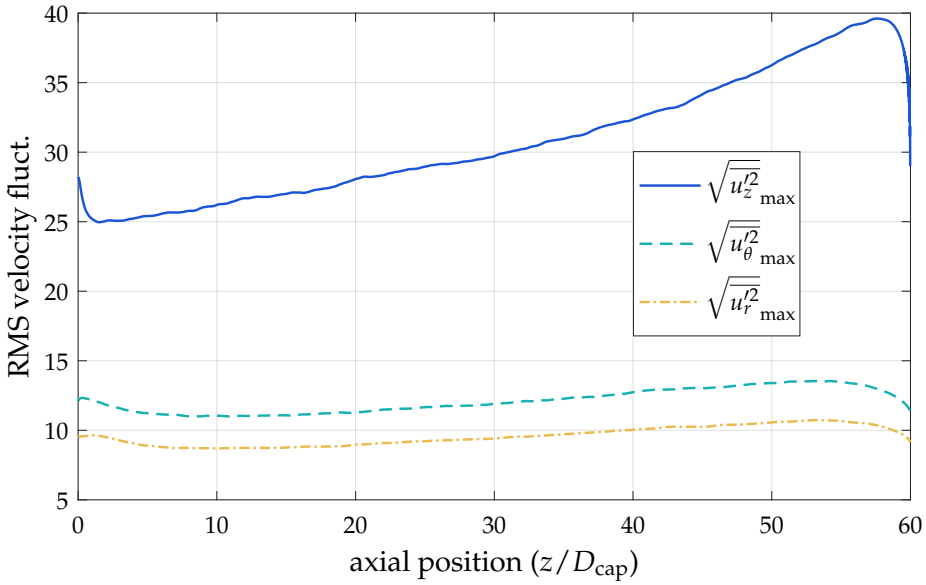

FIGURE 3.24: Maximal root mean squared fluctuations along the axial direction.

Turbulence evolution

We have seen that the general results produced by the computation are close to the ones predicted by the theory of turbulent flows. This leads us to analyze more closely the evolution of the turbulence along the pipe, as this is a feature of interest to evaluate the turbulence affinity of the gas flow present in the considered transfer capillary. Two different values are presented: the fluctuations themselves, and normalized ones. We refer to the latter as turbulence intensities. Different reference velocities can be used for the normalization: the friction velocity as defined in equation 3.44, the local mean axial velocity, or the maximal mean axial velocity, adapted to each cross-section, respectively. The normalization allows us to take into account the strong acceleration of the flow.

We first consider the axial evolution of the two quantities for each velocity component. In figure 3.24, the absolute value of the root-mean-squared fluctuation is represented. The maximal value is considered in each cross-section. Here again, the areas close to the inlet and outlet present a different behavior. Excluding these, the axial fluctuations present an almost steady increase along the pipe. The radial and azimuthal fluctuations both present a very similar behavior, the radial fluctuations only being slightly smaller. Close after the inlet, but for a longer period than the axial component, these fluctuations slightly decrease. Then, they soon start to increase, following the trend of the axial fluctuations until the outlet. This evolution is the first indication that the simulated flow can sustain the turbulence set at its inlet. However, a definitive answer can only be given by the turbulence intensity, because of the strong acceleration.

This quantity is represented in figure 3.25, where the fluctuations are normalized using the friction velocity according to equation 3.44. The axial intensity presents a remarkable behavior. It is nearly constant throughout the capillary. Only the very last sections before the outlet present a strong decrease of the intensity. A slight increase is even observable at the beginning of the pipe, up to about $z/D_{cap} \approx 20$.

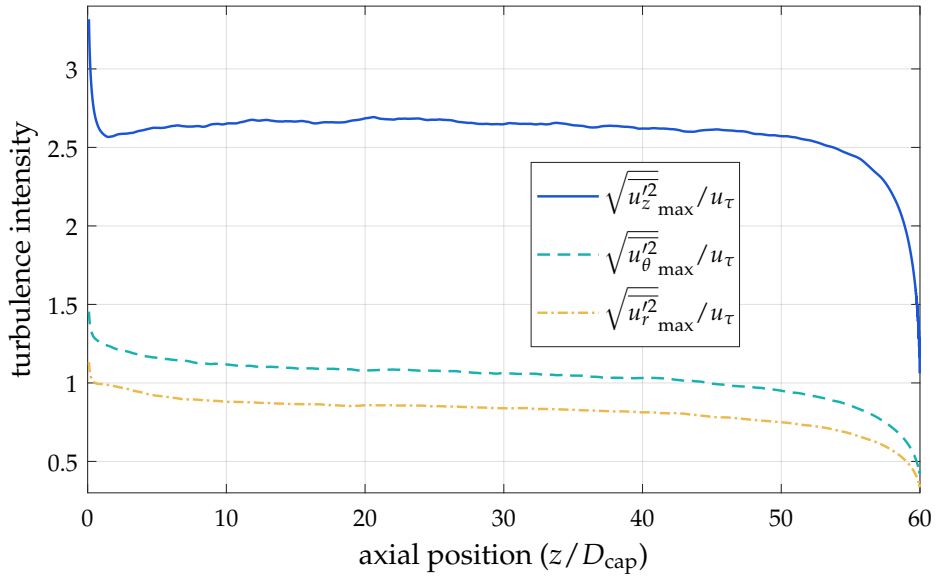

FIGURE 3.25: Turbulence intensity along the axial direction. The fluctuations are normalized using the friction velocity according to equation 3.44.

Here again, both the radial and azimuthal intensities present a very similar pattern. They steadily decrease along the capillary, but in a small proportion (about 15 % between $z/D_{cap} = 10$ and $z/D_{cap} = 50$) compared to the increase of the mean axial velocity of 41 % between the same sections. The fact that the area close to the outlet, where the pressure gradient and the acceleration become very large, shows strongly decreasing intensities is a sign that turbulence cannot be sustained in all conditions. However, the pressure gradient in the main part of the domain, even if not negligible, remains compatible with the development of a turbulent flow.

We further analyze the turbulence intensities within a cross-section located in the middle of the capillary, for $z/D_{cap} = 30$. This location is expected to avoid the inlet and outlet effects. Furthermore, one can reasonably suppose, according to the results presented in figure 3.23 and the axial evolution of the intensities, that this is representative of the majority of the cross-sections in the capillary. The overall behavior computed in the simulation does not strongly differ from experimental results presented in Hinze (1975, p. 629), referring to classic pipe flows and first published in Laufer (1954). However, the Reynolds number of these experimental results (500,000) is significantly greater than the present one.

We first focus on the turbulence intensities normalized with the maximal mean axial velocity, presented in figure 3.26 and compared to data presented in Hinze (1975, pp. 724-728). One can see that all velocity components present a relatively steep increase close to the wall, reach a maximum relatively close for the axial component (at about 0.06 in the distance to the wall normalized with the diameter), a bit farther for the azimuthal direction (about 0.12). The radial component is the last to reach this maximum (about 0.22). All components then decrease and reach a local minimum at the center of the pipe. Both azimuthal and radial components converge towards the same value of about 2.6 %, while the axial component converges towards 3.3 %. It shows that the assumption of isotropic turbulent is not respected in this case, even in the vicinity of the pipe axis, in contrast to the experimental values.

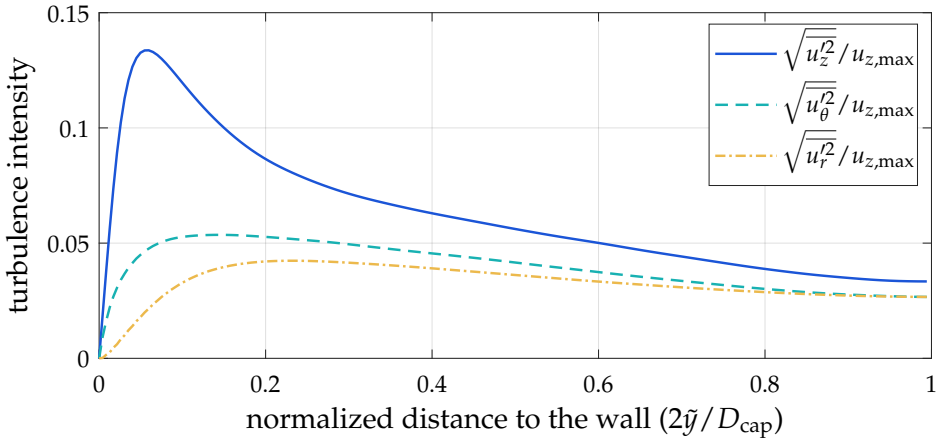

FIGURE 3.26: Turbulence intensity along the radial direction in the central cross-section of the capillary. The fluctuations are normalized using the maximal mean axial velocity in the cross-section and the distance to the wall is normalized using the diameter (it thus varies from 0 at the wall up to 1 at the centerline.)

It is a first sign that the strong pressure gradient might affect the distribution of the turbulent intensity in a cross-section of the system.

Another difference shall be pointed out in the comparison with the experimental results. In the later, no decrease in the turbulence intensity of the axial and azimuthal components is visible close to the wall. This is likely since the boundary layer in the experiment is significantly thinner than in the simulation. This hypothesis is confirmed by the results of the original publication (Laufer 1954). It presents results of another experiment with a Reynolds number of 50,000 along with 500,000. It is then clear that the maxima of the turbulence intensities shift towards the center of the pipe when the wall distance is simply normalized with the diameter. While these distances remain significantly smaller for both experimental Reynolds numbers ($\approx$ 0.002 for $\text{Re} = 500,000$ and $\approx$ 0.02 for $\text{Re} = 50,000$), the results of the simulations appear to be reasonable. This difference can however be overcome by considering the normalization of the wall distance in wall units, as described in equation 3.45 and presented in the following. Overall, however, the results of the simulation remain very similar to the experimental ones and besides the slight divergences reported here, the pressure gradient does not seem to strongly affect the properties of the flow.

We further consider the turbulent intensity, depicted in figure 3.27, normalized using the friction velocity, along the radial direction in the cross-section located in the middle of the pipe. Only the area relatively close to the wall is depicted. In wall units, the thickness of the boundary layer is then similar both in experiments and in the simulation. For instance, the maximal turbulence intensity in the axial direction is reached at $y^+ \approx 15$ in both cases. These maximal values are also similar in both cases, reaching about 2.6. While the intensity of the other components is smaller in both cases, with the radial intensity even smaller than the azimuthal ones, the absolute values are slightly greater in the experiments than in the simulation, with respectively 1.3 and 1.1 for the azimuthal component, and 1.0, resp. 0.85 for the radial component. A definitive reason for this difference is not obvious, but two parameters are likely to influence the results: the lower Reynolds number of the

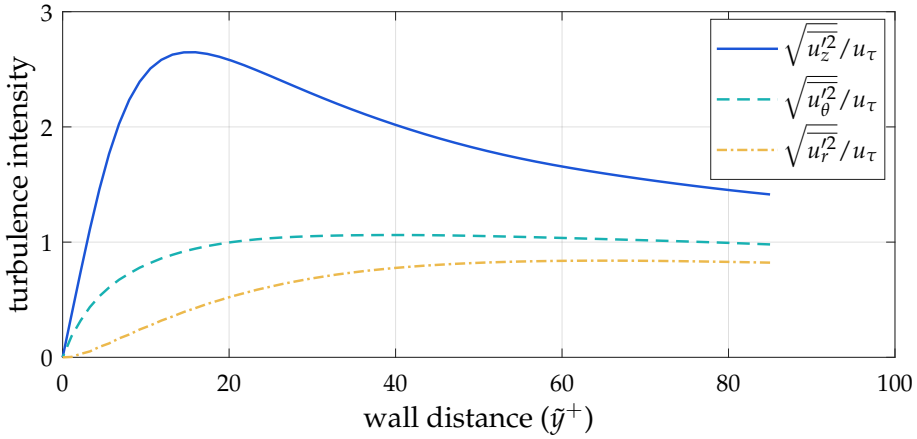

FIGURE 3.27: Turbulence intensity along the radial direction in the central cross-section of the capillary. The fluctuations are normalized using the friction velocity and the distance to the wall is normalized using equation 3.45.

simulation, and again the fact that a strong pressure gradient is present.

A third normalization of the fluctuations is available to compute the intensity: the local mean axial velocity. This is depicted in figure 3.28. Focusing on the axial component, the simulation delivers an intensity of about 35 % close to the wall, in comparison to 30 % for the experiments. This maximum is reached close to the wall, but a small decrease between the wall and the maximum is observed. This is compatible with experiments, also presented in Hinze (1975), which show a similar pattern. Besides these similarities, a major difference can be observed in the behavior of the azimuthal intensity in the vicinity of the wall. While the experiments tend to show convergence towards zero intensity in this region, the results of the simulation present a divergence. It does not mean that the fluctuations diverge in this area. This occurs because both azimuthal fluctuations and local mean axial velocity decrease towards zero, but the former slower than the latter. The difference in the Reynolds numbers between the experiments and the simulation is likely to be the cause of this difference. This supposes that the thickness of the boundary layer, considered in the mean axial velocity, is more affected than the thickness of the effects visible in the azimuthal fluctuations. Furthermore, similar profiles of the fluctuations are reported in direct numerical simulations presented in Friedrich (2007). In these simulations, no pressure gradient is considered and the Mach number of 1.5 is larger than the system considered here. However, the Reynolds number of 6830 is closer to the present simulation than the experimental results. In Friedrich's simulation, the fluctuations of the azimuthal component close to the wall, normalized with the mean local axial velocity, also increase and reach values close to 0.15, very similar to the results reported here. This means that here again, the strong pressure gradient does not seem to significantly affect the properties of the turbulent flow.

Another variable worth considering is the turbulent stress tensor, also called Reynolds stress tensor. It is defined as $\widetilde{\tau}_{ij} = \widetilde{\bar{\rho} u_i'' u_j''}$ and describes the contribution of the velocity fluctuations to the forces applied to flow particles. Four components, normalized with the mean wall shear stress, are represented in figure 3.29. All depicted components converge towards zero close to the wall. Further away, the double correlation of the axial component is dominant, reaching values slightly larger

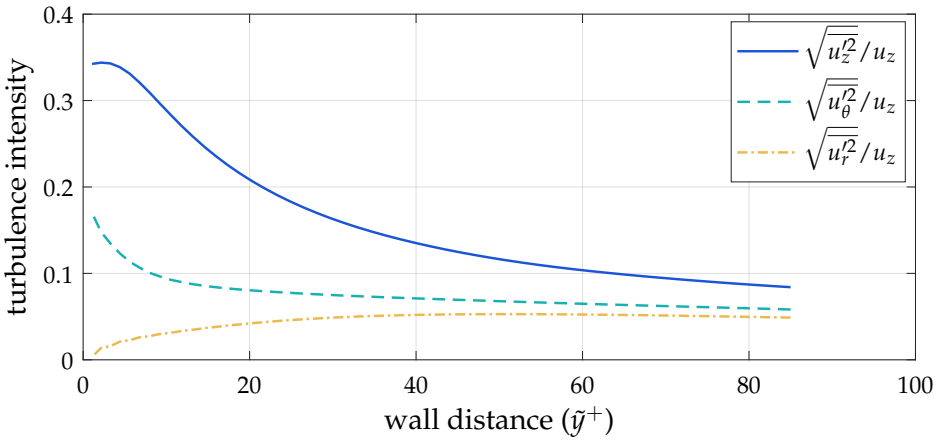

FIGURE 3.28: Turbulence intensity along the radial direction in the central cross-section of the capillary. The fluctuations are normalized using the local mean axial velocity and the distance to the wall is normalized using equation 3.45.

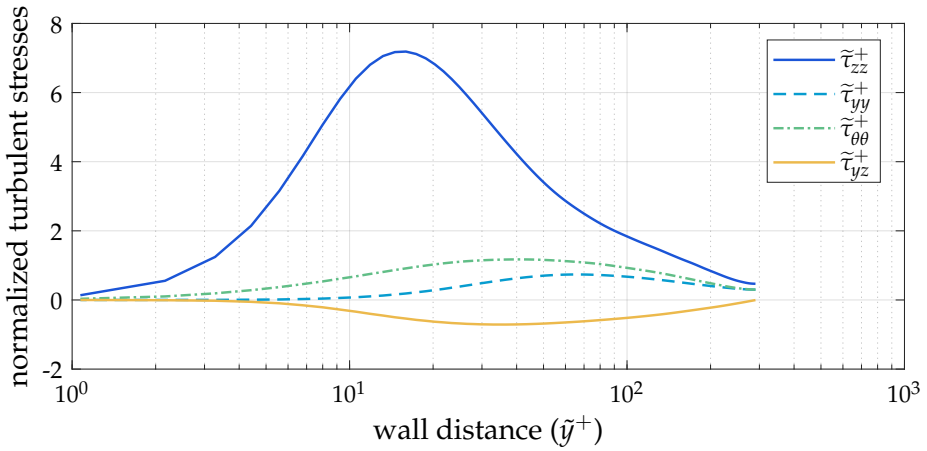

FIGURE 3.29: Reynolds stress tensor components in the radial direction, at $z/D = 30$. The stresses are normalized with the mean wall shear stresses τ_w. The radial components are considered starting from the wall towards the center of the pipe and thus denoted with the index y.

than seven times the mean wall shear stress for a wall distance of about 15. The other correlations reach maxima close to the wall shear stress, and the maximum is reached further away from the wall, around $y^+ \approx 40$ for the correlation of the radial and axial components and the double correlation of the azimuthal component. The double correlation of the radial component, which presents the smallest amplitude, reaches its maximum for $y^+ \approx 65$. It is also worth noting that only the correlation of the radial and axial components is negative, while the others are positive. Again, in this case, the profiles are very similar to others presented in Modesti and Pirozzoli (2019). No direct quantitative comparison is possible, as the parameters of the different cases presented in the publication do not correspond to the present case. However, the qualitative comparison clearly shows that the strong pressure gradient does not significantly affect the Reynolds stresses.

Consequences for the nature of the flow expected in the capillary

It comes out of these results that turbulence can be sustained within capillary flows. That means that one cannot exclude the occurrence of a turbulent regime. The simulation shows that a turbulent flow set at the inlet of the capillary expand throughout the domain. However, the question remains to know what conditions are applied at the inlet of a capillary in a real device. It cannot be answered on a global basis, though, as many parameters are potentially involved. No device can create a perfect turbulent pipe flow as used in the computation and it represents a limit case. At the other end of the spectrum, the laminar case previously reported represents another limit case of stable flow. However, an obstacle located in front of the capillary can well act as a source of perturbation. The present results tend to show that this perturbation could evolve in a turbulent flow.

We should add at this stage that the Reynolds numbers considered in the simulation are relatively large compared to typical capillaries, which tend to have smaller diameters and thus proportionally smaller Reynolds numbers. Thus, the Reynolds numbers presented here represent an upper limit of what is typically found in commercial devices, where capillary of 0.5 mm can be considered as large. Nevertheless, transitory phenomena are not unlikely due to the perturbations necessarily produced upstream of the capillary. The origin of these perturbations is very diverse but some elements can be cited in the case of a typical mass spectrometer. First, the ESI source can be involved. Depending on the device, this source may be located on the same axis as the capillary and then necessarily creating perturbations into the flow. Furthermore, some devices use a buffer gas, intended to support the desolvation of the droplets created at the source. This additional gas flow may as well produce perturbations of the main flow entering the capillary. Also, the capillary itself, and more precisely its inner shape, can create perturbations, e.g. if the shape is not exactly cylindrical, or the surface rough. The edge located at the entrance of the capillary is an additional element likely to create perturbations.

3.4 Results of the gas flow in the ion funnel

We now focus on the next stage of a classic mass spectrometry device: the ion funnel. The gas flow in this chamber undergoes the first pumping, lowering the pressure to values around 2 to 3 orders of magnitudes lower than the atmospheric pressure present at the other side of the capillary. The ultimate goal is to extract the ions from the underlying gas phase to perform the intended analysis in the best conditions possible. The ion funnel acts as a first, rough separation between air and ions.

While the gas is pumped out, the ions are focused towards the axis of the system to be transferred into the next chamber, where further similar operations at lower pressure levels can occur. In this section we describe the gas flow found in such a device using the Navier-Stokes equations, first focusing on traditional design and then exploring a possible evolution. It has been performed using an open-source program developed in the department of numerical fluid dynamics at Technische Universität Berlin and called WABBIT[3]. It can be used for adaptive multi-resolution simulations. This feature has not been used in this work, as it makes use of axisymmetric equations and boundary conditions for which the multi-resolution has not been fully tested yet.

In both cases, the geometry is fixed and enforced by the volume penalization method described in section 3.1.4. The temperature of the objects present in the domain is set to the room temperature $T_0 = 298.15\,\mathrm{K}$. Three boundary conditions are not represented by a wall and need a specific setting: the inlet, which corresponds to the end of the capillary, the outlet, located at the end of the funnel, which allows the ions to enter the next chamber, and the pump. These conditions are enforced using sponge terms as described in section 3.1.4. This technique has been developed and validated in Krah (2018).

3.4.1 Setting of the pressure level

The pressure level in the chamber is determined by the quantity of gas pumped out of the system. In the simulations, this is ruled by the velocity of the gas leaving the system and enforced via a sponge area. This velocity is estimated considering the quantity of gas introduced in the system through the capillary, the pressure, and temperature estimated at the pump and assuming that the quantity of gas transmitted in the next chamber is negligible compared to the other quantities.

The quantity of gas coming from the capillary is associated with the mass flow $\dot{m}_{\mathrm{in}}$. It can be estimated using the cross-section area of the capillary A_{in} and mean values of the density ρ_{in} and velocity v_{in}:

$$\dot{m}_{\mathrm{in}} = A_{\mathrm{in}} \rho_{\mathrm{in}} v_{\mathrm{in}} \,. \tag{3.47}$$

These values are known from the capillary simulations.

The mass flow at the pump can be estimated the same way:

$$\dot{m}_{\mathrm{pump}} = A_{\mathrm{pump}} \rho_{\mathrm{pump}} v_{\mathrm{pump}} \,. \tag{3.48}$$

A_{pump} is the area through which the gas is pumped out and is known from the geometry; v_{pump} is the velocity we are looking for to set up the boundary conditions; ρ_{pump} is an estimation of the density of the pumped gas. This is *a priori* unknown. We use the ideal gas law to transform it, as pressure and temperature can be easier estimated. The pressure p_{pump} is a parameter of the simulation and is chosen as the surrounding pressure in the chamber. The temperature T_{pump} is chosen as 298.15 K, *i.e.* the room temperature. It follows:

$$\dot{m}_{\mathrm{pump}} = A_{\mathrm{pump}} v_{\mathrm{pump}} \frac{p_{\mathrm{pump}}}{R_{\mathrm{s}} T_{\mathrm{pump}}} \,, \tag{3.49}$$

with R_{s} the specific ideal gas constant for air.

3. The source code of WABBIT can be found there: `https://github.com/adaptive-cfd/WABBIT`

Supposing that both mass flows are equal, one gets an expression for the gas velocity at the pump outlet:

$$v_{\text{pump}} = \rho_{\text{in}} \frac{R_{\text{s}} T_{\text{pump}}}{p_{\text{pump}}} \frac{A_{\text{in}}}{A_{\text{pump}}} v_{\text{in}} \,. \tag{3.50}$$

The system is considered axially symmetric. As a consequence, the area of the pump outlet is not the real area in the physical device but the equivalent one, considered on the entire perimeter of the chamber. With r_{pump} the distance between the symmetry axis and the pump outlet (which is equivalent to $D_{\text{chb}}/2$) and l_{pump} the length of this outlet in the axial direction, it follows $A_{\text{pump}} = 2\pi\, r_{\text{pump}}\, l_{\text{pump}}$. The area of the inlet is simply expressed with the capillary diameter D_{cap}. The final expression of the gas velocity at the pump outlet is:

$$v_{\text{pump}} = \rho_{\text{in}} \frac{R_{\text{s}} T_{\text{pump}}}{p_{\text{pump}}} \frac{D_{\text{cap}}^2}{8\, r_{\text{pump}}\, l_{\text{pump}}} v_{\text{in}} \,. \tag{3.51}$$

Because the pumping area used in this estimation does no match the pumping area of a real device, this also affects the value derived here. Thus, it does not represent the physical velocity that can be found in reality. It should however ensure that the global state within the chamber is equivalent to the one found in the device.

Furthermore, this estimation presents some uncertainties, including the temperature of the gas at the pump outlet and the quantity transferred to the next chamber which is not taken into account. This means that the estimation given in equation 3.51 may have to be adapted to effectively reach the expected pressure in the chamber.

The velocity is not the usual setting used to define the pressure level in typical conditions. The volume flow of the pump $\dot{\mathcal{V}}_{\text{pump}}$ is the classic value given. It can be gained by multiplying the velocity by the fictive pumping area considered:

$$\dot{\mathcal{V}}_{\text{pump}} = v_{\text{pump}} A_{\text{pump}} = 2\pi\, v_{\text{pump}} r_{\text{pump}}\, l_{\text{pump}} \,. \tag{3.52}$$

This value would however not directly fit the specification of the pump connected to the chamber. Non negligible losses may indeed occur between the chamber and the pump itself.

3.4.2 General settings

In this section, we describe general parameters used for all flow simulations of the ion funnel.

Capillary outlet

A 1.0 mm diameter capillary is considered. As references for the inlet, we use values of a 6.0 cm long capillary with adiabatic, non-slip wall boundary wall conditions. The values from the capillary simulation are not directly enforced. An average over the section is performed and the resulting density $\rho_{\text{IF,in}}$ and pressure $p_{\text{IF,in}}$ are directly set as references for the sponge terms. The velocity profile is considered only in the axial direction (*i.e.* the radial component is neglected and set to zero, which is close to the solution previously computed). An artificial profile is used for the axial

velocity, following the settings described in Krah (2018):

$$u_z(r) = \frac{u_{\mathrm{IF,in}}}{2}\left(1 - \tanh\left(\pi\frac{2r - D_{\mathrm{cap}} + \delta}{\delta}\right)\right). \tag{3.53}$$

The form factor δ is defined as $\delta = 0.025\, D_{\mathrm{cap}}$. The inlet conditions are thus not exactly the same as found in the capillary simulation but expected close enough to deliver results similar to the ones of a real device.

Transition towards next chamber

At the other end of the funnel, another sponge area is defined to mimic the strong pressure decrease expected in the following chamber. This is realized by setting a specific pressure, low enough to reproduce the expected acceleration. This value is given in the parameters of the simulation. The density is also penalized. The enforced value is ruled by a condition on the temperature: the gas should have the same temperature as the surrounding walls, that is 298.15 K. The velocity components, however, are not penalized.

Pumping area

The pumping occurs in the area located at the upper right corner of the domain. As described in section 3.4.1, this is used to define the pressure level in the funnel. The corresponding implementation occurs in two stages:

- in a first sponge area, located in the direct vicinity of the physical domain, the velocity defined in section 3.4.1 to set the pressure is enforced. Density and pressure are not penalized;
- in a second sponge area, located between the first sponge area and the wall, an energy and mass sink is implemented to cancel the flow accumulation that would otherwise result from the first stage. The velocity components are not penalized.

The parameters of the first stage are directly defined by the pump velocity and the local values of the field. For the second stage, references for the density and pressure are defined. Their values are actualized each time step to correspond to the mean density and pressure present in the entire domain. This allows an efficient cancellation of the accumulated flow without creating an area with values that strongly differ from the rest of the computation.

Numerical treatments

Fourth-order central schemes are used for the spatial derivatives. Converged results are expected and one lets the simulation run until the mean pressure and density in the domain reach constant values. The time integration is performed using a Runger-Kutta-Chebyshev scheme with four steps (see Sommeijer, Shampine, and Verwer (1998)). It allows us to choose a time step larger than the limit theoretically set by the penalization constant.

The results are treated after each time step using the methodology described in Bogey, de Cacqueray, and Bailly (2009). The goal of this filter is to capture the shock structures expected in supersonic flows. It solves the issue often occurring that the traditional thickness of the shocks is not well resolved on the computational grid.

Background pressure	1 mbar	3 mbar
Points - axial direction	2048	2048
Points - radial direction	2048	2048
Length - axial direction (m)	1.786×10^{-1}	1.786×10^{-1}
Length - radial direction (m)	5.555×10^{-2}	5.555×10^{-2}
Time step (s)	9.0×10^{-9}	9.0×10^{-9}
Penalization constant	5.0×10^{-10}	5.0×10^{-10}
Sponge constant	5.0×10^{-8}	5.0×10^{-8}
Pump velocity ($m \cdot s^{-1}$)	8.5	2.2
Inlet axial velocity ($m \cdot s^{-1}$)	395	395
Inlet radial velocity ($m \cdot s^{-1}$)	0	0
Inlet pressure (Pa)	3.4542×10^{4}	3.4542×10^{4}
Inlet density ($kg \cdot m^{-3}$)	5.087×10^{-1}	5.087×10^{-1}
Outlet pressure (Pa)	50	50
Objects temperature (K)	298.15	298.15

TABLE 3.3: Parameters used to compute the gas flow of the ion funnel - classic design.

Adapting the resolution to these structures would however lead to a prohibitive number of points in the grid. It selectively treats the solution of the Navier-Stokes equations only in the areas where the gradients are too steep to keep the global structure, even if the intrinsic grid cells are too coarse. Furthermore, the implementation is conservative, such that the energy of the system remains unchanged by this treatment.

3.4.3 Traditional conception

The traditional conception considered here is the design described in section 2.1.2. The simulation regarding this design have been first developed in Krah (2018), and further extended in Kyriakidis (2019), with slight modifications regarding the computation of the dynamic viscosity. The simulations from which the results are presented have been conducted in collaboration with Loukas Kyriakidis.

Two different pressure levels in the chamber have been considered: 1 mbar and 3 mbar. The corresponding parameters are listed in table 3.3.

General results

We first show a general overview of the results produced for both pressure levels. Figures 3.30 and 3.31 present the velocity magnitude with arrows describing the direction of the flow. The length of the arrows is the same for all positions considered. The areas where immersed objects are present are not represented.

It shows that in both cases, a Mach disk is present after the capillary, where a shock-wave is observed in the flow variables. Along the symmetry axis, pressure, density, and velocity (in the axial direction) present a jump in this area. This pattern is well described in Franquet et al. (2015) and corresponds to a so-called very highly underexpanded jet. Its size is affected by the pressure level though. The lower pressure induces a larger disk, located further away from the capillary outlet within the ion funnel. This is coherent with the estimations done for the position and size of the Mach disk from experimental data, as reported in Franquet et al. (2015). The

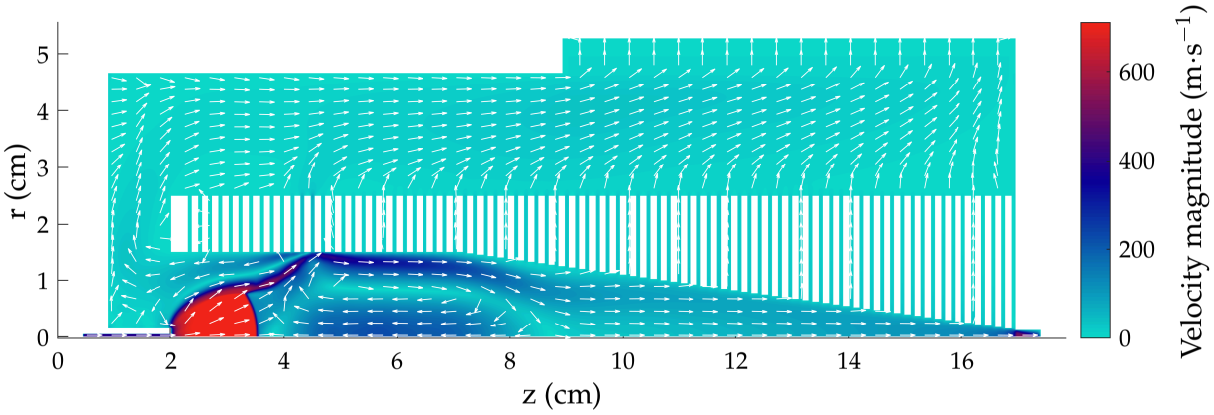

FIGURE 3.30: Velocity magnitude and direction of the flow in the ion funnel - classic design. Background pressure of 100 Pa.

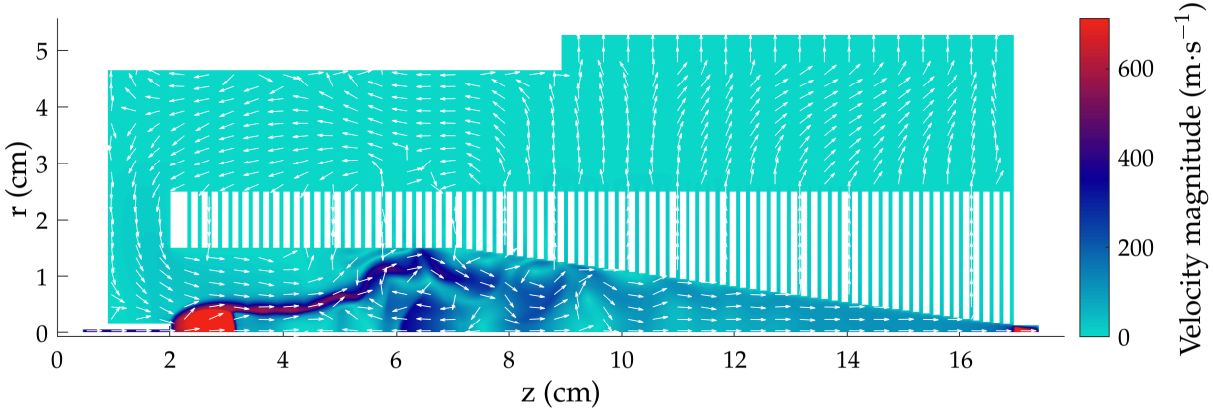

FIGURE 3.31: Velocity magnitude and direction of the flow in the ion funnel - classic design. Background pressure of 300 Pa.

	L_{MD}	D_{MD}
Simulation - 100 Pa	14.6 mm	15.0 mm
Prediction - 100 Pa	15.0 mm	7.43 mm
Simulation - 300 Pa	11.0 mm	7.87 mm
Prediction - 300 Pa	10.6 mm	5.08 mm

TABLE 3.4: Comparison of the position and size of the Mach disk in the simulation and prediction based on experimental data and reported in Franquet et al. (2015).

quantitative results are provided in table 3.4, where L_{MD} is the distance between the outlet of the capillary and the Mach disk and D_{MD} corresponds to the diameter of the Mach disk. The predictions are computed using the following formula:

$$L_{MD} = 0.69 D_{cap} M_e \sqrt{\gamma \eta_e}\,, \tag{3.54}$$

$$D_{MD} = 0.612 D_{cap} \left(\sqrt{\eta_e} - 1.0\right)\,, \tag{3.55}$$

with D_{cap} the diameter of the capillary, M_e the Mach number at the capillary exit, γ the adiabatic index for air, and η_e the pressure ratio between the capillary exit and the chamber. The pressure ratio considered does not directly use the pressure levels of 100 Pa and 300 Pa, as this corresponds to the pressure outside of the electrodes. We rather use 200 Pa and 400 Pa, respectively, which correspond to mean pressure levels inside the funnel cavity after the Mach disk. The results for the position of the disk are very close to the estimations. However, the simulated diameters seem significantly greater than the prediction. This is certainly caused by the fact that the domain in which the gas flows is rather complicated. The first aspect is the shape of the capillary. The pattern of the shock structure interacts with the external edge of the capillary. Further, the structure coming out of the Mach disk interacts with the electrodes of the ion funnel. It is thus not surprising that the simulated diameter does not correspond to the prediction.

The Reynolds number has been represented in figures 3.32 and 3.33 for both background pressure levels. It appears that the values remain in a significant part of the domain well below 1000 (the highest represented), strongly hinting to laminar conditions in the first pumping chamber. The only higher values are located close to the capillary exit and reflect the conditions described in the previous sections. The present results show however that the Reynolds values strongly decrease once in the pumping chamber. It means that the flow there is expected to be laminar, even if the capillary flow is turbulent. This also justifies the use of a two-dimensional computation model, in the limits explained in the following.

Limits of the model

Because of the very low pressure and densities found in the domain, the continuity approximation necessary to apply the Navier-Stokes equations may not be fulfilled in the entire domain. This is an intrinsic issue of the model used, which cannot be completely fixed within the frame of the tools used. The only solution would be to consider another method to simulate rarefied gas flows. In some other work (Zhou and Ouyang 2016), especially because of a very large span of pressure

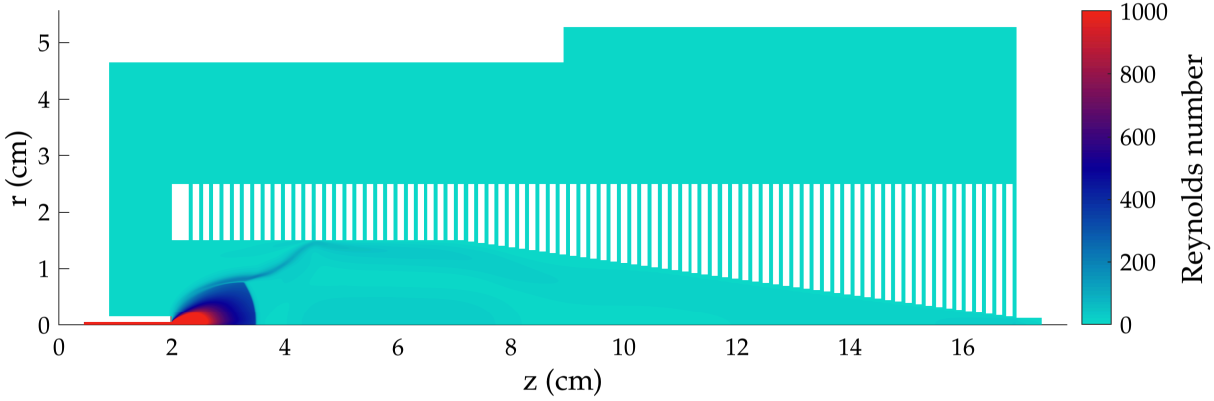

FIGURE 3.32: Reynolds number in the ion funnel - classic design. Background pressure of 100 Pa. The scale is limited to 1000, all higher values being depicted with the same color.

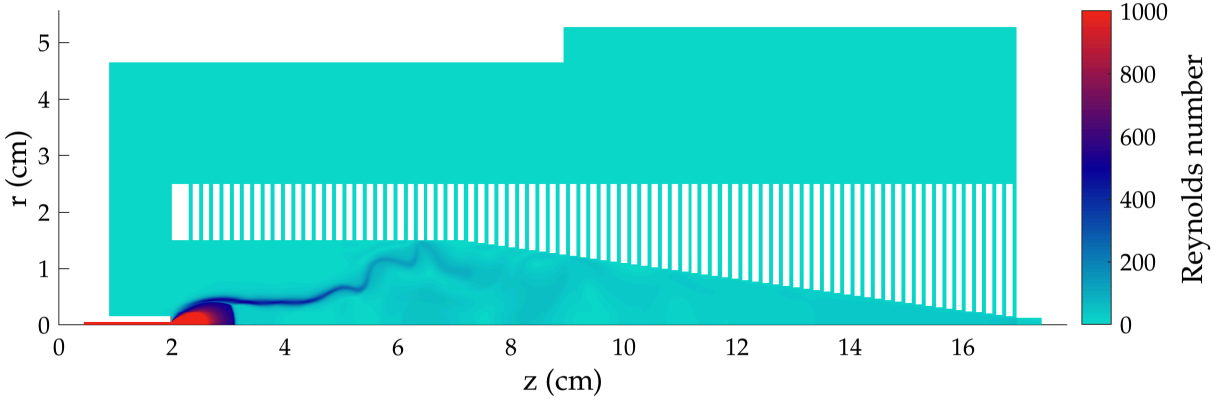

FIGURE 3.33: Reynolds number in the ion funnel - classic design. Background pressure of 300 Pa. The scale is limited to 1000, all higher values being depicted with the same color.

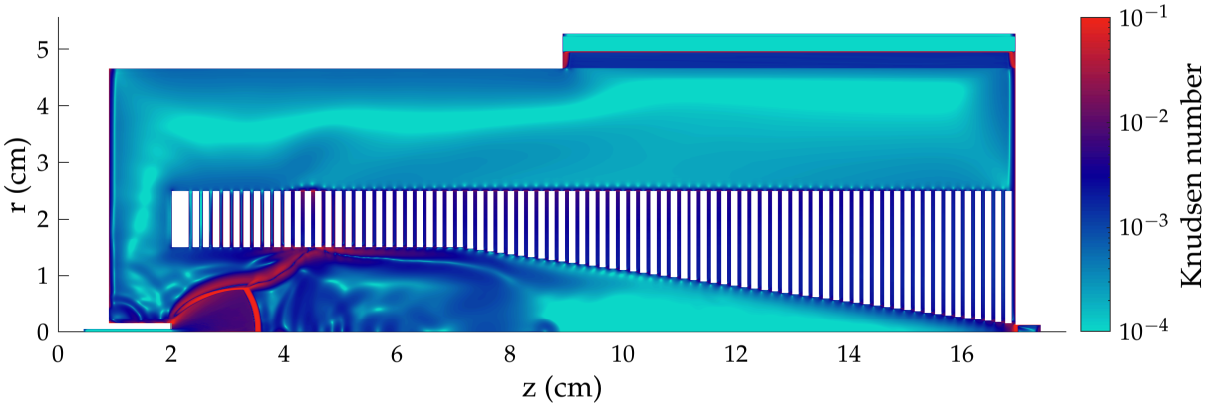

FIGURE 3.34: Knudsen number in the ion funnel - classic design. Background pressure of 100 Pa.

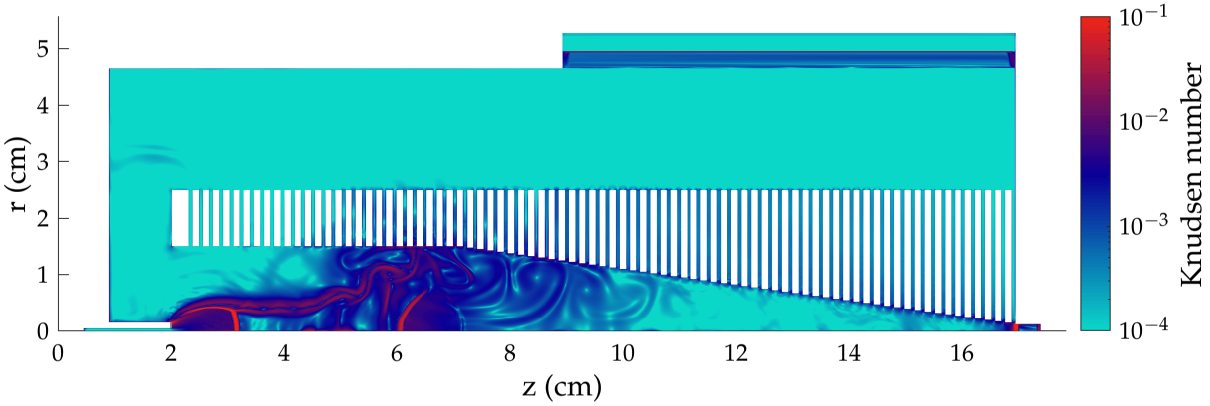

FIGURE 3.35: Knudsen number in the ion funnel - classic design. Background pressure of 300 Pa.

levels considered, a hybrid method combining the Navier-Stokes equation for high-pressure regions and a direct simulation Monte-Carlo (DSMC) for low-pressure regions was developed. In the present work, the expected pressure levels are not so low and such methodology was not considered. We show, however, to which extent the results respect the hypotheses bound to the model used.

The criterion to consider the limit of the continuum assumption is the Knudsen number Kn. It is defined as the ratio between the mean free path of the gas molecules λ and a characteristic length of the system L. This criterion ensures that each gas molecule encounters enough collisions during it trajectory so that the behavior of the gas is well approximated by macroscopic considerations and the individual molecules do not influence the global results.

One considers that the assumption is valid when the Knudsen number is smaller than 0.1, as described in Shen (2006, p. 2). This means that the Navier-Stokes equations may not be valid for values of Kn larger than 0.1. For values between 0.1 and 0.01, the Navier-Stokes may be used but with adapted parameters, especially for the boundary conditions. Below the threshold of 0.01, the ordinary Navier-Stokes equations can be used. The choice of the characteristic length L is however critical and not obvious in a complex system such as the ion funnel. Here we use a local criterion defining a comparison length based on the density gradient, following Shen (2006):

$$L = \frac{\rho}{\|\nabla\rho\|}\,, \tag{3.56}$$

where $\|\nabla\rho\|$ represents the magnitude of the gradient of the density.

The mean free path λ can be relatively easily computed for ideal gases. In Bird, Stewart, and Lightfoot (2001, section 1.4) e.g., it reads:

$$\lambda = 3\frac{\mu}{\rho}\sqrt{\frac{\pi}{8R_sT}}\,. \tag{3.57}$$

The Knudsen number thus follows:

$$\mathrm{Kn} = 3\frac{\mu}{\rho^2}\sqrt{\frac{\pi}{8R_sT}}\|\nabla\rho\|\,. \tag{3.58}$$

This is presented for the two levels of pressure considered in figures 3.34 and 3.35. It shows that there are areas where the continuum assumption is not valid anymore. This is especially the case close to the shock-wave fronts after the expansion of the flow resulting from the capillary, as well as close to the outlet leading to the following chamber at the end of the funnel. The latter is however not as critical, as it is already included in the sponge area used to enforce the conditions representing the lower pressure level of the next chamber. It means that by definition this area does not represents a physical state.

The lower pressure level in figure 3.34 is also visible by the fact that the Knudsen number between the electrodes and the pump outlet is visibly higher than in the case of a pressure level of 300 Pa as represented in figure 3.35. In both cases, however, it remains below the threshold of 0.01 between the electrodes, which means that no specific adaptation of the Navier-Stokes equation is necessary a priori. Nevertheless, this criterion clearly shows that the gas flow simulations in the ion funnel bring the model to its limits.

Furthermore, the geometry considered here remains a simplification compared to the real device. Especially the assumption of an axially symmetric system is only

Background pressure	1.4 mbar
Points - axial direction (-)	2048
Points - radial direction (-)	2048
Length - axial direction (m)	1.662×10^{-1}
Length - radial direction (m)	4.40×10^{-2}
Time step (s)	1.0×10^{-9}
Penalization constant (1)	7.5×10^{-9}
Sponge constant (1)	1.0×10^{-7}
Pump velocity ($m \cdot s^{-1}$)	8.08
Inlet axial velocity ($m \cdot s^{-1}$)	395
Inlet radial velocity ($m \cdot s^{-1}$)	0
Inlet pressure (Pa)	3.4542×10^{4}
Inlet density ($kg \cdot m^{-3}$)	5.087×10^{-1}
Outlet pressure (Pa)	30
Objects temperature (K)	298.15

TABLE 3.5: Parameters used to compute the gas flow of the ion funnel - evolution of the design.

partially correct. This condition is well fulfilled in the cavity, where the ions are supposed to travel through. However, the pumping does not occur all around the domain, as modeled here, but is limited to a few specific areas. Only a fully three-dimensional simulation could take this into account. Even then, the electric connections present in the chamber to set the potential of the electrodes as well as the fixings to put them in place would not be properly considered, making such a simulation prohibitively time expensive. Thus, the present results should be carefully considered, when compared to experimental data, as they only deliver an insight into the gas flow occurring in the first pumping chamber.

3.4.4 Possible evolution of the geometry

A possible evolution of the design, described in section 2.1.3 is also considered. The pressure level in the chamber is about 1.4 mbar, and the corresponding parameters are listed in table 3.5. It does not reach the same level as the simulation using the classic design but still represents a typical value that could be found in usual operating conditions. Furthermore, the results presented here are not fully converged. The simulation requires lots of computing time on the in-house cluster used for this purpose. However, the general features are not significantly evolving anymore and the description presented here is expected to fairly represent a fully converged case.

General results

The general pattern of the flow is presented in figure 3.36. It displays a different structure than the traditional design. First, no Mach disk is visible but a diamond shock structure. This is typical for moderately expanded jets, as described in Franquet et al. (2015). This difference can be explained by the presence of the diverging outlet after the capillary. It allows the gas flow to adapt before effectively entering the chamber, reaching about 580 Pa at the end of the structure. This leads to a significantly smaller pressure ratio between the outlet and the ambient conditions in the funnel area and thus a different kind of expansion. The pressure ratio further

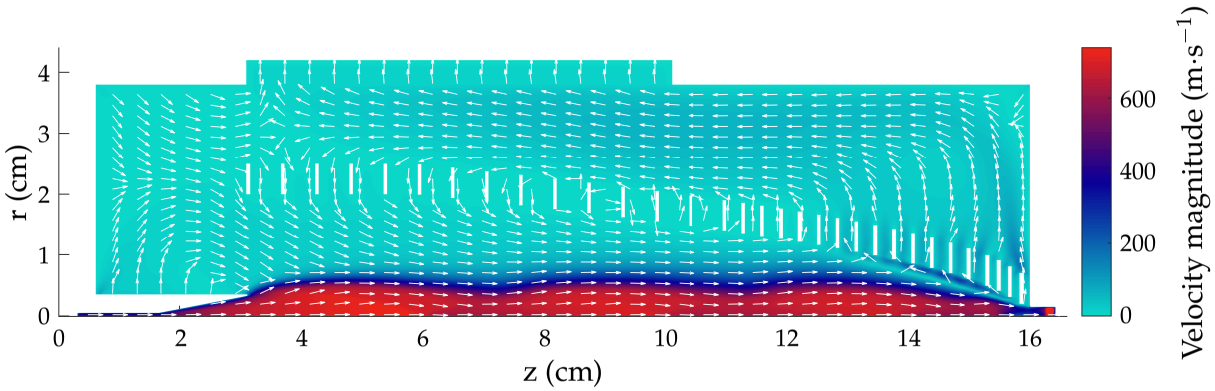

FIGURE 3.36: Velocity magnitude and direction of the flow in the ion funnel - evolution of the design. Background pressure of 140 Pa.

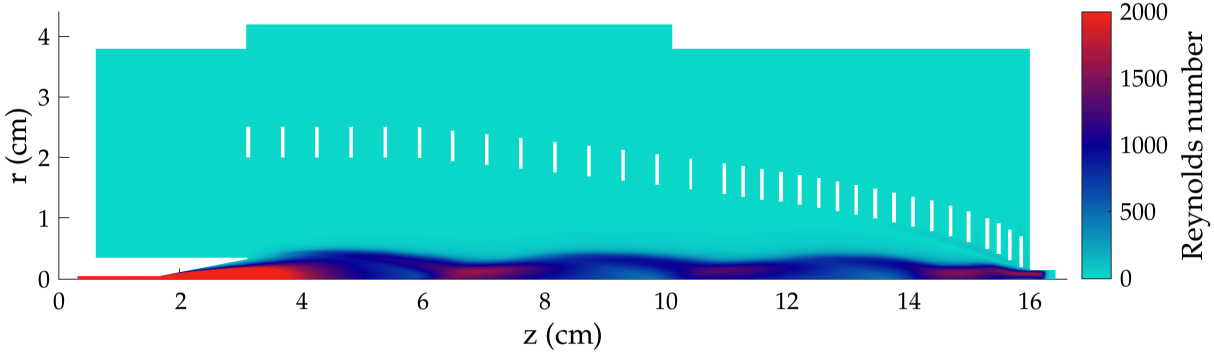

FIGURE 3.37: Reynolds number in the ion funnel - evolution of the design. Background pressure of 140 Pa. The scale is limited to 2000, all higher values being depicted with the same color.

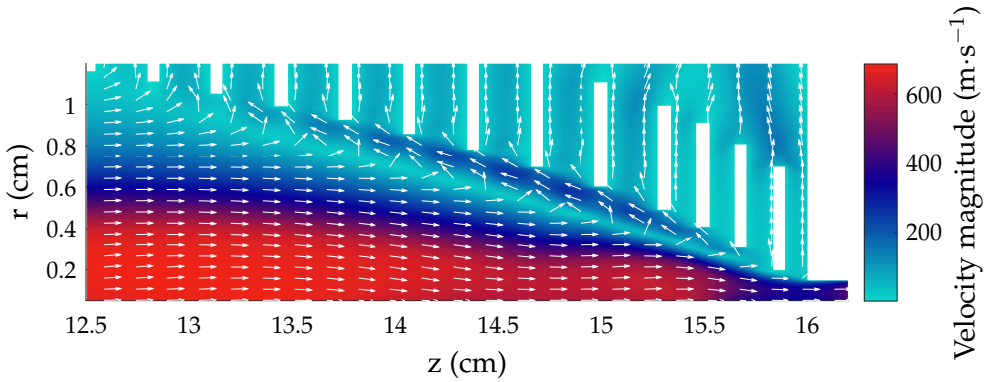

FIGURE 3.38: Velocity magnitude and flow direction in the vicinity of the recirculation zone.

impacts the size of the shock cells, a higher ratio bringing larger cells. Different operating conditions may thus lead to different numbers of cells.

The analysis of the Reynolds number within the system also shows that this is larger than for the classic design. The results are presented in figure 3.37. Still using the diameter of the capillary, 1.0 mm, as reference length, some parts of the shock cell structure cross the threshold of 1,000. Also, the choice of this characteristic length may be questionable in this case, as the diameter of the capillary outlet is also a legitimate candidate and would further increase the values. It is thus not completely excluded that turbulent conditions occur. Nevertheless, the laminar conditions depicted here still present an accurate picture of the conditions one might expect in such systems, as significant areas of the domain do have rather low values of the Reynolds number.

A main difference with the traditional design is that a large part of the mass flow pumped out goes between the last few electrodes. We understand this behavior by two different factors. First, the structure of the shock cell keeps the main stream relatively close to the axis, compared to the structure observed with the previous design. The interaction with the electrodes thus only occurs for a smaller diameter of the cavity. Second, the parabolic shape of the cavity implies that the electrodes reach small inner diameters further down the axial dimension. The combination of these factors implies that the interaction between the jet flow and the electrodes occurs very close to the outlet.

Thus, it appears that these conditions are not necessarily optimal for the transmission of the ions. It indeed means that the area where the ions should be collimated by the electric fields is also the area where one would expect the strongest radial driving forces due to the gas flow. Furthermore, and again in contrast with the classic design, no significant vortex structure appears in the core of the cavity. It can be understood as a consequence of the absence of a Mach disk. This structure is followed by a recirculation zone in the considered cases involving the classic design but it cannot occur in the present case. Nevertheless, another pattern can be observed with this evolution of the design. Indeed, a backward flow occurs in the final section of the funnel in the vicinity of the tips of the electrodes. We interpret this structure as a reflection of part of the flow against some of the last electrodes. The parabolic form of the cavity and thus the steep decrease of the inner radius of the electrodes further induces the recirculation. First, it implies that the cross-section

of the electrodes directly exposed to the incoming flow is relatively large, compared to the linear decrease of the inner radius in the traditional design. Second, it creates a hollow space between the core of the flow and the electrodes in which such recirculation can occur. A close-up illustration of this phenomenon is presented in figure 3.38. The distribution of the axial velocity along the cavity is also problematic. Large values are indeed found in a very large part of the domain and only strongly decreases close to the transition into the next chamber. That means a priori that the ions transported through this flow would keep a significant velocity throughout the chamber before being transmitted.

This behavior remains to be tested with simulations involving such ions. If confirmed, it would however go against a common practice that consists in *thermalizing* the ions previously created. This procedure attempts to homogenize the different kinetic and thermal energies of the analyte ions, to create favorable conditions for the following steps of the analysis. In the traditional design, the Mach disk plays this role. Between it and the next chamber, it allows for relatively calm conditions, where the velocity of the ions is reduced and leveled. Some designs also integrate a so-called *jet disrupter*. This is a small electrode, fixed in the center of the domain and for which a specific electric potential (DC) can also be set. The description of such a design can be found e.g. in Kelly et al. (2010). It proved to be helpful to improve the operative conditions of the ion funnel, even if the detailed mechanisms involved are not well explained so far. It is likely though to help the formation of the buffer zone that is present in the traditional design.

Continuity approximation

Here again, we check whether the continuity approximation necessary to apply the Navier-Stokes equation is still valid. Figure 3.39 presents the Knudsen number computed with the same method as used for the traditional design in section 3.4.3.

Only few regions do not respect the condition of a Knudsen number lower than 10^{-1}: only the area close to the tip of the capillary outlet shows values larger than this threshold. Further, the regions where specific slip boundary conditions should be applied are the ones around the last electrodes before the funnel outlet, around their edges. That means that the gas flow here may be slightly underestimated, given that the enforced non-slip conditions are not perfect. We still consider that the results represent reasonably well the real gas flow and that this should not have a significant influence on the results of the trajectory of the ions.

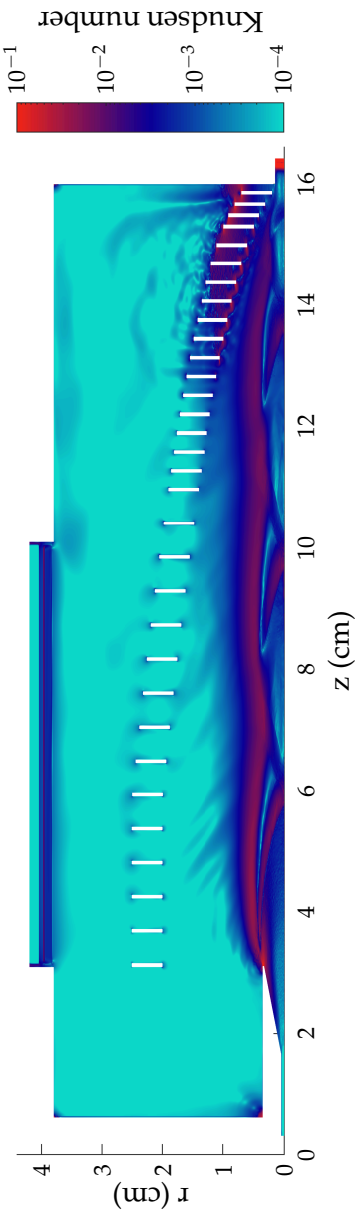

FIGURE 3.39: Knudsen number in the ion funnel - evolution of the design.

Chapter 4

Electric fields

Alongside the gas flow, electric fields play a significant role in the trajectory of the ions. Given the intrinsic charge of the particles considered, different effects are at stake. First, this leads to interaction among them. This is referred to as space charge effects (SCE) and is a significant part of the electric effects considered. Further, external electric fields can be applied in the system. It is the case at almost all stages, from the production of charges droplets in the electrospray ionization to the analysis of the species present (sometimes combined with magnetic fields) and of course the ion funnel specifically studied here. Both aspects, SCE and external fields, and their integration in the simulation of the trajectory of the ions are presented in this chapter.

4.1 Interaction between the particles

4.1.1 Electric field and potential theory

Since the particles considered in the present work are charged, electric forces between them should be taken into account. First assuming that these particles are fixed in the domain, an attraction force between ions of opposite charge and a repulsion force between ions of the same charge are given by Coulomb's law. To simplify the system, we consider only two distinct particles as point charges. The force of particle 1 applied on particle 2, $\vec{F}_{1\to 2}$, is expressed as follows:

$$\vec{F}_{1\to 2} = k\frac{q_1\, q_2}{r_{1\to 2}^2}\vec{e}_{1\to 2}\,, \tag{4.1}$$

where k is the Coulomb constant, q_1 and q_2 the respective charges of particles 1 and 2, $\vec{e}_{2\to 1}$ the unit vector pointing from particle 2 towards particle 1 and $r_{2\to 1}$ the distance between both particles. This formula, as well as all other ones presented in this section, can be found e.g. in Purcell (1965, chapters 1 and 2).

Applying the superposition principle and in the presence of n particles, the resulting force on particle i is

$$\vec{F}_{\to i} = \sum_{\substack{1\leqslant j\leqslant n\\ j\neq i}} k\frac{q_i\, q_j}{r_{i\to j}^2}\vec{e}_{i\to j}\,. \tag{4.2}$$

From this expression, one can derive the concept of the electric field. One considers another set of n charged particles. The electric field is defined at any position in space expect where the particles are located and it describes the effect caused by the set of particles. From this field, and for a given position, the force applied to a test particle is gained by multiplying with the test charge. The charge and position of

the set are denoted by q_j and $\vec{r}_j$, respectively and the test particle has a charge q and its position is represented by $\vec{r}$. The electric field $\vec{E}$ at position $\vec{r}$ is given by

$$\vec{E}(\vec{r}) = \sum_{j=1}^{n} k\, q_j \frac{\vec{r}_j - \vec{r}}{\left|\vec{r}_j - \vec{r}\right|^3} . \tag{4.3}$$

The resulting force $\vec{F}$ applied on the test particle is then:

$$\vec{F}(\vec{r}) = q\, \vec{E}(\vec{r}) . \tag{4.4}$$

It can be shown that the resulting force, e.g. for only one set of fixed particles and by extension for an arbitrary set, is conservative and can be expressed as the gradient of a scalar field V, called electric potential. The potential is expressed as follows:

$$V(\vec{r}) = \sum_{j=1}^{n} \frac{k\, q_j}{\left|\vec{r}_j - \vec{r}\right|} . \tag{4.5}$$

The electric field is then given by:

$$\vec{E}(\vec{r}) = -\nabla V(\vec{r}) . \tag{4.6}$$

4.1.2 Computation of the interaction

Equations 4.3 and 4.5 imply that the computation of the electric field and/or potential of a set of n particles at a given position requires a number of operations growing with n. Thus, computing the resulting force on each particle of this set induced by the presence of the other grows with n^2.[1] For a large number of particles considered, the simple computation of this interaction can become very expensive. Our goal is to compute the interaction between ions, which are present in large amounts, even if the electric currents considered overall remain small. For example, a current of 10 nA represents more than 60,000 singly charged particles entering the domain during the period of an ion funnel operating with a frequency of 1 MHz. It means that the computational costs could become prohibitive to simulate the systems we want to consider. Thus, two strategies have been used to overcome this issue.

Fast Multipole Method (FMM)

The first strategy consists in using a specific algorithm that delivers an approximation of both the electric field and potential. This method has been first described in Cheng, Greengard, and Rokhlin (1999) and we only give a summary of the method in the following section. The basic idea is that the domain is divided into different sub-domains. In each sub-domain, a multipole expansion can be done. The field generated by the charges present in the sub-domain is approximated with a chosen precision outside of this domain. Using the same principle, the field created by charges outside a given sub-domain can be approximated inside the domain. This is called a local expansion. Translations of the different transformations can be defined, and this leads to an algorithm that expresses the field at any point in the domain, while the complexity of the computation only grows with the number on

1. This is $n \cdot (n-1)$ as there are $n-1$ other particles to consider for each of the n particles. When n is large enough, n gets negligible compared to n^2 and only the latter remains relevant for this rough estimation.

charges considered n (to be compared with n^2 for a direction computation). While the overhead induced by this algorithm, which also increases with the precision required, is high, the better scaling means that this method is well suited to compute the interaction between the charged particles when their number is large, as this is the case in the systems that we consider.

The algorithm being relatively complex to implement efficiently, we use an implementation developed by a cooperation of German research groups and called *ScaFaCoS* (Scalable Fast Coulomb Solver) further described in Arnold et al. (2013). The library is written in C with interfaces in Fortran and offers different methods to compute electrostatic and gravitational fields, including the aforementioned FMM.[2]

Artificial charge factor

Besides the usage of an efficient algorithm to compute the interaction between the ions, one can further reduce the computational effort by using an artificial charge factor. The goal is to compute the Coulombic electric field by using a lower number of ions than required to reproduce the expected electric currents. This is achieved by multiplying the electric charge of the ions, when computing the field, with an arbitrary factor. It means that each particle considered for the computation of the field stands for several ones of the simulated species. The results of the simplification can be tested against this parameter. When the field is considered far from the charge holders, this modification should not have any significant influence. However, it could have some effects on the interaction of particles that are located close to each other. One can then expect higher side effects due to this simplification when considering higher concentrations of particles.

The artificial charge factor is only used to define the electric currents that we set, e.g. in the setting of the incoming ions, and the computation of the Coulombic electric field. However, the motion of a particular ion is performed using the real charge prescribed by the considered species, independently of the cause of the movement considered (interaction, external field, etc.). A validation of this behavior is presented in appendix G.

4.2 External electric fields

In many aspects of the mass spectrometry devices considered throughout this work, external electric fields play a significant role. While the production of the ions using electrospray ionization (ESI) has not been modeled, the electric fields used to guide the ions in the following chambers are essential to simulate their trajectory. Therefore, we focus in this section on the model considered and its implementation.

4.2.1 Properties of the electric fields considered

The capillary part of the system is not directly concerned by the external fields. It is an enclosed domain where all surrounding surfaces but inlet and outlet are set at the same potential. If one excludes the space charge effects, taken into account separately, and neglecting the effects at both ends of the capillary, no strong influence of external fields is expected.

2. The library is further described at this address: `http://www.scafacos.de/` and the latest implementation is available here: `https://github.com/scafacos/scafacos`.

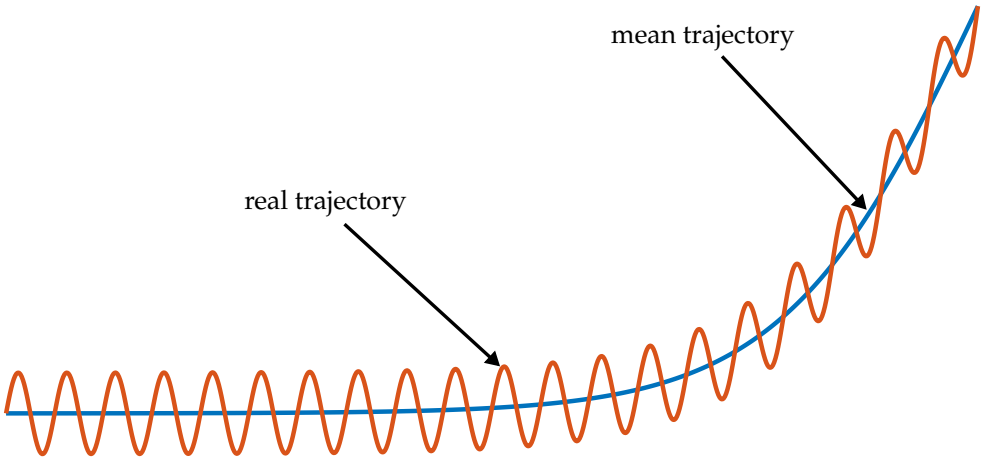

FIGURE 4.1: Real trajectory (red) and approximated trajectory (blue) as seen in the model of the effective electric field.

In the first pumping chamber, where the ion funnel is located, external electric fields are extensively used to focus the ions towards the central axis of the system and to transport them towards the next chamber. Two kinds of fields are typically used: a DC (for direct current), time-independent field resulting from a potential gradient which participates in pushing the ions towards the next chamber and thus basically creating a force in the axial direction of the domain. These effects add up to the driving by the gas flow.

The other kind of field is an RF (for radio-frequency) field, which uses a harmonic time dependency and the specific geometry of the electrodes present in the chamber to create a force in the radial direction, towards the central axis of the system. This second force counters the driving force of the gas flow caused by the pump.

4.2.2 Assumptions regarding the RF-field

The classic model

The principle of the RF-field typically found in ion funnels is to use a harmonic field. Because of its non-homogeneity, it induces, alongside the expected oscillations, an effective force towards the central axis. A model can be derived for such fields. A clear review of this derivation is found in Gerlich (1992, pp. 10-26). It delivers an effective field, that is a field constant in time but able to reproduce the effective force of the harmonic field. It thus describes the effective trajectory of the particles, leaving the oscillations out. This relies on several assumptions. Especially, the amplitude of the oscillations should be small enough. Also, the instantaneous electric field should vary smoothly enough in the domain, such that it can be correctly approximated by a first-order expansion.

One considers an oscillating electric field, that can be described as follows:

$$\vec{E}_{\mathrm{RF}}(\vec{x}, t) = \vec{E}_0(\vec{x}) \cdot \cos(\omega t). \tag{4.7}$$

$\vec{E}_0$ describes the form of the field over the domain that drives the effective force and $f = \frac{\omega}{2\pi}$ is the frequency of the considered field. Considering a charged particle of

mass m and charge q in a vacuum moving within this field, one can show that its time-averaged trajectory can be described by an effective force:

$$\vec{F}_{\text{eff}} = -\frac{q^2}{4m\omega^2}\nabla\left(\vec{E}_0 \cdot \vec{E}_0\right) . \tag{4.8}$$

We invite the reader to refer to Gerlich (1992, pp. 12-17) for further details regarding the steps leading to this formula and the assumptions met. It basically assumes that the oscillations in the trajectory of the particle can be neglected and derives the effective force that describes the average trajectory of the particle, as schematically represented in figure 4.1. It appears that this force is expressed as the gradient of a scalar field. It is thus conservative and a corresponding potential can be defined. To keep the similarity with an electric field $\vec{E}_{\text{eff}}$, one keeps the form $\vec{F}_{\text{eff}} = q\,\vec{E}_{\text{eff}}$. It follows

$$\vec{E}_{\text{eff}} = -\nabla V_{\text{eff}} \tag{4.9}$$

with the effective electric potential

$$V_{\text{eff}} = \frac{q}{4m\omega^2}\vec{E}_0 \cdot \vec{E}_0 . \tag{4.10}$$

The effective field does not only depend on the position via the field $\vec{E}_0$ but also on the species considered via charge and mass. This model has been widely used in connection with the ion funnel and was discussed in further publications, e.g. in Kelly et al. (2010). To ensure the validity of this approximation, a dedicated criterion, the *adiabaticity*, has been defined. It takes into account the assumptions mentioned before. First tests using an elementary gas flow and specific conditions for the ion funnel operation parameters, described in Kyriakidis (2019) show however that these assumptions might be broken. This launched the reflection to develop new strategies to simulate systems involving the different effects encountered. The straightforward path is to avoid modeling the effects of the RF-field and to use a time discretization fine enough to resolve a period of such fields. A second option consists in integrating, in the model, the fact that the ions are not in a vacuum but in gas. This is presented in the next section.

Considering the underlying gas flow

Besides the validity of the assumptions made to derive the classic model of the effective electric field, the very presence of the underlying gas flow has been neglected. Everything is derived as if the ions were moving in a vacuum. While fully understandable in a first approach of the problem, given the low gas density reached in comparison with normal conditions, this assumption might hide some effects or at least alter the form of the effective field derived. In section 2.2, the equation of motion considered for the ions integrates adapted terms to take into account the underlying gas as well as its local velocity. This model can be used to derive a modified form of effective RF-field.

Following the very same steps as presented in Gerlich (1992), and an equivalent notation, we define $\vec{r}$ as the position vector, and $\dot{\vec{r}}$ and $\ddot{\vec{r}}$ its first and second total time derivatives, respectively. The gas velocity field is described with $\vec{u}_{\text{f}}$ and the RF electric field with $\vec{E}(\vec{r},t) = \vec{E}_0(\vec{r})\cos(\omega t)$, where ω is the angular frequency of the electric field applied and $\vec{E}_0$ the spatial distribution of the field amplitude. We consider a single particle of mass m and denote the particle response time τ_{P}.

The considered differential equation reads:

$$\ddot{\vec{r}} + \frac{1}{\tau_P}\dot{\vec{r}} = \frac{q}{m}\vec{E}_0 \cos(\omega t) + \frac{1}{\tau_P}\vec{u}_f \,. \tag{4.11}$$

It corresponds to equation 2.18, where no DC-field is applied and no SCE effects are considered because only one particle is present. In the limit of a vacuum, the particle response time τ_P tends to very large values and the additional terms in the equation vanish in this limit (the gas velocity field becoming undefined). The trajectory is then again described with the classic equation used in Gerlich (1992).

In the first step of the derivation, the different fields involved are considered as homogeneous, that is $\vec{E}_0$, $\vec{u}_f$, and τ_P are considered independent from $\vec{r}$. This does not represent the reality but should only be seen as a preliminary step to gain the form of the solution, before introducing the spatial variations using expansion terms. The general solution of this homogeneous system reads:

$$\vec{r}(t) = \vec{r}(0) - \tau_P \dot{\vec{r}}(0)\, e^{-\frac{t}{\tau_P}} + \frac{q\vec{E}_0}{m\left(\frac{1}{\tau_P^2} + \omega^2\right)}\left(\frac{1}{\tau_P \omega}\sin(\omega t) - \cos(\omega t)\right) . \tag{4.12}$$

We further set a specific form for the position vector, following the general solution of the homogeneous equation:

$$\vec{r}(t) = \vec{R}_0(t) - \vec{b}\cos(\omega t) + \vec{c}\sin(\omega t)\,, \tag{4.13}$$

where $\vec{R}_0$ describes the effective displacement of the particles. The vectors $\vec{b}$ and $\vec{c}$ are defined as follows:

$$\vec{b} = \frac{q}{m\left(\frac{1}{\tau_P^2} + \omega^2\right)}\vec{E}_0 \,, \tag{4.14}$$

$$\vec{c} = \frac{q}{m(\omega\tau_P)\left(\frac{1}{\tau_P^2} + \omega^2\right)}\vec{E}_0 \,. \tag{4.15}$$

The effects of the gas flow, which are supposedly not oscillating, are included in $\vec{R}_0$. One further derives a differential equation for $\vec{R}_0$. This is done by replacing $\vec{r}$ by its specific form 4.13 in equation 4.11. One also assumes that the harmonic correction terms are small and their amplitude slowly evolving. This means that the spatial evolution of the considered fields is small in the range of the harmonic oscillations caused by the RF electric field. Using limited expansions of the electric and gas velocity fields as well as of the particle response time, the different terms can be rewritten as follows:

$$\vec{E}_0(\vec{r}) = \vec{E}_0\left(\vec{R}_0 - \vec{b}\cos(\omega t) + \vec{c}\sin(\omega t)\right) \tag{4.16}$$

$$\approx \vec{E}_0(\vec{R}_0) - (\vec{b}\cdot\nabla)\vec{E}_0(\vec{R}_0)\cos(\omega t) + (\vec{c}\cdot\nabla)\vec{E}_0(\vec{R}_0)\sin(\omega t)\,. \tag{4.17}$$

The gas velocity field can be similarly expanded:

$$\vec{u}_f(\vec{r}) = \vec{u}_f\left(\vec{R}_0 - \vec{b}\cos(\omega t) + \vec{c}\sin(\omega t)\right) \tag{4.18}$$

$$\approx \vec{u}_f(\vec{R}_0) - (\vec{b}\cdot\nabla)\vec{u}_f(\vec{R}_0)\cos(\omega t) + (\vec{c}\cdot\nabla)\vec{u}_f(\vec{R}_0)\sin(\omega t) \tag{4.19}$$

Finally, the same treatment is applied to the particle response time τ_P:

$$\tau_P(\vec{r}) = \tau_P\left(\vec{R}_0 - \vec{b}\cos(\omega t) + \vec{c}\sin(\omega t)\right) \tag{4.20}$$

$$\approx \tau_P\left(\vec{R}_0\right) - \left(\vec{b}\cdot\nabla\tau_P\right)\cos(\omega t) + (\vec{c}\cdot\nabla\tau_P)\sin(\omega t), \tag{4.21}$$

where $\vec{b}\cdot\nabla\tau_P$ and $\vec{c}\cdot\nabla\tau_P$ are evaluated at $\vec{R}_0$. This notation holds throughout this section.

As τ_P appears as its inverse in equation 4.11, one expresses it explicitly, using again a limited expansion. We also denote $\tau_P\left(\vec{R}_0\right)$ with $\tau_{P,0}$:

$$\frac{1}{\tau} \approx \frac{1}{\tau_{P,0} - \left(\vec{b}\cdot\nabla\tau_P\right)\cos(\omega t) + (\vec{c}\cdot\nabla\tau_P)\sin(\omega t)} \tag{4.22}$$

$$\approx \frac{1}{\tau_{P,0}}\left(1 + \frac{\vec{b}\cdot\nabla\tau_P}{\tau_{P,0}}\cos(\omega t) - \frac{\vec{c}\cdot\nabla\tau_P}{\tau_{P,0}}\sin(\omega t)\right) \tag{4.23}$$

To write the differential equation related to the effective trajectory, it is necessary to consider the first and second derivatives in time of the position vector using the form described in equation 4.13:

$$\dot{\vec{r}} = \dot{\vec{R}}_0 - \cancel{\cos(\omega t)\,\dot{\vec{b}}} + \omega\sin(\omega t)\,\vec{b} + \cancel{\sin(\omega t)\,\dot{\vec{c}}} + \omega\cos(\omega t)\,\vec{c} \tag{4.24}$$

$$\ddot{\vec{r}} = \ddot{\vec{R}}_0 + \cancel{\omega\sin(\omega t)\,\dot{\vec{b}}} + \omega^2\cos(\omega t)\,\vec{b} + \cancel{\omega\cos(\omega t)\,\dot{\vec{c}}} - \omega^2\sin(\omega t)\,\vec{c} \tag{4.25}$$

The terms including time derivatives of $\vec{b}$ or $\vec{c}$ and ultimately of $\vec{E}_0$ and τ_P are neglected with respect to the other terms. This again relies on the assumption that the spatial variation of the fields (and thus their time derivative following the oscillations of the position $\vec{r}$) is small, so that only terms similar to homogeneous fields are relevant.

The next step to build the new model is to replace the derived approximations in the different terms of equation 4.11 and to average over time. We further denote the time averaging with the notation $\langle\ldots\rangle_t$. The first term on the left-hand side to consider is the second time derivative of the position, from which the time average delivers:

$$\left\langle\ddot{\vec{r}}\right\rangle_t \approx \ddot{\vec{R}}_0\,. \tag{4.26}$$

The second term on the left-hand side first requires to consider the product of the expansions 4.23 and 4.24:

$$\begin{aligned}\frac{1}{\tau_P}\dot{\vec{r}} \approx \frac{1}{\tau_{P,0}}&\left(1+\frac{\vec{b}\cdot\nabla\tau_P}{\tau_{P,0}}\cos(\omega t)-\frac{\vec{c}\cdot\nabla\tau_P}{\tau_{P,0}}\sin(\omega t)\right)\cdot\\ &\left(\dot{\vec{R}}_0+\omega\sin(\omega t)\,\vec{b}+\omega\cos(\omega t)\,\vec{c}\right) \qquad (4.27)\\ \approx \frac{1}{\tau_{P,0}}&\dot{\vec{R}}_0+\frac{\vec{b}\cdot\nabla\tau_P}{\tau_{P,0}^2}\cos(\omega t)\dot{\vec{R}}_0-\frac{\vec{c}\cdot\nabla\tau_P}{\tau_{P,0}^2}\sin(\omega t)\dot{\vec{R}}_0\\ &+\frac{\omega}{\tau_{P,0}}\sin(\omega t)\,\vec{b}+\frac{\omega}{\tau_{P,0}^2}\left(\vec{b}\cdot\nabla\tau_P\right)\cos(\omega t)\sin(\omega t)\,\vec{b}\\ &-\frac{\omega}{\tau_{P,0}^2}\left(\vec{c}\cdot\nabla\tau_P\right)\sin^2(\omega t)\,\vec{b}+\frac{\omega}{\tau_{P,0}}\cos(\omega t)\,\vec{c}\\ &+\frac{\omega}{\tau_{P,0}^2}\left(\vec{b}\cdot\nabla\tau_P\right)\cos^2(\omega t)\,\vec{c}-\frac{\omega}{\tau_{P,0}^2}\left(\vec{c}\cdot\nabla\tau_P\right)\sin(\omega t)\cos(\omega t)\,\vec{c} \qquad (4.28)\end{aligned}$$

The time average follows, further replacing the vectors $\vec{b}$ and $\vec{c}$ with their values, taken at the average position and thus neglecting the terms of higher order:

$$\begin{aligned}\left\langle\frac{1}{\tau_P}\dot{\vec{r}}\right\rangle_t &\approx \frac{1}{\tau_{P,0}}\dot{\vec{R}}_0-\frac{\omega\vec{c}\cdot\nabla\tau_P}{2\tau_{P,0}^2}\,\vec{b}+\frac{\omega\vec{b}\cdot\nabla\tau_P}{2\tau_{P,0}^2}\,\vec{c} \qquad (4.29)\\ &\approx \frac{1}{\tau_{P,0}}\dot{\vec{R}}_0+\frac{\omega}{2\tau_{P,0}^2}\frac{q}{m\left(\omega\tau_{P,0}\right)\left(\frac{1}{\tau_{P,0}^2}+\omega^2\right)}\frac{q}{m\left(\frac{1}{\tau_{P,0}^2}+\omega^2\right)}\left(\vec{E}_0\cdot\nabla\tau_P\right)\vec{E}_0\\ &\quad-\frac{\omega}{2\tau_{P,0}^2}\frac{q}{m\left(\frac{1}{\tau_{P,0}^2}+\omega^2\right)}\frac{q}{m\left(\omega\tau_{P,0}\right)\left(\frac{1}{\tau_{P,0}^2}+\omega^2\right)}\left(\vec{E}_0\cdot\nabla\tau_P\right)\vec{E}_0 \qquad (4.30)\\ &\approx \frac{1}{\tau_{P,0}}\dot{\vec{R}}_0\,. \qquad (4.31)\end{aligned}$$

The first term on the right-hand side of equation 4.11 delivers, after averaging the terms of equation 4.17:

$$\left\langle\frac{q}{m}\vec{E}_0\cos(\omega t)\right\rangle_t \approx -\frac{q}{2m}\left(\vec{b}\cdot\nabla\right)\vec{E}_0\left(\vec{R}_0\right) \qquad (4.32)$$

Given the fact that $\vec{E}_0$ is an electric field, it can be written as the gradient of a scalar field. As a consequence, it is rotation-free ($\nabla\times\vec{E}_0=\vec{0}$) and it follows:

$$(\vec{E}_0\cdot\nabla)\vec{E}_0=\frac{1}{2}\nabla(\vec{E}_0\cdot\vec{E}_0)-\vec{E}_0\times(\nabla\times\vec{E}_0)=\frac{1}{2}\nabla(\vec{E}_0\cdot\vec{E}_0) \qquad (4.33)$$

Replacing $\vec{b}$ in equation 4.32 and using the property just derived one obtains:

$$\left\langle\frac{q}{m}\vec{E}_0\cos(\omega t)\right\rangle_t \approx -\frac{q^2}{4m^2\left(\frac{1}{\tau_{P,0}^2}+\omega^2\right)}\nabla(\vec{E}_0\cdot\vec{E}_0)\,. \qquad (4.34)$$

Finally, the second term on the right-hand side of equation 4.11 is again the product of expansions 4.23 and 4.19. This first step delivers, where $\vec{u}_f(\vec{R}_0)$ is shortened as

$\vec{u}_{\mathrm{f},0}$:

$$\begin{aligned}\frac{1}{\tau_\mathrm{P}}\vec{v}_\mathrm{f}(\vec{r}) \approx \frac{1}{\tau_{\mathrm{P},0}} &\left(1+\frac{\vec{b}\cdot\nabla\tau_\mathrm{P}}{\tau_{\mathrm{P},0}}\cos(\omega t)-\frac{\vec{c}\cdot\nabla\tau_\mathrm{P}}{\tau_{\mathrm{P},0}}\sin(\omega t)\right)\\ &\left(\vec{u}_{\mathrm{f},0}-(\vec{b}\cdot\nabla)\vec{u}_{\mathrm{f},0}\cos(\omega t)+(\vec{c}\cdot\nabla)\vec{u}_{\mathrm{f},0}\sin(\omega t)\right) \qquad (4.35)\\ \approx \frac{1}{\tau_{\mathrm{P},0}}\vec{u}_{\mathrm{f},0} &- \frac{(\vec{b}\cdot\nabla)\vec{u}_{\mathrm{f},0}}{\tau_{\mathrm{P},0}}\cos(\omega t)+\frac{(\vec{c}\cdot\nabla)\vec{u}_{\mathrm{f},0}}{\tau_{\mathrm{P},0}}\sin(\omega t)\\ &+\frac{\vec{b}\cdot\nabla\tau_\mathrm{P}}{\tau_{\mathrm{P},0}^2}\cos(\omega t)\,\vec{u}_{\mathrm{f},0}-\frac{\vec{b}\cdot\nabla\tau_\mathrm{P}}{\tau_{\mathrm{P},0}^2}\cos^2(\omega t)\,(\vec{b}\cdot\nabla)\vec{u}_{\mathrm{f},0}\\ &+\frac{\vec{b}\cdot\nabla\tau_\mathrm{P}}{\tau_{\mathrm{P},0}^2}\cos(\omega t)\sin(\omega t)\,(\vec{c}\cdot\nabla)\vec{u}_{\mathrm{f},0}\\ &-\frac{\vec{c}\cdot\nabla\tau_\mathrm{P}}{\tau_{\mathrm{P},0}^2}\sin(\omega t)\,\vec{u}_{\mathrm{f},0}+\frac{\vec{c}\cdot\nabla\tau_\mathrm{P}}{\tau_{\mathrm{P},0}^2}\sin(\omega t)\cos(\omega t)\,(\vec{b}\cdot\nabla)\vec{u}_{\mathrm{f},0}\\ &-\frac{\vec{c}\cdot\nabla\tau_\mathrm{P}}{\tau_{\mathrm{P},0}^2}\sin^2(\omega t)\,(\vec{c}\cdot\nabla)\vec{u}_{\mathrm{f},0}\,. \qquad (4.36)\end{aligned}$$

Averaging this expression over time, one ends up with:

$$\left\langle\frac{1}{\tau_\mathrm{P}}\vec{v}_\mathrm{f}(\vec{r})\right\rangle_t \approx \frac{1}{\tau_{\mathrm{P},0}}\vec{u}_{\mathrm{f},0}-\frac{\vec{b}\cdot\nabla\tau_\mathrm{P}}{2\tau_{\mathrm{P},0}^2}(\vec{b}\cdot\nabla)\vec{u}_{\mathrm{f},0}-\frac{\vec{c}\cdot\nabla\tau_\mathrm{P}}{2\tau_{\mathrm{P},0}^2}(\vec{c}\cdot\nabla)\vec{u}_{\mathrm{f},0}\,. \qquad (4.37)$$

This expression still contains terms involving the gradients of the approximated fields (particle response time and gas velocity). They are both multiplications of terms of first-order in the expansion of the fields considered here. Thus, they are of second order. To remain coherent with the approximations made so far, only the first term in equation 4.37 should be further considered and it follows:

$$\left\langle\frac{1}{\tau_\mathrm{P}}\vec{v}_\mathrm{f}(\vec{r})\right\rangle_t \approx \frac{1}{\tau_{\mathrm{P},0}}\vec{u}_{\mathrm{f},0}\,. \qquad (4.38)$$

Assembling the results of equations 4.26, 4.31, 4.34, and 4.38, one finally gets the new equation of motion for the effective trajectory:

$$\ddot{\vec{R}}_0+\frac{1}{\tau_{\mathrm{P},0}}\dot{\vec{R}}_0=-\left(\frac{q}{m}\right)^2\frac{1}{4\left(\frac{1}{\tau_{\mathrm{P},0}^2}+\omega^2\right)}\nabla\left(\vec{E}_0\cdot\vec{E}_0\right)+\frac{1}{\tau_{\mathrm{P},0}}\vec{u}_{\mathrm{f},0}\,. \qquad (4.39)$$

While the terms due to the presence of the gas flow are simply approximated using the value of the fields at the average position along the trajectory of the particle, the term describing the effects of the RF electric field takes a similar form as described in Gerlich (1992). Here again, in the limit of very large values for $\tau_{\mathrm{P},0}$, that is for systems close to vacuum conditions, one gets back to the classic model. However, for smaller values, one can show that the magnitude of the effective electric field is dampened by the surrounding gas flow, compared to the model in a vacuum. It can be interpreted as the consequence of the interaction between ions and gas molecules that perturb the motion caused by the electric field.

One can further identify this expression in terms of effective electric force $\vec{F}_{\text{eff}}$, by simply multiplying with the mass of the particle:

$$\vec{F}_{\text{eff}} = -\frac{q^2}{4m}\frac{1}{\frac{1}{\tau_{\text{P}}^2}+\omega^2}\nabla\left(\vec{E}_0\cdot\vec{E}_0\right), \tag{4.40}$$

and similarly, an effective electric field $\vec{E}_{\text{eff}}$ can be easily defined:

$$\vec{E}_{\text{eff}} = -\frac{q}{4m}\frac{1}{\frac{1}{\tau_{\text{P}}^2}+\omega^2}\nabla\left(\vec{E}_0\cdot\vec{E}_0\right). \tag{4.41}$$

The new equation of motion thus reads:

$$\ddot{\vec{R}}_0 + \frac{1}{\tau_{\text{P},0}}\dot{\vec{R}}_0 = -\frac{q}{m}\vec{E}_{\text{eff},0} + \frac{1}{\tau_{\text{P},0}}\vec{u}_{\text{f},0}\,, \tag{4.42}$$

where $\vec{E}_{\text{eff},0}$ is the electric field at the position $\vec{R}_0$. However, the factor in front of the gradient depends on the position via the particle response time. Thus one cannot define any effective electric potential, as this is the case for the classic formulation in vacuum.

This form of effective field has already been presented in Tolmachev et al. (1997), using a different demonstration. It is derived from the Langevin equation describing the Brownian motion of a particle. Here we considered the specific form of the equation of motion 4.11, which does not include the Brownian effects on the trajectory of the particle. Nevertheless, one finds in both cases an equivalent correction factor applied to the effective RF-field in vacuum $\vec{E}_{\text{eff,vac}}$ to take into account the presence of the gas in $\vec{E}_{\text{eff}}$:

$$\vec{E}_{\text{eff}} = \frac{\tau_{\text{P}}^2\omega^2}{1+\tau_{\text{P}}^2\omega^2}\vec{E}_{\text{eff,vac}}\,. \tag{4.43}$$

4.2.3 Computation of the external fields

The external fields considered throughout this work are computed, similarly to the fields resulting from the space charge effects, using the electrostatic framework. This means that knowing the electric potential at the boundaries of the domain considered, basically in our case the electrodes of the ion funnel, we solve Gauss' law that reads:

$$\nabla\cdot\vec{E}_{\text{ext}} = \frac{\rho_{\text{C}}}{\varepsilon_0}\,, \tag{4.44}$$

where ρ_{C} is the electric charge density in the domain and ε_0 the vacuum permittivity. While the charge density represents, in theory, the ions present in the field, we choose for practical reasons to disconnect both effects, a simplification explained in 4.3.2. This implies that the charge density considered here is zero and Gauss' law simplifies as follows:

$$\nabla\cdot\vec{E}_{\text{ext}} = 0\,. \tag{4.45}$$

The electric field, in the hypothesis of electrostatics, is considered as a conservative field and can be expressed using a scalar potential V_{ext}:

$$\vec{E}_{\text{ext}} = \nabla V_{\text{ext}}\,. \tag{4.46}$$

Replacing the electric field in equation 4.45 by its expression from 4.46 and one ends up solving the Laplace equation:

$$\nabla \cdot \nabla V_{\text{ext}} = \Delta V_{\text{ext}} = 0\,, \tag{4.47}$$

where Δ is the so-called Laplace operator.

This last equation is the one solved to compute the electric potential and following the electric field in the free space domain of the ion funnel. The code used was developed in the department of Numerical Fluid Dynamics at Technische Universität Berlin. It was first used and validated within Kyriakidis (2019) master's thesis, and allows to compute electric fields on 2D grids, either representing a (Cartesian) 2D domain or an axially symmetric one when specific conditions are enforced. The axially symmetric implementation, which has been used in this work, is further detailed in section 4.4.1.

4.3 Estimations used to develop the model

4.3.1 Neglected magnetic field

The systems studied in this work include the movement of charged elements in an electric field. Without further assumptions, one should not only consider the electric field itself but also the magnetic field created by the movement of the elements. This would require solving the Maxwell equations in some way or the other. It represents a significant increase in complexity compared to the simple assumption of an electrostatic field though. We would like to show here, that in a first approximation, the magnetic field created by the ions can be neglected.

Following the same argumentation as presented in Bernier (2014), the force $\vec{F}_{\text{elec}}$ that is applied to an ion is the Lorentz force, expressed as the following (see D. J. Griffiths (2013, chapter 5) e.g. for references of all following relations):

$$\vec{F}_{\text{elec}} = q\left(\vec{E} + \vec{u}_{\text{P}} \times \vec{B}\right)\,, \tag{4.48}$$

with $\vec{E}$ the electric field at the position of the ion seen as a point particle, $\vec{B}$ the magnetic field, q the charge of the ion and $\vec{u}_{\text{P}}$ its velocity. In the work presented here, we neglect the second term of this expression. In order to justify this choice, we estimate the magnetic field, without solving the underlying Maxwell equations. A means to proceed is to express the magnetic field using the Biot-Savart law. It considers a steady-state where an electric current density $\vec{j}$ is defined in a volume V. The resulting magnetic field $\vec{B}$ reads:

$$\vec{B}\left(\vec{r}\right) = \frac{\mu_0}{4\pi}\int_V \left(\vec{j}\left(\vec{r}\right) \times \frac{\vec{r} - \vec{r'}}{\left|\vec{r} - \vec{r'}\right|^3}\right) \mathrm{d}r'^3\,, \tag{4.49}$$

with μ_0 the permeability of free space. In the case of the ion funnel, the assumption of a steady-state remains questionable. However, and in a similar view as adopted when deriving the effective RF-field, we assume that the oscillations of the ions do not significantly impact their global behavior. Especially, this means that the electric current density $\vec{j}$ can be considered as constant over time. Thus the magnetostatic approximation required to use the Biot-Savart law is fulfilled. The equation 4.49 is expressed for a continuum but can be transformed into a discrete formulation to be

directly compared with the electric field 4.3 representing the space charge effects. The electric current density $\vec{j}$ can be expressed as $\rho\vec{u}_{\mathrm{P}}$, with ρ the electric charge density and $\vec{u}_{\mathrm{P}}$ the velocity field of the charge holders. In a discrete notation, it becomes $q_i\vec{u}_{\mathrm{P},i}$ and it follows

$$\vec{B}\left(\vec{r}\right) = \frac{\mu_0}{4\pi}\sum_{j=1}^{n} q_j\vec{u}_{\mathrm{P},j} \times \frac{\vec{r}_j - \vec{r}}{\left|\vec{r}_j - \vec{r}\right|^3}\,. \tag{4.50}$$

Both electric (expressed as equation 4.3) and magnetic components in the Lorentz force 4.48 present similar forms. A rough comparison can then be done using equivalent terms in the sum, especially the charge denoted as q_{eq} and the particle velocity $\vec{u}_{\mathrm{p,eq}}$. It follows

$$\frac{\left|\vec{u}_{\mathrm{P}} \times \vec{B}\right|}{\left|\vec{E}\right|} \sim \frac{\mu_0 q_{\mathrm{eq}} v_{\mathrm{p,eq}}^2}{4\pi}\frac{1}{kq_{\mathrm{eq}}}\,. \tag{4.51}$$

The constant k of the electric field can further be expressed as $\frac{1}{4\pi\epsilon_0}$ (see D. J. Griffiths (2013, p. 60)), where ϵ_0 is the permittivity of free space. Furthermore, the different constants are related to the speed of light c with $c^2\epsilon_0\mu_0 = 1$. The comparison between the electric and magnetic fields can thus be approximated as:

$$\frac{\left|\vec{u}_{\mathrm{P}} \times \vec{B}\right|}{\left|\vec{E}\right|} \sim \mu_0\epsilon_0 v_{\mathrm{p,eq}}^2 = \frac{v_{\mathrm{p,eq}}^2}{c^2}\,. \tag{4.52}$$

One can conclude that the contribution of the magnetic field to the forces exerted onto the ions can be neglected when their velocity is small compared to the speed of light. This condition is always fulfilled in our simulations and we thus only consider the contribution of the electric field.

However, this estimation does not include the external fields created by electrodes for example, as only the fields created by the ions themselves are included in the comparison. Thus, it is not more than a first approach. Here again, only a consideration of the Maxwell equations with proper boundary conditions would allow us to deliver the exact result.

4.3.2 Decoupling of the electric fields

The global electric field can be expressed using the Poisson equation. This is an extension of the Laplace equation 4.47 used for the external electric field when charges are present within the free domain considered. It can be derived from Gauss' law, equation 4.44, exactly as the Laplace equation. The Poisson equation reads, following D. J. Griffiths (2013, p. 84):

$$\Delta V_{\mathrm{elec}} = \frac{\rho_{\mathrm{C}}}{\epsilon_0}\,, \tag{4.53}$$

where ρ_{C} is again the charge density in the domain and V_{elec} the total electric potential. This potential is influenced by two effects: the presence of the ions which create a charge density different from zero and the boundary conditions imposed by the elements present in the domain, such as the electrodes in the ion funnel. The potential can then be divided into two components, the first one describing the electric

potential in the absence of charges, V_{ext}, and the second one describing the modification due to the presence of the ions, V_{SCE}. The Poisson equation is linear and one can write:

$$\Delta V_{\text{elec}} = \Delta V_{\text{ext}} + \Delta V_{\text{SCE}} \,. \tag{4.54}$$

V_{ext} is exactly the potential described in section 4.2. The Laplace equation 4.47 still holds and it follows:

$$\Delta V_{\text{SCE}} = \frac{\rho_{\text{C}}}{\epsilon_0} \,, \tag{4.55}$$

This equation is very similar to the one for the total electric potential 4.53. It differs by the boundary conditions that must be enforced at the end of the free space, i.e. at the walls. It is not anymore ruled by the potential imposed on the elements present in the domain (this being described by V_{ext}) but must get a unique value, typically zero.

This condition defines the error made in this work by computing that part of the total potential using the Coulombic forces as described in 4.1.2. Using formula 4.5, the boundary condition is set to zero very far away from the charges and not at the walls. This error can be assumed to remain limited for two reasons. First, the ions are considered as lost as soon as they hit a wall. This means that no accumulation of charges can occur in the vicinity of a boundary, limiting the magnitude of the electric field possibly created by the free charges. Second, the electrodes present in the domain where high concentrations of ions are expected, typically at the end of the ion funnel, intend to further focus the ions and thus increasing the distance between the regions of high charge density and the boundaries. This further limits the error caused by the approximation of the potential created by the presence of the ions.

In the core regions of the domain, far away from the walls, we thus expect a very good approximation of the electric field used to compute the trajectory of the ions. In the areas close to the walls, the approximation is expected a priori not as good, but still correct enough to accurately describe the loss mechanisms we are interested in.

4.4 Results of the external electric fields

In this section, we present the methodology used to compute the external electric fields created by the electrodes present in the domain and the corresponding results.

4.4.1 Principle of the LAPLACE solver used

In both designs of ion funnels considered in this work, two different kinds of external electric fields are considered, as has already been mentioned: a time constant one, further referred to as *direct current* or DC-field, and a harmonic one, further referred to as *radio-frequency* or RF-field. While an effective field can be computed for the RF-field, the computation of the potential via the Laplace equation 4.47 is the first step. To this end, a code developed in the CFD department at TU Berlin and fitted for this case has been used. It allows us to consider a domain where objects are immersed, for which the potential is known and to compute the resulting electric potential in the free space. In our case, these objects are typically the electrodes forming the funnel, the capillary, and the housing of the chamber.

The principle of the computation is to discretize the entire domain, including the objects, and to build a linear system of equations that has to be solved to get

the value of the potential at every point of the grid. There are two kinds of points. Either it is located in an immersed object, and the value of the potential is known. Or it is in the free space, and one knows that the Laplacian of the potential is zero. For the second category, the Laplacian is expressed using the neighbor points via finite differences schemes. The domain considered is axially symmetric and we make use of cylindrical coordinates. The Laplace equation then reads:

$$\Delta V_{\text{ext}} = \frac{1}{r}\frac{\partial}{\partial r}\left(r\frac{\partial V_{\text{ext}}}{\partial r}\right) + \frac{\partial^2 V_{\text{ext}}}{\partial z^2} = 0\,. \tag{4.56}$$

A slice of the domain in the azimuthal direction is discretized, using an orthogonal grid. The grid points are equidistant for each direction, but the grid spacing can differ between the radial and axial directions. The coordinates of the grid points are denoted by $\left(r_{\text{i}}, z_{\text{j}}\right)$, where i and j are the indices defining the considered point in the radial and axial directions, respectively. The grid spacing can be defined as $h_r = r_{\text{i}+1} - r_{\text{i}}$ in the radial direction and $h_z = z_{\text{j}+1} - z_{\text{j}}$ in the axial direction. The indices i and j can be chosen arbitrarily. We use the following notation: $V_{\text{ext}}\left(r_{\text{i}}, z_{\text{j}}\right) = V_{\text{ext;i,j}}$.

The second derivative in the axial (z) direction is computed using a classic second-order central derivative :

$$\frac{\partial^2 V_{\text{ext}}}{\partial z^2}\left(r_{\text{i}}, z_{\text{j}}\right) = \frac{V_{\text{ext;i,j}-1} - 2V_{\text{ext;i,j}} + V_{\text{ext;i,j}+1}}{h_z^2} + \mathcal{O}\left(h_z^2\right)\,. \tag{4.57}$$

The radial term cannot be treated as easily, because it is a combination of coordinates and derivative terms. To keep the second order used in the axial direction, a combination of forward and backward derivatives with first order of accuracy are used. One can obtain the global second-order accuracy by averaging the two possible options: backward inner derivative with forward outer derivative on the one hand and forward inner derivative with backward outer derivative on the other hand. This results in the following discretization:

$$\begin{aligned}\frac{1}{r}\frac{\partial}{\partial r}\left(r\frac{\partial V_{\text{ext}}}{\partial r}\right)\left(r_{\text{i}}, z_{\text{j}}\right) =& \frac{\left(r_{\text{i}-1} + r_{\text{i}}\right) V_{\text{ext;i}-1,\text{j}} + \left(r_{\text{i}} + r_{\text{i}+1}\right) V_{\text{ext;i}+1,\text{j}}}{2r_{\text{i}}h_r^2} \\ &- \frac{\left(r_{\text{i}-1} + 2r_{\text{i}} + r_{\text{i}+1}\right) V_{\text{ext;i,j}}}{2r_{\text{i}}h_r^2} + \mathcal{O}\left(h_r^2\right)\,.\end{aligned} \tag{4.58}$$

The form and order of accuracy of this finite differences scheme are derived in appendix E.

The housing of the chamber encompasses the outer boundaries of the domain. Thus, there is no need for specific treatment of the boundaries for the axial direction and the upper radial direction. The lower radial boundary coincides with the symmetry axis of the domain and has to be treated separately. The radial term present in the Laplace equation 4.56 is not well defined for r approaching zero. Using the product rule, this term can be rewritten:

$$\frac{1}{r}\frac{\partial}{\partial r}\left(r\frac{\partial V_{\text{ext}}}{\partial r}\right) = \frac{\partial^2 V_{\text{ext}}}{\partial r^2} + \frac{1}{r}\frac{\partial V_{\text{ext}}}{\partial r}\,. \tag{4.59}$$

Because of the symmetry of the system and thus of the solution, the potential is an even function in the radial direction, assuming that one extends the radial coordinates in the negative values. The potential being a solution of the Laplace equation, its regularity further imposes that its first derivative is zero at the symmetry axis.

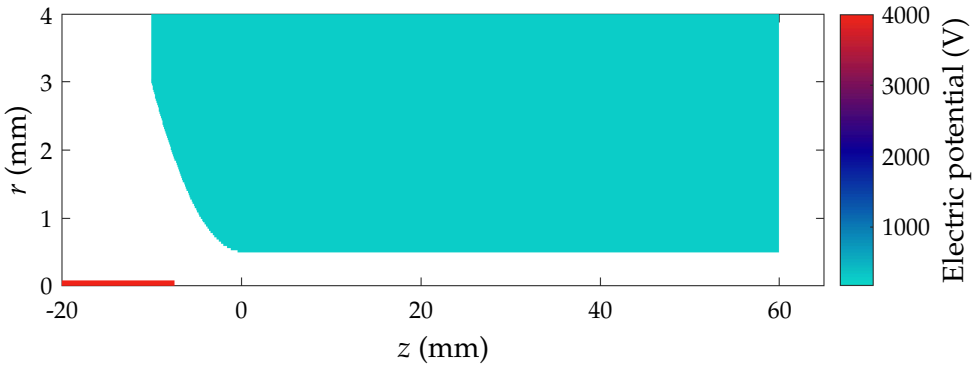

FIGURE 4.2: DC potential set in the capillary. Both dimensions are not to scale.

While the first term in 4.59 is not problematic, the second one is undefined for r approaching zero. One can, however, apply L'Hôpital's rule:

$$\lim_{r\to 0} \frac{1}{r}\frac{\partial V_{\text{ext}}}{\partial r} = \frac{\partial^2 V_{\text{ext}}}{\partial r^2}\,. \tag{4.60}$$

It follows:

$$\lim_{r\to 0} \frac{1}{r}\frac{\partial}{\partial r}\left(r\frac{\partial V_{\text{ext}}}{\partial r}\right) = 2\frac{\partial^2 V_{\text{ext}}}{\partial r^2}\,. \tag{4.61}$$

We can thus apply directly the second-order central derivative already used in the axial direction. Using the symmetry once again, stating that the potential holds the same value on both sides of the axis, it follows:

$$\lim_{r\to 0} \frac{1}{r}\frac{\partial}{\partial r}\left(r\frac{\partial V_{\text{ext}}}{\partial r}\right) = 4\left.\frac{V_{\text{ext;i+1,j}} - V_{\text{ext;i,j}}}{h_r^2}\right|_{r=0} + \mathcal{O}\left(h_r^2\right)\,. \tag{4.62}$$

Using equations 4.57, 4.58, and 4.62, one builds a linear system of equation corresponding to the Laplace equation. Its inversion, using standard, built-in algorithms, delivers the value of the potential at the grid points. The electric field, necessary to perform the simulations of the trajectory of the ions, is then gained by computing the gradient of the potential.

4.4.2 Results for the capillary

Even if the external electric fields within the capillary are expected to be very small, we show here some results supporting this assumption. In figure 4.2, the setup for the computation is presented. The capillary is considered with its funnel-shaped inlet. Its potential is set to 250 V. The diameter of the capillary is 1.0 mm and it has a length of 6 cm. In the lower-left corner of the domain, a needle is inserted to represent the emitter of the electrospray ionization. Its potential is set to 4000 V. It ends 7.5 mm before the straight part of the capillary and thus lies well within the inlet of the capillary. These parameters are chosen to describe a typical setup for the devices considered throughout this work.

The results for the magnitude of the electric field are presented in figure 4.3. Different radial positions within the capillary, covering the entire cross-section, are considered. The only area where significant values of the electric field are found lie

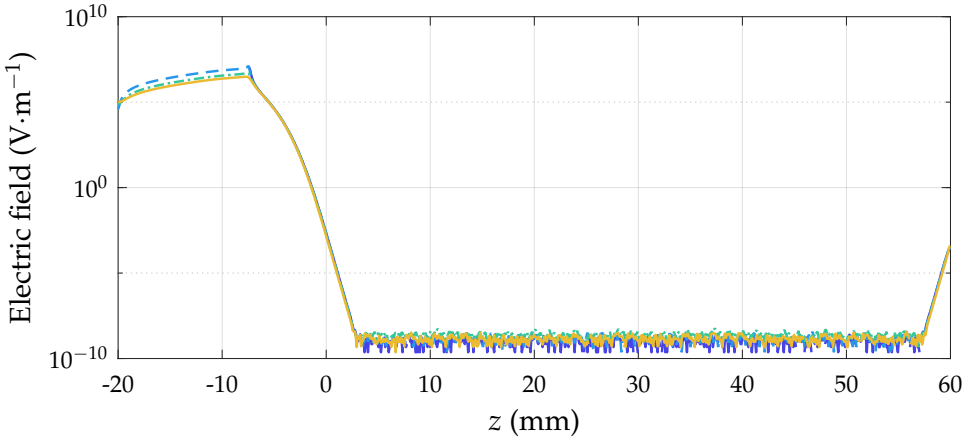

FIGURE 4.3: Electric field expected within the capillary. The different lines represent different radial positions within the capillary.

Location	Potential (V)
Capillary	250
First electrode	150
Last electrode	50
Ground	0

TABLE 4.1: Potential set for the DC-field in the ion funnel - classic design.

in the inlet area, that is where the electrospray ionization occurs. However, within the capillary, the values of the field are much lower, reaching a priori zero, considering machine precision, for the major part of the domain. Regions with higher field magnitudes are found inside the capillary at both ends, representing the boundary effects. But even these remain small, with maximal values of about $10^{-4}\mathrm{V}\cdot\mathrm{m}^{-1}$. In comparison, the electric field of two singly charged ions separated by 0.1 mm creates a field in the order of magnitude of $10^{-1}\mathrm{V}\cdot\mathrm{m}^{-1}$. This justifies that no external electric fields are considered for the capillary.

4.4.3 Results for the ion funnel - classic design

In the classic design, 82 electrodes are placed within the domain and are set to different potentials. Alongside the potential set to the capillary, the outlet, and the casing of the chamber, this creates the electric field expected to guide the ions through the tunnel. The electrodes have a time-dependent potential to create the RF-field previously described, while the potential remains constant for the other parts of the system. We thus split the computation and the results presented here in the time constant potential (DC-field) and the alternating potential (RF-field).

DC-field

The DC-field helps the ions to progress in the axial direction, towards the next chamber. This is achieved with a progressive increase or decrease in the potential of

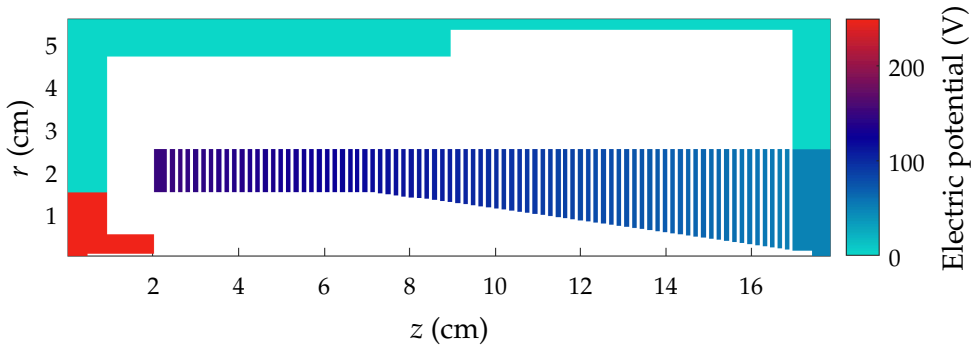

FIGURE 4.4: Electric DC potential set in the ion funnel - classic design.

the electrodes in this direction. For positively charged ions, the potential decreases and vice versa for negatively charged ions. We consider here a decreasing potential.

Each electrode has a fixed potential, ruled by the linear decrease between the first and the last electrode. The potential difference between them is thus sufficient to describe the setup. From the electric point of view, the last electrode is enclosed within the casing and is thus part of the wall. The capillary area, encompassing a part of the wall is set to a specific potential. The rest of the casing is set to the ground, chosen as zero. This set up is depicted in figure 4.4. and the corresponding values are listed in table 4.1

The potential within the free area is then computed using the Laplace solver and the results are presented in figure 4.5. One can see that inside the funnel, that is within the cavity formed by the electrodes, the field created is close to uniform along the axial direction. This is a direct result of the linear distribution of the potential and the constant spacing between the electrodes. Deviations can be observed, especially close to the objects present in the field. The main deviation is close to the capillary, because of the strong potential difference between the capillary and the first electrode and their respective shapes. It thus follows an expansion path from the capillary towards the electrodes. Some small deviations can also be observed close to the electrodes, which are linked to the presence of the edges of the objects. The potential being constant within an object and linear between the objects, the resulting field is not mathematically smooth at this transition, which creates these irregularities, potentially amplified by the numerical computation.

RF-Field

The primary RF-field intends to prevent the ions to fly between the electrodes by creating an electric force towards the symmetry axis of the domain. This is achieved by using a time-dependent potential applied to the electrodes. For this computation, a specific potential is only set for the electrodes located within the chamber with all other objects considered at the ground. The potential of the electrodes varies in time, following a harmonic profile, with a phase delay of π between two consecutive electrodes (equivalent to a flip of the sign of the potential). Following, two parameters define this field: its angle frequency ω and the amplitude $V_{\mathrm{RF},0}$. The variation of the

FIGURE 4.5: Electric DC potential in the free field and direction of the electric DC-field in the ion funnel - classic design. The length of the arrows is constant over the entire domain, only their direction refers to the electric field. Only the area around the funnel cavity is represented.

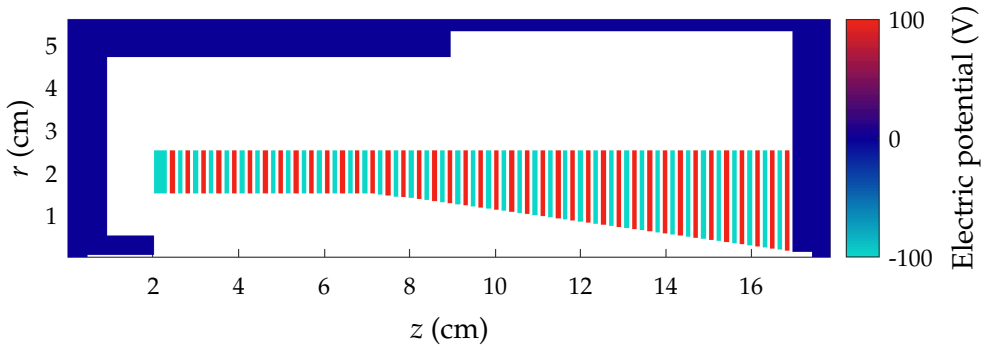

FIGURE 4.6: Electric RF potential set in the ion funnel with an amplitude of 100 V - classic design.

amplitude tunes the strength of the field in our work, while the frequency is kept constant.

The electric field $\vec{E}_0$ described in section 4.2.2 is thus computed considering that the potential of the electrodes is the amplitude $V_{\mathrm{RF},0}$ multiplied alternatively with 1 or -1. The settings of the potential of the different objects are represented in figure 4.6. The resulting electric field $\vec{E}_0$ in the free space is represented in figure 4.7 and the basis for the effective fields, $\nabla\left(\vec{E}_0 \cdot \vec{E}_0\right)$, in figure 4.8. The latter clearly shows that the RF-fields concentrate their effect close to the tip of the electrodes, while no significant effects are expected further away from the electrodes, in the center of the cavity of the ion funnel. One can then either compute in real-time the RF-field as described in equation 4.7 or derive the corresponding effective fields from equations 4.10 and 4.41.

The field can be further analyzed to show how such a field can limit the number of ions that reach the electrodes. We can gain a first insight into the forces that the ions experience by looking at the potential in the vicinity of several electrodes. In figure 4.9, the potential is represented along the radial direction for different axial positions. It can be observed that the potential varies between -100 V and 100 V between two successive electrodes. It shows also that, for a positively charged ion, the electrodes with positive potential exert a repulsive force onto the ion, while the electrodes with negative potential exert an attractive force.

For larger radial positions, an area of constant potential can be found either because it represents the potential of an electrode and is thus a boundary condition of the field, or because the Laplace equation between two straight electrodes roughly delivers a linear profile depending only from the distance to these electrodes. Because of boundary effects close to the tips of the electrodes, the behavior can be more complex there. The electric potential shows for some positions local maxima or minima before reaching this almost constant value between the electrodes. This means that a positive force, shortly followed by a negative one, can be encountered, and vice versa. However, the global trend between the symmetry axis and the area of constant potential would deliver only one kind of force, either positive or negative, depending on the axial position considered.

Furthermore, this is only an instantaneous picture, as the potential varies with high frequencies in time, leading to attractive areas becoming repulsive and repulsive areas becoming attractive. According to Gerlich (1992), these oscillations lead to a shift of the trajectory, in the case of vacuum, towards regions of weaker fields,

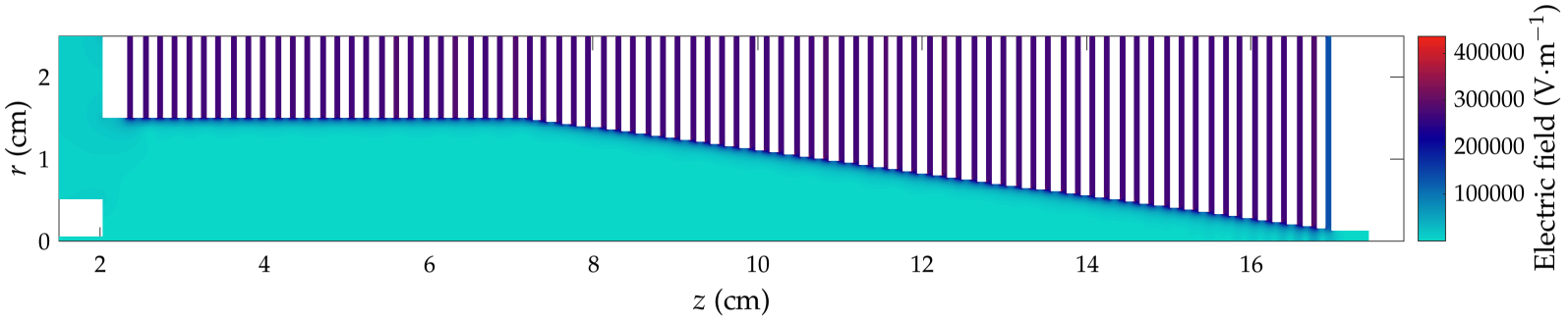

FIGURE 4.7: Magnitude of the instantaneous electric RF-field $\vec{E}_0$ with an amplitude of 100 V - classic design. Only the area around the funnel cavity is represented.

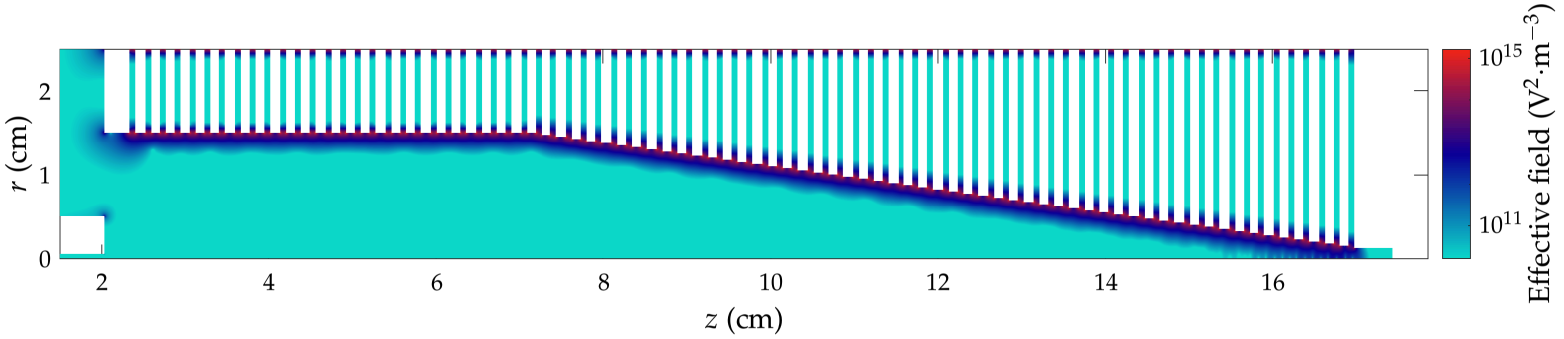

FIGURE 4.8: Magnitude of the basis of the effective electric RF-field $\nabla\left(\vec{E}_0 \cdot \vec{E}_0\right)$ with an amplitude of 100 V - classic design. Only the area around the funnel cavity is represented and a logarithmic scale of the amplitude is used.

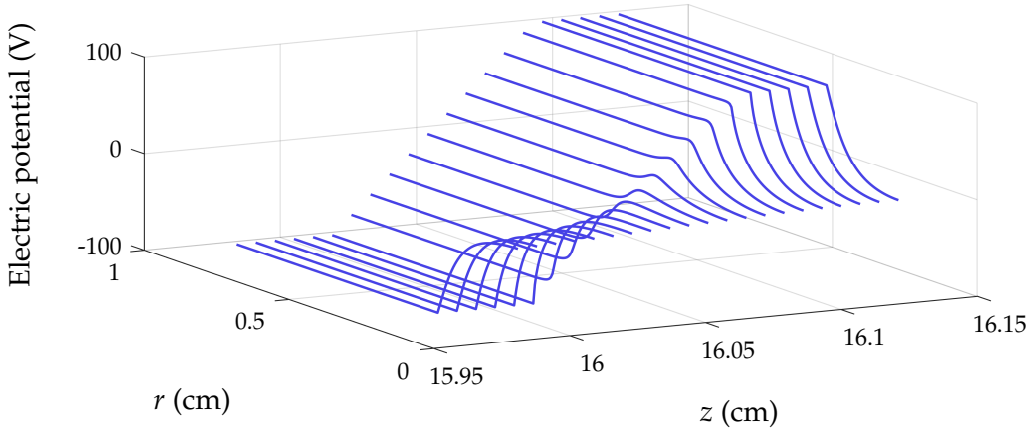

FIGURE 4.9: Electric potential $\vec{V}_0$ with an amplitude of 100 V - classic design. One dimensional representation along the radial direction, for several axial positions and in the vicinity of two consecutive electrodes.

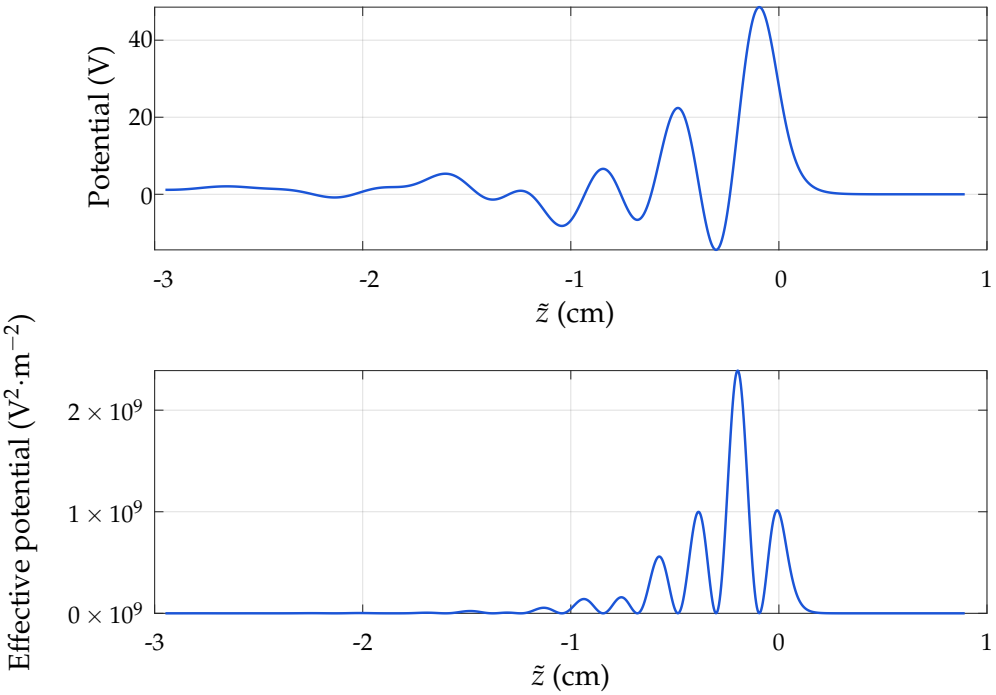

FIGURE 4.10: Top: electric potential close to the outlet. Bottom: form of the effective potential. In both figures, the axial coordinate z is re-scaled into $\tilde{z}$ to be zero at the right wall of the first pumping chamber (at the end of the funnel.)

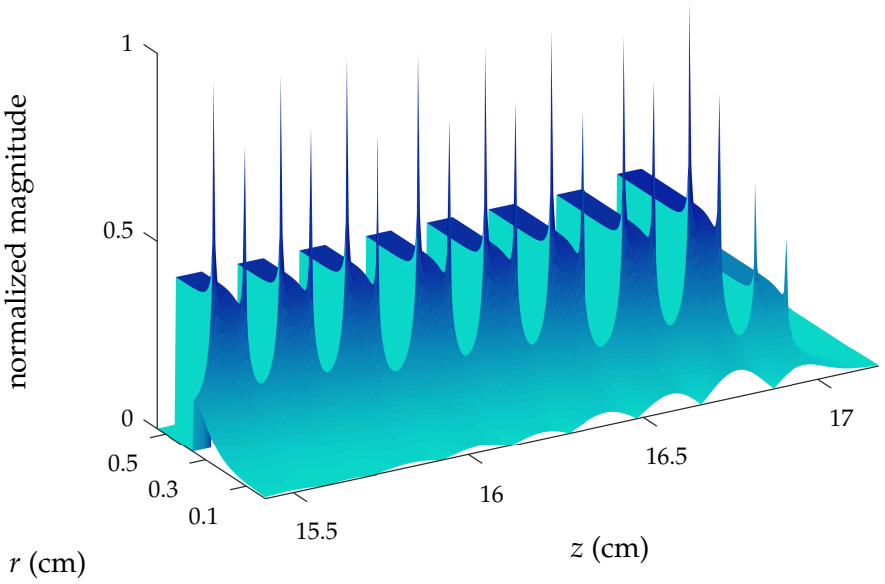

FIGURE 4.11: Magnitude of the RF electric field close to the outlet of the funnel, normalized with the highest value reached in the area considered.

that are in our case in the center of the cavity. As shown in section 4.2.2, taking into account the underlying gas flow does not modify the form of the effective field, but only its amplitude. Thus the same effects of a shift towards the symmetry axis are expected. One exception shall be mentioned here. At the end of the cavity, where the inner diameter of the electrodes becomes close to the distance between two successive electrodes, the assumption that the resulting electric field presents a lower value in the center of the cavity gets broken. This leads to so-called trapping effects. It can be easily understood when considering the instantaneous potential, as well as the form of the effective potential along the symmetry axis of the domain, as depicted in figure 4.10. Local minima of the potential are present, thus attracting the positively charged ions (local maxima playing this role for negatively charged ions). This is especially remarkable in the effective potential. Indeed, this shows that, on average, such trapping zones are expected in the domain. They are thus not only temporarily present because of the harmonic nature of the instantaneous field. This effect is further described with the results of the trajectory of the ions in section 5.2.2.

The numerical computation leads to the formation of peaks of the electric field at the edges of the electrodes. This is not surprising, as the Laplace equation is known to create irregularities at edges, resulting in infinite fields in some conditions. This has been reported for cases similar to the present ones in Smedt and Bladel (1987) and Lui et al. (1999), for example. This phenomenon can be observed for the ion funnel in figure 4.11. It was validated in Kyriakidis (2019) that these peaks are physical and no numerical artifacts by modifying the resolution of such computation and considering the evolution of the solution. These structures remain even with a very fine grid. As a consequence, one can expect very large electric forces applied to

Location	Potential (V)
Capillary	250
First electrode	150
Last electrode	50
Ground	0

TABLE 4.2: Potential set for the DC-field in the ion funnel - evolution of the design.

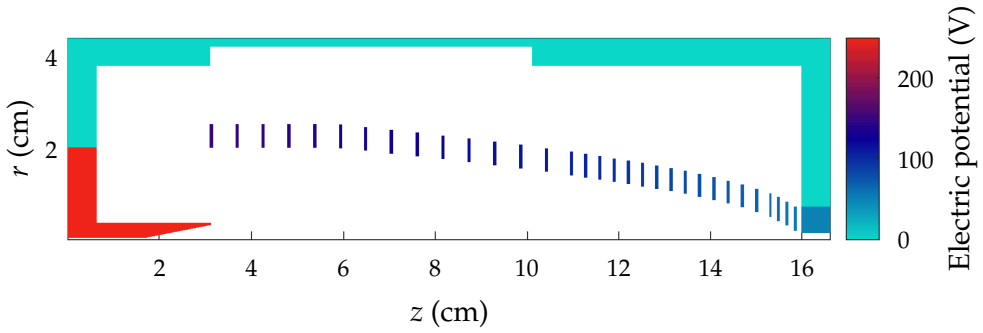

FIGURE 4.12: Electric DC potential set in the ion funnel - evolution of the design.

the ions when they arrive in the vicinity of the edges of the electrodes.

4.4.4 Results for the ion funnel - evolution of the design

DC-field

The computation of the electric fields for the tentative evolution of the design is very similar to the one performed for the traditional design. The main difference is a smaller number of electrodes and a non-uniform spacing between the electrodes, which plays a role in the DC-field. The values set for the potential are listed in table 4.2 and the distribution of the potential of the different objects is presented in figure 4.12. In this case, again, the last electrode, from an electric point of view, remains enclosed within the casing at the outlet of the funnel. Similarly, the potential of the capillary encompasses a part of the wall to represent the holder of the capillary. All other walls are set to the ground, chosen as 0 V.

The results in the free space are presented in figure 4.13. The potential difference between two consecutive electrodes for the DC-field remains constant but the different spacing means that the field in the axial direction is not as uniform as the one created in the traditional design. This builds different levels of forces driving the ions towards the outlet of the funnel, while these forces are mostly uniform in the traditional design. Especially, in the vicinity of the outlet, the spacing between the electrodes is smaller. This means that the force towards the end of the cavity is greater there than earlier in the trajectory of the ions. This effect is expected. This area is indeed the one where the competition between the axial and radial driving forces is critical to limit the losses of ions. A larger axial displacement may help to avoid that the ions move too fast towards the electrodes by following the gas flow. It

FIGURE 4.13: Electric DC potential in the free field and direction of the electric DC-field in the ion funnel - evolution of the design. The length of the arrows is constant over the entire domain, only their direction refers to the electric field. Only the area around the funnel cavity is represented.

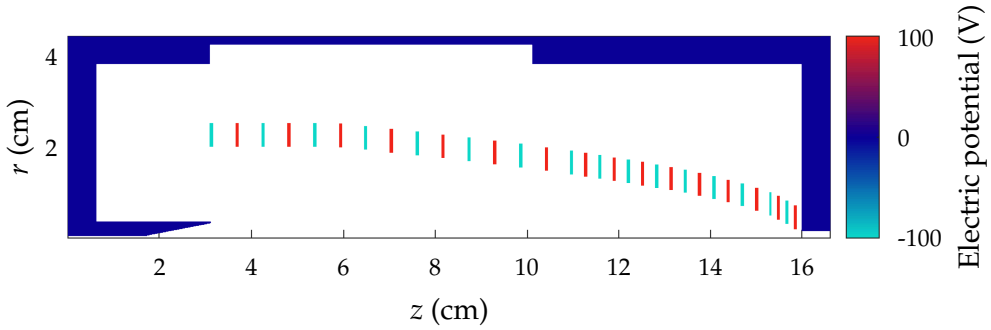

FIGURE 4.14: Electric RF potential set in the ion funnel with an amplitude of 100 V - evolution of the design.

remains difficult though to isolate the effects of the DC field compared to the much stronger ones induced by the RF-field, which are presented now.

RF-Field

The RF-fields (instantaneous and effective) are computed in a similar way as for the traditional design. The electric potential set in the different objects present in the computational domain is displayed in figure 4.14. The resulting field amplitude $\vec{E}_0$ used for the time-dependent computation and the gradient of its scalar product $\nabla\left(\vec{E}_0 \cdot \vec{E}_0\right)$ are considered and presented in figures 4.15 and 4.16. Here again, the different spacing at different stages in the funnel implies that the effects are stronger at its end. This can be well observed in the magnitude of the instantaneous field (figure 4.15). It is significantly higher between the last four electrodes than between the previous ones, which indicates that the effects of such a field are expected to be stronger in this area. The effective field confirms this tendency. Between the first electrodes, where the spacing is maximal, high magnitudes are observed only around the tips of the electrodes and not in between. We could thus expect that the trajectory of ions passing between such electrodes would be only slightly affected by the RF electric effects. It creates a more effective barrier in the entire space between the less distant electrodes at the end of the cavity.

Given the shape of the gas flow presented in section 3.4.4, one can expect, however, that the trajectories of the ions remain relatively close to the symmetry axis. It is thus not necessarily negative to favor higher electrical forces in the area where the ions should effectively be concentrated. It remains to show, however, under which conditions the usual amplitudes of the RF-field are sufficient to counter the drive by the gas flow and whether such values are realistic.

Furthermore, the trapping effect described in the traditional design is present again, especially around the last few electrodes. The steeper slope of the cavity, at the end of the funnel, helps to reduce the area potentially concerned by the trapping effects but does not fully eliminate it. A direct comparison of both designs is presented in figure 4.17. It shows that the basis of the effective potential $\nabla\left(\vec{E}_0 \cdot \vec{E}_0\right)$ forms deeper wells in the axial direction with the classic design than the studied evolution. This unwanted feature is thus limited, as fewer ions can be trapped in such areas during their trajectory. Here again, this does not state, however, whether the

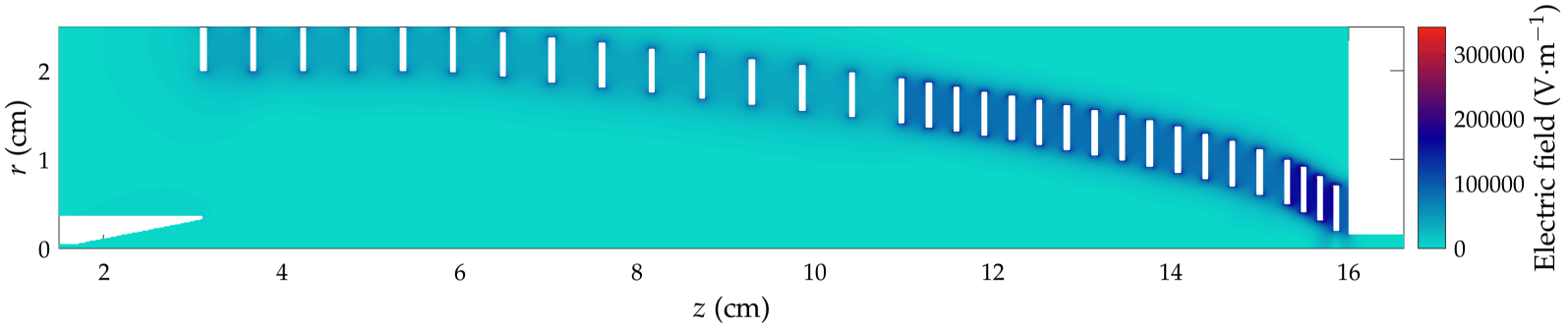

FIGURE 4.15: Magnitude of the instantaneous electric RF field $\vec{E}_0$ with an amplitude of 100 V - evolution of the design. Only the area around the funnel cavity is represented.

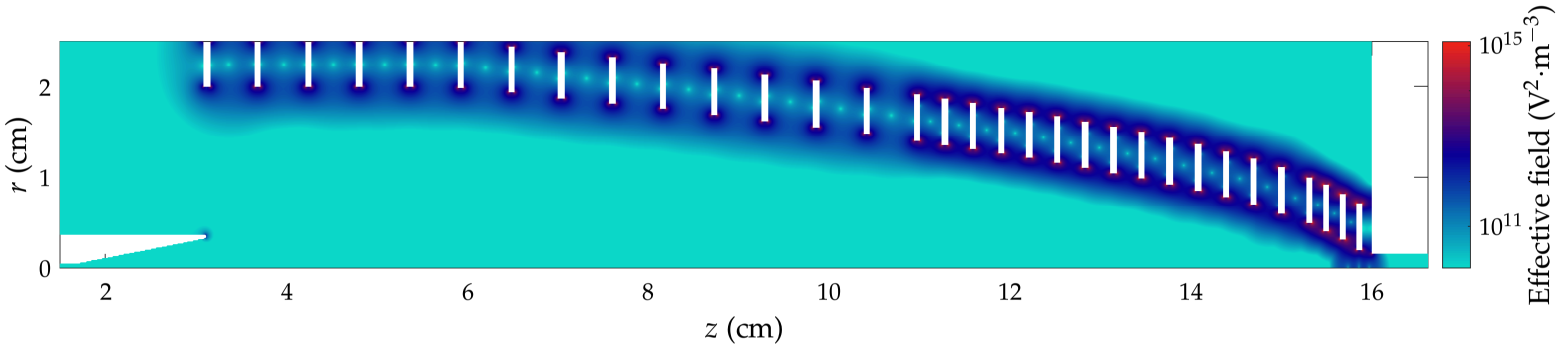

FIGURE 4.16: Magnitude of the basis of the effective electric RF-field $\nabla\left(\vec{E}_0 \cdot \vec{E}_0\right)$ with an amplitude of 100 V - evolution of the design. Only the area around the funnel cavity is represented and a logarithmic scale of the amplitude is used.

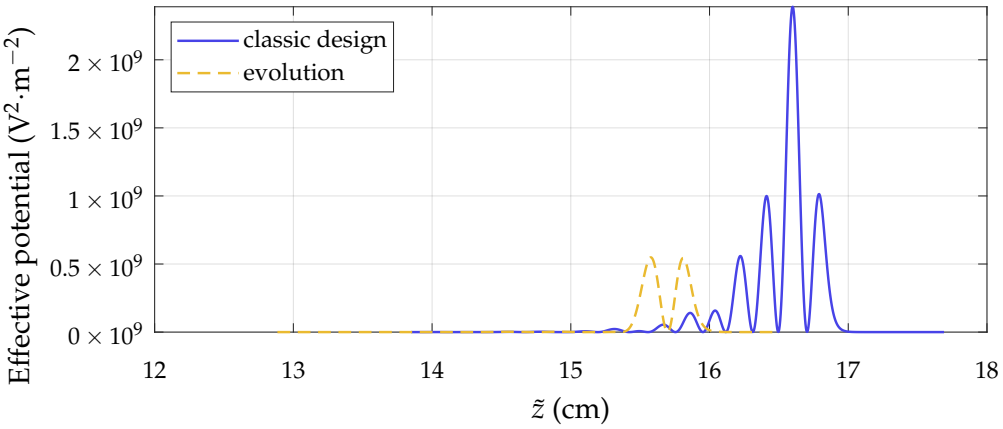

FIGURE 4.17: Shape of the basis of the effective potential along the centerline of the cavity, comparing the results for both designs. The axial coordinate z is re-scaled into $\tilde{z}$ to be zero at the right wall of the first pumping chamber (at the end of the funnel.)

correlated radial effects are strong enough to guide the ions towards the following chamber.

Chapter 5

Trajectory of the ions

In the previous chapters, we have described the tools and data necessary to perform the simulation. Three configurations have been presented in section 2.1: the capillary, a conventional ion funnel, and a tentative evolution of the ion funnel design. The motion of the ions is simulated according to the model described in section 2.2. The gas flow has been simulated using the Navier-Stokes equation listed in chapter 3. Different programs have been used to produce data for the capillary (see 3.2 and 3.3) and the ion funnels (see 3.4). In all cases, the space charge effects described in section 4.1.2 are considered, taking into account the interaction between the ions due to their electric charge. For the ion funnels, one additionally considers the external electric fields created by the electrodes placed in the domain, as exposed in section 4.2. Using these results, the trajectory of a representative set of particles can be computed and the results are presented in the following section.

5.1 Laminar capillary

We first present the results of particle simulations within the capillary. These results have been published in Bernier et al. (2020). Several parameters were considered. Following the results of the gas flow, the geometry (length and diameter) of the capillary varies. We also took into account the thermal conditions at the wall. In addition, we studied the influence of the species involved as well as their quantity.

In all cases, we only consider the straight part of the capillary, thus excluding the funnel-shaped inlet. The simulated ions are introduced at the beginning of this domain and distributed over the cross-section of the pipe. The ions are not all created in the same cross-section, to avoid the formation of sliced clusters, but scattered in the axial direction over a span roughly representing their transport during one time step. The desolvation process of the droplets created during the ionization process is neither simulated nor considered. This can be seen as the assumption that all droplets were vaporized before the end of the capillary inlet, only letting gaseous ions enter the pipe. This is an approximation as it is commonly assumed that some droplets make their way through parts of the capillary, heating being assumed to help to increase the vaporization rate. The goal of the simulations presented in this section is however to show the influence of different parameters regarding the transmission of the ions. Adding a complex phenomenon such as desolvation would not strongly change the results presented, in our understanding, while adding new parameters in the system which are not easily defined, such as the proper mechanism to produce the gas phase ions.

Two different ions distribution over the cross-section of the capillary are considered. First, a normal distribution centered on the axis of the capillary. Its standard

deviation σ can vary and has been chosen as dependent on the radius of the capillary: $\sigma = 5 \cdot 10^{-2} R_{\text{cap}}$. This choice was made to approximate experimental values presented in Bernier et al. (2018). Second, a homogeneous distribution where the newly created ions are evenly distributed over the entire cross-section. The former tries to mimic the effects of the funnel-shaped inlet collimating the ions towards the axis of the capillary. The latter is however a limit case. While in traditional setups, the charge is assumed to be spread over the entire cross-section of the straight capillary, a homogeneous distribution remains unrealistic. We thus consider the second distribution as an extreme comparison, the conventional case being likely to lie between the two presented here. Unless for section 5.1.3, we use rhodamine B (mass $m = 479.02\,\text{Da}$, number of electric charges $z = 1$) as test species to refer to experiments presented in Bernier et al. (2018).

5.1.1 General behavior and thermal conditions

In a nutshell, two different displacements of the ions can be considered, related to two different causes. The axial displacement is the main one, permitting the transmission of the ions into the following chamber. It is mainly caused by the gas, the ions following the flow. The radial displacement is also important, as it is directly related to the losses when the ions hit the walls, in the model considered here. In this direction, no significant gas flow occurs, as can be seen from the streamlines in figure 3.4 for an exemplary flow. The space-charge driven velocity is mainly responsible for this radial displacement. This can be qualitatively observed in figure 5.1, where the expansion of the initial ion distribution visible at the beginning of the straight part of the capillary is mainly caused by the electric forces.

Estimations and simple model

One can develop a simple estimation based on this model. We consider a cloud of ions set at the beginning of the pipe, located within a radius r_0, which expands while being transported downstream, reaching exactly the capillary radius R_{cap} at its outlet. The length of the capillary is denoted by L_{cap}. This set of ions at the inlet thus represents the transmitted ions. In the cases where losses occur, we assume the lost ions are initially located at radial positions larger than r_0 and hit the wall before reaching the outlet. They surround the inner ions and do not influence their expansion. We thus first assume that all ions are transmitted to simplify the demonstration.

At any position along the pipe, we call $\tilde{r}$ the radius delimiting the transmitted and lost ions sets. At any position, the inequality $r_0 < \tilde{r} < R_{\text{cap}}$ holds. We further assume that the axial displacement of the ions can be averaged over the cross-section of the pipe and along the pipe. We call the velocity of the ions in this direction u_{av}. The transmitted current I_{trans} represents the charge transported by the ions located in the cross-section of radius $\tilde{r}$ at any axial position and one can write

$$I_{\text{trans}} = Q u_{\text{av}}\,, \tag{5.1}$$

where Q is the charge density per unit length, or the electric charge contained in an infinitesimally thin slice of the domain and within the radius $\tilde{r}$. Given the assumption made that all ions considered here are transmitted, I_{trans} and thus Q remain constant along the capillary. This quantity can also be used to estimate the electric field $\vec{E}$ created by the charges contained within this slice. We assume that the electric

field has the following form:

$$\vec{E} = E_r\,(r,z)\,\vec{e}_r\,, \tag{5.2}$$

This means that the electric field has only a component in the radial direction. This is a rough approximation as the expansion should induce components in the axial direction which we neglect here. According to Gauss's law (see equation 4.44), the divergence of the electric field can be related to the charge density:

$$\nabla \cdot \vec{E} = \frac{\rho_\mathrm{C}}{\varepsilon_0}\,, \tag{5.3}$$

where ε_0 is the permittivity of vacuum and ρ_C the electric charge density. The latter can be expressed using charge density per unit length Q and the radius of the slice $\tilde{r}$ for positions within $\tilde{r}$:

$$\rho_\mathrm{C} = \frac{Q}{\pi\tilde{r}^2}\,. \tag{5.4}$$

It equals zero otherwise. The divergence of the electric field can be expressed in cylindrical coordinates. Given the form 5.2, only the radial derivative is to be considered and it follows:

$$\nabla \cdot \vec{E} = \frac{1}{r}\frac{\partial r E_r\,(z)}{\partial r} = \begin{cases} \frac{Q}{\pi\tilde{r}^2\varepsilon_0}, & \text{for } 0 \le r \le \tilde{r} \\ 0, & \text{for } \tilde{r} < r \end{cases} \tag{5.5}$$

We consider the solution of this differential equation, assuming that the electric field is finite for $r = 0$ and converges to zero far away from the capillary. It reads:

$$E_r = E = \begin{cases} \frac{Qr}{2\pi\tilde{r}^2\varepsilon_0}, & \text{for } 0 \le r \le \tilde{r} \\ \frac{Q}{2\pi r\varepsilon_0}, & \text{for } \tilde{r} < r \end{cases} \tag{5.6}$$

The velocity of the ions in the radial direction u_drift can be estimated by multiplying the mobility K with the local electric field: $u_\mathrm{drift} = KE$. For $r = \tilde{r}$, this velocity can be identified as the expansion rate of the ion cloud, which is the time derivative of the radius $\tilde{r}$:

$$\frac{\mathrm{d}\tilde{r}}{\mathrm{d}t} = \frac{KQ}{2\pi\tilde{r}\varepsilon_0} = \frac{KI_\mathrm{trans}}{2\pi\tilde{r}\varepsilon_0 u_\mathrm{av}}\,. \tag{5.7}$$

The resulting differential equation can be integrated between the inlet ($t = 0$ and $\tilde{r} = r_0$) and the outlet ($t = T = \frac{L_\mathrm{cap}}{u_\mathrm{av}}$ and $\tilde{r} = R_\mathrm{cap}$):

$$\frac{1}{2}\left(R_\mathrm{cap}^2 - r_0^2\right) = \frac{KI_\mathrm{trans}L_\mathrm{cap}}{2\pi\varepsilon_0 u_\mathrm{av}^2}\,. \tag{5.8}$$

From this expression, one can see that the transmitted current varies depending on the radius of the initial ion cloud r_0^2. A maximum can be reached for the hypothetical case $r_0 = 0$, which corresponds to an infinite charge density in the inlet. While simplified in comparison to the simulations presented hereafter, this model allows some predictions:

- the transmitted current is linearly dependent (up to a constant offset) on R_cap^2, i.e. on the cross-section area of the capillary;
- the transmitted current is inversely proportional (up to a constant offset) to the length of the capillary, assuming that the average velocity u_av remains constant;

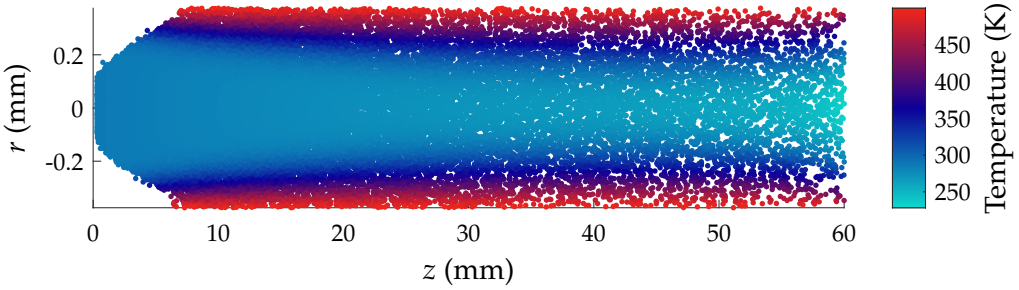

FIGURE 5.1: Exemplary distribution of ions in a capillary with a normal distribution. The current there is 60 nA and the color of the position represents the local temperature of the surrounding gas. The temperature of the wall is 500 K. Radial and axial dimensions of the figure are not to scale.

- a slower flow induces a lower transmitted current.

This model can be extended to a flat distribution. In such a case, a homogeneous distribution of ions fills the entire cross-section of the inlet. We denote δ the transmission ratio, defined as the transmitted part of the incoming current I_{in}. For a flat distribution, this is simply represented as the ratio of the area of the transmitted ions cloud considered at the inlet (that is within r_0) to the entire cross-section of the capillary. It follows:

$$\delta = \frac{I_{\text{trans}}}{I_{\text{in}}} = \frac{r_0^2}{R_{\text{cap}}^2} \,. \tag{5.9}$$

Replacing this last expression using equation 5.8, one can express the transmission ratio as follows:

$$\delta = 1 - \frac{K I_{\text{trans}} L_{\text{cap}}}{\pi \varepsilon_0 u_{\text{av}}^2 R_{\text{cap}}^2} \,, \tag{5.10}$$

or with I_{in} as a variable instead of I_{trans}:

$$\delta = \left(1 - \frac{K I_{\text{in}} L_{\text{cap}}}{\pi \varepsilon_0 u_{\text{av}}^2 R_{\text{cap}}^2} \right)^{-1} \,. \tag{5.11}$$

The last two expressions can appear counter-intuitive at first. They indeed predict that the maximal transmission ratio is reached for zero incoming (or transmitted) current. This is however coherent with the picture of the losses developed here. The higher the incoming current, the higher the space charge effects. As a consequence, high losses follow, leading to a smaller transmission ratio. On the other hand, when the incoming current is very small, the space charge effects are almost negligible and unitary transmission can occur. The predictions developed here can now be confronted with the results of the simulations performed with the capillary.

Thermal conditions

Figures 5.1 and 5.2 present snapshots of the positions of the particles during their transfer, for a normal and a flat initial distribution, respectively. Both initial currents are different, 60 nA for the normal distribution and 2.5 µA for the flat distribution, to reach a similar transmitted current of about 12.5 nA. The position of the ions is represented with the local gas temperature, reproducing the picture presented for

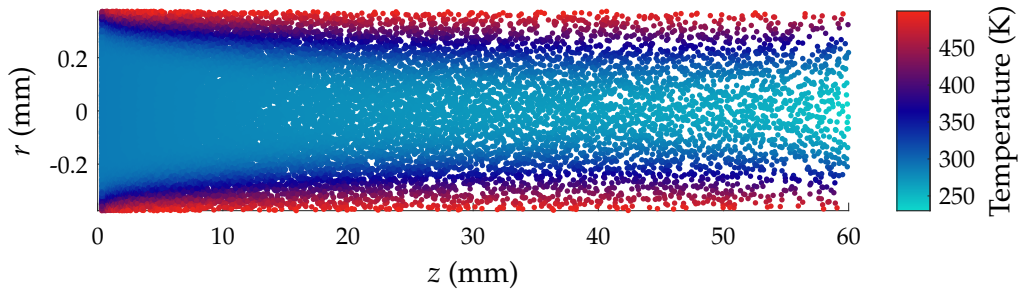

FIGURE 5.2: Exemplary distribution of ions in a capillary with a flat distribution in the inlet. The current there is 2.5 µA and the color of the position represents the local temperature of the surrounding gas. The temperature of the wall is 500 K. Radial and axial dimensions of the figure are not to scale.

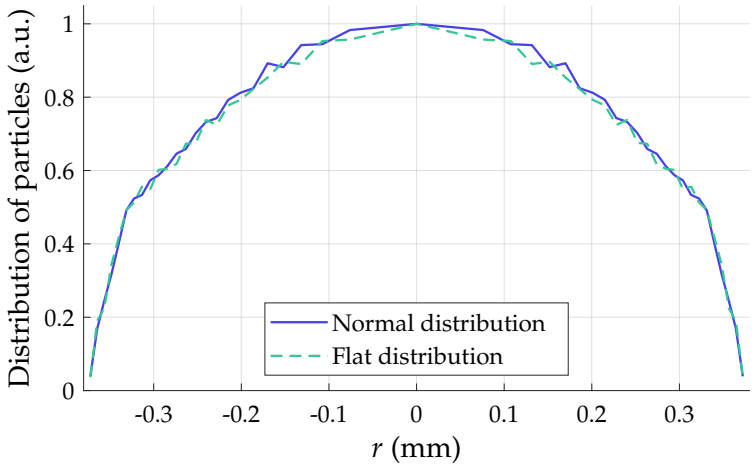

FIGURE 5.3: Distribution of the transmitted ions at the outlet of a capillary, for a normal and flat distribution of ions inserted at the inlet (same cases as for figures 5.1 and 5.2, respectively). The distribution is given in arbitrary units, normalized to 1 at the center of the pipe.

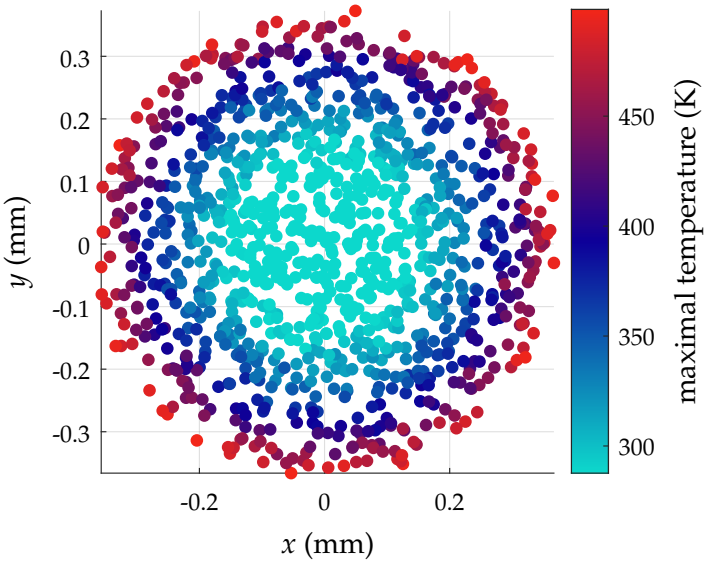

FIGURE 5.4: Maximal temperature of the surrounding gas encountered by the ions during their flight through the capillary, from their introduction in the inlet until transmission at the end of the capillary. It represents the same case as in figure 5.1.

the gas flow in section 3.2. From this global picture, a distribution of the transmitted ions at the outlet of the capillary can be inferred, see figure 5.3. No significant difference appears between both initial conditions. The transmitted ions are distributed over the entire section of the outlet, with higher concentrations close to the axis. For larger diameters, one can observe a wider plateau shaped in the central area. Closer to the walls, where the losses occur, a steep decrease of the concentration is observed and it reaches almost zero. This is amplified by the fact that not only the interaction between the ions but also the Brownian motion participates in the losses at this point. In the central area, the stochastic movements only shift the position, without altering the global distribution.

From this picture, one can further infer the thermal conditions the ions undergo during their transfer through the capillary. We have already stated that this is an important factor as thermal energy can induce molecular transformations of the ions, such as fragmentation, unfolding, or declustering. While not modeled in this work, one can gain a first insight into this phenomenon by looking at the highest temperature the ions experience. The geometry of the pipe and especially its diameter is here of great importance. As we showed in the study of the gas flow, heating is only effective within a layer close to the walls, roughly independent from the diameter of the pipe. This means that for the thinner capillary, where the diameter is small enough for the high temperatures to reach the core of the gas flow, all ions experience similar thermal conditions throughout the transfer. However, for larger diameters, as considered here, a strong stratification of the gas temperature is observed. This leads to a strong difference in the thermal conditions the ions undergo during their transfer.

This phenomenon is represented in figure 5.4. It represents the highest temperature the ions experienced over their trajectory. It is clear that the ions getting out of the capillary close to the wall experience the highest temperature. But it also shows that a priori only very few ions, if any, experience high temperatures and

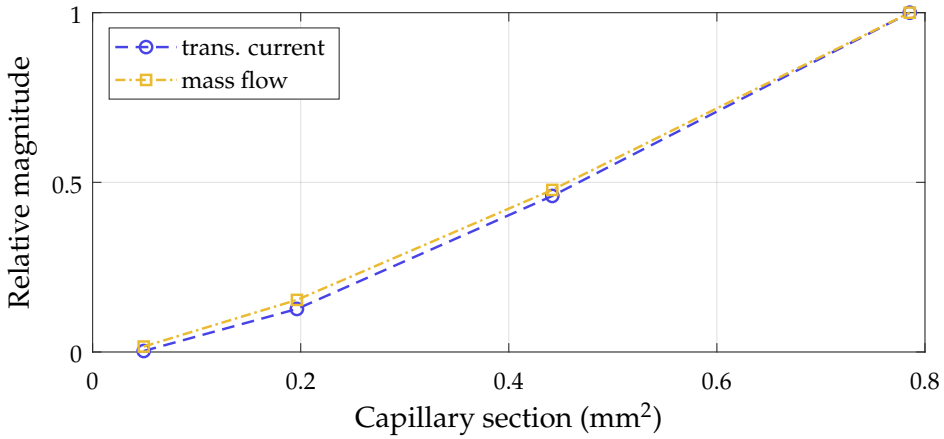

FIGURE 5.5: Evolution of the transmitted current for capillaries of different diameters (0.25 mm, 0.50 mm, 0.75 mm and 1.00 mm) and the corresponding mass flow. Both quantities are normalized to ones computed for the largest capillary diameter. In all cases, the temperature of the capillary wall is 500 K with a length of 6.0 cm. The current is the maximum transmitted through the capillaries for the given conditions.

return to the central part of the flow. This builds up a strong stratification within the transferred ions. The highest temperature encountered by the ions transmitted in the central area is the temperature at the inlet of the capillary. Along their path, the gas temperature monotonously decreases. The ions transmitted in the peripheral area experience, in contrast, a temperature close to the wall temperature. As a consequence, if transformations of the ions occur, a spatial localization can likely be observed at the outlet. The ions transmitted in the central area might have been preserved, while the ones transmitted close to the walls are likelier to have transformed. In cases where ions of large dimensions should be transferred intact in the next chambers, e.g. in native mass spectrometry, this could be used to select the transmitted ions, using for instance a skimmer to exclude the outermost ions.

This also confirms the conclusion drawn from the gas flow. The heating of the capillary, when intended to accelerate the desolvation process of the droplets created during the ionization, is less efficient for wider capillaries, where the inner flow remains cold. In such a case, it is of great importance to only let droplets with a short lifetime enter the capillary, i.e. droplets of smaller size.

5.1.2 Influence of the geometry and heating

Geometry

The influence of the geometry of the capillary is considered with two parameters: the length of the capillary and its diameter. First considering the diameter, its influence varies mostly with the quantity of gas that is transmitted through it. The maximal transmitted current for different diameters is presented in figure 5.5, along with the transmitted mass flow, where the results are normalized with the values from the widest capillary. It appears that both quantity are strongly correlated. Furthermore, both are roughly scaling with the cross-section of the capillary, which is related to the chocked state of the flow. In a traditional Hagen-Poiseuille flow, the

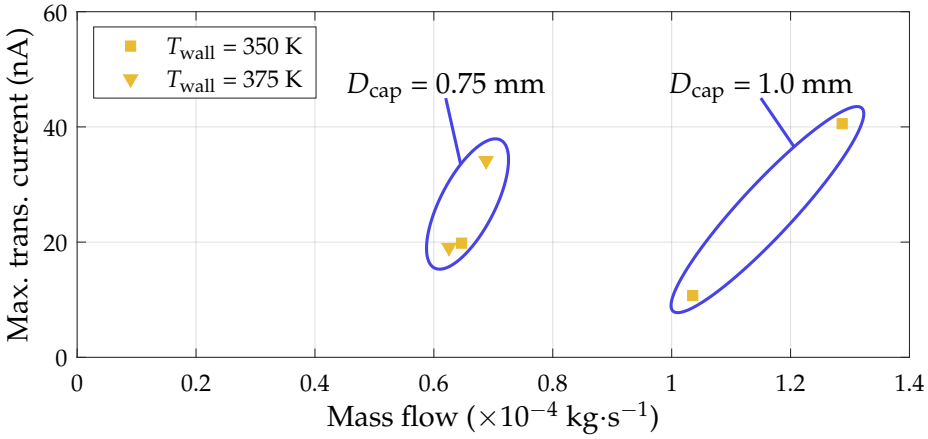

FIGURE 5.6: Evolution of the transmitted current for capillaries of different lengths. Two different sets of simulations are presented, representing two diameters (0.75 mm and 1.00 mm), and two different lengths for each diameter. The results are presented with respect to the air mass flow through the capillary.

mass flow $\dot{m}$ is related to the square of the cross-section A (see e.g. Schlichting and Gersten (2017, p. 117)):

$$\dot{m} = \frac{A^2 \Delta p}{8\pi\mu L}, \tag{5.12}$$

with Δp the pressure difference between both ends of the pipe, μ the viscosity, and L the length of the pipe. However, this equation only holds for small pressure differences. This is not the case for the flows presented here, where chocking occurs. The dependency of the transmitted current with the area is however coherent with the simplified model presented in 5.1.1 as can be seen in equation 5.8.

The variation of the length of the capillary is also essential in the transmission of the ions. Looking at the results in figure 5.6, one can see that for a longer capillary, the decrease in the transmitted current is much higher than the decrease in the flow rate. The latter can again be explained by the chocked state of the flow. It is ruled by two factors: the cross-section the gas is flowing through and the maximal velocity reached at the end of the pipe. Both elements remain constant when the length varies, leading to relatively similar gas flows. However, small changes still occur. This is due to friction's effects taking greater importance when the length of the capillary increases. The boundary layer gets thicker with increasing length, theoretically up to a parabolic profile, meaning that the effective cross-section discussed in section 3.2 reduces with the length, causing a slight diminution of the quantity of gas transmitted.

The stronger decrease of the transmitted current is related to the longer travel time of the ions within the capillary. As a consequence, the expansion due to space charge effects occurs during a longer period. To schematize the behavior, the initial distribution of ions keeps expanding towards the walls, while being transported towards the outlet by the underlying gas flow. This means that the longer the pipe is and thus the journey through the capillary, the farther the ions drift towards the wall until they get lost.

These results show that the transmitted current is strongly affected by the geometry of the capillary. Maximization of the transmission requires the widest and

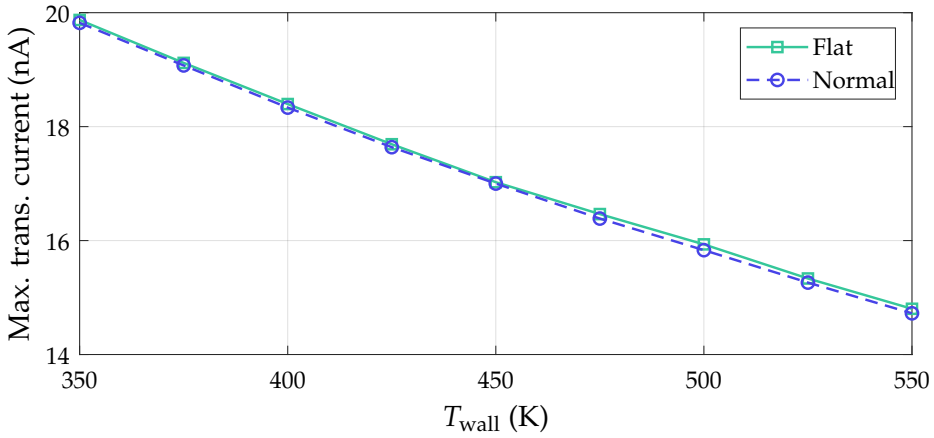

FIGURE 5.7: Evolution of the maximal transmitted current for capillaries with different wall temperatures. All cases are simulated for a 0.75 mm wide and 6.0 cm long capillary. Results are presented for a normal and flat distribution of the ions in the inlet area.

shortest possible geometry. This has already been predicted by the simple model previously developed and summarized in equation 5.8. A trade-off is necessary though, as a wide capillary let enter more gas in the next chamber, and should be compensated by a powerful pump. Long and thin pipes also reduce the transmission but might enhance the desolvation process, allowing the production of a larger quantity of gas-phase ions. This is however also related to the heating of the flow, which has an intrinsic influence on the transmission as well.

Heating and effects of the initial distribution

Heating marginally modifies the gas flow through the pipe. One can observe in figure 3.3 that lower wall temperatures lead to higher axial velocity. This means that the ions transported by the gas spend more time within the capillary and thus drift closer to the walls, yielding higher losses. The higher temperature also induces higher mobility values, enhancing the motion causing losses. This explains the results presented in figure 5.7 where the maximal transmitted current through the same capillary slightly decreases when the wall temperature increases. This result is also coherent with experimental results presented in Bernier et al. (2018). Furthermore, the maximal transmission is similar for both tested initial distribution over the inlet cross-section, normal or flat. This implies that the mechanism behind this maximum is independent of the distribution of the ions. This phenomenon, called space-charge limit, illustrates the saturation of the capillary due to high electric charge densities contained within the relatively small domain of the capillary.

As we have already argued, the losses are mainly due to repulsive electric forces pushing the ions towards the walls. For relatively small charge densities and a normal distribution centered on the capillary axis, theses forces are not strong enough to cause any loss, as can be seen in figure 5.8 for the lowest incoming currents. Unitary transmission can be reached in such conditions. Slightly increasing the current and thus the initial charge density induces a stronger drift towards the walls and losses appear. This phenomenon explains why the transmission ratio decreases while the transmitted current still increases. At a certain point though, the stronger space

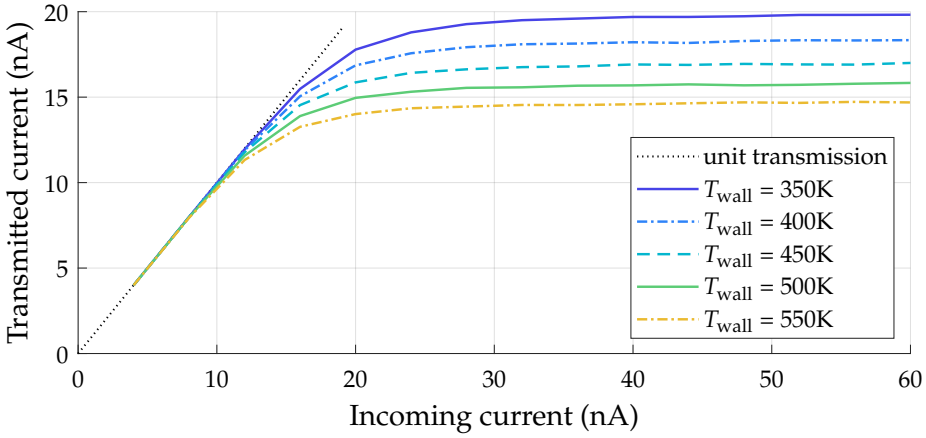

FIGURE 5.8: Evolution of the transmitted current for capillaries with different wall temperatures. All cases are simulated for a 0.75 mm wide and 6.0 cm long capillary. Results are presented for a normal distribution of the ions in the inlet area. Results are compared with a unitary transmission represented by a dashed line.

charge effects due to a higher charge density at the inlet increase the lost current in the same proportion than the increase in the incoming current, leading to the observed saturation.

In the case of a flat distribution at the inlet, the evolution is slightly different. Losses are observed even for very low incoming currents. This can be explained by the fact that ions are introduced very close to the wall. As a consequence, the probability of losses, even close to the inlet, is intrinsically higher than for the normal distribution. Furthermore, the ions introduced close to the wall are barely transported by the flow, as the velocity magnitude is close to zero. This creates an accumulation of ions and thus leads to stronger space charge effects in this area, facilitating the losses. This phenomenon is not very realistic and shows that the flat distribution should be considered as a limit case to be compared with the normal distribution but not as describing physical operating conditions. It also explains why the saturation due to space charge effects is reached for much higher currents with the flat distribution ($\approx 2\,\mu A$) than with the normal one($\approx 50\,nA$).

The rationale behind the transmission in the case of a flat distribution can further be explained using the estimation of the transmission ratio derived in equation 5.10 and 5.11. Setting r_0 to zero in equation 5.8, one can also express the maximal transmitted current as:

$$I_{max} = \frac{\pi \varepsilon_0 u_{av}^2 R_{cap}^2}{2KL_{cap}}. \tag{5.13}$$

The transmission ratio thus becomes:

$$\delta = 1 - \frac{I_{trans}}{I_{max}}. \tag{5.14}$$

This dependency is represented for the simulations performed in figure 5.9. It shows that the predicted linear dependency is well reproduced. However, the resulting slope falls short of crossing one for incoming current approaching zero. This is understood as the consequence of the simplification of a constant axial velocity over the cross-section. It thus neglects the previously described accumulation in the inlet

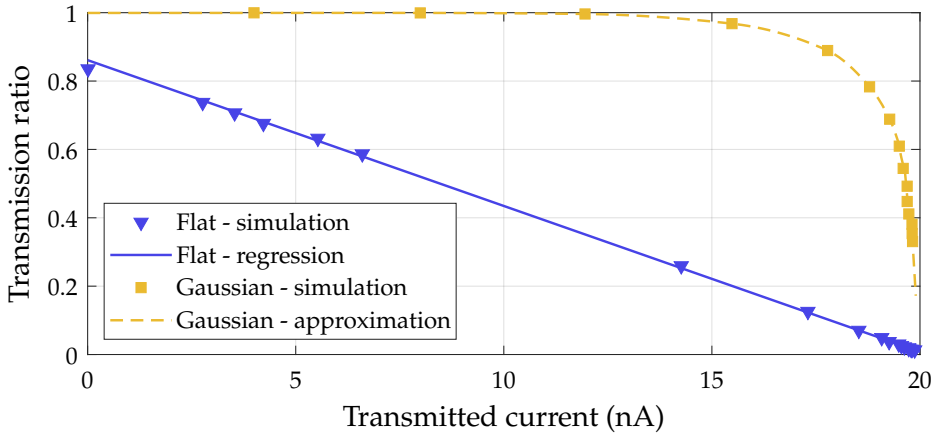

FIGURE 5.9: Transmission ratio represented with respect to the transmitted current for a normal and flat initial distribution of the ions. All simulations are computed for a capillary with 0.75 mm diameter and 6.0 cm length. In all cases, the wall temperature is set to 350 K.

and caused by the non-slip boundary conditions enforced at the walls. Nevertheless, the difference is significant when compared with the results of the normal distribution. Such measurements, relatively easy to realize in a device, could deliver some information regarding the distribution of ions at the inlet of the capillary. This also shows that a concentration of the ion distribution around the axis of the capillary is important to improve efficiency of the transmission compared to more diffused distributions, even if the maximal transmitted current remains the same in all cases.

5.1.3 Mix of species

So far, we concentrated our investigation on a single species, rhodamine B. However, in a realistic scenario, several species are produced during the ionization process and we thus further focus on results involving different kinds of ions, having different masses, charge state, and reduced mobility. This aspect is interesting because some experimental results tend to show that the transmission ratio might depend on the involved species. This was reported by Page et al. (2009), where the study of inlet capillaries of different lengths shows a transmission bias correlated with the mobility of the species involved.

This effect is quantified using the enhancement factor F_e defined in the paper mentioned before. It compares the transmitted signal of a species in the mix for different capillary length, considering the same incoming current. It is specifically computed as the ratio between the transmitted intensity of a short capillary and the transmitted intensity of a long capillary as measured by a mass spectrometer. This is here interpreted as the ratio of the transmitted currents: $F_e = \frac{I_{\text{trans,short cap}}}{I_{\text{trans,long cap}}}$. We have already mentioned that a shorter capillary leads to higher transmission ratios. Therefore, this enhancement factor is larger than one. It varies depending on the species though and it is higher for species most affected by the increase of the length. The experimental study showed that the species with the highest reduced mobility present the highest enhancement factor.

Species	F_e for normal distribution	F_e for flat distribution	Reduced mobility ($cm^2\ V^{-1}\ s^{-1}$)	m/z
bradykinin 3^+	2.018	1.908	1.352	354.3
neurotensin 3^+	1.840	1.810	1.207	558.5
fibrinopeptide A 2^+	1.602	1.776	1.033	769.0

TABLE 5.1: Enhancement factors computed as the ratio of the transmitted current in the short capillary (length of 3.8 cm) towards the long capillary (6.0 cm). The diameter is 0.75 mm in all cases. The incoming current is 60 nA for the normal distribution and 2.5 µA for the flat one. The reduced mobility is for a N_2 buffer gas as reported in Page et al. (2009) but used here in the air for qualitative results.

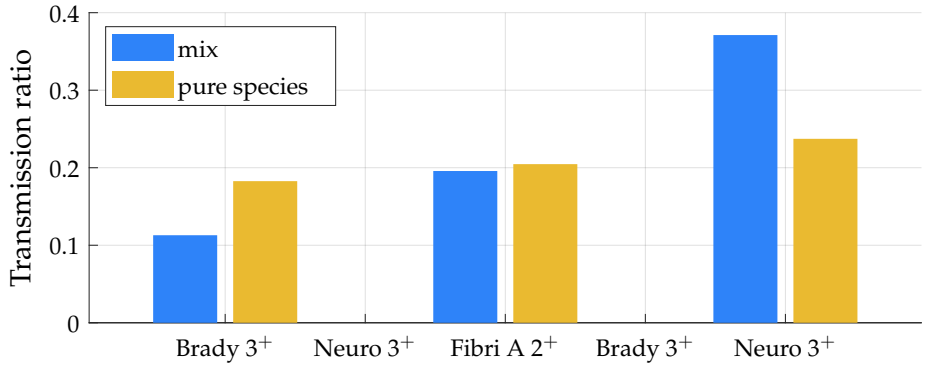

FIGURE 5.10: Comparison of the transmission ratio of different species considered, either within a mix or alone. All simulations are performed for a 0.75 mm wide and 6.0 cm long capillary with a wall temperature of 500 K. The ions are inserted in the domain with a normal distribution.

The relative importance of the different effects involved is complex to define and we use simulations to get a better understanding of this phenomenon. The mix consists of three different species already considered in Page et al. (2009): bradykinin 3^+, neurotensin 3^+, and fibrinopeptide A 2^+. Their respective parameters, along with the enhancement factors are presented in table 5.1. It appears that the correlation found between reduced mobility and enhancement factor experimentally found is correctly reproduced in the simulations. No quantitative comparison can be performed though for two different reasons. First, the exact composition of the mix entering the capillary in the experiment depends on many factors that are hard to measure. It is thus not known and cannot be reproduced in the simulations. Second, the enhancement factor computed in the experiment uses the signal of the mass spectrometer, that is further downstream in the device. The experimental values might thus be affected by other biases caused in other stages located between the capillary outlet and the chamber where the mass spectrum is measured which are hard to quantify. In spite of these quantitative uncertainties, the results of the simulation further show that once again, the distribution at the inlet does not affect the tendency. The ions with larger mobility present higher enhancement factors in both cases tested.

While this picture confirms the measurements, we need further simulations to understand some of the processes involved in the bias in transmission. We especially

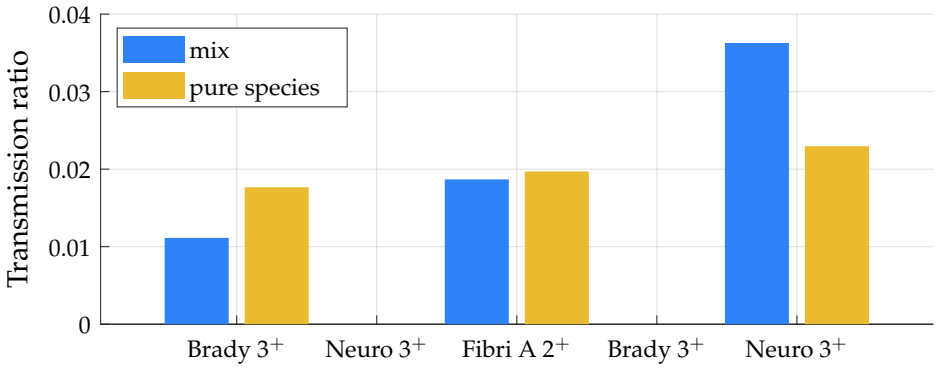

FIGURE 5.11: Comparison of the transmission ratio of different species considered, either within a mix or alone. All simulations are performed for a 0.75 mm wide and 6.0 cm long capillary with a wall temperature of 500 K. The ions are inserted in the domain with a flat distribution.

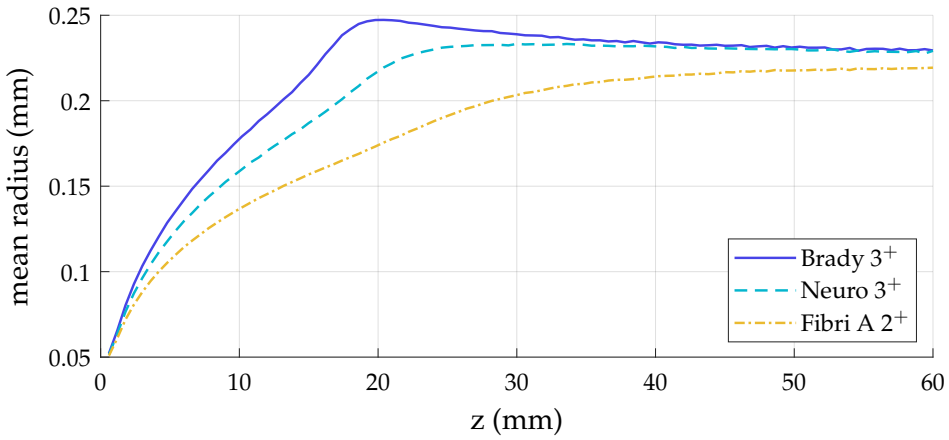

FIGURE 5.12: Mean radial position of the ions along the capillary depending on the species. The results are presented for a 0.75 mm wide and 6.0 cm long capillary with a wall temperature of 500 K and a normal initial distribution of the ions.

compare the transmission ratio of a species in a mix and the corresponding ratio for the species considered alone. The results are presented in figures 5.10 and 5.11, again for the two initial distributions considered. In both cases, the transmission ratio of the species with the highest mobility (bradykinin) is lower in the mix compared to the species alone, while the inverse is true for the species with the smallest mobility (fibrinopeptide). This difference can be explained when considering the mean radius of the ions discriminated by species along the capillary, as depicted for the normal distribution in figure 5.12. One can see that the mean radius of the species with large mobility increases more rapidly, leading to higher losses, while the species with the smaller mobility remains closer to the axis, enhancing its transmission. The same considerations for the flat distribution do not deliver clear cut results when considering the entire set of ions. The transmission ratio being much smaller, the large majority of particles considered is indeed lost. However, the same picture arises by limiting the scope to the ions located close to the axis at the inlet, which are likely to be transmitted.

This phenomenon can be interpreted as follows. From the initial distribution, the ion of the species with the highest mobility, while submitted to the same electric field, are drifted farther away towards the walls. This leads to the difference in the mean radius already observed. The fact that the difference in the mean radius is more pronounced close to the inlet is also coherent with this explanation. Indeed, the charge density and following the space charge effects are larger in the first parts of the capillary. They progressively decrease along the pipe because of the expansion that occurs. The difference in the radial velocity is thus more pronounced at the beginning of the travel of the ions. For symmetry reasons, the ions located farther from the axis of the capillary experience larger electric forces. This difference in the radial distribution of the species leads the ions with the largest mobility to experience larger radial forces and thus are likelier to get lost. As a consequence, the relative concentrations of the different species found at the outlet of the capillary and in the subsequent stages of the device do not represent the concentrations of the initial sample anymore. This transmission bias is further increased for longer capillaries, as shown by the values of the enhancement factor because the selective losses occur during a longer period.

Quantitative comparisons of intensities measured by a mass spectrometer should thus be considered carefully. They indeed may not represent the proportions of the different species present in the sample analyzed. To minimize this error, one should tend to keep the capillary as short as possible. Here again, a trade-off between the importance of this bias and other effects such as desolvation is necessary.

5.2 Ion funnel - classic design

Following the results of the transmission of ions through the capillary, we simulated the trajectory in the ion funnel. We used a classic design as presented in section 2.1.2. The results presented here were computed independently from the previous simulations. The final part of the capillary is part of the domain considered, but we do not simulate the transport of ions within it. The ion beam is created by introducing ions at the end of the capillary. The distribution of the new ions uses the third distribution described in section 2.3.3. It intends to reproduce a typical distribution that can be found in this section and presented in figure 5.3.

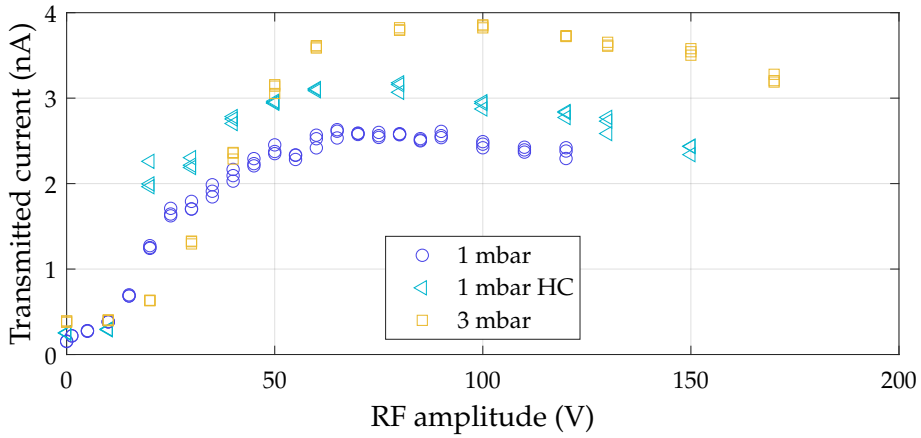

FIGURE 5.13: Transmitted current measured in the chamber following the ion funnel. Three measurements are given for each set of parameters. The results are provided for the two concentrations of the analyte and a background pressure of 1 mbar (the case with a higher concentration is denoted with HC) as well as for a background pressure of 3 mbar.

The two different flow fields presented in section 3.4.3, representing different pressure levels, are considered for the fluid part. The space charge effects and the external electric field presented in section 4.4.3 are also taken into account.

Experimental results have been measured by Paul Fremdling, from the University of Oxford, at the facility of the Max Planck Institute in Stuttgart. The geometry used in the simulations tends to reproduce this device and the pressure levels in the gas flow simulations have been chosen in accordance. These experiments will guide the interpretation of the simulation's results to determine how good the model presented in this work can reproduce the behavior of a typical ion funnel.

5.2.1 Experimental reference

In order to define a clear framework for the simulation, we first analyze the results of the experimental measurements performed on the existing device. Rhodamine B is considered as test species throughout the experiments. Different series of results are presented, where the following parameters vary:

- the amplitude of the RF-fields;
- the background pressure in the funnel;
- the concentration of the test ions in the sample.

In each case, the following parameters can be measured:

- the electric current issued from the ESI emitter, characterizing the sprayed charges;
- the electric current measured at the capillary, representing the losses through the capillary;
- the electric current coming in the chamber located after the ion funnel, representing the ion beam that would be further transported in the mass spectrometer.

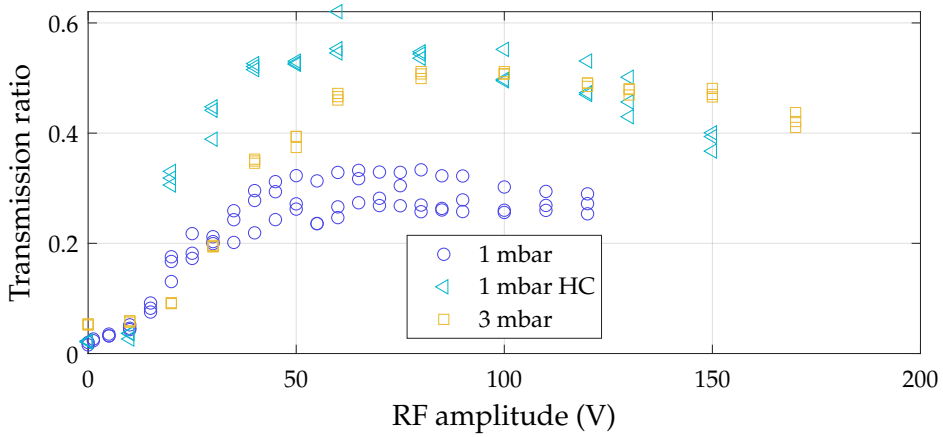

FIGURE 5.14: Transmission ratio measured between the capillary and the chamber following the ion funnel. Three measurements are given for each set of parameter. The results are provided for the two concentrations of analyte and a background pressure of 1 mbar (the case with a higher concentration is denoted with HC) as well as for a background pressure of 3 mbar.

The latter is the transmitted current, directly measured shortly after the ion funnel. The difference between the other currents delivers values for the current entering the ion funnel from the capillary. It is thus possible to directly compute the transmission ratio from these three measurements.

Three different cases are considered: a concentration of $1 \times 10^{-5}\,\mathrm{mol \cdot L^{-1}}$ of rhodamine B in the sprayed solution at two different pressure levels: 1 mbar and 3 mbar; and a higher concentration of $1 \times 10^{-4}\,\mathrm{mol \cdot L^{-1}}$ in combination with the lower presser level of 1 mbar. In all cases, the amplitude of the RF field varies between 0 V and at least 120 V. The results of the transmitted currents and transmission ratios are presented in figures 5.13 and 5.14. Each point represented is an average of 300 measurements.

Different behaviors are remarkable. First, the transmission strongly depends on the amplitude of the RF-field. With zero amplitude, that is when the DC-Feld is considered as the only external electric field, a very small amount of ions reach the next chamber. With increasing amplitudes of the RF-field, a steep increase of the transmitted current can be observed. This clearly shows the effect of the ion funnel and the force created by the alternating electric field that retains the ions inside the cavity. In all cases, the transmitted current reaches a maximum when the amplitude is further increased. For higher amplitudes of the RF-field, the transmitted current presents a decrease but remains significant in the range of amplitudes considered. The other parameters, pressure level and concentration of the analyte in the sprayed solution, do not strongly modify this behavior. Only the number of charges measured and the amplitudes for which the different trends are observed differ. Especially, higher pressure in the chamber leads to a slight shift of high transmission towards higher amplitudes of the RF-field: at about 60 V for a background pressure of 1 mbar and about 80 V for 3 mbar. Furthermore, in the case of a higher concentration of the species, the transmitted current is slightly higher than with the lower concentration. Most remarkable, though, is that the transmission ratio also strongly increases.

In the experimental data set presented here, the measured values can strongly

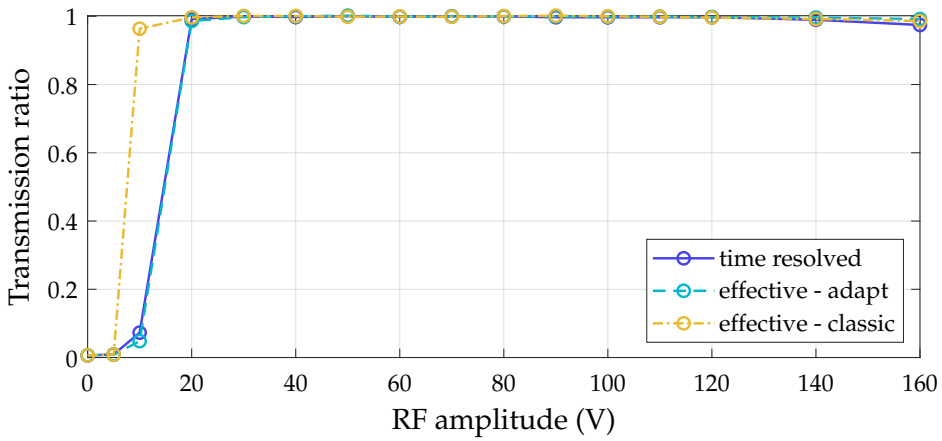

FIGURE 5.15: Transmission ratio computed from the simulation with rhodamine B and a current of about 5 nA issued form the capillary, comparing the different implementations of the RF electric field.

vary between different experiments. Especially, the behavior of the emitter seems to be very sensitive to parameters not fully controlled. In some cases, this leads to noticeable changes during a single series of measurements. We thus try in the following to focus on global trends rather than quantitatively reproduce the profiles presented here.

5.2.2 Influence of the RF electric field and its implementation

To compare the results of the simulation with the experimental ones, we first consider the lower pressure level of 1 mbar and consider the influence of the radio-frequency electric field. We have presented several implementations of these effects in section 4.2.2:

- the direct computation of the alternating electric field, time-resolved;
- the effective electric field as developed in the classic model, assuming that the ions are transported in a vacuum;
- the effective electric field taking into account the presence of the underlying gas flow.

All three options are presented to compare the results and the influence of the implementation chosen.

General results

The transmission ratio for the different implementations over a reasonable span of amplitudes of the alternating electric field is presented in figure 5.15. The first element to consider here is that in the three cases, the RF electric field shows its ability to limit the losses. While almost no transmission is observed when only the DC-field is present, the transmission ratio rapidly increases with the amplitude of the RF-field and reaches values very close to 1, that is total transmission, for amplitude values starting with 20 V, both for the time-resolved field and for the adapted effective field. In the case of the traditional effective field, as derived in the classic

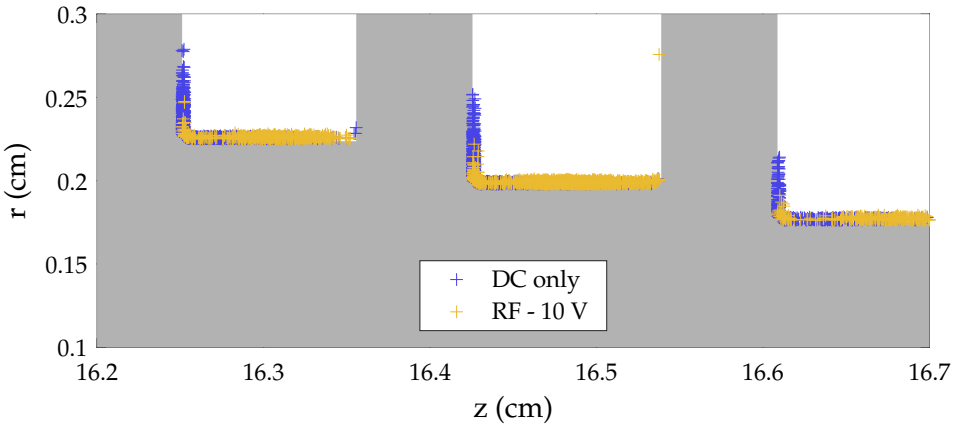

FIGURE 5.16: Location of the losses at the tips of electrodes, without RF-field and with a weak one (amplitude of 10 V), time-resolved. The shape of the electrodes is depicted in the background.

model, the transmission is very high with an amplitude of only 10 V. This illustrates well the expected effects of the alternating electric field. It creates an effective force towards the center of the cavity and thus reduces the number of ions lost due to the gas flow between the electrodes. This can be seen comparing the location of the losses between simulations without RF-field and with an RF-field at moderate amplitude, to still allow some losses. In the first case, the losses are located at the tip of the electrodes and at their sides, whereas in the second case the losses are much more concentrated at the tip, as can be seen in figure 5.16. The losses at the sides of the electrodes are a clear sign that ions follow the gas flow between the electrodes. However, the DC-field pushes the ions towards the surfaces of the electrodes until they are lost. Such losses are far less abundant when the RF-filed is switched on. This indicates that the ions do not enter the space between two electrodes, illustrating the force created by the alternating field to keep them within the cavity formed by the funnel.

Furthermore, differences between the implementations can be observed. The implementation resolving over time the alternation of the polarity of the electrodes, as well as the adapted effective field, show a later increase of the transmission ratio with increasing values of the RF-field amplitude when compared to the classic implementation of the effective field. This can be interpreted as the fact that the gas present in the chamber weakens the effects of the electric force created by the RF-field. Indeed, the main difference between the two implementations of the effective field is the consideration of the underlying gas. This tends to show that this single modification allows for a better description, taking as reference the time-resolved implementation, which does not make any assumption a priori on the effects of such field.

However, some limitations apply to all models and especially to the time-resolved one. The influence of the gas flow, as described in equation 2.5, relies on the hypothesis that the interactions between the gas molecules and the ions occur often enough. The effect described is thus a statistical behavior. One can estimate the number of collisions of the air molecules on a surface equivalent to the collision cross-section A_{CCS} of rhodamine B in nitrogen, to fix the idea. This surface can be estimated to $3.97 \times 10^{-18}\,\mathrm{m}^2$. Following Bird, Stewart, and Lightfoot (2001, p. 23)

the average collision rate per unit area, Z, can also be estimated to:

$$Z = \frac{\rho A_{\mathrm{CCS}}}{2}\sqrt{\frac{2k_{\mathrm{B}}\mathcal{N}_{\mathrm{A}}^{3}T}{\pi M_{\mathrm{air}}^{3}}}, \tag{5.15}$$

with ρ and T the local density and temperature, respectively, k_{B} the Boltzmann constant, $\mathcal{N}_{\mathrm{A}}$ the Avogadro constant, and M_{air} the equivalent molar mass of air. For a density of $1 \times 10^{-3}\,\mathrm{kg \cdot m^{-3}}$ and a temperature of 300 K, which are values close to the ones found at the end of the ion funnel, it delivers a collision rate of $9.66 \times 10^{6}\,\mathrm{s^{-1}}$. This means that during a period of the RF-field, one can expect roughly 10 collisions between rhodamine B ions and air molecules. This is rather low but shows one of the limits of the approach chosen here. However, the effects of the gas flow also depend on the particle response time, which is in such conditions rather large. Under the same conditions, it is estimated at $5.6 \times 10^{-7}\,\mathrm{s}$, which is slightly more than half of the period. Thus, the model does not strongly enforce the velocity of the gas flow and in the regions where the electric fields are strong, it is likely to be dominant. Nevertheless, these estimations show that the model used is again pushed at its limits and should not be extended to regions where the underlying gas is even more rarefied, as both the fluid dynamics and the trajectory of the ions would not be properly simulated. In such cases, a Direct Simulation Monte Carlo method encompassing both the air molecules and the ions would be more suited.

As previously mentioned, the effective fields are only valid for specific domains for which the assumptions made to derive the new form are valid. For the classic form of the effective field, a semi-empirical criterion can be defined. It is called the adiabaticity parameter and shall remain below the threshold of 0.3 to ensure that the results remain satisfactory. In all cases considered here, for the largest amplitude (120 V) and for rhodamine B, the maximum value reached in the domain is below 0.02. We can thus assume that the results provided with the effective field are still within the domain of validity. The adapted form of the effective field relies on the same assumptions as the classic form. Thus, a similar condition is expected. However, this does not take into account the influence of the gas flow, which has also been approximated with the assumption of a smooth transition within the oscillations of the ions. The threshold of 0.3 may thus be over estimated in this case. Nevertheless, the flow fields are not less smooth than the electric fields, especially in vicinity of the electrode edges, such that we do not expect the condition for the adapted effective field to strongly differ. The time-resolved field does not present such restrictions, as no specific assumption is made regarding its influence on the trajectory of the ions. As such, all formulations of the electric forces may deliver acceptable results over the range of amplitudes of the RF-field considered here.

In the cases where almost total transmission is reported, that is for high amplitudes of the RF-field, the distribution of the particles within the cavity of the funnel highlights the presence of specific structures. This is related to the so-called trapping effect. A closer look at this phenomenon is proposed in the next section.

Study of the trapping behavior of the alternating field

The trapping effect of the RF-field is a well-known phenomenon of the ion funnel. It has already been presented in a publication by Shaffer et al. (1999), a couple of years after the first presentation of the ion funnel. We mentioned it when describing the effective potential, represented along the symmetry axis of the chamber in figure 4.10. It appears where the inner radius of the electrodes becomes relatively

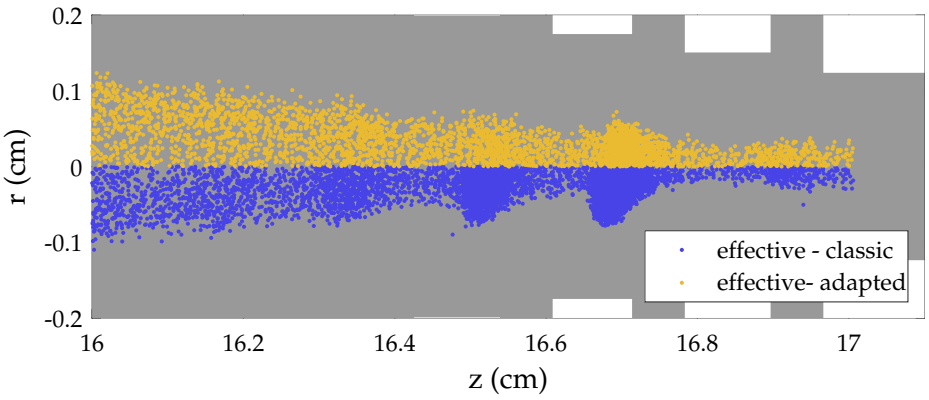

FIGURE 5.17: Position of the particles in the domain, with trapping effect. Results computed with both versions of the effective RF-field, The shape of the electrodes is depicted in the background.

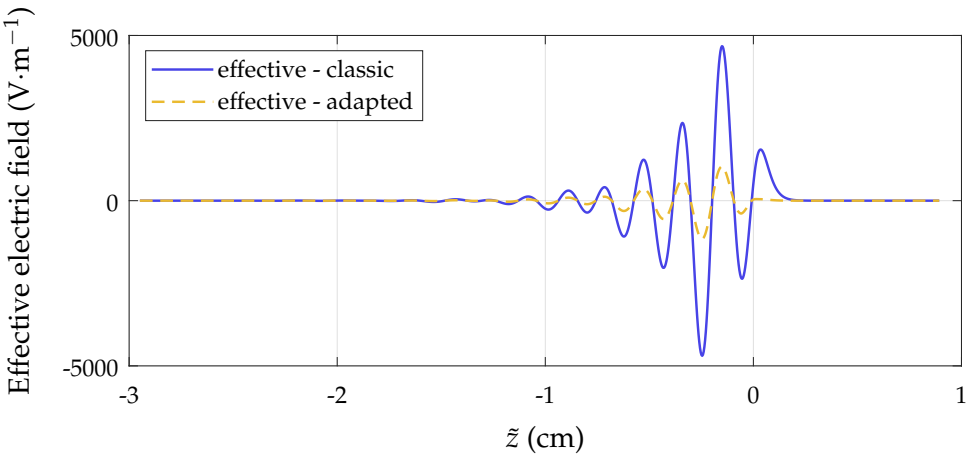

FIGURE 5.18: Effective electric field along the axis of the system in the axial direction. The two implementations of the effective field are compared for the example of rhodamine B and the computed gas flow. The axial position is shifted to be zero at the end of the chamber (beginning of the transition area.)

small, in the order of magnitude of the distance between the electrodes. This is because the average radio-frequency effects span in the radial direction in the vicinity of the electrodes' tip. For sufficiently large inner radii, the effects are almost absent of the center of the cavity, where the gas flow and the DC-field, as well as the space charge effects, are largely responsible for the motion of the ions. However, when the inner diameter of the electrodes becomes too small, the RF effects reach the center of the cavity. This creates a potential well, where the ions accumulate as long as the other effects are not strong enough to counter it.

This happens when the number of ions becomes high enough so that space charge effects allow the ions to leave the potential well. This situation can be observed in figure 5.17, where the results are computed with both versions of the effective RF-field. Here again, the time-resolved implementation (not represented) and the adapted effective field deliver very similar results. In the center of the cavity, shortly before the transmission into the next chamber, accumulations of ions occur. Both versions of the effective RF-field show similar behaviors. However, the adapted version, where the gas flow is taken into account, shows smaller accumulations areas. This can be well understood by the fact that the correction brought to the classic model weakens the magnitude of the force applied to the ions, as already observed in the transmission ratio. This can also be seen in the profiles of the effective field in the axial direction in figure 5.18. Lower space charge effects are thus able to counter the effects of the adapted RF-field. Nevertheless, the radial effects of the RF-field remain strong enough to further guide the ions toward the end of the cavity and into the next chamber, so that total transmission is simulated.

This subject has been extensively described in Kelly et al. (2010). It especially shows that the dimensions of the last electrode of the funnel play a significant role. Reasoning in terms of an estimation of the effective potential, they could derive a relation for the depth of the potential well close to the axis compared to the maximal potential, reached close to the tip of the electrodes. This relation could show that doubling the inner diameter of the last electrode in the original design could reduce the depth of the potential well by a factor larger than 10. Another major factor is the spacing between two successive electrodes. The smaller this distance, the less critical the formation of the potential wells. It indeed increases the force magnitude close to the tip of the electrodes for a given amplitude and thus enhances the overall effects of the RF-field while avoiding the critical case of the spacing being similar to the inner diameter of the electrodes.

Comparison with the experimental results

Several differences can be pointed out in comparison with the experimental data. First, the transmission ratio of the simulations, which reaches unity, lies significantly higher than the experimental one, reaching a maximum of about 60 % with the high concentration of the analyte. A hypothesis can be drawn regarding this difference. The currents measured in the experiment register all charges. The emitter produces charged droplets and not directly gas-phase ions. However, the simulations only consider gas-phase ions. This means that if the desolvation process is not completed for some droplets, they may still be counted in the current entering the ion funnel while presenting a different behavior than the ions computed here. This could affect the transmission ratio considered in the experiments and lead to an underestimation, compared to the one reported in the simulations. The available data set does not allow us to conclude about these points though and further detailed experiments

would be necessary to establish precisely which current enters the ion funnel and whether this can lead to unitary transmission.

Second, it can be observed that the increase of the transmission with the amplitude of the RF-field occurs in the simulation for smaller amplitudes than in the experiments. With an amplitude of 20 V, the unitary transmission is reached in the simulation, while the maximum transmission is observed in the experiment for about 60 V. An explanation can be proposed for this difference. In the simulation, the transmission is counted directly at the end of the cavity formed by the ion funnel. In contrast, the transmitted current is measured in the experiments well within the next chamber. Between both chambers lies a pinhole which presents similarities to the capillary considered before. Its length is shorter (about 1 mm), but it still presents an enclosed cylindrical form through which the ions need to travel.

As already mentioned, the effect of the RF-field is to guide the ions towards the symmetry axis of the domain. The higher the amplitude of the field is, the stronger this collimation. In the transition between the chambers, the external electric fields are supposedly reduced and an expansion similar to the one described in the simulations of the capillary can occur. As a consequence, when the amplitude of the RF-field is too small, some ions enter the transition area very close to the walls and can lead to significant losses.

This phenomenon was reproduced with an amplitude of 20 V. When considering the ions as transmitted 2 mm further in the transition area, the transmission ratio significantly decreases from 99 % to 68 %. A similar issue was dealt with in a work by Mayer and Borsdorf (2016), where the shape of the transition zone between the ion funnel and the following vacuum chamber varied. Three configurations are considered: a capillary (straight pipe), a pinhole (diverging shape), and a nozzle (converging/diverging shape). A significant effect on the transmission was simulated, the latter option showing significantly higher transmission than the other ones. While not all parameters are comparable to the present ones (the ion funnel operates at atmospheric pressure, which is not the case in the present work), it emphasizes the importance of the transition between the ion funnel and the following chamber to reach high efficiency in the transmission of ions.

Third, no significant decrease in the transmission can be observed in the simulation for higher values of the amplitude of the RF-field. While the simulations seem to indicate a slight reduction of the transmission ratio for an amplitude of 160 V, especially for the time-resolved field, this is not to the same extent as experimentally measured. This indicates that the simulations may omit to consider a parameter that plays a significant role in the experiment. Here again, a hypothesis can be formulated regarding this difference. The analyte, rhodamine B, is sprayed from a solution of water and ethanol. It is thus possible that solvent molecules are ionized alongside the analyte, thus being potentially transferred through the ion funnel. As these ions are significantly lighter than the analyte, their behavior within the funnel is different. Furthermore, their ratio mass to charge is too low to be detected by mass spectrometry in the device used for the experiments. While further experiments are programmed to determine whether these ion species, or further ones, are effectively present after the ion funnel alongside rhodamine B, simulations where conducted to determine the influence on the global transmission ratio.

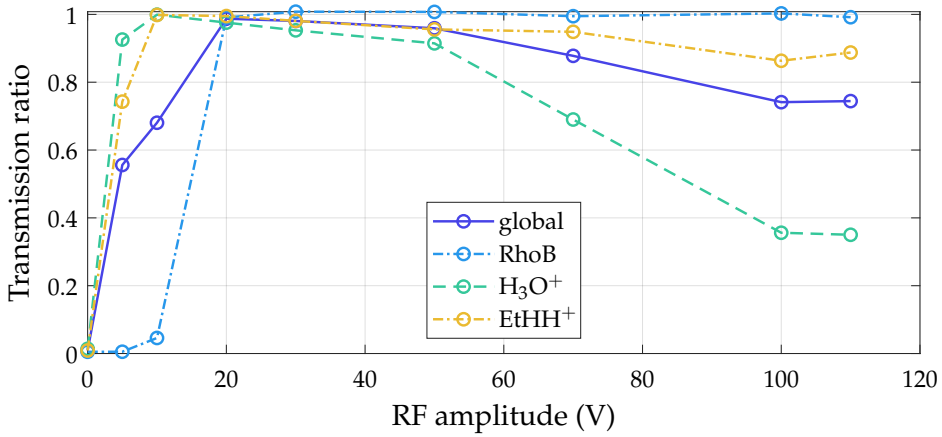

FIGURE 5.19: Transmission ratio computed from the simulation considering a stoechiometric mix of rhodamine B, hydronium and ethyloxonium ions. The current issued from the capillary is about 5 nA and the RF field is resolved in time.

5.2.3 Consideration of ionized solvent molecules

To estimate whether the involvement of ionized solvent molecules can reproduce a decrease of the transmission for relatively high amplitudes of the RF-field, simulations involving a mix of three species are considered. It contains in stoichiometric quantities rhodamine B, hydronium (H_3O^+), and ethyloxonium ($C_2H_7O^+$) ions. The relative quantity does not intend to reproduce a realistic mix but rather to introduce the three species and observe their behavior with similar statistical properties. The results are presented in figure 5.19.

It shows that these lighter ions lead to a lower transmission ratio when the amplitude of the RF-field reaches values larger than about 50 V. This hypothesis is thus compatible with the experimental results and would mean that at least part of the decrease in the measured transmission ratio could be attributed to unexpected species. The explanation for the losses of lighter ions with comparably lower amplitudes can be attributed to larger mobility values. This means that when the variations of the electric field occur, the oscillations induced in the trajectory of the ions are larger when the mobility is larger. Furthermore, considering larger amplitudes of the RF-field implies that the force experienced by the ions also gets larger. These oscillations can be a source of losses, as they can lead the ions to hit the electrodes present in the domain. As a consequence, the lighter ions, which for the same RF-field show larger oscillations, are lost for smaller amplitudes than rhodamine B in this case.

Nevertheless, these simulations cannot properly show to what extent this hypothesis is responsible for the transmission profile measured in the experiments. Especially, it is not confirmed whether the solvent molecules are present in the ion beam, let alone in quantities significant enough to explain the drop in transmission. Also, the lighter ions seem to be more easily transmitted for lower amplitudes of the RF-field and thus also affecting this part of the characteristic. Further measurements are programmed, which could qualitatively show whether hydronium and ethyloxonium ions are present after the ion funnel and thus whether this hypothesis can be confirmed.

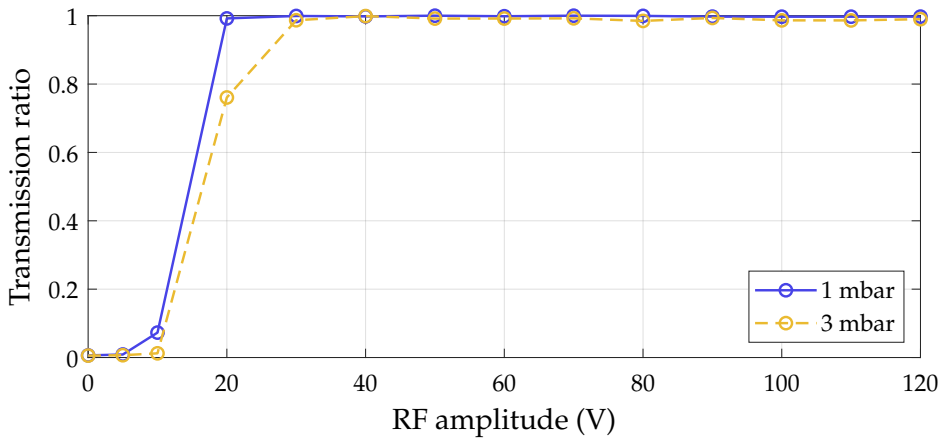

FIGURE 5.20: Transmission ratio of rhodamine B depending on the amplitude of the RF-field for two different pressure levels. The current issued from the capillary is about 5 nA and the RF field is resolved in time.

5.2.4 Influence of the pressure level

Similar simulations have been conducted with the other gas flow results computed for a background pressure of 3 mbar, however only with the time-resolved RF-field A comparison of the transmission ratio with the two different pressure levels, the other parameters being the same, is presented in figure 5.20. In both cases, the behavior is very similar. The transmission ratio starts to rise for a high enough amplitude of the RF-field and reaches then soon afterward almost total transmission. This happens for the lower pressure level with an amplitude of 20 V and for the higher pressure level with 30 V. This slight difference shows that proper functioning of the ion funnel shifts toward higher amplitudes of the RF-field when the pressure of the underlying gas flow increases.

This difference is not only due to the modification of the flow fields. Indeed, the higher pressure level induces a modification of the local mobility of the ions and thus a different response to the RF electric field. Especially, the temperature between both cases can be roughly considered as similar, independently from the pressure level. This means that mobility values, according to equation 2.7, become smaller for higher pressure levels. In such conditions, the effects of the RF-field are attenuated and a larger amplitude is needed to counter the effects of the gas flow.

The experiments performed in Stuttgart confirm this tendency, as reported in figure 5.13. A significant increase of the transmitted current with a pressure of 1 mbar is measured in the experiment for an amplitude of 20 V. For a pressure of 3 mbar, an amplitude of 40 V is necessary to reach this threshold. Nevertheless, and for both cases, this does not mean that the maximal transmission is reached for such small amplitudes. This effect, as already mentioned, can be attributed, at least partly, to the losses occurring in the transition zone between the chamber where the ion funnel is located and the chamber where the current is measured. This dependency is not unexpected and has already been reported during the initial characterization of the concept of ion funnel. Especially, characteristics, based either on the current measured at the final electrode of the device or in the following octopole, were reported in Shaffer et al. (1998) and Shaffer et al. (1999). Both publications show that higher amplitudes of the RF-field are required to reach maximal transmission.

5.2.5 Summary

Following the presented results, several aspects of the simulations can be analyzed in further detail. Globally, the typical behavior of an ion funnel could be reproduced. In the absence of RF-field, only a very small transmission of the ion beam is simulated. Increasing the amplitude of this field, however, strongly limits the losses that occur within the ion funnel and a significantly higher transmission can be observed. The impact of the pressure level within the ion funnel can also be relatively well reproduced. However, some aspects of the transmission remain to be improved in the simulations.

First, the transmission in the absence of RF-field is significantly lower in the simulations than the experimental measurements. No obvious reason appears for this difference, though. Especially, the simulated current, considered at the end of the ion funnel, does not take into account the transition into the next chamber, where the experimental values are taken. This difference should even lead to a lower transmitted current predicted by the simulation than reported here. Several potential explanations can be put forward. Given the limitations of the flow simulations that we have already exposed in section 3.4.3, some differences between the fields considered for the simulation and the reality may explain a difference in the behavior of the ions. This hypothesis could also be supported by the fact that several simplifications were made to compute the gas flow, besides the limitations of the model used. For example, the device is not strictly axially symmetric. Furthermore, the pressure level measured in the experiments is also a local value, that may not exactly match the pressure level considered in the simulation. Moreover, it cannot be excluded that some differences may exist between the electric fields considered in the simulation and the one experienced by the ions. The geometry considered in the simulation reproduces relatively accurately the ion funnel of the experiment. Nevertheless, some boundary conditions or potentials could remain approximations. This especially applies to the DC-field, which plays a significant role when no RF-field is considered. However, it is expected that the electric fields are more accurate than the flow fields, as fewer assumptions are needed. In both cases, it is yet difficult to foresee which influence these differences would have on the behavior of the ions and whether this can explain the lower transmission that is recorded.

The decrease of the transmission for high amplitudes of the RF-field could not be reproduced to the same extent as in the experiments. While no definitive explanation for this can be proposed so far, this could be related to the presence of other species than the expected one. Indeed, lighter ions with larger reduced mobility values may experience losses for lower amplitudes than rhodamine B and thus be responsible for the lower measured transmission in such operating conditions. Their presence could also explain a slightly higher current measured in the absence of Rf-field, as the force induced by the DC-field would be stronger for these lighter species. This hypothesis remains to be tested with further experiments.

Regarding the implementation of the RF-field, the present results seem to indicate that the adaptation of the effective RF-field to take into account the presence of the gas is an improvement compared to the classic form. The former indeed delivers results consistently similar to the ones obtained when considering the time-resolved field. The only difference observed is for very high amplitudes, where the losses seem slightly higher with the time-resolved field than with the effective one. This adapted effective field could thus allow us to perform simulations with larger time steps and potentially reduce the computing time. However, both effective fields can only deliver physical results when the hypotheses made to derive them are fulfilled.

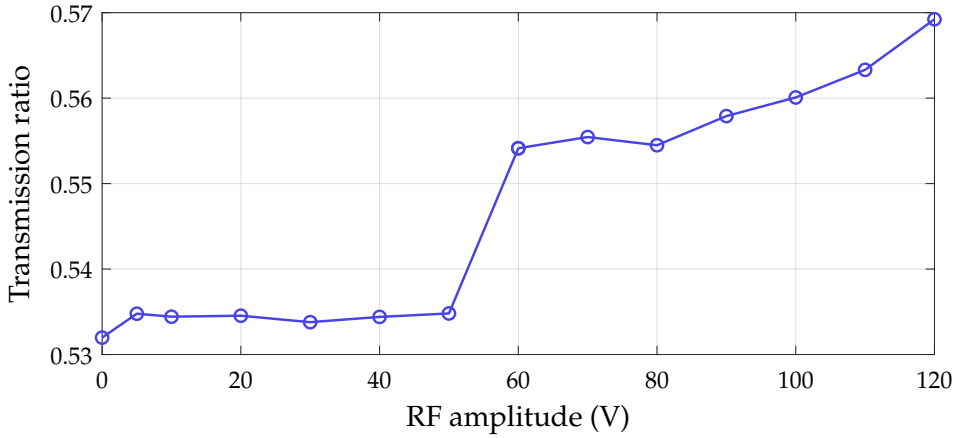

FIGURE 5.21: Transmission ratio of rhodamine B depending on the amplitude of the RF-field with the evolution of the design. The current issued from the capillary is about 5 nA and the adapted effective RF-field is used.

This means that the oscillations of the fields around the effective trajectory should be small enough, such that the surrounding parameters vary smoothly. In the case of very large amplitudes of the RF-field, this is certainly not the case anymore, even if a specific threshold remains difficult to define.

5.3 Ion funnel - evolution of the design

We also conducted simulations involving ions in the ion funnel with the evolution of the design presented in section 2.1.3. This design does not exist so that no comparison with experimental data can be shown. Nevertheless, these simulations show what can happen and whether an improvement of the transmission can be expected.

5.3.1 General results

Similarly to the classic design, we explore the influence of the amplitude of the RF electric field on the transmission. The amplitude ranges from 0 V (corresponding to a DC-only electric field) to 120 V. All simulations are performed using the adapted formulation of the effective RF-field. However, the artificial charge factor is of 250 for the amplitudes lower than 50 V and 1500 for the larger amplitudes. Figure 5.21 presents the transmission ratio over the range of amplitudes considered. In contrast to the classic design, no strong influence of the amplitude can be observed. In all cases, the transmission ratio remains roughly around 55 %. This shows that the new design is not suitable for the effective transmission of ions through the funnel. We can imagine a similar chamber without electrodes. While the detailed gas flow may differ, we expect a similar transmission, so that this ion funnel structure appears to not be really adapted to its purpose. This is further analyzed in the next section.

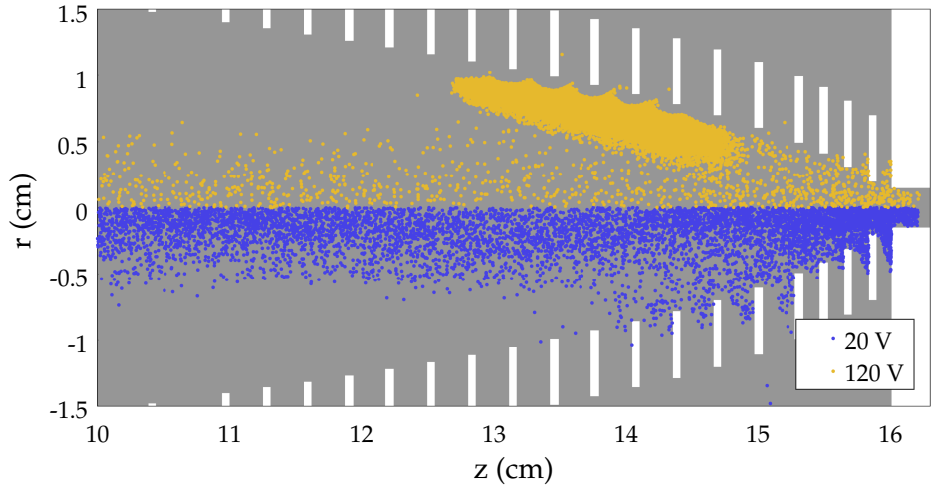

FIGURE 5.22: Accumulation of ion in the recirculation zone of the evolution of the ion funnel design depending on the amplitude of the RF-field applied to the electrodes.

5.3.2 Details regarding the failings of the design

The first element to mention is the significant transmission even in the absence of any RF-field. This indicates that the gas flow, combined with the DC-field, is sufficient to transport a large number of ions through the chamber. While this may appear like a good feature, this also means that the ions are basically traveling through the chamber without strong disturbances and thus acquire a relatively large velocity all along the transfer through the chamber, compared to the traditional design. At the very end of the funnel, between the last electrodes of the system, this behavior flips. The new design induces a reduction of the velocity of the gas flow, while the classic design present an acceleration of the flow. However, this may not reverse the tendency, especially for heavy ions. They indeed acquire large kinetic energy, while the low density in the region means that the response time is large. It follows that such ions are likely to keep a large velocity. On the other hand, in the classic design, their acceleration may be delayed for the same reasons. In the cases simulated, one can locally observe larger velocities at the outlet in the classic design than in the evolution. However, the considered species, rhodamine B, remains relatively light in comparison to the ions usually considered, especially in native applications. From these results, one can conclude that adding a funnel-shaped outlet to capillary does not help to bring better conditions for the transfer of ions through the pumping chamber. While it helps to adapt the pressure levels, it completely modifies the structure of the flow and especially the form of the shock structures expected: no Mach disk is present but diamond shock cells.

Furthermore, the recirculation zone, described in the results of the gas flow in section 3.4.4, explains the lack of higher transmission when the amplitude of the RF-field increases. Indeed, when the electric effects become strong enough to prevent the ions to get lost while flying through the electrodes located at the end of the funnel, the backward flow means that these ions are not transported in the direction of the outlet but backward in the direction of the capillary, along the tip of the electrodes. This behavior can be highlighted by comparing the distribution of the ions in the domain for different levels of amplitudes of the RF-field, as presented in

figure 5.22 For low levels, with the example of 20 V, we can see that the ions that do not directly focus into the outlet hit the electrodes and get lost. No significant influence of the RF-field can be observed. For higher amplitudes, with the example of 120 V, the effects of the RF-field are strong enough to prevent most of the ions to get lost by directly traveling between the electrodes. Some still get lost, though, as the RF-field remains too low. However, they reach the end of the recirculation zone and build a strong accumulation. From there, the space charge effects become significant and the ions either are reintroduced in the main flow, where they can be transported again towards the end of the funnel, or they are pushed further towards the electrodes and get lost. In all cases, it does not help to enhance the transmission, as the effects of the RF-field creates a recirculation triggered by the structure of the gas flow. As a consequence, it does not push the ions farther enough into the area where they could be directly transmitted, as happens in the traditional design, and only shifts the location of the losses up-stream. Worth noting is also the absence of a notable trapping effect in the central area of the cavity, in contrast with the classic design.

This shows that the two main modifications brought into the design of the funnel negatively impact the transmission of the ions. First, the adapted outlet of the capillary, by modifying the pattern of the supersonic flow, creates unwanted conditions for the transmission into the second pumping chamber. Furthermore, the parabolic shape of the cavity allows for the formation of a recirculation zone in the flow field. This means that the effect of the RF-field does not enhance the transmission but rather shifts the location of the losses.

5.3.3 Conclusions for the design of the ion funnel

The previous results let us draw some conclusions regarding the possible evolution of the design of the ion funnel. First, a straight outlet of the capillary seems to be profitable for the qualitative aspect of the transmission. It indeed allows the supersonic flow to create a pattern involving a Mach disk, as long as the pressure in the pumping chamber is low enough. In the area located after the disk, the gas flow is subsonic and the ions can slow down, independently of their mass. This also means that the chamber should be long enough so that this area of low gas velocity is large enough. Further, the shape of the cavity formed by the electrodes should avoid being too steep in the vicinity of the chamber's outlet. Straight or even convex shapes of the cavity should help prevent the formation of recirculation zones of the gas flow, and thus ensure that the effects of the RF-field applied to the electrodes effectively enhances the transmission towards the next chamber.

Chapter 6

Conclusions

The results of the different simulations performed throughout this work are now summarized to draw some conclusions about the findings.

6.1 Capillary

The first focus of the present work was to better understand the processes involved in the transport of ions through an inlet capillary. This part of the device is located at the entry of the atmospheric pressure interface typically used in combination with electrospray ionization. The simulations performed first describe the gas flow that can be expected in the capillary. These results are then used to show which parameters can affect the transmission of the ions through the capillary, which is an important factor to improve the sensibility of classic usages involving mass spectrometry or to allow the development of new applications, such as soft-landing. We also considered the eventuality of a turbulent flow in such capillary, to identify whether the strong pressure ratio affects the otherwise expected properties.

6.1.1 Expected nature of the capillary flow

Despite several works (especially Wißdorf et al. 2016 and M. Skoblin et al. 2017), it is still not well known whether the gas flow within the capillary is laminar or turbulent. We proposed here to study several properties of capillary flows. No definitive answer regarding their expected turbulent or laminar nature is proposed, but a closer insight into both is offered.

Following some preliminary work (Bernier et al. 2018), we first investigated the possibility of a laminar flow. It results in chocked flows, due to the strong pressure gradient between both ends of the capillary. As a consequence, the different parameters tested, either changing the geometry of the domain (length and diameter) or the temperature at the walls, all produce similar pressure and axial velocity profiles along the pipe length. This especially leads to strong accelerations and steep pressure drop towards the end of the capillary. Nevertheless, interesting properties can be observed, depending on the parameters considered.

The strong acceleration leads to the occurrence of a supersonic area close to the inlet. This is caused by the evolution of the boundary layer thickness along the capillary. It tends to get thinner close to the outlet. As a consequence, it creates an effective convergent-divergent nozzle, which allows sonic conditions well inside the pipe. While having already been reported, both experimentally (Murphy and Miller 1984) and numerically (Lijo, Kim, and Setoguchi 2010), this aspect is rarely evoked in the description of pipe flow, where the assumption of sonic conditions at the outlet is very common.

The heating of the capillary, which is often used in traditional devices, has also been investigated for such flows. This parameter is important as it plays a role in different processes involved in the transport of ions. Even if these are not directly addressed in this work, it includes the supposed effect of heating on the desolvation of the charged droplets created by the electrospray ionization as well as the transformation of the gas-phase ions (unfolding, declustering, fragmentation, etc.). The laminar simulations thus show that the heating effects are strongly located close to the walls, in a layer whose thickness only weakly depends on the diameter of the pipe. This means that while the high temperature set in thin pipes can reach the center of the domain, and thus potentially influence the transport of the electric charges, this is not the case for wider capillaries. With diameters of 0.75 mm or greater, the temperature of the gas close to the symmetry axis is barely affected by the heating. In such cases, the heating is limited to a boundary layer and only effective close to the wall.

Furthermore, this influences the velocity field encountered within the capillary. First, a higher wall temperature leads to slightly smaller axial velocities. As a consequence, the mass flow, which indicates the quantity of gas transported during a given period, is reduced. Second, when the heating is strong enough, a specific profile of the axial velocity is encountered in the cross-section of the capillary. A local maximum, located off the axis, is simulated. Such a profile is rather unexpected, as usually the maximum is located at the axis. However, the conservative variable in the Navier-Stokes equations, the momentum, keeps the usual profile. This phenomenon can be explained by the balance between the trigger of the flow, the pressure gradient, and the inertia of the fluid particles, whose mass is strongly affected by the heating.

While all these results apply to laminar flows, no clear criterion could be defined to predict the occurrence of turbulence within the system. Elementary tests tend to show that within the lengths of the capillary considered here, typical for real devices, even a rather strong perturbation of the flow at the inlet was not able to deliver signs of the appearance of turbulence. The relatively high Reynolds numbers in the considered systems would however speak for the possibility of transitional or turbulent flows. We thus analyzed the properties of a fully turbulent flow set in the inlet of the capillary, while maintaining the strong pressure gradient and thus the acceleration of the flow. Especially, it was of interest whether these specific parameters influence the otherwise well-described properties of a turbulent pipe flow. The results tend to show that the resulting turbulent flow can be sustained throughout the capillary and that no significant difference in the traditional properties of the flow is to be reported, compared to experimental or numerical characterizations of pipe flows without pressure gradient. This means that it cannot be excluded a priori that a turbulent flow occurs in the capillary. As such, the inlet conditions at the entry of the capillary are susceptible to play a significant role in the consecutive nature of the gas flow.

6.1.2 Transport of ions through laminar flows

The results of the laminar flow in the capillary were also used to perform simulations of the transport of ions. Different parameters could be considered, such as the geometry of the capillary, the operating conditions, as well as the species involved. The simulations include the effects of the transport by the gas flow, diffusion, and the space charge effects due to the electric charge of the ions.

The variation of the geometric parameters clearly shows that the gas mass flow influences the transmission. The latter increases roughly linearly with the area of the cross-section, as does the maximal transmitted current. However, another strong influence results from the length of the capillary. While the quantity of gas transmitted is only weakly affected by a difference in the length of the capillary, tremendous variations are computed for the transmitted current. Both parameters could be integrated into a simplified model. It describes the transmission as the expansion of ions initially located close to the axis of the capillary. With an estimation of the space charge effects and the transport of the ions, it could relatively well reproduce the results of the simulation: the transmitted current is proportional to the area of the cross-section of the capillary and inverse proportional to its length. Assuming that the ions are homogeneously distributed at the inlet of the capillary, the characteristic built by reporting the transmission ratio with respect to the transmitted current delivers a straight line, also predicted in the model. Different distribution of ions at the inlet, e.g. a normal distribution in the simulations, delivers another characteristic. This could help, experimentally, to identify the kind of distribution present in a real device.

The results presented here could also reproduce the space charge limit of the capillary, which represents the maximal quantity of electric charges transmitted during a given time. This reflects the fact that a higher current at the inlet induces larger space charge effects during the transmission of the ions and as a consequence larger losses. This limit is however dependent on different factors, among them heating. As have already been recalled, the temperature set at the walls of the capillary influences the properties of the flow. This can be observed by a space charge limit (or maximal current transmitted through the capillary) which decreases with increasing temperature. This effect could previously be reported experimentally (Bernier et al. 2018) and thus confirms that the implementation used here can reproduce key aspects of the transmission.

While the previous results were conducted with the test species rhodamine B, we also considered a mix of species. Especially, we could qualitatively reproduce the transmission bias experimentally exposed in Page et al. (2009). This phenomenon describes the differences in the behavior of the different species, based on their reduced mobility. The transmission is over-proportionally affected for species with larger reduced mobility when the length of the capillary increases. This phenomenon can also be observed when comparing the transmission ratio of each species within a mix and the transmission ratio of an equivalent current of each species alone. The species with high values of reduced mobility are negatively affected when mixed with other species (and vice versa). This could be related to a faster motion of the ions with larger mobility towards the walls of the capillary. They are thus more likely to get lost during the transfer than species with smaller reduced mobility, which tend to remain closer to the center of the capillary. This effect can have consequences when not only the detection of species is considered but also the relative intensities of their signal registered in the mass spectrometer. These are likely not reproducing the relative concentrations in the analyzed sample.

6.2 Ion funnel

We also dedicated the work to the study of the transmission of ions through the chamber following the capillary, with the example of the ion funnel. This chamber intends to achieve a first separation between the gas entering the device via the

capillary and the ions. Several effects are involved in the transmission of the ions. Similarly to the capillary, gas flow, diffusion, and space charge effects are considered. In addition, external electric fields play a role. A periodic field is applied on the electrodes present in the domain. It aims to confine the ions in the cavity created by these electrodes and guides them towards the next chamber of the device.

In the traditional design, several simulations were performed and compared to experimental results. Different implementations of the RF-field have been tested and their results compared, principally with the test species rhodamine B. Considering a variation of the amplitude of the RF-field, from 0 to values up to 160 V, one could build a characteristic of the transmission. It clearly shows that the RF-field is necessary to allow a significant transmission. When only the DC-field is considered, that is with zero RF-amplitude, almost no transmission is reported. Increasing this amplitude leads to an increase in the transmission ratio. Above a specific threshold the simulations predict total transmission. This threshold seems to depend on the implementation of the RF-field considered. Especially, the classic formulation of the effective field, reported in Gerlich (1992) and which assumes that the ions are moving in a vacuum, delivers a smaller threshold than the adapted effective field or than the time-resolved field. The latter both deliver very similar results. This seems to indicate that the modification of the effective field, to take into account the presence of the gas flow, brings a significant improvement to the description of the system. The methodology exposed in this work was also able to reproduce the trapping effect, which is known to create a dependency on the species parameters, especially the mass to charge m/z ratio.

However, only a small decrease in the transmission could be observed for high amplitudes within the range considered. Regarding this aspect, the time-resolved field seems to show larger losses. But they remain in all implementations much more limited than the experiments, which clearly show a maximal transmission for amplitudes of about 80 V to 100 V. While no confirmation can be given yet, a potential explanation for this difference is that some solvent molecules or other unexpected species could be ionized in the ESI process. These present a much smaller m/z ratio than rhodamine B and could thus suffer losses within the considered range of amplitude. Simulations integrating such ions show that the transmission ratio decreases for amplitudes starting from 70 V. Their presence should however be experimentally confirmed to validate such hypothesis and the relative concentration adapted compared to the analyte ions. Furthermore, another difference between the simulation and the experiments is the threshold from which significant transmission is observed. It is delayed towards larger amplitudes in the experiments, compared to the simulations. According to the present results, this can be related to the fact that the ions must go through a transition area between the first pumping chamber where the ion funnel is located and the following chamber. This leads to the possibility of losses in a similar manner as what has been described within the capillary. This however mostly affects the lower amplitudes. In such cases, the effects of the RF-field are strong enough to avoid losses within the ion funnel but too weak to collimate the ions close to the symmetry axis of the system. The expansion in the transition area thus leads to losses. For higher amplitudes, the transmitted ions are very close to the axis. They can thus further expand and enter the next chamber before hitting the walls. No significant losses are then expected at this stage.

Finally, the influence of the pressure level within the chamber has also been considered. In the simulation, as well as in the experiments, high transmission is delayed towards higher amplitudes of the RF-field when the pressure level is increased. This is related to the stronger effects of the gas flow when the pressure

increases. It is then necessary to increase the force applied by the electric fields to counter the influence of the flow. Here again, the program used here is able to reproduce, qualitatively, such effects.

Considering an evolution of the design of the ion funnel, we performed several simulations involving the new formulation of the effective field. Intending to anticipate the possible efficiency of such a design, it turns out that the changes made from the classic design did not bring the expected change. Two main effects are to blame. First, the additional outlet at the end of the capillary strongly affects the pattern of the flow and thus eliminates the relatively quiet zone that appeared after the Mach disk in the classic design. The ions involved in the transport cannot thermalize and keep a relatively large velocity throughout the transport within the cavity formed by the electrodes. The ions involved in the simulations are relatively light, compared to large and heavy ions that can be found in native mass spectrometry. As a consequence, no significant difference in the velocity of the ions could be shown at the outlet of the funnel between both designs. It is however to expect, due to inertia reasons, that such a flow would not create the expected conditions for a proper transmission into the lower pressure chambers of the device for an acceptable range of m/z ratios.

Furthermore, the steep decrease in the inner diameter of the electrodes towards the end of the cavity allows the gas flow to create a recirculation zone. Thus, while the transmission in the absence of any electric RF-field is significantly higher than with the classic design, no meaningful improvement of the transmission could be observed for the range of amplitudes tested. Indeed, it prevents the ions to pass through the spacing between the electrodes, but because of the recirculation, these are not redirected towards the outlet of the funnel but rather backward, where they accumulate.

These two issues raised by the simulations show us that the evolution of the design tested here does not improve the transmission of the ions. It even shows that a straight end of the capillary into the first pumping chamber helps to create favorable conditions for the thermalization of the ions before transmission into further chambers. It also proved that a too steep decrease in the inner radius of the electrodes prevents an overall improvement of the transmission by the action of the RF-field. While the trapping effects are reduced, the possibility of the apparition of a recirculation zone means that the ions prevented from getting lost at the electrodes are not effectively reintroduced into the transmitted stream. Further designs should thus concentrate on straight or convex forms of the cavity, rather than the tested concave one.

6.3 Outlook

We have developed in this work a set of tools able to reproduce the behavior of ions moving in a gas flow with a certain accuracy. This has been applied to two different sections of a typical device used in mass spectrometry: the transfer capillary between the production of ions and the first pumping chamber, as well as this first pumping chamber fitted with an ion funnel. These tools could allow simulations aiming at improving the devices currently used. It could especially be helpful to increase the number of ions that can be transferred through the system. This evolution may indeed open up new applications e.g. in the domain of soft landing.

Nevertheless, some aspects of the methodology need to be further enhanced. In the case of the first pumping chamber, the gas flow computed here lies at the boundaries of the applicability of the equations considered. While such systems are very difficult to study experimentally, it would be necessary to define specific parameters to validate the computational results. This could be, for example, gaining access to shock waves' pattern created by the jet entering the chamber. Other aspects of the implementation could be done differently. The unification of the different computations within a single framework would reduce the complexity of the simulations currently performed and would allow us to avoid some approximations done so far. For example, all electric effects could be unified in a single computation, using the Poisson equation rather than the Laplace equation. All effects would thus be taken into account within a single electric field, rather than splitting the space charge effects on the one hand and the external fields on the other hand. Also, the diffusion effects could be integrated into the equation of motion, using a stochastic force. Thus, the random shift of the positions would not be needed anymore and tailored numerical treatment could be applied to improve the numerical accuracy of the implementation.

Besides these possible improvements and even if some validations remain to be performed, the current methodology offers reliable insights into the processes behind the transport of ions in the atmospheric pressure interface of mass spectrometer devices and as such presents good potential to develop new designs.

List of Figures

List of Tables

List of Abbreviations

ACF	**A**rtificial **C**harge **F**actor
API	**A**tmospheric **P**ressure **I**onization
BW	**B**ack**w**ard
CFD	**C**omputanional **F**luid **D**ynamics
CFL	**C**ourant **F**riedrichs **L**ewy (number)
CCS	**C**ollision **C**ross-**S**ection
DC	**D**irect **C**urrent
DESI	**D**esorption **E**lectro**s**pray **I**onization
DSMC	**D**irect **S**imulation **M**onte **C**arlo
DNA	**D**eoxyribo**n**ucleic **A**cid
DNS	**D**irect **N**umerical **S**imulation
EI	**E**lectron **I**onization or **E**lectron **I**mpact
ESI	**E**lectro**s**pray **I**onization
FMM	**F**ast **M**ultipole **M**ethod
FW	**F**ord**w**ard
GC	**G**as **C**hromatography
IF	**I**on **F**unnel
LC	**L**iquid **C**hromatography
MALDI	**M**atrix-**A**ssisted **L**aser **D**esorption **I**onization
MD	**M**ach **D**isk
MS	**M**ass **S**pectrometry
NSF	**N**avier-**S**tokes **F**ortran
PRT	**P**article **R**esponse **T**ime
RANS	**R**eynolds **A**veraged **N**avier-**S**tokes
RF	**R**adio **F**requency
RMS	**R**oot **M**ean **S**quare
RNA	**R**ibo**n**ucleic **A**cid
SCE	**S**pace **C**harge **E**effects
SLIM	**S**tructures for **L**ossless **I**ons **M**anipulations
ScaFaCoS	**Sca**lable **Fa**st **Co**ulomb **S**olver
TOF	**T**ime **o**f **F**light
VPM	**V**olume **P**enalization **M**ethod
WABBIT	**W**avelet **A**adapted **B**lock-**B**ased solver for **I**nteractions with **T**urbulence

Physical Constants

Speed of light	$c = 2.997\,924\,58 \times 10^{8}\,\mathrm{m\,s^{-1}}$
Heat capacity at constant pressure (air)	$c_\mathrm{P} = 1.005\,\mathrm{J \cdot K^{-1} \cdot kg^{-1}}$
Elementary charge	$e = 1.602\,177\,33 \times 10^{-19}\,\mathrm{C}$
Coulomb constant	$\mathrm{k} = 8.987\,551\,79 \times 10^{9}\,\mathrm{kg \cdot m^{-3} \cdot s^{-2} \cdot C^{-2}}$
Boltzmann constant	$k_0 = 1.380\,648\,52 \times 10^{-23}\,\mathrm{J \cdot K^{-1}}$
Unified atomic mass unit	$m_\mathrm{u} = 1.660\,538\,921 \times 10^{-27}\,\mathrm{kg}$
Avogadro constant	$\mathcal{N}_\mathrm{A} = 6.022\,141\,29 \times 10^{23}$
Standard pressure	$p_0 = 1 \times 10^{5}\,\mathrm{Pa}$
Prandtl number (air)	$\mathrm{Pr} = 0.71$
Universal gas constant	$R = 8.314\,462\,1\,\mathrm{m^2 \cdot kg \cdot s^{-2} \cdot K^{-1} \cdot mol^{-1}}$
Specific gas constant (air)	$R_\mathrm{s} = 287\,\mathrm{m^2 \cdot s^{-2} \cdot K^{-1}}$
Standard temperature	$T_0 = 273.15\,\mathrm{K}$
Permittivity of free space	$\epsilon_0 = 8.854\,187\,81 \times 10^{-12}\,\mathrm{F \cdot m^{-1}}$
Permeability of free space	$\mu_0 = 1.256\,637\,06 \times 10^{-6}\,\mathrm{H \cdot m^{-1}}$

List of Symbols

A	pipe cross section	m^2
A_0	perturbation amplitude	$m \cdot s^{-1}$
a_P	particle (ion) acceleration	$m \cdot s^{-2}$
$\vec{B}$	magnetic field	T
c_p	specific heat capacity at constant pressure	$J \cdot K^{-1} \cdot kg^{-1}$
D	diffusion constant	$m \cdot s^{-1}$
D_{cap}	diameter of the capillary	m
$D_{cap,fun}$	local diameter of the capillary inlet	m
$D_{cap,in}$	max. diameter of the capillary inlet	m
$D_{cap,out}$	max. diameter of the capillary outlet (ion funnel - new design)	m
$D_{cap,Sp}$	max. diameter of the capillary sponge area	m
D_{chb}	diameter of the first pumping chamber	m
d_{elec}	spacing between electrodes	m
$D_{IF,in}$	inner diameter of the electrode (ion funnel)	m
$D_{IF,out}$	outer diameter of the electrode (ion funnel)	m
d_{out}	distance between last electrode and outlet (ion funnel)	m
D_{out}	diameter of the first pumping chamber outlet	m
$\vec{e}_r$,$\vec{e}_\theta$,$\vec{e}_z$	basis unit vector in cylindrical coordinates	-
$\vec{e}_x$,$\vec{e}_y$,$\vec{e}_z$	basis unit vector in Cartesian coordinates	-
$E_{u_i u_j}$	energy spectrum of turbulence for i and j components	$m^3 \cdot s^{-2}$
$\vec{E}_0$	basic form of the radio frequency electric field	$V \cdot m^{-1}$
$\vec{E}_{DC}$	electric field (direct current)	$V \cdot m^{-1}$
$\vec{E}_{eff}$	effective electric field	$V \cdot m^{-1}$
$\vec{E}_{RF}$	electric field (radio frequency)	$V \cdot m^{-1}$
$\vec{E}_{SCE}$	electric field (space charge effects)	$V \cdot m^{-1}$
F_e	enhancement factor	-
$\vec{F}_{DC}$	electric force applied on the ions (direct current)	N
$\vec{F}_{elec}$	electric force applied on the ions (global)	N
$\vec{F}_{eff}$	effective electric force applied on the ions	N
$\vec{F}_{fluid}$	force applied by the surrounding gas on the ions	N
$\vec{F}_{net}$	resulting force applied on the ions	N
$\vec{F}_{RF}$	electric force applied on the ions (radio frequency)	N
$\vec{F}_{SCE}$	electric force applied on the ions (space charge effects)	N
h_r, h_z	grid spacing in radial and axial directions, respectively	m
I_{in}	incoming electric current	A
I_{lost}	lost electric current	A
I_{max}	maximal transmitted electric current	A
I_{trans}	transmitted electric current	A
J	Jacobian determinant	m
K	ion mobility	$m^2 \cdot V^{-1} \cdot s^{-1}$

K_0	reduced ion mobility	$\mathrm{m}^2 \cdot \mathrm{V}^{-1} \cdot \mathrm{s}^{-1}$
Kn	Knudsen number	-
L_{cap}	length of the capillary	m
$L_{\mathrm{cap,in}}$	length of the capillary inlet	m
L_{chb}	length of the first pumping chamber	m
l_{elec}	thickness of the electrode (ion funnel)	m
L_{elec}	length of the electrode (ion funnel)	m
l_{pump}	length of the pumping area (first pumping chamber)	m
m	mass of the ion	kg
$\dot{m}$	mass flow	$\mathrm{kg} \cdot \mathrm{s}^{-1}$
$\underline{\underline{m}}$	metric factors	m
p	pressure	Pa
Pr	Prandtl number	-
q	ion electric charge	C
Q	charge density per unit length	$\mathrm{C} \cdot \mathrm{m}^{-1}$
$r\,,\theta\,,z$	cylindrical coordinates	m
$\tilde{r}$	radius of the slice containing the transmitted ions in the capillary	m
R_{cap}	capillary radius	m
Re	Reynolds number	-
T	fluid temperature	K
u_{av}	average axial velocity in capillary	$\mathrm{m} \cdot \mathrm{s}^{-1}$
$\vec{u}_{\mathrm{f}}/\vec{u}$	fluid velocity	$\mathrm{m} \cdot \mathrm{s}^{-1}$
$u_r\,,u_\theta\,,u_z$	cylindrical fluid velocity components	$\mathrm{m} \cdot \mathrm{s}^{-1}$
$u_x\,,u_y\,,u_z$	Cartesian fluid velocity components	$\mathrm{m} \cdot \mathrm{s}^{-1}$
u_τ	friction velocity	$\mathrm{m} \cdot \mathrm{s}^{-1}$
V_0	basic form of the radio frequency electric potential	V
V_{elec}	electric potential	V
V_{ext}	electric potential due to external causes	V
V_{SCE}	electric potential due to space charge effects	V
$\vec{v}_{\mathrm{P}}$	velocity of a charged particle	$\mathrm{m} \cdot \mathrm{s}^{-1}$
v_{pump}	gas velocity at the pump outlet (ion funnel)	$\mathrm{m} \cdot \mathrm{s}^{-1}$
$\dot{\mathcal{V}}_{\mathrm{pump}}$	Volume flow at the pump outlet (ion funnel)	$\mathrm{m}^3 \cdot \mathrm{s}^{-1}$
x_{P}	particle (ion) position	m
$x\,,y\,,z$	Cartesian coordinates	m
$\tilde{y}$	distance from the wall	m
$\tilde{y}^*$	viscous length scale	m
$\tilde{y}^+$	normalized distance from the wall	-
$\tilde{z}$	shifted axial position	m
γ	adiabatic index	-
Δ	Laplace operator	-
Δt	time step	s
η_{Sp}	sponge factor	s
η_{VPM}	volume penalization factor	s
κ_θ	wavenumber in azimuthal direction	m^{-1}
κ_z	wavenumber in axial direction	m^{-1}
λ	thermal conductivity	$\mathrm{W} \cdot \mathrm{m}^{-1} \cdot \mathrm{K}^{-1}$
μ	dynamic viscosity	$\mathrm{Pa} \cdot \mathrm{s}$
$\bar{\mu}_{\mathrm{w}}$	mean kinematic viscosity	$\mathrm{m}^2 \cdot \mathrm{s}^{-1}$
$\xi\,,\eta\,,\zeta$	computational coordinates	-

ρ	fluid density	$\mathrm{kg} \cdot \mathrm{m}^{-3}$
ρ_C	charge density	$\mathrm{C} \cdot \mathrm{m}^{-3}$
ρ_P	ion concentration	m^{-3}
$\bar{\rho}_\mathrm{w}$	mean fluid density at the wall	$\mathrm{kg} \cdot \mathrm{m}^{-3}$
σ	standard deviation of the normal distribution	m
$\underline{\underline{\tau}}$	fluid stress tensor	Pa
τ_P	particle response time	s
$\bar{\tau}_{zr,\mathrm{w}}$	mean shear stress at the wall	Pa
$\vec{\phi}$	heat flux	$\mathrm{W} \cdot \mathrm{m}^{-1}$
χ_Sp	sponge mask function	-
χ_VPM	volume penalization mask function	-
ω	angular frequency (ion funnel - RF potential)	rad
∇	nabla operator	-

Appendix A

Mathematical operators

The general form of the Navier-Stokes equations presented in section 3.1.1 uses coordinate independent operators. It involves different notation, especially the nabla operator, which take different meaning depending on the variables it is applied to. Theses notations are properly defined here.

An interpretation in Cartesian coordinates, which provides simple forms, as well as in cylindrical coordinates, mostly used in this work, is also presented. (x, y, z) are the Cartesian coordinates and $\vec{e}_x$, $\vec{e}_y$, $\vec{e}_z$ their respective unit vectors. (r, θ, z) are the cylindrical coordinates and $\vec{e}_r$, $\vec{e}_\theta$, $\vec{e}_z$ their respective unit vectors. The indices, written after the vectors or matrices, denote the set of coordinates considered for the corresponding representation. Furthermore, the sign $\bullet$ represents the variable on which the different operators are applied.

Outer product

The outer product is denoted with the operator $\bullet \otimes \bullet$ and is applied between two vectors $\vec{u}$ and $\vec{v}$. The results is a second order tensor (or matrix).

Interpretation in Cartesian coordinates

$$\vec{u} \otimes \vec{v} = \begin{pmatrix} u_x v_x & u_x v_y & u_x v_z \\ u_y v_x & u_y v_y & u_y v_z \\ u_z v_x & u_z v_y & u_z v_z \end{pmatrix}_{x,y,z} \tag{A.1}$$

Interpretation in cylindrical coordinates

$$\vec{u} \otimes \vec{v} = \begin{pmatrix} u_r v_r & u_r v_\theta & u_r v_z \\ u_\theta v_r & u_\theta v_\theta & u_\theta v_z \\ u_z v_r & u_z v_\theta & u_z v_z \end{pmatrix}_{r,\theta,z} \tag{A.2}$$

Divergence (vector)

The divergence, applied to a vector field $\vec{v}$, delivers a scalar field. It is represented by $\nabla \cdot \bullet$.

Interpretation in Cartesian coordinates

$$\nabla \cdot \vec{v} = \frac{\partial v_x}{\partial x} + \frac{\partial v_y}{\partial y} + \frac{\partial v_z}{\partial z} \tag{A.3}$$

Interpretation in cylindrical coordinates

$$\nabla \cdot \vec{v} = \frac{1}{r}\frac{\partial r v_r}{\partial r} + \frac{1}{r}\frac{\partial v_\theta}{\partial \theta} + \frac{\partial v_z}{\partial z} \tag{A.4}$$

Divergence (tensor)

The divergence, applied to a second order tensor field $\underline{\underline{\tau}}$, delivers a vector field. It is also represented by $\nabla \cdot \bullet$. In Cartesian coordinates, it corresponds to the vectorial divergence of each column of the tensor.

Interpretation in Cartesian coordinates

$$\nabla \cdot \underline{\underline{\tau}} = \begin{pmatrix} \frac{\partial \tau_{xx}}{\partial x} + \frac{\partial \tau_{yx}}{\partial y} + \frac{\partial \tau_{zx}}{\partial z} \\ \frac{\partial \tau_{xy}}{\partial x} + \frac{\partial \tau_{yy}}{\partial y} + \frac{\partial \tau_{zy}}{\partial z} \\ \frac{\partial \tau_{xz}}{\partial x} + \frac{\partial \tau_{yz}}{\partial y} + \frac{\partial \tau_{zz}}{\partial z} \end{pmatrix}_{x,y,z} \tag{A.5}$$

Interpretation in cylindrical coordinates

$$\nabla \cdot \underline{\underline{\tau}} = \begin{pmatrix} \frac{\partial \tau_{rr}}{\partial r} + \frac{1}{r}\frac{\partial \tau_{\theta r}}{\partial \theta} + \frac{\partial \tau_{zr}}{\partial z} + \frac{\tau_{rr} - \tau_{\theta\theta}}{r} \\ \frac{\partial \tau_{r\theta}}{\partial r} + \frac{1}{r}\frac{\partial \tau_{\theta\theta}}{\partial \theta} + \frac{\partial \tau_{z\theta}}{\partial z} + \frac{\tau_{r\theta} - \tau_{\theta r}}{r} \\ \frac{\partial \tau_{rz}}{\partial r} + \frac{1}{r}\frac{\partial \tau_{\theta z}}{\partial \theta} + \frac{\partial \tau_{zz}}{\partial z} + \frac{\tau_{rz}}{r} \end{pmatrix}_{r,\theta,z} \tag{A.6}$$

Gradient

The gradient is applied to a scalar field φ and delivers a vector field. It is represented by $\nabla \bullet$.

Interpretation in Cartesian coordinates

$$\nabla \varphi = \begin{pmatrix} \frac{\partial \varphi}{\partial x} \\ \frac{\partial \varphi}{\partial y} \\ \frac{\partial \varphi}{\partial z} \end{pmatrix}_{x,y,z} \tag{A.7}$$

Interpretation in cylindrical coordinates

$$\nabla \varphi = \begin{pmatrix} \frac{\partial \varphi}{\partial r} \\ \frac{1}{r}\frac{\partial \varphi}{\partial \theta} \\ \frac{\partial \varphi}{\partial z} \end{pmatrix}_{r,\theta,z} \tag{A.8}$$

Covariant derivative

The covariant derivative is applied to a vector field $\vec{u}$ and delivers a second order matrix. It is represented by $\nabla \otimes \bullet$. This is not a standard notation but is used consistently throughout this work.

Interpretation in Cartesian coordinates

$$\nabla \otimes \vec{v} = \begin{pmatrix} \frac{\partial v_x}{\partial x} & \frac{\partial v_x}{\partial y} & \frac{\partial v_x}{\partial z} \\ \frac{\partial v_y}{\partial x} & \frac{\partial v_y}{\partial y} & \frac{\partial v_y}{\partial z} \\ \frac{\partial v_z}{\partial x} & \frac{\partial v_z}{\partial y} & \frac{\partial v_z}{\partial z} \end{pmatrix}_{x,y,z} \tag{A.9}$$

Interpretation in cylindrical coordinates

$$\nabla \otimes \vec{v} = \begin{pmatrix} \frac{\partial v_r}{\partial x} & \frac{1}{r}\frac{\partial v_r}{\partial \theta} - \frac{v_\theta}{r} & \frac{\partial v_r}{\partial z} \\ \frac{\partial v_\theta}{\partial r} & \frac{1}{r}\frac{\partial v_\theta}{\partial \theta} + \frac{v_r}{r} & \frac{\partial v_\theta}{\partial z} \\ \frac{\partial v_z}{\partial r} & \frac{1}{r}\frac{\partial v_z}{\partial \theta} & \frac{\partial v_z}{\partial z} \end{pmatrix}_{r,\theta,z} \tag{A.10}$$

Appendix B

Axial symmetric derivative operators using metric factors

The formulation of the axial symmetric Navier-Stokes equations using metric factors has been presented in section 3.1.3. In this appendix, we provide some details about the transformation performed, starting from coordinates independent operators into their expression in cylindrical coordinates, with the assumption of an axial symmetric solution.

The first step goes over describing the relation between Cartesian and cylindrical coordinates.

$$x = \cos\left(\theta\left(\eta\right)\right) r\left(\xi,\zeta\right) , \tag{B.1}$$

$$y = \sin\left(\theta\left(\eta\right)\right) r\left(\xi,\zeta\right) , \tag{B.2}$$

$$z = z\left(\xi,\zeta\right) , \tag{B.3}$$

where x, y, z represent the classic Cartesian coordinates, ξ, η, ζ the computational coordinates, and r, θ, z the transformations between computational and cylindrical coordinates. (z represents here both the transformation to and the third cylindrical coordinates itself for the sake of simplicity).

In the following, the computational variables written in subscripts indicate a partial derivative with respect to this variable. Thus it holds $u_\xi = \frac{\partial u}{\partial \xi}$ for any field u.

The dependency of θ with respect to η does not matter, as long as θ_η is a constant. This term always appears with the metric factors, either directly (for ξ and ζ directions) or by multiplication (for the θ direction). Those are however divided by the Jacobian determinant, which includes this term as well, leading to no influence of this parameter on the results.

In this case, one can write the metric factors as follows:

$$\underline{m}^\xi = \begin{pmatrix} y_\eta z_\zeta - z_\eta y_\zeta \\ z_\eta x_\zeta - x_\eta z_\zeta \\ x_\eta y_\zeta - y_\eta x_\zeta \end{pmatrix} = \begin{pmatrix} \theta_\eta \cos\left(\theta\right) r z_\zeta \\ \theta_\eta \sin\left(\theta\right) r z_\zeta \\ -\theta_\eta r r_\zeta \end{pmatrix} , \tag{B.4}$$

$$\underline{m}^\eta = \begin{pmatrix} y_\zeta z_\xi - z_\zeta y_\xi \\ z_\zeta x_\xi - x_\zeta z_\xi \\ x_\zeta y_\xi - y_\zeta x_\xi \end{pmatrix} = \begin{pmatrix} -\sin\left(\theta\right)\left(z_\zeta r_\xi - r_\zeta z_\xi\right) \\ \cos\left(\theta\right)\left(z_\zeta r_\xi - r_\zeta z_\xi\right) \\ 0 \end{pmatrix} , \tag{B.5}$$

$$\underline{m}^\zeta = \begin{pmatrix} y_\xi z_\eta - z_\xi y_\eta \\ z_\xi x_\eta - x_\xi z_\eta \\ x_\xi y_\eta - y_\xi x_\eta \end{pmatrix} = \begin{pmatrix} -\theta_\eta \cos\left(\theta\right) r z_\xi \\ -\theta_\eta \sin\left(\theta\right) r z_\xi \\ \theta_\eta r r_\xi \end{pmatrix} . \tag{B.6}$$

The Jacobian determinant is as well:

$$J = r\theta_\eta \left(z_\zeta r_\xi - r_\zeta z_\xi \right) . \tag{B.7}$$

The implementation then follows further steps. The starting point of the transformation is the Cartesian right-hand side, corresponding to the skew-symmetric equation described in section 3.1.1 and directly implemented as described in Reiss and Sesterhenn (2014).

The different steps of the transformation are:

1. to write the needed operators (divergence, gradient) using the metric factors;
2. to replace the Cartesian variables, considering the transformation in cylindrical coordinates and the simplifications through the axial symmetry;
3. to define a specific angle for the considered two-dimensional domain - this is $\theta = 0\,[2\pi]$ throughout this appendix.

The choice of $\theta = 0\,[2\pi]$ does not only allow to strongly simplify the expressions of the metric factors. It also represents a plane in which the unit vectors of Cartesian and cylindrical coordinates are equal. This means that the vector and matrix notations presented it, derived in Cartesian coordinates, also represents the cylindrical vectors and matrices in cylindrical coordinates. This choice is arbitrary, though, given the axial symmetry of the solutions. One could well choose any other angle, to gain back similar expressions. However, this would require to take into account the transformations between the unit vectors.

Considered Variables

This given, one needs transformation rules between the Cartesian (v_x, v_y, v_z) and cylindrical (v_r, v_θ, v_z) vector components:

$$\begin{array}{rcl|rcl} v_x &=& \cos(\theta)\, v_r - \sin(\theta)\, v_\theta & v_r &=& \cos(\theta)\, v_x + \sin(\theta)\, v_y \\ v_y &=& \sin(\theta)\, v_r + \cos(\theta)\, v_\theta & v_\theta &=& -\sin(\theta)\, v_x + \cos(\theta)\, v_y \\ v_z &=& v_z & v_z &=& v_z \end{array} \tag{B.8}$$

The scalar parameters are identical in all coordinates systems and no specific notation is used.

Divergence Operator

The divergence operator exists in two different forms: conservative and non-conservative. Those are defined with the metric factors as follows, where α is an index between 1 and 3 and ξ^α stands for the corresponding computational coordinate.

Conservative form:

$$J\left(\nabla \cdot \underline{v}\right) = \sum_\alpha \frac{\partial \left(\underline{m}^\alpha \cdot \underline{v} \right)}{\partial \xi^\alpha} . \tag{B.9}$$

Non-conservative form:

$$J\left(\nabla \cdot \underline{v}\right) = \sum_\alpha \underline{m}^\alpha \cdot \frac{\partial \underline{v}}{\partial \xi^\alpha} . \tag{B.10}$$

In both cases, one should make sure to first replace the vector components with the Cartesian ones, before substituting with the cylindrical ones, which are eventually used in the axial symmetric formulation.

Conservative Divergence Formulation

$$
\begin{aligned}
J\left(\nabla \cdot \underline{v}\right) = & \frac{\partial}{\partial \xi}\left(\theta_\eta \cos\left(\theta\right) r z_\zeta v_x + \theta_\eta \sin\left(\theta\right) r z_\zeta v_y - \theta_\eta r r_\zeta v_z\right) \\
& + \frac{\partial}{\partial \eta}\left(-\sin\left(\theta\right)\left(z_\zeta r_\xi - r_\zeta z_\xi\right) v_x + \cos\left(\theta\right)\left(z_\zeta r_\xi - r_\zeta z_\xi\right) v_y\right) \\
& + \frac{\partial}{\partial \zeta}\left(-\theta_\eta \cos\left(\theta\right) r z_\xi v_x - \theta_\eta \sin\left(\theta\right) r z_\xi v_y + \theta_\eta r r_\xi v_z\right) \qquad \text{(B.11)} \\
= & \frac{\partial}{\partial \xi}\left(\theta_\eta \cos^2\left(\theta\right) r z_\zeta v_r - \theta_\eta \cos\left(\theta\right) \sin\left(\theta\right) r z_\zeta v_\theta\right) \\
& + \frac{\partial}{\partial \xi}\left(\theta_\eta \sin^2\left(\theta\right) r z_\zeta v_r + \theta_\eta \cos\left(\theta\right) \sin\left(\theta\right) r z_\zeta v_\theta - \theta_\eta r r_\zeta v_z\right) \\
& + \frac{\partial}{\partial \eta}\left(\left(z_\zeta r_\xi - r_\zeta z_\xi\right)\left(-\cos\left(\theta\right) \sin\left(\theta\right) v_r + \sin^2\left(\theta\right) v_\theta\right)\right) \\
& + \frac{\partial}{\partial \eta}\left(\left(z_\zeta r_\xi - r_\zeta z_\xi\right)\left(+\cos\left(\theta\right) \sin\left(\theta\right) v_r + \cos^2\left(\theta\right) v_\theta\right)\right) \\
& + \frac{\partial}{\partial \zeta}\left(-\theta_\eta \cos^2\left(\theta\right) r z_\xi v_r + \theta_\eta \cos\left(\theta\right) \sin\left(\theta\right) r z_\xi v_\theta\right) \\
& + \frac{\partial}{\partial \zeta}\left(-\theta_\eta \sin^2\left(\theta\right) r z_\xi v_r - \theta_\eta \cos\left(\theta\right) \sin\left(\theta\right) r z_\xi v_\theta + \theta_\eta r r_\xi v_z\right) \qquad \text{(B.12)} \\
= & \frac{\partial}{\partial \xi}\left(\theta_\eta r\left(z_\zeta v_r - r_\zeta v_z\right)\right) + \frac{\partial}{\partial \eta}\left(\left(z_\zeta r_\xi - r_\zeta z_\xi\right) v_\theta\right) \\
& + \frac{\partial}{\partial \zeta}\left(-\theta_\eta r\left(z_\xi v_r - r_\xi v_z\right)\right) \qquad \text{(B.13)} \\
J\left(\nabla \cdot \underline{v}\right) = & \frac{\partial}{\partial \xi}\left(\theta_\eta r\left(z_\zeta v_r - r_\zeta v_z\right)\right) + \frac{\partial}{\partial \zeta}\left(-\theta_\eta r\left(z_\xi v_r - r_\xi v_z\right)\right) \qquad \text{(B.14)}
\end{aligned}
$$

It appears that the result does not depend on the chosen angle θ, which is consistent with the fact that the divergence delivers a scalar value, which by definition is independent of the chosen coordinate system.

To keep some similarity with the general formulation of the Navier-Stokes equations, one chooses a specific angle ($\theta = 0$) and one directly applies the metric factors. In this case, this delivers:

$$
J\left(\nabla \cdot \underline{v}\right) = \frac{\partial}{\partial \xi}\left(m_1^\xi v_r + m_3^\xi v_z\right) + \frac{\partial}{\partial \zeta}\left(m_1^\zeta v_r + m_3^\zeta v_z\right). \qquad \text{(B.15)}
$$

Non-Conservative Divergence Formulation

$$\begin{aligned}
J\left(\nabla\cdot\underline{v}\right) &= \theta_\eta\cos\left(\theta\right)rz_\zeta(v_x)_\xi+\theta_\eta\sin\left(\theta\right)rz_\zeta(v_y)_\xi-\theta_\eta rr_\zeta(v_z)_\xi\\
&\quad-\sin\left(\theta\right)\left(z_\zeta r_\xi-r_\zeta z_\xi\right)(v_x)_\eta+\cos\left(\theta\right)\left(z_\zeta r_\xi-r_\zeta z_\xi\right)(v_y)_\eta\\
&\quad-\theta_\eta\cos\left(\theta\right)rz_\xi(v_x)_\zeta-\theta_\eta\sin\left(\theta\right)rz_\xi(v_y)_\zeta+\theta_\eta rr_\xi(v_z)_\zeta \qquad \text{(B.16)}\\
&= \theta_\eta\cos\left(\theta\right)rz_\zeta\left(\cos\left(\theta\right)(v_r)_\xi-\sin\left(\theta\right)(v_\theta)_\xi\right)\\
&\quad+\theta_\eta\sin\left(\theta\right)rz_\zeta\left(\sin\left(\theta\right)(v_r)_\xi+\cos\left(\theta\right)(v_\theta)_\xi\right)-\theta_\eta rr_\zeta(v_z)_\xi\\
&\quad+\left(z_\zeta r_\xi-r_\zeta z_\xi\right)\theta_\eta\left(\sin^2\left(\theta\right)v_r+\cos\left(\theta\right)\sin\left(\theta\right)v_\theta\right)\\
&\quad+\left(z_\zeta r_\xi-r_\zeta z_\xi\right)\theta_\eta\left(\cos^2\left(\theta\right)v_r-\cos\left(\theta\right)\sin\left(\theta\right)v_\theta\right)\\
&\quad-\theta_\eta\cos\left(\theta\right)rz_\xi\left(\cos\left(\theta\right)(v_r)_\zeta-\sin\left(\theta\right)(v_\theta)_\zeta\right)\\
&\quad-\theta_\eta\sin\left(\theta\right)rz_\xi\left(\sin\left(\theta\right)(v_r)_\zeta+\cos\left(\theta\right)(v_\theta)_\zeta\right)+\theta_\eta rr_\xi(v_z)_\zeta \qquad \text{(B.17)}\\
J\left(\nabla\cdot\underline{v}\right) &= \theta_\eta r\left(z_\zeta(v_r)_\xi-r_\zeta(v_z)_\xi\right)+\left(z_\zeta r_\xi-r_\zeta z_\xi\right)\theta_\eta v_r\\
&\quad-\theta_\eta r\left(z_\xi(v_r)_\zeta+r_\xi(v_z)_\zeta\right) \qquad \text{(B.18)}
\end{aligned}$$

Once again, one can transform it back using the metric factors for $\theta = 0$ in order to get a notation that is closer to the general one:

$$J\left(\nabla\cdot\underline{v}\right) = m_1^\xi(v_r)_\xi+m_3^\xi(v_z)_\xi+\theta_\eta m_2^\eta v_r+m_1^\zeta(v_r)_\zeta+m_3^\zeta(v_z)_\zeta\,. \qquad \text{(B.19)}$$

Gradient Operator

The gradient operator exists as well in two different forms. The general notation using metric factors is similar to the divergence and is given for any scalar field φ.

Conservative form:

$$J\left(\nabla\varphi\right)=\sum_\alpha\frac{\partial\left(\varphi\ m^\alpha\right)}{\partial\xi^\alpha}\,. \qquad \text{(B.20)}$$

Non-conservative form:

$$J\left(\nabla\varphi\right)=\sum_\alpha\frac{\partial\varphi}{\partial\xi^\alpha}\ m^\alpha\,. \qquad \text{(B.21)}$$

The specific notation is similarly obtained by replacing the metric factors with their values for the arbitrary coordinates. However one single step is needed, as the scalar field φ does not depend on the coordinate system considered.

Conservative Gradient Formulation

$$J\left(\nabla\varphi\right)=\begin{pmatrix}\frac{\partial}{\partial\xi}\left(\theta_\eta\cos\left(\theta\right)rz_\zeta\varphi\right)+\frac{\partial}{\partial\eta}\left(-\sin\left(\theta\right)\left(z_\zeta r_\xi-r_\zeta z_\xi\right)\varphi\right)+\frac{\partial}{\partial\zeta}\left(-\theta_\eta\cos\left(\theta\right)rz_\xi\varphi\right)\\ \frac{\partial}{\partial\xi}\left(\theta_\eta\sin\left(\theta\right)rz_\zeta\varphi\right)+\frac{\partial}{\partial\eta}\left(\cos\left(\theta\right)\left(z_\zeta r_\xi-r_\zeta z_\xi\right)\varphi\right)+\frac{\partial}{\partial\zeta}\left(-\theta_\eta\sin\left(\theta\right)rz_\xi\varphi\right)\\ \frac{\partial}{\partial\xi}\left(-\theta_\eta rz_\zeta\varphi\right)+\frac{\partial}{\partial\zeta}\left(\theta_\eta rz_\xi\varphi\right)\end{pmatrix} \qquad \text{(B.22)}$$

$$=\begin{pmatrix}\cos\left(\theta\right)\left(\theta_\eta\frac{\partial}{\partial\xi}\left(rz_\zeta\varphi\right)-\theta_\eta\left(z_\zeta r_\xi-r_\zeta z_\xi\right)\varphi-\theta_\eta\frac{\partial}{\partial\zeta}\left(rz_\xi\varphi\right)\right)\\ \sin\left(\theta\right)\left(\theta_\eta\frac{\partial}{\partial\xi}\left(rz_\zeta\varphi\right)-\theta_\eta\left(z_\zeta r_\xi-r_\zeta z_\xi\right)\varphi-\theta_\eta\frac{\partial}{\partial\zeta}\left(rz_\xi\varphi\right)\right)\\ -\left(\theta_\eta\frac{\partial}{\partial\xi}\left(rz_\zeta\varphi\right)-\theta_\eta\frac{\partial}{\partial\zeta}\left(rz_\xi\varphi\right)\right)\end{pmatrix} \qquad \text{(B.23)}$$

Choosing $\theta = 0$ and replacing with the general form of the metric factors, one obtains

$$J(\nabla\varphi) = \begin{pmatrix} \frac{\partial}{\partial\xi}\left(m_1^\xi\varphi\right) - \theta_\eta m_2^\eta\varphi + \frac{\partial}{\partial\zeta}\left(m_1^\zeta\varphi\right) \\ 0 \\ \frac{\partial}{\partial\xi}\left(m_3^\xi\varphi\right) + \frac{\partial}{\partial\zeta}\left(m_3^\zeta\varphi\right) \end{pmatrix}. \tag{B.24}$$

Non-Conservative Gradient Formulation

$$J(\nabla\varphi) = \begin{pmatrix} \theta_\eta\cos(\theta)\, r z_\zeta\frac{\partial\varphi}{\partial\xi} - \sin(\theta)\left(z_\zeta r_\xi - r_\zeta z_\xi\right)\frac{\partial\varphi}{\partial\eta} - \theta_\eta\cos(\theta)\, r z_\xi\frac{\partial\varphi}{\partial\zeta} \\ \theta_\eta\sin(\theta)\, r z_\zeta\frac{\partial\varphi}{\partial\xi} + \cos(\theta)\left(z_\zeta r_\xi - r_\zeta z_\xi\right)\frac{\partial\varphi}{\partial\eta} - \theta_\eta\sin(\theta)\, r z_\xi\frac{\partial\varphi}{\partial\zeta} \\ -\theta_\eta r z_\zeta\frac{\partial\varphi}{\partial\xi} + \theta_\eta r z_\xi\frac{\partial\varphi}{\partial\zeta} \end{pmatrix} \tag{B.25}$$

Choosing $\theta = 0$ and replacing with the general form of the metric factors, one obtains

$$J(\nabla\varphi) = \begin{pmatrix} m_1^\xi\frac{\partial\varphi}{\partial\xi} + m_1^\zeta\frac{\partial\varphi}{\partial\zeta} \\ 0 \\ m_3^\xi\frac{\partial\varphi}{\partial\xi} + m_3^\zeta\frac{\partial\varphi}{\partial\zeta} \end{pmatrix}. \tag{B.26}$$

Perspectives

One can see that the conservative form of the divergence and the non-conservative form of the gradient remains the same as in the general case, so no specific treatment should be provided for the terms using those expressions. The non-conservative form of the divergence as well as the conservative form of the gradient present on the other hand additional terms, that should be explicitly given in the new right-hand side.

However, the Navier-Stokes equations do not only contain those basics operators but also more complex ones, especially the tensor divergence (corresponding to the divergence operator applied to a second-order tensor) and the covariant derivative (corresponding to a gradient operator applied to a vector field).

Those "second-order" operators can be easily handled in the Cartesian coordinate systems. The tensor divergence is the vector divergence of each column of the considered tensor and each row of the covariant derivative represents the gradient of the corresponding component of the vector:

- **For the tensor divergence** three different vectors should be considered: $\underline{\tau}_{:x}$, $\underline{\tau}_{:y}$, and $\underline{\tau}_{:z}$, representing the first, second and third columns of tensor $\underline{\underline{\tau}}$, respectively, from which the common divergence is computed;
- **For the covariant derivative** three different scalar fields should be considered: v_x, v_y, and v_z, from which the common gradient is computed.

In both cases, one replaces the Cartesian components v_x, v_y, and v_z using the transformation B.8 (twice in the case of the tensor) and eventually follows the same steps as for the common divergence and gradient operators. The main difference is that the θ dependency differs because of the additional coordinates transformation.

The implemented right-hand side uses only the conservative form of the tensor divergence. Replacing the corresponding components in B.11, one can show that the

η derivative delivers an additional term. Considering, once again, the solution for $\theta = 0$, the tensor divergence becomes:

$$J\left(\nabla \cdot \underline{\tau}_{:x}\right) = \frac{\partial}{\partial \xi}\left(m_1^{\xi}\tau_{rr} + m_3^{\xi}\tau_{rz}\right) - \theta_{\eta} m_2^{\eta}\tau_{\theta\theta} \tag{B.27}$$

$$+ \frac{\partial}{\partial \zeta}\left(m_1^{\zeta}\tau_{rr} + m_3^{\zeta}\tau_{rz}\right), \tag{B.28}$$

$$J\left(\nabla \cdot \underline{\tau}_{:y}\right) = \frac{\partial}{\partial \xi}\left(m_1^{\xi}\tau_{\theta r} + m_3^{\xi}\tau_{\theta z}\right) + \theta_{\eta} m_2^{\eta}\tau_{r\theta} \tag{B.29}$$

$$+ \frac{\partial}{\partial \zeta}\left(m_1^{\zeta}\tau_{\theta r} + m_3^{\zeta}\tau_{\theta z}\right), \tag{B.30}$$

$$J\left(\nabla \cdot \underline{\tau}_{:z}\right) = \frac{\partial}{\partial \xi}\left(m_1^{\xi}\tau_{zr} + m_3^{\xi}\tau_{zz}\right) + \frac{\partial}{\partial \zeta}\left(m_1^{\zeta}\tau_{zr} + m_3^{\zeta}\tau_{zz}\right), \tag{B.31}$$

where the additional terms are written in red.

As well it uses only the non-conservative form of the covariant derivatives, for which specific terms should also be considered. Replacing φ successively by v_x, v_y, and v_z in B.25 delivers for $\theta = 0$, where the specific terms are marked in red:

$$J\left(\nabla v_x\right) = \begin{pmatrix} m_1^{\xi}\frac{\partial v_r}{\partial \xi} + m_1^{\zeta}\frac{\partial v_r}{\partial \zeta} \\ -\theta_{\eta} m_2^{\eta} v_{\theta} \\ m_3^{\xi}\frac{\partial v_r}{\partial \xi} + m_3^{\zeta}\frac{\partial v_r}{\partial \zeta} \end{pmatrix}, \tag{B.32}$$

$$J\left(\nabla v_y\right) = \begin{pmatrix} m_1^{\xi}\frac{\partial v_{\theta}}{\partial \xi} + m_1^{\zeta}\frac{\partial v_{\theta}}{\partial \zeta} \\ \theta_{\eta} m_2^{\eta} v_r \\ m_3^{\xi}\frac{\partial v_{\theta}}{\partial \xi} + m_3^{\zeta}\frac{\partial v_{\theta}}{\partial \zeta} \end{pmatrix}, \tag{B.33}$$

$$J\left(\nabla v_z\right) = \begin{pmatrix} m_1^{\xi}\frac{\partial v_z}{\partial \xi} + m_1^{\zeta}\frac{\partial v_z}{\partial \zeta} \\ 0 \\ m_3^{\xi}\frac{\partial v_z}{\partial \xi} + m_3^{\zeta}\frac{\partial v_z}{\partial \zeta} \end{pmatrix}. \tag{B.34}$$

Appendix C

Laminar capillary with adiabatic boundary conditions

We carried out simulations of laminar flows through the capillary with adiabatic wall boundary conditions. While not directly representing conditions typically found in a mass spectrometry device, it is a typical case study in fluid dynamics and thus worth mentioning. Especially, the results of the laminar flow can be compared to experimental data and are used as a reference for the turbulent case presented in section 3.3.

Influence of the pressure level in the sponge area

The pressure drop is artificially enforced by setting a significantly lower pressure in the sponge area than the atmospheric pressure at the inlet. It remains to show, however, that the level chosen in the sponge area does not affect the behavior of the flow within the physical areas of the pipe, that is the funnel-shaped inlet and the straight part. To this end, we performed two simulations of a pipe with 1.0 mm diameter and 6.0 cm length for the straight part. In both cases, non-slip, adiabatic wall boundary conditions are enforced and the only difference relies on the pressure level set in the sponge area: 10 132.5 Pa in one case and 2026.5 Pa in the other. This represents respectively 10 % and 5 % of the atmospheric pressure set at the inlet.

The results computed in both cases are very similar, with no significant difference encountered. The relative error in the pressure field is represented in figure C.1, where only the straight part of the domain is considered. It is computed as the absolute value of the difference between both results, normalized with the values found for the larger pressure level. It results in a maximum error of about 0.14 %. In the other fields, the maximal relative error is slightly larger: 0.3 % for the density and 0.5 % for the velocity magnitude. These values remain nevertheless very small and we consider that a pressure level of 10 % of the inlet value is low enough to deliver correct results within the physical domain.

Comparison with experimental data

Furthermore, adiabatic simulations can be handily compared to experimental data, as this is a typical case in fluid dynamics. We compare here the results for the pressure drop along the capillary for different diameters and compare them to the experimental data as reported in the work by Frössel (1936). The pressure values along the pipe are normalized with the atmospheric pressure set in the inlet and the axial position with the diameter. The latter uses the beginning of the funnel-shaped inlet as the origin and not the beginning of the straight part as done in other sections

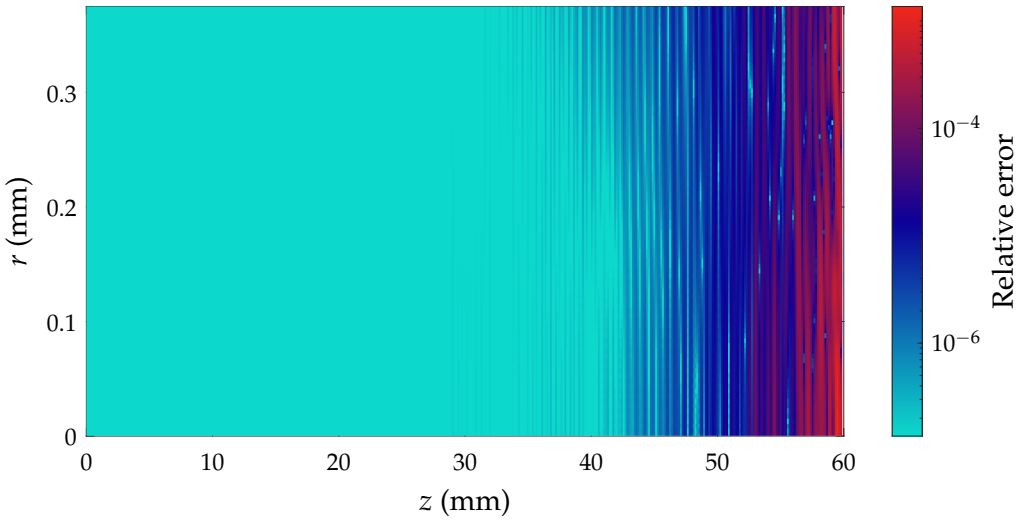

FIGURE C.1: Relative error in the pressure field for different pressure levels set in the sponge area. In both cases, the capillary is 6.0 cm long and 1.0 mm wide. The reference pressure represents 10 % and 5 % of the atmospheric pressure set at the inlet. Only half of the domain is represented, the other being symmetric.

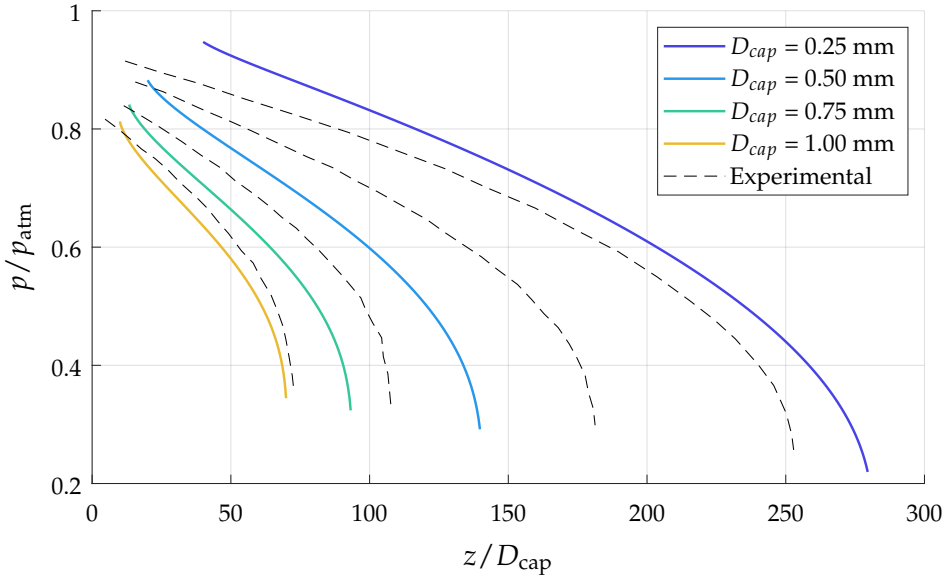

FIGURE C.2: Pressure along the straight part of the capillary for different diameters, compared with experimental data extracted from Frössel (1936).

of this work. However, the results in the funnel-shaped inlet are not represented, as the variation of the diameter in this part of the domain also affects the pressure drop. All cases represented have a 6.0 cm long straight part. It appears that the simulated data is relatively close to the experimental profiles. Especially the strong drop in the pressure level close to the outlet is similar. Larger differences can be observed for small values of z/D_{cap}, but these are interpreted as the influence of the funnel shape chosen for the inlet. We thus conclude that the simulations performed for the laminar flow of the capillary represent well the actual physical state occurring in such situations.

Appendix D

Turbulent variables

The description of turbulent flows is based on several variables, which are presented here. Most of them are used in the presentation of the turbulent capillary flow in section 3.3.

REYNOLDS decomposition and associated variables

Typically, a turbulent flow is decomposed into a time-independent part, the base flow, and variations around this reference, the fluctuations. This decomposition is attributed to Reynolds (1895). The instantaneous flow is then simply expressed as the sum of the base flow and the momentary fluctuation of the considered parameter:

$$\rho\left(\vec{x},t\right) = \overline{\rho}\left(\vec{x}\right) + \rho'\left(\vec{x},t\right) \tag{D.1}$$
$$u_x\left(\vec{x},t\right) = \overline{u}_x\left(\vec{x}\right) + u'_x\left(\vec{x},t\right) \tag{D.2}$$
$$u_y\left(\vec{x},t\right) = \overline{u}_y\left(\vec{x}\right) + u'_y\left(\vec{x},t\right) \tag{D.3}$$
$$u_z\left(\vec{x},t\right) = \overline{u}_z\left(\vec{x}\right) + u'_z\left(\vec{x},t\right) \tag{D.4}$$
$$p\left(\vec{x},t\right) = \overline{p}\left(\vec{x}\right) + p'\left(\vec{x},t\right) \tag{D.5}$$

where ρ is the density of the fluid, u_x, u_y, and u_z its Cartesian velocity components and p the local pressure. By definition, the time average of the fluctuations delivers zero.

From this decomposition, the intensity of the turbulence can be defined, following Dryden and Kuethe (1930) by considering the root-mean-square value of the fluctuations for an absolute quantity:

$$\sqrt{\overline{\phi'^2}}$$

for an arbitrary variable ϕ. This absolute value delivers a relative intensity when the absolute value is divided by the local mean value:

$$\frac{\sqrt{\overline{\phi'^2}}}{\overline{\phi}}.$$

Specific case of compressible flows - FAVRE average

and others including the effect of the fluctuations. This approach paved the way to the Reynolds-Averaged-Navier-Stokes (RANS) equations and further to turbulence models.

However, in the case of compressible flow, the Reynolds decomposition does not deliver the same simplification. Thus an adapted decomposition was proposed by Favre (1965). It considers a different mean value for the velocity components, denoted by $\widetilde{u}_x$, $\widetilde{u}_y$ and $\widetilde{u}_z$, defined as follows:

$$\overline{\rho}\widetilde{u}_x = \overline{\rho u_x} \tag{D.6}$$
$$\overline{\rho}\widetilde{u}_y = \overline{\rho u_y} \tag{D.7}$$
$$\overline{\rho}\widetilde{u}_z = \overline{\rho u_z} \tag{D.8}$$

where the bar represents the traditional time average as used in the Reynolds definition. Based on this specific average, called Favre average, a new decomposition can be defined:

$$u_x(\vec{x},t) = \widetilde{u}_x(\vec{x}) + u_x''(\vec{x},t) \tag{D.9}$$
$$u_y(\vec{x},t) = \widetilde{u}_y(\vec{x}) + u_y''(\vec{x},t) \tag{D.10}$$
$$u_z(\vec{x},t) = \widetilde{u}_z(\vec{x}) + u_z''(\vec{x},t) \tag{D.11}$$

In the RANS equations and for incompressible flows, the average of the fluctuations can be interpreted as a tensor R_{ij}, in index notation, called Reynolds stress tensor and defined as:

$$R_{ij} = \rho\overline{u_i' u_j'}, \tag{D.12}$$

where ρ is the constant density of the flow. In the case of compressible flow, this definition can be adapted to:

$$R_{ij} = \overline{\rho}\widetilde{u_i'' u_j''} = \overline{\rho u_i'' u_j''}. \tag{D.13}$$

Appendix E

Finite differences scheme used in the LAPLACE solver

The finite differences schemes used in the Laplace operators have been presented with a specific order of accuracy in section 4.4.1. While the terms in the axial direction are standard and the demonstration of the order of accuracy can be easily performed, the terms in the radial direction, impacted by the usage of cylindrical coordinates, are specifically treated here.

Radial term of the LAPLACE operator

We first consider the axial symmetric Laplace operator in cylindrical coordinates (r, θ, z):

$$\Delta\phi = \frac{1}{r}\frac{\partial}{\partial r}\left(r\frac{\partial\phi}{\partial r}\right) + \frac{\partial^2\phi}{\partial z^2}\,. \tag{E.1}$$

The radial term is built as a combination of first-order derivatives and involves the radial coordinates. To reach a sufficient order of accuracy, a specific choice of finite difference schemes is considered. Each first-order derivative is computed as a backward or forward scheme, that is with first order of accuracy, a priori. Two combinations are considered: a backward scheme for the inner derivative followed by a forward scheme for the outer derivative and vice versa. These combinations are then averaged to deliver the final scheme. Denoting the forward scheme with the exponent FW and the backward scheme with BW, this can be outlined as the following:

$$\frac{1}{r}\frac{\partial}{\partial r}\left(r\frac{\partial\phi}{\partial r}\right) \approx \frac{1}{2}\left(\frac{1}{r}\frac{\partial^{\mathrm{FW}}}{\partial r}\left(\frac{\partial^{\mathrm{BW}}\phi}{\partial r}\right) + \frac{1}{r}\frac{\partial^{\mathrm{BW}}}{\partial r}\left(\frac{\partial^{\mathrm{FW}}\phi}{\partial r}\right)\right)\,. \tag{E.2}$$

We show in the following that this builds a finite difference scheme with second order of accuracy. Therefore, the Taylor series expansions of the field ϕ around r_i are needed. We consider an equidistant grid in the radial direction with a grid spacing h_r. The values of the different fields at a given, arbitrary point located in the radial direction, excluding the boundaries, are denoted with the index i. The next neighbors are similarly denoted with the indices $i-1$ and $i+1$, respectively. With the

assumption that ϕ is at least three times derivable, it follows:

$$\phi_{i+1} = \phi_i + h_r \left.\frac{\partial \phi}{\partial r}\right|_i + \left.\frac{h_r^2}{2}\frac{\partial^2 \phi}{\partial r^2}\right|_i + \left.\frac{h_r^3}{6}\frac{\partial^3 \phi}{\partial r^3}\right|_i + \mathcal{O}\left(h_r^4\right) , \tag{E.3}$$

$$\phi_{i-1} = \phi_i - h_r \left.\frac{\partial \phi}{\partial r}\right|_i + \left.\frac{h_r^2}{2}\frac{\partial^2 \phi}{\partial r^2}\right|_i - \left.\frac{h_r^3}{6}\frac{\partial^3 \phi}{\partial r^3}\right|_i + \mathcal{O}\left(h_r^4\right) . \tag{E.4}$$

$$\tag{E.5}$$

These two expansions allow us to derive the simple forward and backward schemes (in color) and the error made, respectively:

$$\left.\frac{\partial \phi}{\partial r}\right|_i = \frac{\phi_{i+1} - \phi_i}{h_r} - \left.\frac{h_r}{2}\frac{\partial^2 \phi}{\partial r^2}\right|_i - \left.\frac{h_r^2}{6}\frac{\partial^3 \phi}{\partial r^3}\right|_i + \mathcal{O}\left(h_r^3\right) , \tag{E.6}$$

$$\left.\frac{\partial \phi}{\partial r}\right|_i = \frac{\phi_i - \phi_{i-1}}{h_r} + \left.\frac{h_r}{2}\frac{\partial^2 \phi}{\partial r^2}\right|_i - \left.\frac{h_r^2}{6}\frac{\partial^3 \phi}{\partial r^3}\right|_i + \mathcal{O}\left(h_r^3\right) . \tag{E.7}$$

$$\tag{E.8}$$

These schemes can then be applied to the combinations in equation E.2. The first combination delivers:

$$\begin{aligned}
\frac{\partial^{\mathrm{FW}}}{\partial r}\left(r\frac{\partial^{\mathrm{BW}}\phi}{\partial r}\right) = & \frac{1}{h_r}\left(r_{i+1}\left.\frac{\partial^{\mathrm{BW}}\phi}{\partial r}\right|_{i+1} - r_i\left.\frac{\partial^{\mathrm{BW}}\phi}{\partial r}\right|_i\right) \\
& - \left.\frac{h_r}{2}\frac{\partial^2}{\partial r^2}\left(r\frac{\partial \phi}{\partial r}\right)\right|_i - \left.\frac{h_r^2}{6}\frac{\partial^3}{\partial r^3}\left(r\frac{\partial \phi}{\partial r}\right)\right|_i + \mathcal{O}\left(h_r^3\right) \\
= & \; r_{i+1}\left(\frac{\phi_{i+1} - \phi_i}{h_r^2} + \left.\frac{1}{2}\frac{\partial^2 \phi}{\partial r^2}\right|_{i+1} - \left.\frac{h_r}{6}\frac{\partial^3 \phi}{\partial r^3}\right|_{i+1}\right) \\
& - r_i\left(\frac{\phi_i - \phi_{i-1}}{h_r^2} + \left.\frac{1}{2}\frac{\partial^2 \phi}{\partial r^2}\right|_i - \left.\frac{h_r}{6}\frac{\partial^3 \phi}{\partial r^3}\right|_i\right) \\
& - \left.\frac{h_r}{2}\frac{\partial^2}{\partial r^2}\left(r\frac{\partial \phi}{\partial r}\right)\right|_i + \mathcal{O}\left(h_r^2\right) ,
\end{aligned} \tag{E.9}$$

and the second combination:

$$\begin{aligned}
\frac{\partial^{\mathrm{BW}}}{\partial r}\left(r\frac{\partial^{\mathrm{FW}}\phi}{\partial r}\right) = & \frac{1}{h_r}\left(r_i\left.\frac{\partial^{\mathrm{FW}}\phi}{\partial r}\right|_i - r_{i-1}\left.\frac{\partial^{\mathrm{FW}}\phi}{\partial r}\right|_{i-1}\right) \\
& + \left.\frac{h_r}{2}\frac{\partial^2}{\partial r^2}\left(r\frac{\partial \phi}{\partial r}\right)\right|_i - \left.\frac{h_r^2}{6}\frac{\partial^3}{\partial r^3}\left(r\frac{\partial \phi}{\partial r}\right)\right|_i + \mathcal{O}\left(h_r^3\right) \\
= & \; r_i\left(\frac{\phi_{i+1} - \phi_i}{h_r^2} - \left.\frac{1}{2}\frac{\partial^2 \phi}{\partial r^2}\right|_i - \left.\frac{h_r}{6}\frac{\partial^3 \phi}{\partial r^3}\right|_i\right) \\
& - r_{i-1}\left(\frac{\phi_i - \phi_{i-1}}{h_r^2} - \left.\frac{1}{2}\frac{\partial^2 \phi}{\partial r^2}\right|_{i-1} - \left.\frac{h_r}{6}\frac{\partial^3 \phi}{\partial r^3}\right|_{i-1}\right) \\
& + \left.\frac{h_r}{2}\frac{\partial^2}{\partial r^2}\left(r\frac{\partial \phi}{\partial r}\right)\right|_i + \mathcal{O}\left(h_r^2\right) .
\end{aligned} \tag{E.10}$$

The average of both combinations further delivers:

$$\begin{aligned}
\frac{\partial}{\partial r}\left(r\frac{\partial \phi}{\partial r}\right)\bigg|_i = & \frac{(r_{i-1}+r_i)\,\phi_{i-1} - (r_{i-1}-2r_i+r_{i+1})\,\phi_i + (r_i+r_{i+1})\,\phi_{i+1}}{2h_r^2} \\
& + \frac{1}{2}\left(\frac{r_{i-1}}{2}\,\frac{\partial^2\phi}{\partial r^2}\bigg|_{i-1} - \frac{r_i}{2}\,\frac{\partial^2\phi}{\partial r^2}\bigg|_i - \frac{r_i}{2}\,\frac{\partial^2\phi}{\partial r^2}\bigg|_i + \frac{r_{i+1}}{2}\,\frac{\partial^2\phi}{\partial r^2}\bigg|_{i+1}\right) \\
& + \frac{h_r}{2}\left(+\frac{r_{i-1}}{6}\,\frac{\partial^3\phi}{\partial r^3}\bigg|_{i-1} + \frac{r_i}{6}\,\frac{\partial^3\phi}{\partial r^3}\bigg|_i - \frac{r_i}{6}\,\frac{\partial^3\phi}{\partial r^3}\bigg|_i - \frac{r_{i+1}}{6}\,\frac{\partial^3\phi}{\partial r^3}\bigg|_{i+1}\right) \\
& - \frac{h_r}{2}\,\frac{\partial^2}{\partial r^2}\left(r\frac{\partial\phi}{\partial r}\right)\bigg|_i + \frac{h_r}{2}\,\frac{\partial^2}{\partial r^2}\left(r\frac{\partial\phi}{\partial r}\right)\bigg|_i + \mathcal{O}\left(h_r^2\right) \\
= & \frac{(r_{i-1}+r_i)\,\phi_{i-1} - (r_{i-1}-2r_i+r_{i+1})\,\phi_i + (r_i+r_{i+1})\,\phi_{i+1}}{2h_r^2} \\
& + \frac{1}{4}\left(r_{i-1}\,\frac{\partial^2\phi}{\partial r^2}\bigg|_{i-1} - 2r_i\,\frac{\partial^2\phi}{\partial r^2}\bigg|_i + r_{i+1}\,\frac{\partial^2\phi}{\partial r^2}\bigg|_{i+1}\right) \\
& + \frac{h_r}{12}\left(r_{i-1}\,\frac{\partial^3\phi}{\partial r^3}\bigg|_{i-1} - r_{i+1}\,\frac{\partial^3\phi}{\partial r^3}\bigg|_{i+1}\right) + \mathcal{O}\left(h_r^2\right) . \qquad \text{(E.11)}
\end{aligned}$$

From this form, the term of zeroth and first order of accuracy can further be estimated using Taylor series expansions of the derivatives of ϕ around r_i. Especially, one can write:

$$\frac{\partial^2\phi}{\partial r^2}\bigg|_{i-1} = \frac{\partial^2\phi}{\partial r^2}\bigg|_i - h_r\,\frac{\partial^3\phi}{\partial r^3}\bigg|_i + \mathcal{O}\left(h_r^2\right) , \qquad \text{(E.12)}$$

$$\frac{\partial^2\phi}{\partial r^2}\bigg|_{i+1} = \frac{\partial^2\phi}{\partial r^2}\bigg|_i + h_r\,\frac{\partial^3\phi}{\partial r^3}\bigg|_i + \mathcal{O}\left(h_r^2\right) , \qquad \text{(E.13)}$$

$$\frac{\partial^3\phi}{\partial r^3}\bigg|_{i-1} = \frac{\partial^3\phi}{\partial r^3}\bigg|_i - h_r\,\frac{\partial^4\phi}{\partial r^4}\bigg|_i + \mathcal{O}\left(h_r^2\right) , \qquad \text{(E.14)}$$

$$\frac{\partial^3\phi}{\partial r^3}\bigg|_{i+1} = \frac{\partial^3\phi}{\partial r^3}\bigg|_i + h_r\,\frac{\partial^4\phi}{\partial r^4}\bigg|_i + \mathcal{O}\left(h_r^2\right) . \qquad \text{(E.15)}$$

Assuming an equidistant grid in the radial direction, that it $r_{i-1} = r_i - h_r$ and $r_{i+1} = r_i + h_r$, it follows for the second derivatives terms in equation E.11:

$$\begin{aligned}
r_{i-1}\,\frac{\partial^2\phi}{\partial r^2}\bigg|_{i-1} &= (r_i - h_r)\left(\frac{\partial^2\phi}{\partial r^2}\bigg|_i - h_r\,\frac{\partial^3\phi}{\partial r^3}\bigg|_i + \mathcal{O}\left(h_r^2\right)\right) \\
&= r_i\,\frac{\partial^2\phi}{\partial r^2}\bigg|_i - h_r\,\frac{\partial^2\phi}{\partial r^2}\bigg|_i - r_i h_r\,\frac{\partial^3\phi}{\partial r^3}\bigg|_i + \mathcal{O}\left(h_r^2\right) , \qquad \text{(E.16)} \\
r_{i+1}\,\frac{\partial^2\phi}{\partial r^2}\bigg|_{i+1} &= (r_i + h_r)\left(\frac{\partial^2\phi}{\partial r^2}\bigg|_i + h_r\,\frac{\partial^3\phi}{\partial r^3}\bigg|_i + \mathcal{O}\left(h_r^2\right)\right) \\
&= r_i\,\frac{\partial^2\phi}{\partial r^2}\bigg|_i + h_r\,\frac{\partial^2\phi}{\partial r^2}\bigg|_i + r_i h_r\,\frac{\partial^3\phi}{\partial r^3}\bigg|_i + \mathcal{O}\left(h_r^2\right) . \qquad \text{(E.17)}
\end{aligned}$$

Reintroducing these expansions in equation E.11, all terms of zeroth and first order of accuracy cancel each other:

$$
\begin{aligned}
& r_{i-1} \left.\frac{\partial^2 \phi}{\partial r^2}\right|_{i-1} - 2r_i \left.\frac{\partial^2 \phi}{\partial r^2}\right|_{i} + r_{i+1} \left.\frac{\partial^2 \phi}{\partial r^2}\right|_{i+1} && \text{(E.18)} \\
= \; & r_i \left.\frac{\partial^2 \phi}{\partial r^2}\right|_{i} - h_r \left.\frac{\partial^2 \phi}{\partial r^2}\right|_{i} - r_i h_r \left.\frac{\partial^3 \phi}{\partial r^3}\right|_{i} - 2r_i \left.\frac{\partial^2 \phi}{\partial r^2}\right|_{i} \\
& + r_i \left.\frac{\partial^2 \phi}{\partial r^2}\right|_{i} + h_r \left.\frac{\partial^2 \phi}{\partial r^2}\right|_{i} + r_i h_r \left.\frac{\partial^3 \phi}{\partial r^3}\right|_{i} + \mathcal{O}\left(h_r^2\right) = \mathcal{O}\left(h_r^2\right) . && \text{(E.19)}
\end{aligned}
$$

The third derivative terms only need to be expanded up to $\mathcal{O}(h_r)$ because they are multiplied by h_r. It follows:

$$
r_{i-1} \left.\frac{\partial^3 \phi}{\partial r^3}\right|_{i-1} = (r_i - h_r)\left(\left.\frac{\partial^3 \phi}{\partial r^3}\right|_{i} + \mathcal{O}(h_r)\right) = r_i \left.\frac{\partial^3 \phi}{\partial r^3}\right|_{i} + \mathcal{O}(h_r) , \qquad \text{(E.20)}
$$

$$
r_{i+1} \left.\frac{\partial^3 \phi}{\partial r^3}\right|_{i+1} = (r_i + h_r)\left(\left.\frac{\partial^3 \phi}{\partial r^3}\right|_{i} + \mathcal{O}(h_r)\right) = r_i \left.\frac{\partial^3 \phi}{\partial r^3}\right|_{i} + \mathcal{O}(h_r) . \qquad \text{(E.21)}
$$

Once again, it appears that the terms of zeroth order directly cancel each others in equation E.11. The remaining error, of first order, is further multiplied by h_r and it follows second order accuracy.

We can thus express the finite difference scheme used for the radial terms of the Laplace operator as:

$$
\begin{aligned}
\left.\frac{1}{r}\frac{\partial}{\partial r}\left(r\frac{\partial \phi}{\partial r}\right)\right|_{i} = \; & \frac{(r_{i-1} + r_i)\,\phi_{i-1} - (r_{i-1} - 2r_i + r_{i+1})\,\phi_i}{2r_i h_r^2} \\
& + \frac{(r_i + r_{i+1})\,\phi_{i+1}}{2r_i h_r^2} + \mathcal{O}\left(h_r^2\right) . && \text{(E.22)}
\end{aligned}
$$

Appendix F

Estimation of the reduced ion mobility

The reduced ion mobility, used in equation 2.7, defines how different species show different behavior when placed in the same electric field. The value chosen used in the simulations is thus important to differentiate the behavior of different species.

Definition of the mobility

The mobility is a macroscopic representation of the shocks occurring between the ion and gas molecules at a microscopic level. Especially, it can be relatively easily measured, considering a known species in a defined environment. However, some relations have also be derived to estimate this value. The following relation presented in Mason and McDaniel (1988, p. 149) is usually considered as standard in drawing the dependence of the mobility on the characteristics of the considered species and the surrounding gas temperature:

$$K_0(T) = \frac{3q}{16N}\sqrt{\frac{2\pi}{k_B T_0}}\sqrt{\frac{m+M}{mM}}\frac{1}{\Omega}, \tag{F.1}$$

with T_0 the temperature, q the charge of the ion, N the number density of the gas, k_B the Boltzmann's constant, m the mass of the buffer gas molecules, M the mass of the ion and Ω its cross-section. It has been used to the hydronium and ethyloxonium ions in this work.

This reduced mobility only represents a specific value for a defined temperature. Equation 2.7 then takes into account the variations of the mobility for values close to the temperature used for the reduced mobility. However, in the present work, we always consider a normal temperature as a reference for the reduced mobility and compute the variations around this value. While the temperature may vary within a large range for the considered cases, we estimate in first approximation that the resulting simulations still present a proper description of the system.

Empirical estimations

In some cases, this formula can be difficult to use. Thus, some empirical estimations based on average values have been developed. One is used in the program SIMION, which is the current standard for the simulation of particles' trajectories. It

uses the diameter of the ion d_{ion} considered and derives an estimation of the mobility:

$$K_0 = 10^{\Lambda - 9}\,, \tag{F.2}$$

with

$$\Lambda = 4.9137 - 1.4491 \log_1 0\,(d_{\text{ion}}) - 0.2772 \log_1 0\,(d_{\text{ion}})^2 + 0.0717 \log_1 0\,(d_{\text{ion}})^3\,, \tag{F.3}$$

where d_{ion} is in nm and K_0 in $\mathrm{m}^2 \cdot \mathrm{V}^{-1} \cdot \mathrm{s}^{-1}$. Furthermore, the diameter can be estimated using the mass of the ion m:

$$d_{\text{ion}} = 0.120\,415\,405 \left(\frac{m}{1.660\,538\,921 \times 10^{-27}} \right)^{1/3}\,, \tag{F.4}$$

with m in kg and delivering a result in nm. These relations are presented in the supplementary material of Appelhans and Dahl (2005). These relations are used to estimate the mobility of rhodamine B.

Appendix G

Artificial charge factor - Validation

The space charge effects are computed using an artificial charge factor. This means that the Coulomb's forces between the ions are computed in such a way that each particle present in the simulation stands for an arbitrary number of ions in reality. It thus allows for a reduction of the computational costs, while keeping a similar accuracy of the results.

To prove this, two simulations differing only by the artificial charge factor considered are presented in the following and the results are compared. It deals with the transport of ions through the ion funnel, while both RF and DC fields are considered. This case was chosen because it involves all effects present in the ions simulations reported throughout this work. The parameters are listed in table G.1.

In both cases, nearly unitary transmission is expected, so that no significant difference can be found in the transmitted current or the transmission ratio. Both simulations deliver a transmitted current of approximately 4.80 nA. Nevertheless, a deeper comparison of the results can be performed. First, we consider the shape of the accumulations that build under the influence of the RF electric field. These are presented in figure G.1. No significant difference can be observed. This means that despite the different artificial charge factors and thus different computations for the space charge effects, they similarly compensate with the electric field created by the electrodes of the ion funnel. This is also confirmed by the estimation of the local charge density in both cases. This is done by counting the number of particles in each cell of a grid spanning over the domain, multiplying by the artificial charge factor, and dividing by the volume of the considered cell. The results for the two cases, alongside a similar estimation for the other versions of the RF-field, are presented in figure G.2. One can well see that both simulations with a time-resolved field deliver

Case	#1	#2
Gas flow configuration	IF - classic	IF - classic
Pressure level (Pa)	100	100
Species	rhodamine B	rhodamine B
Incoming current (nA)	≈ 4.81	≈ 4.81
Artificial charge factor	250	125
Time step (s)	5.0×10^{-8}	5.0×10^{-8}
RF amplitude (V)	100	100
RF frequency (Hz)	1×10^{6}	1×10^{6}
RF implementation	time resolved	time resolved

TABLE G.1: Parameters of the two simulations used for validating the artificial charge factor.

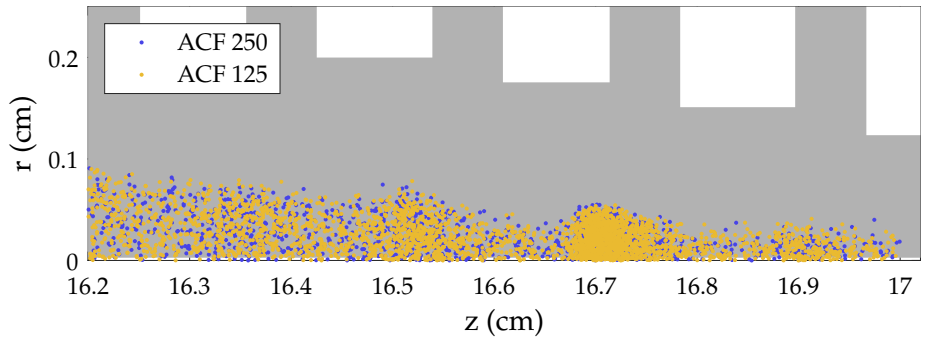

FIGURE G.1: Instantaneous position of the ions close to the outlet of the ion funnel, comparing the two different artificial charge factors considered.

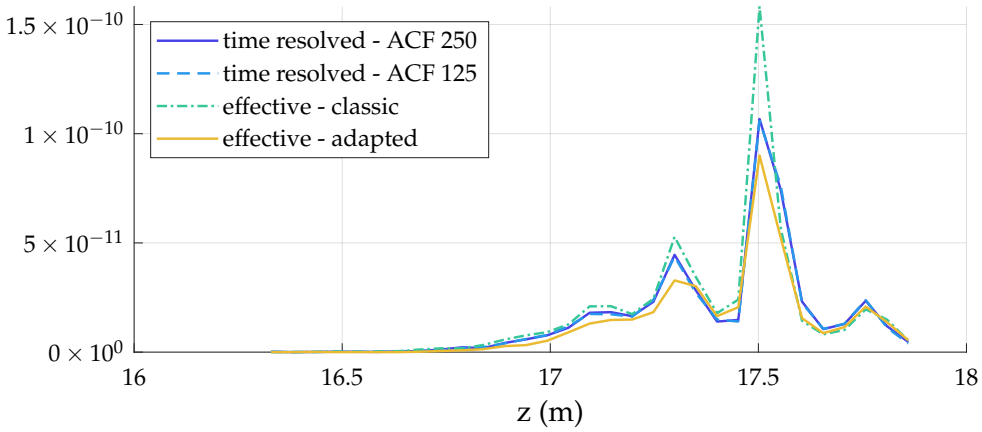

FIGURE G.2: Comparison of the charge density along the axial position, close to the outlet of the funnel and for radial positions located between 1.111 mm and 2.222 mm. The two different artificial charge factors are compared with similar simulations using effective electric RF-fields.

very similar results, while the other simulations, using the effective field, differ more significantly.

These results show that the artificial charge factor used in the simulation only slightly affects the behavior of the system considered. As long as the number of ions present in the domain is significant enough to reproduce the typical trajectory of the ions and to produce the expected space charge effects, no strong sensibility is expected.

Appendix H

DNS of a capillary flow with isothermal walls

In the previous publication Bernier et al. (2018), we argued that the heating of the walls may have an incidence on the affinity of a gas flow through a capillary to turbulence, based on empirical formulas. In order to explore this hypothesis, we performed a simulation similar to the one presented in section 3.3, where the wall boundary conditions are isothermal at a constant temperature of 500 K. In accordance, the inlet data are produced by an auxiliary simulation using the same isothermal boundary conditions.

General results

Snapshots of the fields are presented in figures H.1 and H.2. Two remarks can be done upfront. First, the size of the structures are much larger than the ones found in the DNS performed with adiabatic boundary conditions. This is already the case at the inlet, which means that the data produced by the auxiliary simulation does not deliver the same turbulence intensity than the adiabatic one. Second, a clear evolution is visible along the pipe, the structure in the middle of the capillary being noticeably larger than at the inlet. This means that the perturbation within the flow tend to decay.

The mean values in the domain also show that the flow tends to be very close to the behavior observed in the case of a laminar flow, as presented in section 3.2. The mean axial velocity is displayed in figure H.3 and the mean temperature in figure H.4. These can be directly compared with figures 3.4 and 3.8, respectively, representing the laminar case. Especially, the thickness of the boundary layer in the

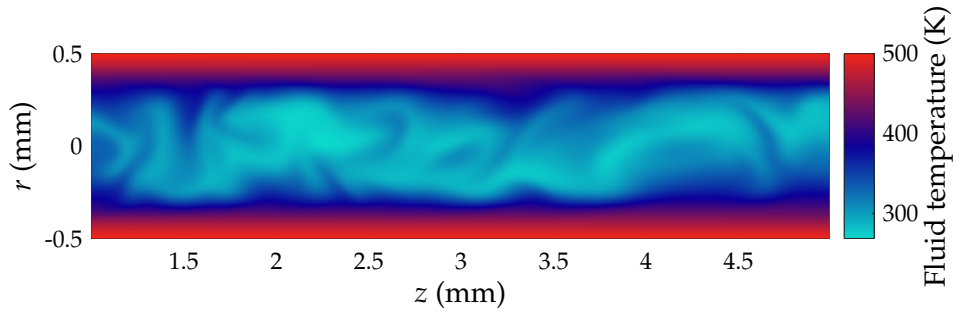

FIGURE H.1: Snapshot of the gas temperature close to the inlet of the capillary. Radial and axial dimensions are represented to scale.

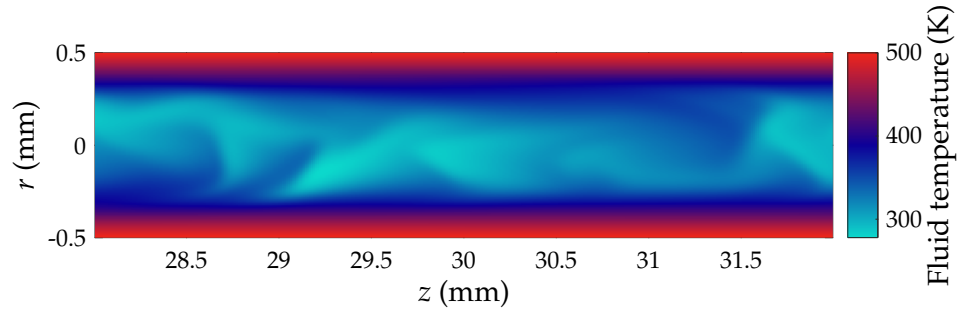

FIGURE H.2: Snapshot of the gas temperature in the central part of the capillary. Radial and axial dimensions are represented to scale.

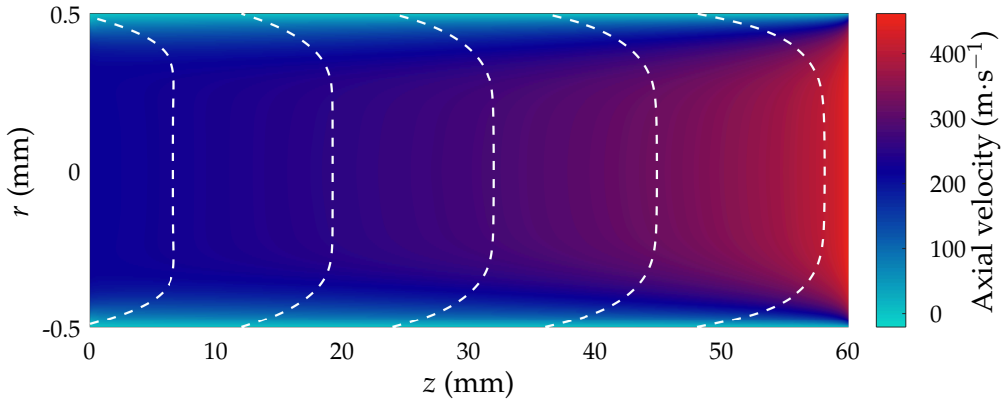

FIGURE H.3: Mean axial velocity component in the capillary domain. The dashed line represents the form of the profile along the radial direction, at the axial position where it touches the wall. Radial and axial dimensions are not to scale.

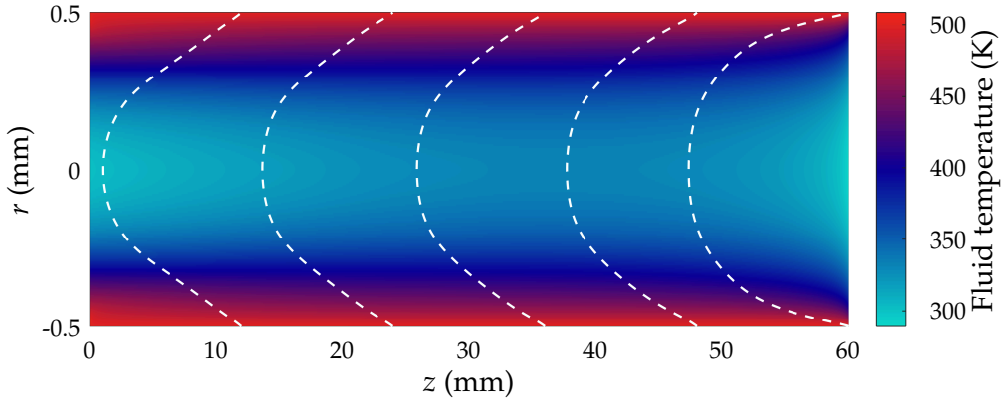

FIGURE H.4: Mean temperature in the capillary domain. The dashed line represent the form of the profile along the radial direction, at the axial position where it touches the wall. Radial and axial dimensions are not to scale.

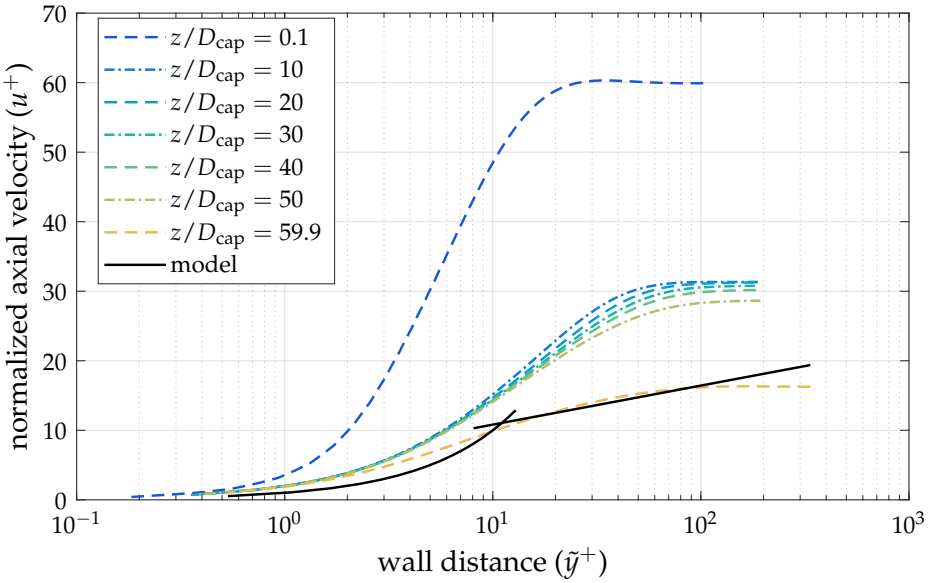

FIGURE H.5: Normalized axial velocity in the cross-section of the pipe represented over the normalized wall distance and for different axial positions along the pipe. The dashed lines represent the standard law, that is $u^+ = \tilde{y}^+$ for lower values of $\tilde{y}^+$ and $u^+ = 1/0.41 \ln \tilde{y}^+ + 5.2$ for larger values of $\tilde{y}^+$.

axial velocity is much closer to the one expected in a laminar flow than in a turbulent one, as visible for the adiabatic case in figure 3.21, for example. This difference can also be observed in the axial velocity profile depicted for cross sections of the capillary in figure H.5. Especially, it does not follow the law of the wall typical for a turbulent flow. Compared to the same wall distances, the normalized velocity reaches larger values faster than expected by the wall function. Furthermore, while two domains are still visible, they do not fit with the traditional limit of $y^+ = 10$, occurring closer to the inner part of the flow. This indicates that the boundary layer is indeed thicker than expected for a turbulent flow. However, this thickness increases along the capillary when considered in normalized dimensions, from 30 at the inlet to about 100 at the outlet.

The difference in the behavior of the flow compared to traditional turbulent pipe flows can also be observed in the profiles of the turbulence intensities in the central cross section of the capillary, as presented in figure H.6. Here again, two different domains can be identified along the radial direction: a first domain where the turbulence intensity rises and drops again, reaching a local minimum roughly at the end of the boundary layer identified with the mean axial velocity. And a second domain over the central part of the system, where the turbulence intensity rises from the end of the boundary layer, reaches a local maximum and drops again toward the middle of the domain. This local minimum remains, however, noticeably greater than the local maximum reached in the boundary layer. Furthermore, the other components of the turbulence intensity (radial and azimuthal) remain significantly lower than the axial component. They are almost zero in the boundary layer and only reaches about 7 % of the axial intensity in the center of the domain. This is in clear contrast with the profiles of the adiabatic case, considering the same normalization. In this case, the maximum in the turbulence intensity is reported within the boundary

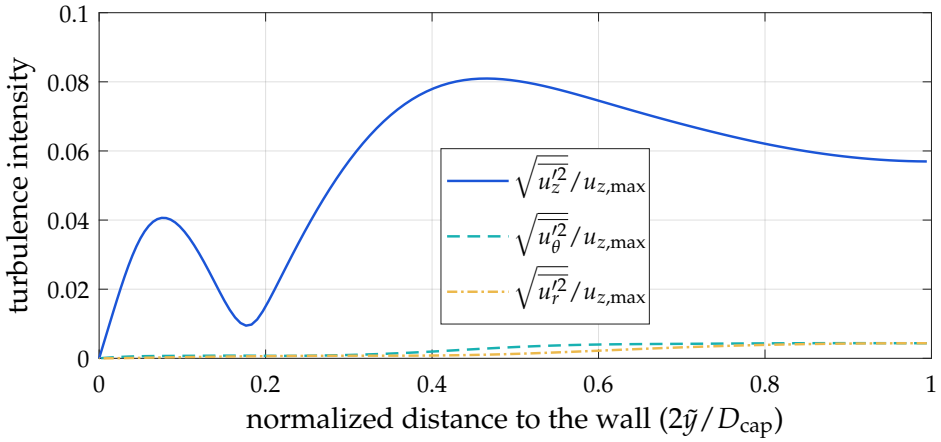

FIGURE H.6: Turbulence intensity along the radial direction in the central cross-section of the capillary. The fluctuations are normalized using the maximal mean axial velocity in the cross-section and the distance to the wall is normalized using the diameter (it thus varies from 0 at the wall up to 1 at the centerline.)

layer and then continuously drop toward the center of the domain. While the maximum intensity in the adiabatic case for the axial component reaches about 13 %, it is limited to 8 % in the isothermal case. Furthermore, the radial and azimuthal components in the adiabatic case present a maximum close to the boundary layer, while it is reached at the centerline in the isothermal case. Furthermore, the abolute values are significantly lower in the latter: clearly less than 1 % for the isothermal boundary conditions versus about 6 % for the adiabatic ones.

These different behaviors can be explained by the influence of the temperature on the viscosity of the gas. Higher temperatures lead to higher viscosity. Thus, the influence of heating in the boundary layer, simulated via the isothermal boundary conditions, leads to significantly larger values of the viscosity than in the adiabatic case. In the latter, however, the maximal intensity of the turbulence can be found at a relatively close distance to the walls. As a consequence, the inner structures of the flow responsible for these fluctuations are undermined by the higher viscosity in the isothermal case. This indeed leads to smaller local Reynolds numbers and thus modify the expected flow. This phenomenon also explains the inherently different inlet data imposed in the primary simulations, as the high temperature close to the walls, also simulated in the auxiliary simulation, limits the possibility of a fully developed turbulent flow for the isothermal case.

Evolution of turbulence

Figures H.7 and H.8 represent the evolution of the maximal RMS velocity fluctuations and turbulent intensity, respectively. In contrast to the results from the adiabatic case, it is remarkable that the radial and azimuthal components, both as RMS fluctuations and as turbulence intensity, are much smaller than the axial one throughout the domain and continuously decrease along the entire capillary. The axial component shows a more complex behavior. Indeed, the RMS fluctuations steadily grow along the first two thirds of the pipe, before sharply declining and regaining a level similar to the one found at the inlet close to the end of the domain.

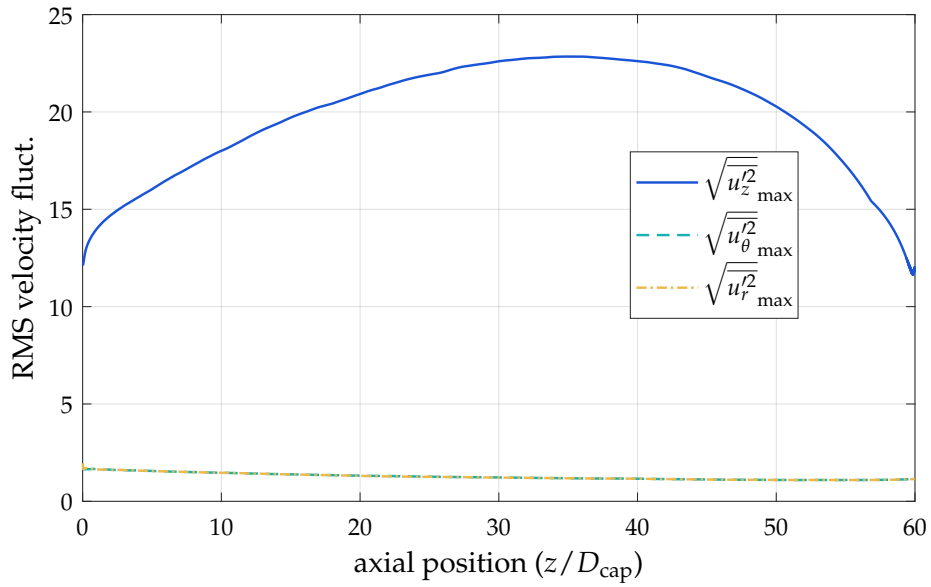

FIGURE H.7: Maximal root mean squared fluctuations along the axial direction.

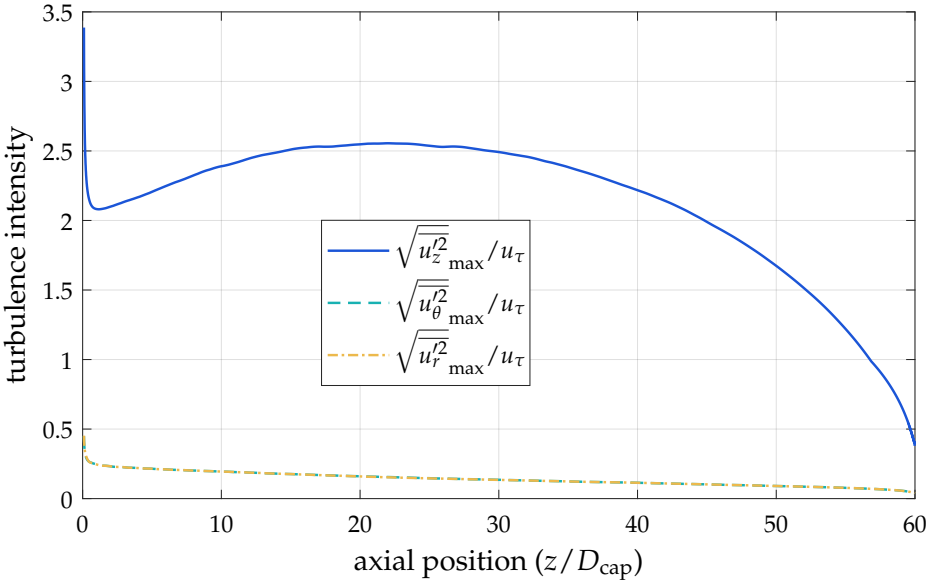

FIGURE H.8: Turbulence intensity along the axial direction. The fluctuations are normalized using the friction velocity according to equation 3.44.

Considered as turbulent intensity, which takes into account the acceleration of the flow, a local maximum is reached after about one third of the length, before declining and reaching a level significantly lower than at the inlet (about 25 % of the inlet level, excluding the adaptation from the data imposed as reference). This shows that this kind of flow does not effectively sustain the fluctuations imposed at its inlet. This is significantly different from the adiabatic case, where the turbulence intensity remains close to constant along a very large section of the capillary. Furthermore, with the exception of the very last part of the pipe just before the outlet, the location of the maximum of the perturbations in the axial component tends to move towards the centerline of the domain. This is a sign of the reduction of the area concerned by the perturbations in the domain while moving forward along it.

As a conclusion, this simulation shows that imposing a high temperature at the walls of the capillary significantly affects the nature of the flow expected. In comparison to the adiabatic case, a perturbation set at the inlet of the domain is less likely to develop into a turbulent flow when the capillary is heated. While the setup considered here does not allows us to provide directly comparable inlet data, this still provides an interesting insight into the mechanisms likely to affect the nature of the flow.

Bibliography

El-Aneed, Anas, Alejandro Cohen, and Joseph Banoub. 2009. "Mass Spectrometry, Review of the Basics: Electrospray, MALDI, and Commonly Used Mass Analyzers." *Applied Spectroscopy Reviews* 44 (3): 210–230. doi:10.1080/05704920902717872.

Angot, P., C.-H. Bruneau, and P. Fabrie. 1999. "A penalization method to take into account obstacles in incompressible viscous flows." *Numerische Mathematik* 81:497–520. doi:10.1007/s002110050401.

Appelhans, A. D., and D. A. Dahl. 2005. "SIMION ion optics simulations at atmospheric pressure." *International Journal of Mass Spectrometry* 244 (1): 1–14. ISSN: 1387-3806. doi:10.1016/j.ijms.2005.03.010.

Arnold, A., F. Fahrenberger, C. Holm, O. Lenz, M. Bolten, H. Dachsel, R. Halver, et al. 2013. "Comparison of scalable fast methods for long-range interactions." *Phys. Rev. E* 88 (6): 063308. doi:10.1103/PhysRevE.88.063308.

Bartlmä, F. 1975. *Gasdynamik der Verbrennung.* Wien: Springer. ISBN: 9783211813003.

Bernier, L. 2014. "Raumladungseffekte von ionengeladenen Gasströmungen durch Kapillaren." Master's thesis, Technische Universität Berlin.

Bernier, L., H. Pinfold, M. Pauly, S. Rauschenbach, and J. Reiss. 2018. "Gas Flow and Ion Transfer in Heated ESI Capillary Interfaces." *Journal of the American Society for Mass Spectrometry* 29 (4): 761–773. doi:10.1021/jasms.8b05795.

Bernier, L., M. Taesch, S. Rauschenbach, and J. Reiss. 2020. "Transfer conditions and transmission bias in capillaries of vacuum interfaces." *International Journal of Mass Spectrometry* 447:116239. ISSN: 1387-3806. doi:10.1016/j.ijms.2019.116239.

Berry, R. S., S. A. Rice, and J. Ross. 2000. *Physical chemistry* [in eng]. 2. ed. Topics in physical chemistry. New York u.a.: Oxford University Press. ISBN: 9780195105896.

Bird, B. R., W. E. Stewart, and E. N. Lightfoot. 2001. *Transport phenomena.* John Wiley & Sons, Inc. ISBN: 9780471410775.

Bogey, C., N. de Cacqueray, and C. Bailly. 2009. "A shock-capturing methodology based on adaptative spatial filtering for high-order non-linear computations." *Journal of Computational Physics* 228 (5): 1447–1465. ISSN: 0021-9991. doi:10.1016/j.jcp.2008.10.042.

Boiron, O., G. Chiavassa, and R. Donat. 2009. "A high-resolution penalization method for large Mach number flows in the presence of obstacles." *Computers & Fluids* 38 (3): 703–714. ISSN: 0045-7930. doi:https://doi.org/10.1016/j.compfluid.2008.07.003.

Brinkman, H. C. 1949. "A calculation of the viscous force exerted by a flowing fluid on a dense swarm of particles." *Flow, Turbulence and Combustion* 1 (1): 27. doi:10.1007/BF02120313.

Chapman, S., and T. G. Cowling. 1991. *The Mathematical Theory of Non-uniform Gases.* 3. ed. Cambridge University Press. ISBN: 9780521408448.

Chen, T.-C., T. L. Fillmore, S. A. Prost, R. J. Moore, Y. M. Ibrahim, and R. D. Smith. 2015. "Orthogonal Injection Ion Funnel Interface Providing Enhanced Performance for Selected Reaction Monitoring-Triple Quadrupole Mass Spectrometry." *Analytical Chemistry* 87 (14): 7326–7331. doi:10.1021/acs.analchem.5b01482.

Chen, T.-C., I. K. Webb, S. A. Prost, M. B. Harrer, R. V. Norheim, K. Tang, Y. M. Ibrahim, and R. D. Smith. 2015. "Rectangular Ion Funnel: A New Ion Funnel Interface for Structures for Lossless Ion Manipulations." *Analytical Chemistry* 87 (1): 716–722. doi:10.1021/ac503564c.

Cheng, H., L. Greengard, and V. Rokhlin. 1999. "A Fast Adaptive Multipole Algorithm in Three Dimensions." *Journal of Computational Physics* 155 (2): 468–498. ISSN: 0021-9991. doi:10.1006/jcph.1999.6355.

Colonius, T. 2004. "Modeling artificial boundary conditions for compressible flow." *Annual Review of Fluid Mechanics* 36 (1): 315–345. doi:10.1146/annurev.fluid.36.050802.121930.

Creaser, C. S., J. R. Griffiths, C. J. Bramwell, S. Noreen, C. A. Hill, and C. L. P. Thomas. 2004. "Ion mobility spectrometry: a review. Part 1. Structural analysis by mobility measurement." *Analyst* 129 (11): 984–994.

Dryden, H. L., and A. M. Kuethe. 1930. "Effect of turbulence in wind tunnel measurements." *National Advisory Committee for Aeronautics - Technical Reports* 342:145–170. https://ntrs.nasa.gov/search.jsp?R=19930091411.

Favre, A. 1965. "Equations des écoulements turbulents compressibles." *Journal de mécanique* 4 (4): 391.

Fenn, J. B., M. Mann, C. K. Meng, S. F. Wong, and C. M. Whitehouse. 1989. "Electrospray ionization for mass spectrometry of large biomolecules." *Science* 246 (4926): 64–71. ISSN: 0036-8075. doi:10.1126/science.2675315.

Franquet, E., V. Perrier, S. Gibout, and P. Bruel. 2015. "Free underexpanded jets in a quiescent medium: A review." *Progress in Aerospace Sciences* 77:25–53. ISSN: 0376-0421. doi:10.1016/j.paerosci.2015.06.006.

Friedrich, R. 2007. "Compressible turbulent flows: Aspects of prediction and analysis." *ZAMM - Journal of Applied Mathematics and Mechanics / Zeitschrift für Angewandte Mathematik und Mechanik* 87 (3): 189–211. doi:10.1002/zamm.200610312.

Frössel, W. 1936. "Strömung in glatten, geraden Rohren mit Über- und Unterschallgeschwindigkeit." *Forschung auf dem Gebiet des Ingenieurwesens A* 7 (2): 75–84. ISSN: 1434-0860. doi:10.1007/BF02592987.

Gaitonde, D. V., and M. R. Visbal. 2000. "Pade-Type Higher-Order Boundary Filters for the Navier-Stokes Equations." *AIAA Journal* 38 (11): 2103–2112. doi:10.2514/2.872.

Gao, Liang, R. Graham Cooks, and Zheng Ouyang. 2008. "Breaking the Pumping Speed Barrier in Mass Spectrometry: Discontinuous Atmospheric Pressure Interface." *Analytical Chemistry* 80 (11): 4026–4032. doi:10.1021/ac800014v.

Gerlich, D. 1992. "Inhomogeneous RF Fields: A Versatile Tool for the Study of Processes with Slow Ions." In *Advances in Chemical Physics*, 1–176. John Wiley & Sons, Ltd. ISBN: 9780470141397. doi:10.1002/9780470141397.ch1.

Gimelshein, N., S. Gimelshein, T. Lilly, and E. Moskovets. 2014. "Numerical Modeling of Ion Transport in an ESI-MS System." *Journal of the American Society for Mass Spectrometry* 25 (5): 820–831. doi:10.1021/jasms.8b04763.

Griffiths, D. J. 2013. *Introduction to electrodynamics.* 4. ed. Pearson, Addison-Wesley. ISBN: 9780321847812.

Griffiths, I. W. 1997. "J. J. Thomson — the Centenary of His Discovery of the Electron and of His Invention of Mass Spectrometry." *Rapid Communications in Mass Spectrometry* 11 (1): 2–16. doi:10.1002/(SICI)1097-0231(19970115)11:1<2::AID-RCM768>3.0.CO;2-V.

Gross, J. H. 2011. *Mass Spectrometry.* 2. ed. Springer-Verlag Berlin Heidelberg. ISBN: 9783642423468. doi:10.1007/978-3-642-10711-5.

Gunaratne, K. D. D., V. Prabhakaran, Y. M. Ibrahim, R. V. Norheim, G. E. Johnson, and J. Laskin. 2015. "Design and performance of a high-flux electrospray ionization source for ion soft landing." *Analyst* 140 (9): 2957–2963. doi:10.1039/C5AN00220F.

Hänel, D. 2004. *Molekulare Gasdynamik.* Vol. 1. Springer-Verlag Berlin Heidelberg. ISBN: 9783540350477. doi:10.1007/3-540-35047-0.

Hawkridge, A. M., L. Zhou, M. L. Lee, and D. C. Muddiman. 2004. "Analytical Performance of a Venturi Device Integrated into an Electrospray Ionization Fourier Transform Ion Cyclotron Resonance Mass Spectrometer for Analysis of Nucleic Acids." *Analytical Chemistry* 76 (14): 4118–4122. doi:10.1021/ac0496771.

Heck, A. J. R. 2008. "Native mass spectrometry: a bridge between interactomics and structural biology." *Nature Methods* 5. ISSN: 1548-7105. doi:10.1038/nmeth.1265.

Hinze, J. O. 1975. *Turbulence.* 2. ed. McGraw-Hill New York. ISBN: 9780070290372.

Kebarle, P., and L. Tang. 1993. "From Ions in Solution to Ions in the Gas Phase." *Analytical Chemistry* 65 (22): 972A–986A. doi:10.1021/ac00070a715.

Kelly, R. T., J. S. Page, R. Zhao, W.-J. Qian, H. M. Mottaz, K. Tang, and R. D. Smith. 2008. "Capillary-Based Multi Nanoelectrospray Emitters: Improvements in Ion Transmission Efficiency and Implementation with Capillary Reversed-Phase LC-ESI-MS." *Analytical Chemistry* 80 (1): 143–149. doi:10.1021/ac701647s.

Kelly, R. T., A. V. Tolmachev, J. S. Page, K. Tang, and R. D. Smith. 2010. "The ion funnel: Theory, implementations, and applications." *Mass Spectrometry Reviews* 29 (2): 294–312. doi:10.1002/mas.20232.

Kolmogoroff, A. N. 1941. "The local structure of turbulence in incompressible viscous fluid for very large Reynolds numbers." *C.R. Acad. Sci. URSS* 30.

Konermann, Lars, Elias Ahadi, Antony D. Rodriguez, and Siavash Vahidi. 2013. "Unraveling the Mechanism of Electrospray Ionization." *Analytical Chemistry* 85 (1): 2–9. doi:10.1021/ac302789c.

Krah, P. 2018. "Numerical investigation of fluid dynamic aspects of an electrodynamic ion funnel." Master's thesis, Technische Universität Berlin.

Kyriakidis, L. 2019. "Investigation of ion transport in an ion funnel with compressible gas flow." Master's thesis, Technische Universität Berlin.

Laufer, J. 1954. "The structure of turbulence in fully developed pipe flow." https://ntrs.nasa.gov/search.jsp?R=19930092199.

Leney, A. C., and A. J. R. Heck. 2017. "Native Mass Spectrometry: What is in the Name?" *Journal of the American Society for Mass Spectrometry* 28. ISSN: 1044-0305. doi:10.1021/jasms.8b05378.

Lijo, V., H. D. Kim, and T. Setoguchi. 2010. "Analysis of Choked Viscous Flows through a Constant Area Duct." *Proceedings of the Institution of Mechanical Engineers, Part G: Journal of Aerospace Engineering* 224 (11): 1151–1162. doi:10.1243/09544100JAERO785.

Lin, B., and J. Sunner. 1994. "Ion transport by viscous gas flow through capillaries." *Journal of the American Society for Mass Spectrometry* 5 (10): 873–885. doi:10.1021/jasms.8b00489.

Litherland, A. E., X-L. Zhao, and W. E. Kieser. 2011. "Mass spectrometry with accelerators." *Mass Spectrometry Reviews* 30 (6): 1037–1072. doi:10.1002/mas.20311.

Liu, Q., and O. V. Vasilyev. 2007. "A Brinkman penalization method for compressible flows in complex geometries." *Journal of Computational Physics* 227 (2): 946–966. ISSN: 0021-9991. doi:10.1016/j.jcp.2007.07.037.

Lui, W. W., C. -. Xu, W.-P. Huang, K. Yokoyama, and S. Seki. 1999. "Full-vectorial mode analysis with considerations of field singularities at corners of optical waveguides." *Journal of Lightwave Technology* 17 (8): 1509–1513. ISSN: 1558-2213. doi:10.1109/50.779183.

Mason, E. A., and E. W. McDaniel. 1988. "Transport Properties of Ions in Gases." John Wiley & Sons, Ltd. ISBN: 9780471883852. doi:10.1002/3527602852.

Mayer, T., and H. Borsdorf. 2016. "Ion transfer from an atmospheric pressure ion funnel into a mass spectrometer with different interface options: Simulation-based optimization of ion transmission efficiency." *Rapid Communications in Mass Spectrometry* 30 (3): 372–378. doi:10.1002/rcm.7451.

Modesti, D., and S. Pirozzoli. 2019. "Direct numerical simulation of supersonic pipe flow at moderate Reynolds number." *International Journal of Heat and Fluid Flow* 76:100–112. ISSN: 0142-727X. doi:10.1016/j.ijheatfluidflow.2019.02.001.

Mohseni, K., and T. Colonius. 2000. "Numerical Treatment of Polar Coordinate Singularities." *Journal of Computational Physics* 157 (2): 787–795. ISSN: 0021-9991. doi:10.1006/jcph.1999.6382.

Murphy, H. R., and D. R. Miller. 1984. "Effects of nozzle geometry on kinetics in free-jet expansions." *The Journal of Physical Chemistry* 88 (20): 4474–4478. doi:10.1021/j150664a005.

Page, J. S., R. T. Kelly, K. Tang, and R. D. Smith. 2007. "Incorporation of a flared inlet capillary tube on a Fourier transform ion cyclotron resonance mass spectrometer." *Journal of the American Society for Mass Spectrometry* 18:1582–1590. ISSN: 1879-1123. doi:10.1016/j.jasms.2007.05.018.

Page, J. S., I. Marginean, E. S. Baker, R. T. Kelly, K. Tang, and R. D. Smith. 2009. "Biases in ion transmission through an electrospray ionization-mass spectrometry capillary inlet." *Journal of the American Society for Mass Spectrometry* 20 (12): 1879–1123. doi:10.1016/j.jasms.2009.08.018.

Pauly, M., M. Sroka, J. Reiss, G. Rinke, A. Albarghash, R. Vogelgesang, H. Hahne, B. Kuster, J. Sesterhenn, K. Kern, et al. 2014. "A hydrodynamically optimized nano-electrospray ionization source and vacuum interface." *Analyst* 139 (8): 1856–1867. doi:10.1039/C3AN01836A.

Peña Fernández, J. J., and J. Sesterhenn. 2017. "Compressible starting jet: pinch-off and vortex ring–trailing jet interaction." *Journal of Fluid Mechanics* 817:560–589. doi:10.1017/jfm.2017.128.

Pirozzoli, S., M. Bernardini, and F. Grasso. 2010. "Direct numerical simulation of transonic shock/boundary layer interaction under conditions of incipient separation." *Journal of Fluid Mechanics* 657:361–393. doi:10.1017/S002211201000171 0.

Prandtl, L., K. Oswatitsch, and K. Wieghardt. 1993. *Führer durch die Strömungslehre* [in ger]. 9., verb. u. erw. Aufl., korr. Nachdr. Braunschweig u.a. : Vieweg. ISBN: 9783528282097.

Purcell, E. M. 1965. *Berkely Physics Course, Vol II Electricity and Magnetism.* McGraw-Hill, Inc. ISBN: 9780070048591.

Rauschenbach, S., M. Ternes, L. Harnau, and K. Kern. 2016. "Mass Spectrometry as a Preparative Tool for the Surface Science of Large Molecules." *Annual Review of Analytical Chemistry* 9 (1): 473–498. doi:10.1146/annurev-anchem-071015-041633.

Reiss, J., and J. Sesterhenn. 2014. "A conservative, skew-symmetric finite difference scheme for the compressible Navier–Stokes equations." *Computers & Fluids* 101:208–219. ISSN: 0045-7930. doi:10.1016/j.compfluid.2014.06.004.

Reynolds, O. 1895. "IV. On the dynamical theory of incompressible viscous fluids and the determination of the criterion." *Philosophical Transactions of the Royal Society of London. (A.)* 186:123–164. doi:10.1098/rsta.1895.0004.

Rinke, G., S. Rauschenbach, S. Schrettl, T. N. Hoheisel, J. Blohm, R. Gutzler, F. Rosei, H. Frauenrath, and K. Kern. 2015. "Soft-landing electrospray ion beam deposition of sensitive oligoynes on surfaces in vacuum." Special Issue: MS 1960 to Now, *International Journal of Mass Spectrometry* 377:228–234. ISSN: 1387-3806. doi:10.1016/j.ijms.2014.06.026.

Schlichting, H., and K. Gersten. 2017. *Boundary-Layer Theory.* Ninth Edition. Springer-Verlag Berlin Heidelberg. ISBN: 9783662529171.

Shaffer, S. A., D. C. Prior, G. A. Anderson, H. R. Udseth, and R. D. Smith. 1998. "An Ion Funnel Interface for Improved Ion Focusing and Sensitivity Using Electrospray Ionization Mass Spectrometry." *Analytical Chemistry* 70 (19): 4111–4119. doi:10.1021/ac9802170.

Shaffer, S. A., K. Tang, G. A. Anderson, D. C. Prior, H. R. Udseth, and R. D. Smith. 1997. "A novel ion funnel for focusing ions at elevated pressure using electrospray ionization mass spectrometry." *Rapid Communications in Mass Spectrometry* 11 (16): 1813–1817. doi:10.1002/(SICI)1097-0231(19971030)11:16<1813::AID-RCM87>3.0.CO;2-D.

Shaffer, S. A., A. Tolmachev, D. C. Prior, G. A. Anderson, H. R. Udseth, and R. D. Smith. 1999. "Characterization of an Improved Electrodynamic Ion Funnel Interface for Electrospray Ionization Mass Spectrometry." *Analytical Chemistry* 71 (15): 2957–2964. doi:10.1021/ac990346w.

Shapiro, A. H. 1953. *The Dynamics and Thermodynamics of Compressible Fluid Flow, Vol. 1.* Vol. 1. Wiley. ISBN: 9780471066910.

Shen, C. 2006. *Rarefied gas dynamics: fundamentals, simulations and micro flows.* Springer-Verlag Berlin Heidelberg. ISBN: 9783540272304. doi:10.1007/b138784.

Skoblin, M. G., A. V. Chudinov, I. V. Sulimenkov, V. S. Brusov, A. A. Makarov, E. R. Wouters, and V. I. Kozlovskiy. 2017. "Numerical simulation of ion transport in an atmosphere-to-vacuum interface taking into account gas dynamics and space charge." *European Journal of Mass Spectrometry* 23 (4): 187–191. doi:10.1177/1469066717719556.

Skoblin, M., A. Chudinov, I. Soulimenkov, V. Brusov, and V. Kozlovskiy. 2017. "Gas Flow in the Capillary of the Atmosphere-to-Vacuum Interface of Mass Spectrometers." *Journal of the American Society for Mass Spectrometry* 28 (10): 2132–2142. doi:10.1021/jasms.8b05402.

Smedt, R. de, and J. G. van Bladel. 1987. "Field singularities near aperture corners" [in English]. *IEE Proceedings A (Physical Science, Measurement and Instrumentation, Management and Education, Reviews)* 134 (8): 694–698(4). ISSN: 0143-702X. doi:10.1049/ip-a-1.1987.0093.

Sommeijer, B. P., L. F. Shampine, and J. G. Verwer. 1998. "RKC: An explicit solver for parabolic PDEs." *Journal of Computational and Applied Mathematics* 88 (2): 315–326. ISSN: 0377-0427. doi:10.1016/S0377-0427(97)00219-7.

Stein, L. 2019. "Simulation and modeling of a Helmholtz resonator under grazing turbulent flow." Doctoral Thesis, Technische Universität Berlin. doi:10.14279/depositonce-8183.

Su, P., H. Hu, J. Warneke, M. E. Belov, G. A. Anderson, and J. Laskin. 2019. "Design and Performance of a Dual-Polarity Instrument for Ion Soft Landing." *Analytical Chemistry* 91 (9): 5904–5912. doi:10.1021/acs.analchem.9b00309.

Tang, K., J. S. Page, R. T. Kelly, and R. D. Smith. 2012. Low pressure electrospray ionization system and process for effective transmission of ions 8173960, filed May 2012.

Thompson, J. F., Z. U. A. Warsi, and C. W. Mastin. 1985. *Numerical Grid Generation: Foundations and Applications.* Elsevier North-Holland, Inc. ISBN: 9780444009852.

Thomson, J. J. 1913. "Bakerian Lecture: Rays of positive electricity." *Proceedings of the Royal Society of London. Series A, Containing Papers of a Mathematical and Physical Character* 89 (607): 1–20. doi:10.1098/rspa.1913.0057.

Tolmachev, A. V., I. V. Chernushevich, A. F. Dodonov, and K. G. Standing. 1997. "A collisional focusing ion guide for coupling an atmospheric pressure ion source to a mass spectrometer." *Nuclear Instruments and Methods in Physics Research Section B: Beam Interactions with Materials and Atoms* 124 (1): 112–119. ISSN: 0168-583X. doi:10.1016/S0168-583X(97)00068-2.

Traeger, J. C. 2016. "The Development of Electron Ionization." In *The Encyclopedia of Mass Spectrometry*, edited by Michael L. Gross and Richard M. Caprioli, 77–82. Boston: Elsevier. ISBN: 9780080438481. doi:10.1016/B978-0-08-043848-1.00008-0.

Tridas, E., J. M. Anthony, R. Guldiken, and R. Schlaf. 2015. "Enhanced simulation of an RF ion funnel including gas turbulence." *Journal of Mass Spectrometry* 50 (1): 206–211. doi:10.1002/jms.3519.

Varentsov, V., and M. Wada. 2004. "Computer experiments on ion beam cooling and guiding in fair-wind gas cell and extraction RF-funnel system." International Workshop on Beam Cooling and Related Topics, *Nuclear Instruments and Methods in Physics Research Section A: Accelerators, Spectrometers, Detectors and Associated Equipment* 532 (1): 210–215. ISSN: 0168-9002. doi:10.1016/j.nima.2004.06.078.

Verbeck, G., W. Hoffmann, and B. Walton. 2012. "Soft-landing preparative mass spectrometry." *Analyst* 137 (19): 4393–4407. doi:10.1039/C2AN35550G.

Whitehouse, C. M., R. N. Dreyer, M. Yamashita, and J. B. Fenn. 1985. "Electrospray interface for liquid chromatographs and mass spectrometers." *Analytical Chemistry* 57 (3): 675–679. doi:10.1021/ac00280a023.

Wißdorf, W., D. Müller, Y. Brachthäuser, M. Langner, V. Derpmann, S. Klopotowski, C. Polaczek, H. Kersten, K. Brockmann, and T. Benter. 2016. "Gas Flow Dynamics in Inlet Capillaries: Evidence for non Laminar Conditions." *Journal of the American Society for Mass Spectrometry* 27 (9): 1550–1563. doi:10.1021/jasms.8b05339.

Wissdorf, W., L. Pohler, S. Klee, D. Müller, and T. Benter. 2012. "Simulation of Ion Motion at Atmospheric Pressure: Particle Tracing Versus Electrokinetic Flow." *Journal of the American Society for Mass Spectrometry* 23 (2): 397–406. doi:10.1021/jasms.8b04218.

Wu, S., K. Zhang, N. K. Kaiser, J. E. Bruce, D. C. Prior, and G. A. Anderson. 2006. "Incorporation of a flared inlet capillary tube on a Fourier transform ion cyclotron resonance mass spectrometer." *Journal of the American Society for Mass Spectrometry* 17:772–779. ISSN: 1044-0305. doi:10.1021/jasms.8b02675.

Wu, X., P. Moin, R. J. Adrian, and J. R. Baltzer. 2015. "Osborne Reynolds pipe flow: Direct simulation from laminar through gradual transition to fully developed turbulence." *Proceedings of the National Academy of Sciences* 112 (26): 7920–7924. ISSN: 0027-8424. doi:10.1073/pnas.1509451112.

Zhou, L., L. Zhai, B. Yue, E. D. Lee, and M. L. Lee. 2006. "New interface plate for microspray ionization mass spectrometry." *Analytical and Bioanalytical Chemistry* 385 (6): 1087–1091. doi:10.1007/s00216-006-0523-1.

Zhou, X., and Z. Ouyang. 2016. "Following the Ions through a Mass Spectrometer with Atmospheric Pressure Interface: Simulation of Complete Ion Trajectories from Ion Source to Mass Analyzer." *Analytical Chemistry* 88 (14): 7033–7040. doi:10.1021/acs.analchem.6b00461.

Zikanov, O. Y. 1996. "On the instability of pipe Poiseuille flow." *Physics of Fluids* 8 (11): 2923–2932. doi:10.1063/1.869071.